Bioengineering Analysis of Traumatic Brain Injury

Shijia Pan

Queens' College

SEPTEMBER 2021

This thesis is submitted for the degree of Doctor of Philosophy

Declaration

This thesis is the result of my own work and includes nothing which is the outcome of work done in collaboration except as declared in the Preface and specified in the text. I further state that no substantial part of my thesis has already been submitted, or, is being concurrently submitted for any such degree, diploma or other qualification at the University of Cambridge or any other University or similar institution except as declared in the Preface and specified in the text. It does not exceed the prescribed word limit for the relevant Degree Committee.

Abstract

Bioengineering Analysis of Traumatic Brain Injury

Shijia Pan

Traumatic brain injury (TBI) is a serious health concern affecting over a million people in the UK. Brain shift and herniation, which are closely related to severe disability or death, are important signs of abnormally elevated intracranial pressure (ICP) or space-occupying intracranial mass after trauma.

This research aims to use medical image computing and biomechanical modelling techniques to characterise the specific deformation field of brain tissues under various TBI scenarios and strengthen the biomechanical understanding across the full spectrum of TBI.

Medical image computing provides the research with a solid clinical grounding. To better interpret the neuro-images, three computational tools have been developed, including a CT preprocessing pipeline, an automatic mid-sagittal plane detector and an automatic brain extractor. Using these tools, a novel concept of midplane shift (MPS) is developed to quantitatively evaluate the brain herniation condition across the mid-sagittal plane. In the meantime, a lesion heatmap is generated to quantify the asymmetric haematoma volumes across the mid-sagittal plane. The MPS heatmaps generated for 33 TBI patients with heterogeneous brain pathologies demonstrate highly similar shift patterns. Together with the lesion heatmap, a brain deformation mechanism has been presented: the brain will not deform randomly in response to trauma, instead, it will only deform in a regulated mechanism so that the deformation is directed and restricted to the soft ventricular region, thanks to the anatomic structures of the head such as the falx. The MPS heatmap, the lesion heatmap, together with the novel CT parameters derived from them, provide a rich abundance of information on intracranial brain herniation, for a more complete overview of TBI from medical images.

Biomechanical modelling, being one of the most important tools in trauma biomechanics, has been used to quantitatively simulate the brain shift and herniation condition caused by various intracranial lesions and increasing ICP. Preliminary finite element models reconstructed from the Virtual Human Project have demonstrated some limitations. To resolve the observed deficiencies, an advanced high-fidelity patient-specific FE brain

model is constructed and explicitly assessed to optimise its injury simulation performance with the help of the developed medical image computing tools. During simulation, the patient-specific traumatic injuries have been reconstructed by imposing both the primary lesion and the secondary injury. The primary lesion simulation is achieved mechanically by "indenting" a rigid lesion surface simulating the shape of the haematoma to the brain model. While the secondary swelling is modelled with a thermal-expansion-based method to simulate the bulging brain. Using this approach, the observed brain herniation can be decomposed into a deformation due to pure mass effect of space-occupying primary lesion and a shift as a result of secondary swelling. The head injuries of six different TBI patients have been reconstructed and simulated using the prescribed method. The realistic case study suggested that the subdural haematoma patients, as compared to the epidural haematoma patients, were exposed to more significant secondary swelling, which agrees well with the historical clinical findings. In addition to the realistic TBI case studies, an idealised traumatic lesion simulation is performed to investigate the role of lesion morphology and the lesion locations of onsets, in brain herniations during TBI. It is suggested by the idealised TBI cases that the brain is more sensitive to lesion that is more concentrated spatially, if lesion volumes and lesion locations were exactly the same. Moreover, in terms of lesion locations, lesions that strikes on the temporal region and the anterior region are more likely to lead to greater brain deformation, if other lesion morphologies were equal and no secondary swelling considered.

Ultimately, the developed tools are expected to help clinicians better understand and predict the brain behaviour after the onset of TBI and during subsequent injury evolution.

Acknowledgements

First and foremost, I would like to extend my sincere gratitude to my supervisor, Prof. Michael Sutcliffe, who has provided continuous encouragements, generous guidance and kind support during my research. It was a great pleasure to work with him.

I am indebted to Mr. Angelos Kolias for taking the time to co-supervise me, for inspiring me with great ideas, for providing clinical imaging data for me, and for sharing his clinical expertise with me.

I am grateful to Dr. Virginia Newcombe for being ever so kind to show interest in my research, for being supportive to provide clinical data set for me and for continuously providing her clinical expertise for me.

I am thankful to Prof. David Menon for sharing his expertise in brain imaging analysis with me.

My colleagues Mr. Hadie Adams, Miss. Selma Tulu and Mr. Eric Thelin have helped with the imaging data annotations and segmentations for the clinical aspects of the thesis. Miss. Sinead Cook, a former MEng student from Prof. Sutcliffe, has inspired me a lot at the beginning of my research. I would also like to thank the W.D.Armstrong Trust for funding this research.

My external collaborators, Dr. Ben Glocker from Imperial College London and Prof. Alain Goriely from University of Oxford, have kindly provided suggestions on the image analysis and brain material properties respectively.

I would like to thank my parents, Mr. Qingguo Pan and Miss. Jianjun Hu. Their love has been an anchor to me all the time. I would also like to thank my partner Mr. Yizhou Shi and my cat Ricecake. Their company is very important to me during my writing-up period.

It would not have been possible for me complete the current research successfully without their help.

Contents

Declaration **3**

Abstract **i**

Acknowledgements **iii**

List of Figures **xiii**

List of Tables **xiv**

1 Background **1**

1.1 Introduction 1

1.2 Clinical review 2

1.2.1 Heterogeneity and complication of traumatic brain injury 2

1.2.2 Assessments of traumatic brain injury 5

1.2.3 TBI treatments and decompressive craniectomy 8

1.3 Bioengineering review 12

1.3.1 TBI on a microscopic level 12

1.3.2 Material models of brain tissue 13

1.3.3 Recent computational models 16

1.3.4 Validation of computer models 20

1.4 Scope of the project 21

2 Computational tools for image analysis **24**

2.1 Introduction 24

2.2 Methods 25

2.2.1 CT preprocessing pipeline 26

2.2.2 Automatic mid-sagittal plane detector 33

2.2.3 Automatic brain extractor 37

2.2.4 3D brain shift analysis 45

2.3 Results 49

2.3.1 CT preprocessing pipeline 49

2.3.2 Automatic mid-sagittal plane detector 55

2.3.3 Automatic brain extractor 58

2.3.4 3D brain shift analysis 63

2.4 Concluding discussion 64

3 Interpretation of CT parameters related to brain deformation 66

3.1 Introduction 66

3.2 Methods 67

3.2.1 Correlation analysis for intracranial mass lesion and brain midline shift 67

3.2.2 Properties of midplane shift (MPS) 71

3.2.3 Intracranial lesion analysis 72

3.3 Results 74

3.3.1 Correlation analysis for intracranial mass lesion and brain midline shift 74

3.3.2 Properties of midplane shift (MPS) 84

3.3.3 Intracranial lesion analysis 91

3.4 Concluding discussion 95

4 Model development **97**

4.1 Introduction 97

4.2 Preliminary model development 98

4.2.1 Construction of Preliminary FE model 98

4.2.2 Experimental simulation using preliminary FE model 100

4.2.3 Preliminary FE model simulation results 102

4.2.4 Concluding discussion 106

4.3 Patient-specific model development 107

4.3.1 Construction of patient-specific FE model 108

4.3.2 Patient specific simulation with realistic model 111

4.3.3 Patient-specific model simulation results 115

4.3.4 Concluding discussion 119

5 Model assessment **121**

5.1 Introduction 121

5.2 Numerical parameter tuning 122

5.2.1 Methods 122

5.2.2 Results 125

5.3 Simulating traumatic brain injury 127

5.3.1 Methods 128

5.3.2 Results 129

5.4 Brain material property . . . 136
5.4.1 Methods . . . 136
5.4.2 Results . . . 138
5.5 Simulating behaviour of ventricles . . . 141
5.5.1 Methods . . . 141
5.5.2 Results . . . 143
5.6 Concluding discussion . . . 149

6 Model simulation **151**
6.1 Introduction . . . 151
6.2 Realistic lesion simulation case studies . . . 152
6.2.1 Methods . . . 152
6.2.2 Results . . . 154
6.3 Idealised traumatic lesion simulations . . . 160
6.3.1 Methods . . . 160
6.3.2 Results . . . 165
6.4 Concluding discussion . . . 174

7 Conclusion and future work **176**
7.1 Conclusion . . . 176
7.1.1 Computational tools for image analysis . . . 176
7.1.2 Interpretation of CT parameters related to brain deformation . . . 177
7.1.3 Biomechanical model development . . . 177
7.1.4 Biomechanical model assessment . . . 178

7.1.5 Biomechanical model simulation 178

7.1.6 Summary 179

7.2 Limitations 179

7.3 Future work 180

List of Figures

1 Anatomic structures covering the brain 3

2 Common types of intracranial haemorrhages 3

3 Complications and importance of different pathophysiologic mechanisms . . 4

4 Illustration of brain herniation types 4

5 Diagram showing the thickness and angles of CT cuts, α. 6

6 Comparison of normal and pathological CT scans 7

7 Midline structures of brain 8

8 Measurement of midline shift 8

9 Common types of decompressive craniectomy 10

10 The patients' outcomes of RESCUEicp trial 11

11 Schematics showing axonal damage due to shearing 13

12 Plots of Young's modulus vs Poisson's ratio for various brain tissues 15

13 The finite element mesh of the high fidelity 3D model of traumatic brain injury 16

14 Finite element model with unilateral craniectomy 17

15 Personalised finite element model of the head 18

16 General FE mesh of one patient 18

17 Contour plots showing deformation of the brain model under chronic subdural haematoma 19

18 Displacement and strain level of the brain tissue after DC 21

19 Flowchart outlining essential steps in CT preprocessing pipeline 26

20 Illustration of image resampling for CT scans. 30

21 Illustration of anterior commissure in sagittal CT slice. 31

22 Illustration of image registration for CT scans. 31

23 Flowchart denoting the algorithm for automatic midplane detector 33

24 Illustration of using PCA to find the principal axis for a 3D object 34

25 Data clouds for skull and candidate planes of symmetry computed by the PCA method 36

26 Illustration of splitting and mirroring procedure for symmetry matching . . 37

27 Definition of orientation and skew angles used in midplane finder algorithm. 37

28 Simplified brain anatomy 38

29 Flowchart denoting the steps for automatic brain extractor 39

30 The performance of BET FSL on original CT scan and smoothed CT scan 39

31 The performance of extra brain remover algorithm 41

32 Flowchart denoting the algorithm for foramen magnum detector 42

33 Illustration of FM on sagittal skull contour 43

34 Illustration of the detected FM and the true FM. 44

35 Example results of the automatic FM detector 45

37 Illustration of the actual midplane and the ideal midplane. 46

36 Manually delineated actual midline and ideal midline shown in different views 46

38 Midplane shift heatmap 48

39 Illustration of the effect of gantry tilt correction 49

40 Distribution of intensities in HU for a typical head CT image 51

41 Example of individual CT head scan before and after registration 53

42 Examples of co-registered CT head scans 54

43 The calculated midplane shown on the volume rendering of a head CT scan 56

44 The performance of the computed midplane at different depth 57

45 Rendering of post-craniectomy scan with computed midplane 58

46 The effect of orientation correction based on the computed midplane 59

47 Examples of computed brain masks and their 3D meshes 60

48 Examples of CTs that are incompatible with current brain extractor 61

49 Automatic and manual intracranial volume analysis. Note, the dashed line indicates automatic volume equal to manual volume. 62

50 Example MPS heatmaps 62

51 The falx cerebri shown in 3D 63

52 Illustration of the lesion annotation methods 69

53 Lesion heat map generated for a SDH patient 73

54 Distribution of midline shifts in TBI scans 75

55 Multivariate linear regression between intracranial mass lesions and MLS. . 80

56 Evaluation of the lesion-MLS model performance in patients under other clinical conditions. 81

57 Overlaid skull contours from computed MPS heat-maps 85

58 Illustration of MPS heatmaps 86

59 Locations of MLS measurements plotted on sagittal skull contour. 89

60 Plots of MLS vs. brain volume shift. 90

61 Example MPS heat-maps. 91

62 Example lesion heat-maps. 93

63 Graphic representation of the relative locations for lesion centroid and MPS centroid on skull contour 94

64 Reconstruction of the preliminary FE model 98

66 Comparison of MPS analysis for experimental simulations and clinical observations. 104

67 Illustration of analytical brain construction using splines and cross-sections in Autodesk Inventor. 109

68 Patient-specific analytical head model including (a) the assembled head, (b) the brain, (c) the cerebellum, (d) the cerebral falx, (e) the tentorium, (f) the ventricles and (g) the skull. 111

69 Illustration of the indentation process (a), (b) and (c) as the rigid lesion surface indents deeper into the brain parenchyma. 112

70 Illustration of the re-creation of unique lesion profiles from a CT slice to the computational model using splines in Inventor. 113

71 Illustration of the re-created unique lesion surface. 114

72 Illustration of the patient's intracranial condition change before and after the attack of SDH. 117

73 Comparison of clinically and experimentally derived MPS for the SDH patient 118

74 Percent error in maximum displacement U_{max} on the surface of third ventricle compared to the finest mesh, plotted against the total number of elements in the brain model 126

75 Brain deformation results from meshes of approximately 3,000 (left), 25,000 (middle) and 500,000 (right) elements respectively. 127

76 Illustration of brain transverse deformation contour under unilateral and universal swelling. 130

77 Illustration of simulation results when swelling effect is superimposed to lesion effect in three different swelling sites. 131

78 Illustration of experimental MLS throughout simulation 133

79 Comparison of clinical MPS (a) and experimental MPS (b) 134

80 Comparison of brain deformation contour under indentation plus thermal expansion (a) and pure thermal expansion (b) 135

81 Plots of simulated MLS at different compressibility. 139

82 Simulated MLS plotted against falx stiffness in logarithmic scale. 141

83 Computational MPS results from models with falx stiffness of (a) 0.1 MPa, (b) 31.5 MPa and (c) 100 MPa respectively. 142

84 Maximum deformation U_{max} on the surface of the third ventricle plotted against ventricular bulk modulus. 145

85 Illustration of model volume change for different effective compressibility of the ventricles. 146

86 Illustration of brain deformation contour at different levels of ventricle bulk modulus (a) 0.0025 MPa (b) 0.025 MPa (c) 0.25 MPa. 147

87 Illustration of maximum displacement U1 on the surface of the three ventricles plotted against ventricle bulk modulus. 149

88 Illustration of pathologies in six different TBI patients. 153

89 Illustration of reconstructed lesion geometry for six different TBI patients plotted on brain silhouette in Autodesk Inventor. 154

90 Illustration of simulated MPS contour and clinical MPS heatmap for six different TBI patients 158

91 Illustration of the relative contributions to MLS. 159

92 Modelling view of the synthetic lesions. 161

93 Synthetic lesion indentation surface 162

94 Overview of synthetic lesions at different locations. 164

95 Comparison of S40 and S80 indentation surfaces. 165

96 llustration of the resultant MLS when synthetic lesions were applied at the five different lesion locations 168

97 Brain response to lesion height 169

98 Brain response to lesions on the saggital axis 169

99 Illustration of the brain deformation condition at axial slice 34 and 38 for lesion locations 1, 2, 3, 4 and 5 respectively 170

100 Comparison of brain MPS at different axial slices for all five lesion locations. 171

101 Overview of brain MPS heat maps 173

List of Tables

1 Definition of clinical terms 2

2 Definition of material models 14

3 Descriptive statistics for the lesion annotation and correlation analysis results 76

4 Multivariate linear regression results 79

5 Mortality rate for severeness and all categories of TBIs under different MLS prediction conditions. 84

6 Statistics for the derived CT parameters from MPS 88

7 The set of units used in ABAQUS simulations for all chapters 100

8 Table of hyperelastic models 137

9 Table of hyperelastic models and the corresponding simulation results. . . . 140

10 Table of basic lesion information for six TBI patients 154

11 Table of basic information for the reconstructed lesion model for six TBI patients 155

12 Table of idealised lesion characteristics 166

13 Table of comparison for the morphological characteristics of S40 and S80 lesion groups 166

Nomenclature

CONT Poroviscoelastic

CPP Cerebral perfusion pressure

CSF Cerebral spinal fluid

CT Computed tomography

DAI Diffuse axonal injury

DC Decompressive craniectomy

EDH Epidural haematoma

FE Finite element

GCS Glasgow coma scale

HU Hounsfield unit

ICH Intracerebral haemorrhage

ICP Intracranial pressure

IVH Intraventricular haemorrhage

MRI Magnetic resonance imaging

PCA Principal component analysis

PCO Peri-contusion oedema

PE Poroelastic

PH Petechial haemorrhage

PN Pneumocephalus

PTA Post traumatic amnesia

PVE Haemorrhagic contusion

PVE Poroviscoelastic

SAH Subarachnoid haemorrhage

SDH Subdural haematoma

TBI Traumatic brain injury

VE Viscoelastic

1 Background

1.1 Introduction

Traumatic brain injury (TBI) has been recognised as a rising health and socioeconomic problem affecting over one million people, at a cost to the economy of £15 billion in the UK each year [1]. TBI is any injury to the brain caused by a sudden onset of external forces, such as direct impact, rapid acceleration, a penetrating object, or blast waves from an explosion [2]. TBI is most frequently associated with falls, road accidents, collisions, sports-related impacts and violence [1]. Recent years have witnessed a surge in the incidence of TBI, mainly due to the boost in motor-vehicle use in low-income and mid-income countries [2]. The rates of inpatient admissions are highest among elderly people who are prone to falls, but are also escalating among children and young adults [1]. Depending on the nature, intensity and duration of the forces [2], the consequences of TBI varies greatly in severity: from headaches and dizziness in the mild cases to permanent neurobiological impairment and death in severe cases [3]. Follow-up studies of TBIs suggest that a significant proportion of the TBI victims, though not diagnosed as severe upon hospital admission, were affected by premature mortality. Moreover, the survivors were likely to live with continuing physical, cognitive, emotional and behavioural problems [1]. Such TBI-related mental and personality disorder, in a long term, could result in high unemployment, financial hardship, loss of independence and substantial family burden. Studies around the globe indicate well beyond doubt that TBI is causally implicated in criminal offending, increasing the likelihood of crime by at least 50% [1]. Overall, TBI has been recognised as the leading cause of death and disability in people aged 1-40 in the UK [4], and is among the top three causes of injury-related medical cost in Europe [2]. Moreover, the costs for TBI-related disability and lost productivity even outweighs the costs for acute medical care, placing a heavy financial burden on the society.

Given the wide-ranging and long-lasting nature of its various related disabilities and disorientations [1], TBI seriously affects the quality of life and well-being of individuals as well as their families. The prevalence of TBI calls for a thorough understanding of its injury progression mechanism. Historically, the primary research topics can be classified as: treatments, assessment measures, outcome predictors, pathology history, guidelines and consensus statements, epidemiology and experimental models of TBI [5]. In fact, over one-third of the top 50 cited articles typically studied predictors of outcome

[5], representing a sustained research focus in such a field. Accurate diagnosis and assessment, together with improved predictors, would further advance our knowledge of TBI mechanisms, enhance the medical decision making capacity, improve patients' outcomes, and ultimately minimise the adverse socioeconomic effects of TBI.

In this first chapter of the thesis, a systematic literature review on TBI was presented. The literature review composed of two main parts: the clinical review and the bioengineering review. On the one hand, the clinical review in section 1.2 introduced the heterogeneity and complication of TBI, its relevant assessment procedures as well as the surgical and non-surgical treatments, from a clinical point of view. On the other hand, the bioengineering review summarised the material models of brain tissue, the recent computational models for TBI and the validation of computer models, from a biomechanical point of view. At the end of chapter 1, the scope of the project was defined.

1.2 Clinical review

Clinical term	**Definition**
Haematoma	Accumulation of blood within the tissue planes
haemorrhages	Leakage of blood outside the blood vessel
Contusion	A region of injured brain tissue where blood capillaries have been ruptured
Diffuse axonal injury (DAI)	Extensive lesions in white matter tracts caused by shearing of brain tissues
Laceration	A deep cut or tear in tissue
Ischemia - hypoxia	Oxygen deprivation caused by insufficient blood supply
Cerebral oedema	Excess accumulation of water in the brain
ICP	Intracranial pressure: the pressure inside the skull
CPP	Cerebral perfusion pressure: the pressure difference driving cerebral blood flow and hence oxygen and metabolite delivery

Table 1: Definition of clinical terms

1.2.1 Heterogeneity and complication of traumatic brain injury

Fundamentally, brain damage could be classified as primary and secondary based on the injury process. Primary injury appears almost immediately at the moment of initial trauma, while secondary injury results from the pathophysiologic processes initiated by the primary injury and develops over a time period of hours and days. Pathophysiology refers to the disordered process or mechanisms associated with disease. The instant effects of primary injury leave a slim chance of medical intervention other than preventing the trauma itself. In contrast, secondary injury is potentially preventable by taking appropriate medical therapies to limit the complications. Table 1 defines the frequent clinical terms associated with TBI.

Pathoanatomy describes the location and anatomic characteristics of the abnormality to be targeted by a treatment [8]. The three main pathoanatomic sequelae of primary injury includes haematoma, contusion and diffuse axonal injury (DAI) [8]. Depending on the nature of the impact force, each of these categories could be subdivided by their location of onset, morphological distribution and multiplicity of different factors. Figure 1 describes the meninges encapsulating the brain. TBI could develop in any compartments of the head: going inwards from outside the skull, the injury types embrace scalp laceration and contusion, skull fracture, epidural and subdural haematoma, subarachnoid haemorrhage, brain contusion and laceration, intraparenchymal haemorrhage, intraventricular haemorrhage and DAI [8]. Figure 2 is a graphic illustration for some of the most typical haemorrhages inside the skull. DAI differs from such haemorrhagic lesions. DAI is characterised by shearing lesions at the grey-white

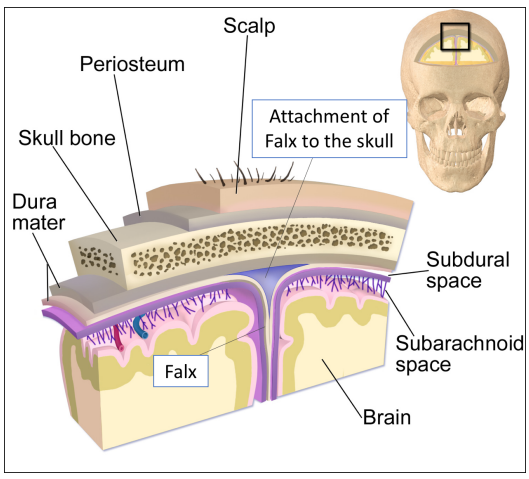

Figure 1: Anatomic structures covering the brain [6]

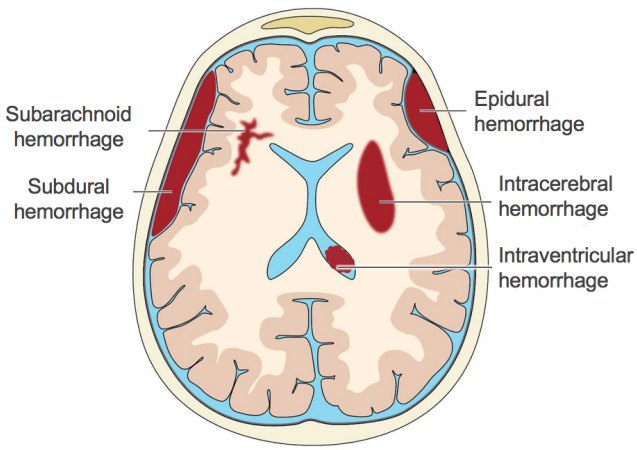

Figure 2: Common types of intracranial haemorrhages [7]

matter junction. Patients with DAI are usually in profound coma and have a poor outcome [8]. Overall, different compartments of the brain possess diverse biomechanical properties and react dissimilarly to trauma, leading to the heterogeneity of TBI patterns. The influence of various pathoanatomic injury characteristics on patients' outcome has long been recognised [8]. Therefore it is critical to develop a reliable and efficient classification system for TBI, and henceforth link specific patterns of injury with proper therapeutic interventions [8] for target-specific TBI management.

The temporal evolution of this primary damage results in sophisticated pathophysiologic cascades and secondary insults associated with inflammatory and neurotoxic process. As shown in Figure 3a and 3b, different primary damages might trigger different pathologies that contribute to different secondary injuries, but ischemic damage is superimposed on all three primary types of TBI. Brain oedema also develops as a result of TBI and the ischemic damage. Owing to the rigid nature of the skull, swelling of brain gives rise to escalating intracranial pressure (ICP), and consequently enhances the reduction of cerebral perfusion pressure (CPP), cerebral blood flow and oxygenation [9]. These effects, in turn, cause a deterioration in astrocytic swelling and worsen the raised ICP and ischemia, forming the vicious cycle of hypoxic ischemic injury. Such a vicious cycle, if left uninterrupted, could become devastating and cause brain herniation and death [9].

Brain herniation is a life-threatening phenomenon which normally occurs as a result of the growing haematoma and increasing ICP after trauma. Herniation refers to brain tissue displacement across a structure within the cranium. According to the locations and directions of the brain tissue motion, herniation can be classified into different

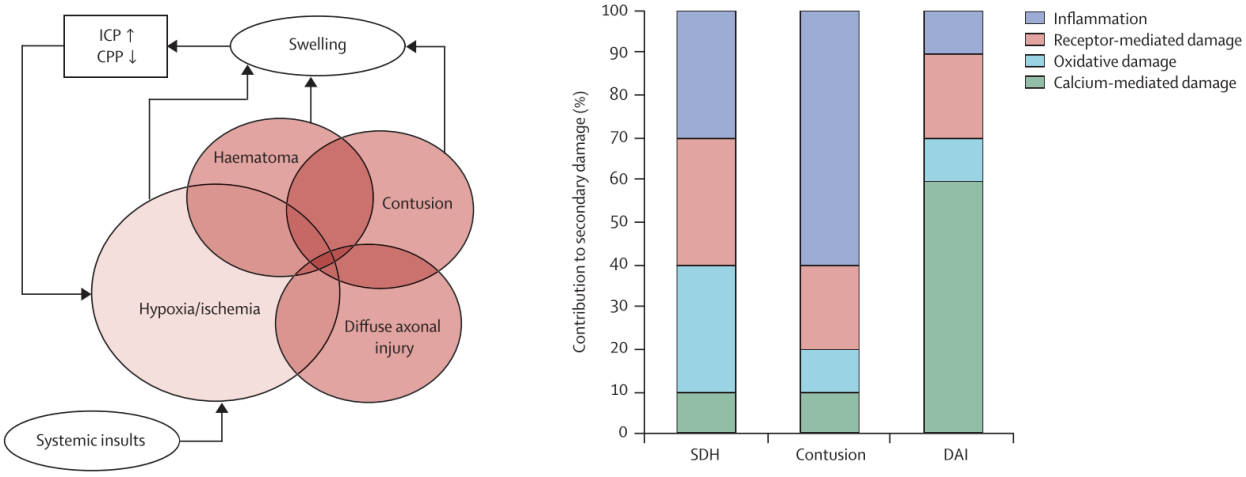

(a) The hypoxic-ischemia vicious cycle caused by various primary damage [2]

(b) The relative importance of different primary damages to secondary damage [2]

Figure 3: Complications and importance of different pathophysiologic mechanisms

types. Figure 4 illustrates the various types of brain herniations, among which subfalcine herniation is most commonly observed clinically. As shown in Figure 4, subfalcine herniation is the displacement of the cingulate gyrus under the falx and across the midline. In the supratentorial region, apart from subfalcine herniation, there exists other herniation types including uncal transtentorial herniation, central tentorial herniation and transcalvarial herniation. Furthermore, in the infratentorial region, upward transtentorial herniation and tonsillar herniation may be present as a result of trauma. It is critical to monitor and treat brain herniation in TBI management systems.

Thanks to the long pathophysiologic process of the secondary insults, opportunities are offered for the clinicians to make appropriate therapeutic decisions and limit adverse health effects. Often, the secondary insults, such as hypoxia, hypertension and seizures, could be considered as therapeutic targets for specific treatments. Alternatively, these could be utilised as prognostic variables to assist clinical decision making process, though challenges exist in monitoring of such pathophysiologic parameters [8].

1.2.2 Assessments of traumatic brain injury

Annually, hospital emergency departments witness a large number of TBI patients, among which the majority have minor or mild head injury and will not need specialist care, but others may suffer life-long disability and even die from the effects of complications of TBI.

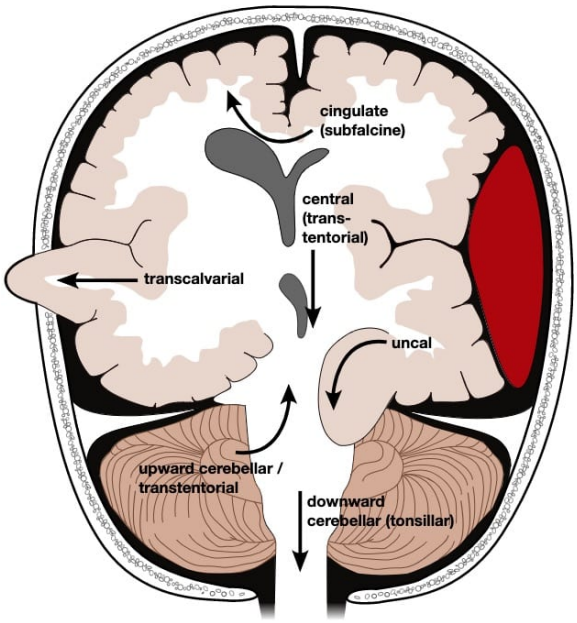

Figure 4: Illustration of brain herniation types [10]

As a result, it is of critical importance to efficiently distinguish the minority who are likely to continue having serious acute intracranial complications [4]. Through effective early detection and initial assessment, specialist intervention could be provided to those with life-threatening injuries to limit or prevent the secondary insults. In the meantime, those with a trivial risk factor can be discharged early to avoid unnecessary crowding on-site.

At present, the primary initial assessment criterion for TBI is the Glasgow Coma Scale (GCS) [11], a clinical scale that evaluates the level of consciousness and clinical severity. The GCS score comprises three components and assesses three aspects of patients' behaviour: motor responsiveness, verbal performance and eye opening [12], leading to a sum score between 3 and 15. Injuries are classified as severe, moderate and mild for GCS scores of 3-8, 9-13 and 14-15 respectively. This GCS score is commonly applied to guide immediate medical care after a brain injury, to continuously track their level of consciousness. Common mild TBI symptoms include fatigue, headaches and feelings of depression [13], which could be resolved by off-the-shelf pain relievers. Historically, good recovery is least associated with more severe TBIs, therefore, moderate and severe TBIs have received further assessments and treatments as compared to mild TBIs. However, follow-up studies of TBI patients indicate surprisingly minor difference in outcomes between moderate and mild TBIs. Namely, over half of the patients diagnosed with apparently mild injury were suffering from moderate and even severe disability a year later [1], which implies a potential flaw in the current GCS classification. In fact, this 15-point GCS has long been favoured by its standardised classification of injury severity and high inter-observer reliability [14]. Nevertheless, the prognostic capabilities of GCS by clinical severity is becoming more limited in modern practice, as the consciousness level may be obstructed in acute setting by confounders such as medical sedation [2]. Moreover, though GCS has proved exceptionally beneficial in early clinical management, it fails to present the specific pathoanatomic types and pathophysiologic mechanisms responsible for neurological deficits. More detailed assessment of brain damage is needed.

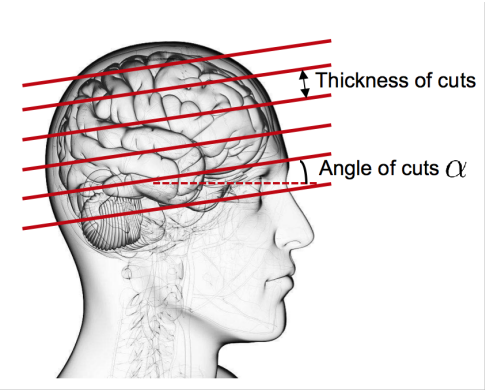

Figure 5: Diagram showing the thickness and angles of CT cuts. Note, α is also the gantry tilt angle.

In addition to GCS score, the length of post-traumatic amnesia (PTA) or loss of consciousness also indicates the severity of TBI. TBI is defined as moderate if the loss of

consciousness is between 15 minutes and 6 hours or a period of PTA between 1 hour and 24 hours [3]. While severe brain injury is characterised by an unconscious state longer than 6 hours, or PTA of greater than 24 hours [3]. Moreover, assessment of structural damage by neuroimaging has become routine in TBI management. In 2003, the NICE clinical guideline [4] has replaced skull radiography with computed tomography (CT) scanning as the primary imaging modality for head injury assessment. CT utilises a combination of X-rays from different angles to take cross-sectional images (known as slices) of the scanned object [15]. CT cuts could be performed at different angles and thickness, as shown in Figure 5, to produce a volumetric (3D) data revealing structures inside the object. Normally a cut thickness between 0.5 and 2 mm is determined as thin-cut , while thickness greater than 3 mm is referred to as thick-cut. CT scans are presented in Hounsfield Unit (HU, also known as CT number). Different substances possess diverse radiodensity and hence are associated with different HU. Namely, in the scenario of TBI, oedema and infarctions are associated with small HU and appear as hypo-dense (dark) structures in CT scans, while haemorrhage and bone trauma is associated with large HU and appear as hyper-dense (bright) structures [15]. As shown in Figure 6a and 6b, CT scans highlight intracranial bleeding, thereby enabling potential pathoanatomic classification. On the whole, CT scanning is preferred to other neuroimaging techniques such as magnetic resonance imaging (MRI) [16] for the following reasons:

- CT scan is usually completed within 5 minutes, while MRI takes up to an hour to complete. Such time efficiency is of critical importance in the acute phase.
- CT is less sensitive to patient movement than MRI
- CT is cheaper than MRI
- CT will not be affected by metal implants in patients

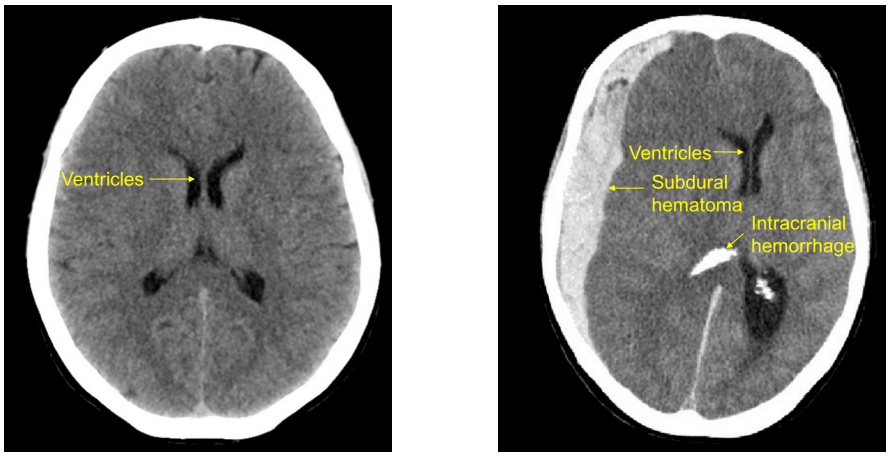

(a) Axial CT slice of a normal patient (b) Axial CT slice of a TBI patient

Figure 6: Comparison of normal and pathological CT scans

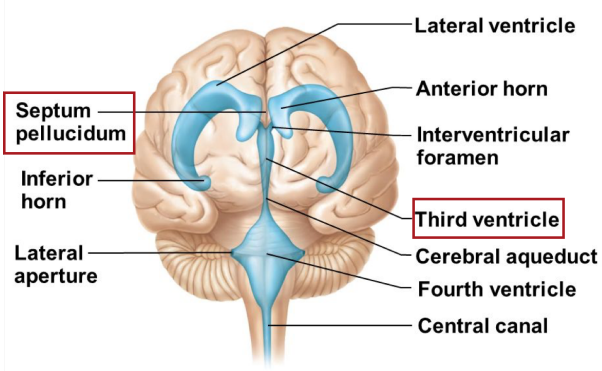

Figure 7: Midline structures of brain highlighted in red rectangular box [18]

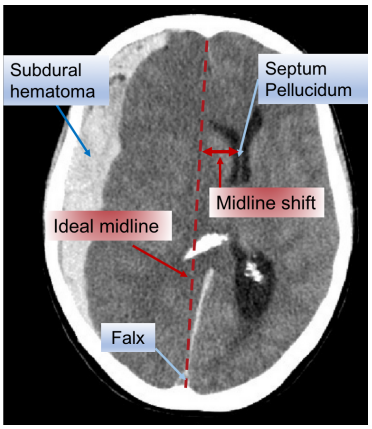

Figure 8: Measurement of midline shift

Midline shift (MLS) is an evident feature on brain CT imaging. It refers to the shift of brain structure from its centre line, caused by brain pathologies including tumour, haematoma or unbalanced pressure. In clinical practice, MLS is measured by the distance between a reference point and an imaginary midline. Three main structures are used as the reference point: the septum pellucidum, pineal gland and the third ventricle, all of which in normal brains, should be in the middle plane separating left and right hemispheres. The septum pellucidum is a thin, vertical double membrane separating the anterior horns of the left and right lateral ventricles, as shown in Figure 7. It is most frequently investigated by the clinicians as an indicator of midline shift. The imaginary midline is constructed by a vertical line connecting the anterior and posterior falx attachment to the skull. Then midline shift is manually measured by drawing a perpendicular line between the ideal midline and the deformed midline structure (*e.g.* septum pellucidum), as shown in Figure 8. In a clinical setting, on the one hand, the magnitude of MLS is considered as an indicator for the severity of TBI: the larger the MLS, the more likely a surgery should be carried out. On the other hand, MLS has serious implications as a prognostic factor to predict the postoperative restoration of consciousness [17] in patients with severe TBI.

Despite theses advantages, CT also encompasses some natural deficiencies. In particular, CT scans are less sensitive to subtle DAI and ischemic damage and as such, some patients with seemingly normal CT scans may suffer from significant unexplained neurological deficit [19, 20]. Besides, CT is a momentary portrayal of the injury, while TBI is a dynamically evolving process. Therefore, more advanced realtime monitoring of physiologic parameters such as continuous ICP and CPP monitoring are of great interest to assist TBI management. The current practice for ICP monitoring is achieved through intraventricular or intraparenchymal catheter with a micro-transducer system. Unfortunately, both of these techniques are invasive in nature and hence are subject to

potential risk of haemorrhages and infections [21]. As a result, continuing research efforts have been directed to the novel development of reliable and non-invasive ICP monitoring techniques. Novel non-invasive ICP monitoring modalities such as the optic nerve sheath diameter monitoring have been reviewed in [22].

1.2.3 TBI treatments and decompressive craniectomy

TBI treatments can be broadly categorised into three branches: neurosurgical interventions, medications and rehabilitation therapies, among which surgery plays an important role in emergency care. The main objectives of neurosurgery includes:

1. Removal of haematoma to prevent further swelling of brain
2. Repair skull fractures to help start the healing process of the skull and surrounding tissues [23]
3. Relieving intracranial hypertension (abnormally elevated ICP)

Medications including anticonvulsants (used to prevent seizures) and diuretics (help remove fluid in the brain) are applied to aid the treatment of TBI. Once the patient's condition becomes stabilised, further rehabilitation therapies are provided to help address physical, emotional and cognitive issues raised due to TBI.

As addressed in section 1.2.1, clinical parameters such as ICP and CPP should be maintained as part of the goal-directed TBI treatment. Among the various physiologic secondary insults, hypertension is considered most crucial as it causes a deterioration in ischemia and suppresses cerebral oxygenation. Normal ICP is between 5-15 mmHg, while in TBI, ICP could exceed 20 mmHg as a result of the primary injury, vascular engorgement, obstruction to cerebrospinal fluid (CSF) flow or brain oedema [21]. On the whole, 77% of TBI patients develop intracranial hypertension [2] and refractory ICP is consistently shown to be independently correlated to poorer outcome [24]. For this reason, modern intensive-care management of severe TBI is based mainly on tiered ICP-driven therapeutic protocols [9]. According to Cryer *et al.* [25], ICP management starts from the first tier, which comprises head-of-bed elevation, sedation and analgesia, as well as ventricular drainage. If the ICP remains greater than 20 mmHg, treatment proceeds to the second tier, which includes mannitol and hypertonic saline therapy and additional assessment of cerebral auto-regulation. If ICP remains refractory to the previous treatments, tier three protocols are performed. The last-tier protocol encompasses barbiturate therapy (a nervous system depressant) and decompressive craniectomy (DC).

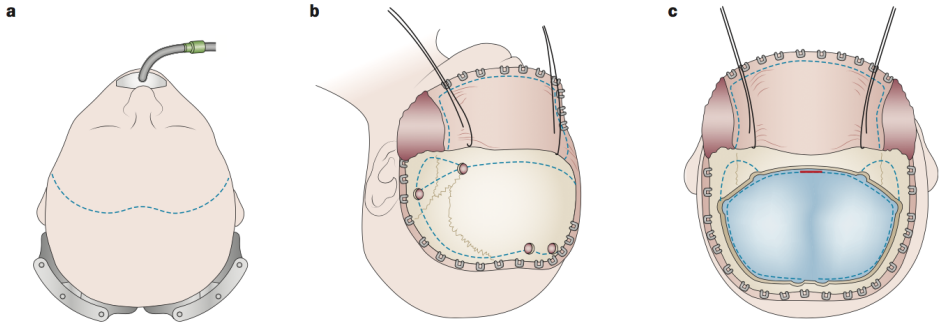

(a) Diagram showing bi-frontal DC [9]

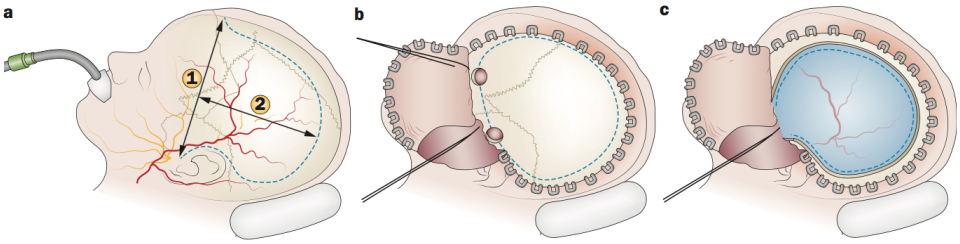

(b) Diagram showing unilateral DC [9]

Figure 9: Common types of decompressive craniectomy

Decompressive craniectomy is a traditional neurosurgical procedure that removes a large portion of the skull, opens the dura and allows the injured and swelling brain to expand outward. In the modern era of TBI management, the role of DC is broadly classified into two categories: the primary treatment in the acute phase leaves out the bone flap after evacuation of a mass lesion, which correlates to the first objective for surgical intervention: removal of haematoma to prevent further swelling of brain; and the secondary treatment deals with intracranial hypertension, diffuse brain injury and brain oedema [9], which correlates to the third objective for surgical treatments: relieving intracranial hypertension (abnormally elevated ICP). The surgical removal of bone flap in DC can be performed in various geometries at different locations: unilateral, bilateral, bi-frontal and bi-frontal with midline bar, among which the bi-frontal DC and unilateral DC (also termed as hemi-craniectomy) are most frequent. Graphic representation of the two most frequent DC are presented in Figure 9. Bi-frontal DC is frequently coupled with bihemispheric and possibly diffuse injuries with refractory hypertension [26]. While unilateral craniectomy is usually carried out on patients with intracranial lesions *e.g.* acute subdural haematoma.

The surgical opening of the skull dates back to centruies ago, commencing with trephination by the ancient Greeks as a practice to reduce increased ICP in patients with

severe traumatic brain injury, subarachnoid haemorrhage and ischemic stroke [9]. Opening of the skull offers additional space for the swelling brain and so it is a natural consequence for the brain to expand outside the skull and potentially mitigate the elevated ICP. This reduction in pressure effectively helps the brain to restore its self-regulating ability and so ICP may be kept at a reduced level thereafter. Secondary injuries such as the risk of herniation may be constrained to a minimum in this case. Physiological improvements in brain tissue oxygenation, cerebral perfusion and neurochemistry have also been reported in literature for severe TBI patients after DC [27, 28].

Despite the increasing evidence suggesting that DC is effective in short term management of ICP [29, 30], the invasive procedure also comes with its early and delayed complications, such as expansion of contralateral mass lesions, wound infections and healing problems, subdural collections and hydrocephalus [26]. The mortality rate and risk of severe disability for severe TBI patients after DC also remains relatively high and clinical trials were undertaken to investigate the efficacy of DC.

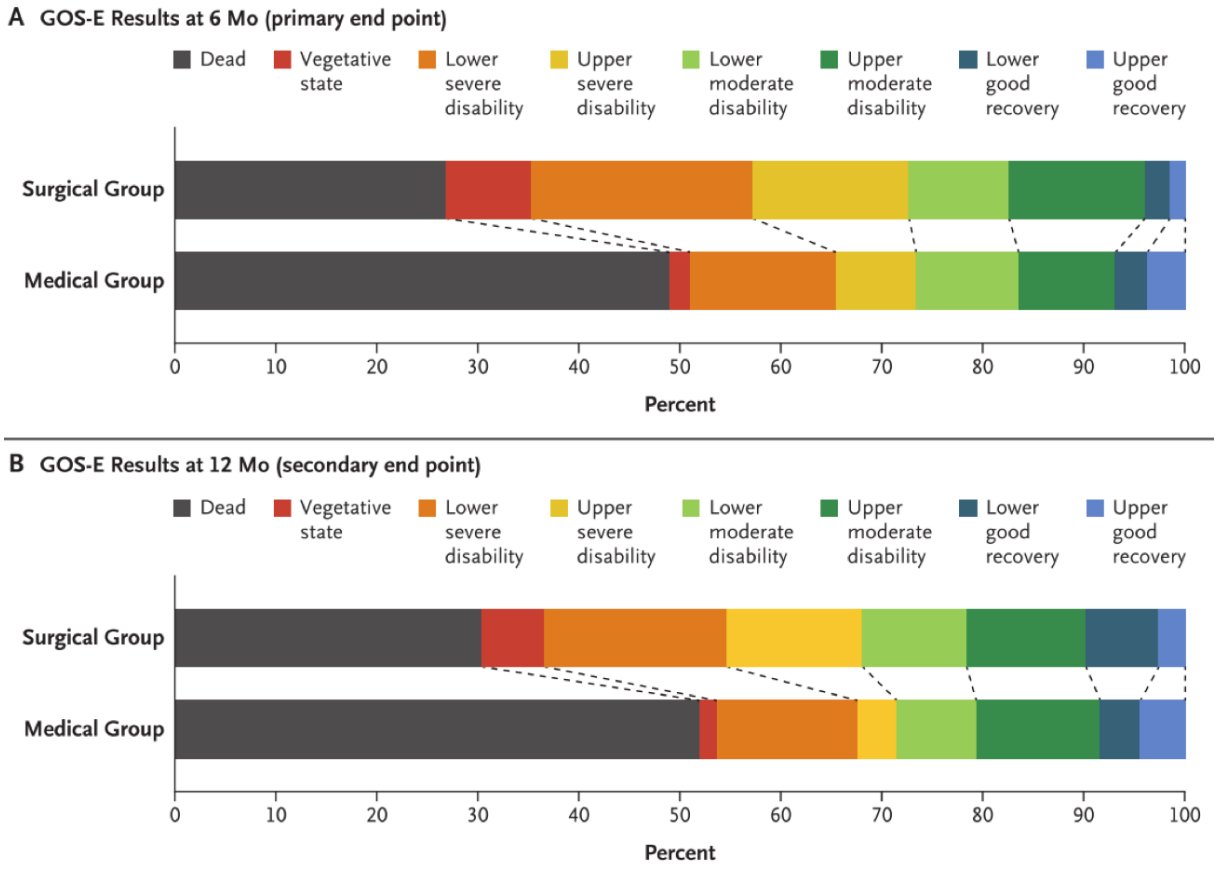

Figure 10: The patients' outcomes of RESCUEicp trial [31]. Please refer to [32] for detailed interpretation of GOS-E terms

The first randomised trial [33] of secondary DC recruited 27 paediatric patients with TBI and elevated ICP, randomly assigned them to receive either medical management alone or medial management together with bi-temporal DC. This pilot study, though it terminated early and was subject to a number of limitations, it has produced initial findings favourable to the patients randomised to early surgery. More recently, the DECRA study [34] was performed with a larger recruitment group. The results of the trial suggested that the practice of early bi-frontal DC, as compared with standard medical care, decreased the mean intracranial pressure and the duration of both ventilatory support and the ICU stay but was associated with a significantly worse outcome at 6 months [34]. Contrary to DECRA, the RESCUEicp study [31] was performed to examine the efficacy of DC as a last-tier therapy: randomisation occurred at the third stage when the observed ICP was greater than 25 mmHg for more than 1 h after the first and second tier medical therapy [31]. The patient's outcome has been evaluated using an extended Glasgow outcome scale (GOS-E) with results presented in Figure 10. As compared to the pure medical management group, the surgical group demonstrated more than a 20-percentage point lower mortality. This survival advantage translated to not only dependent living (from vegetative state to upper severe disability), but also independent living (from moderate disability to good recovery).

Although the RESCUEicp trial provided quantitative evidence to support the survival advantage of secondary DC as the last tier protocol to manage intracranial hypertension, the fact that some survivors suffered from moderately severe or severe disability has serious ethical implications. From the perspective of patients, those with severe disability live a dependent life of daily support, placing substantial financial and mental burden on their families. There is no consensus on whether survival at the expense of severe disability should be considered as satisfactory outcome, though a recent systematic review suggested that three-quarters of the patients and/or caregivers were satisfied with life and did not regret receiving DC [35]. From the perspective of the wider society, the cost-effectiveness of DC should be systematically evaluated, though early studies implied that "aggressive" treatment plan involving DC is better than the "conservative" approaches in terms of cost-effectiveness [36]. Apart from ethical issues, there is continuing debate on the optimal timing and surgical parameters, as well as the long-term functional outcome of DC. Further research efforts are needed to deepen our understanding of decompressive craniectomy.

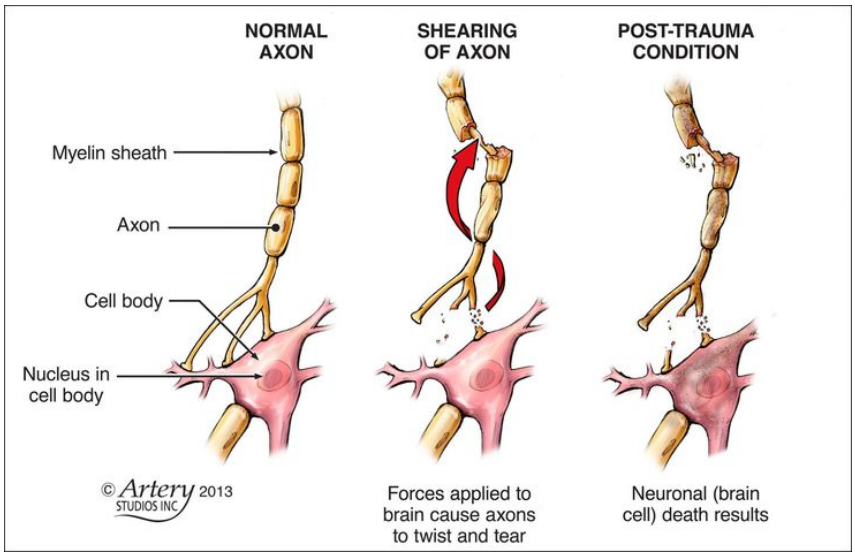

Figure 11: Schematics showing axonal damage due to shearing [39]

1.3 Bioengineering review

1.3.1 TBI on a microscopic level

TBI may occur when external mechanical forces are applied to the brain, either through direct impact forces, rapid accelerations and decelerations, rotational forces or penetration by a projectile. These mechanical forces, on a macro-scale, result in herniation of brain structures and disruption of normal brain function. Whereas on a micro-scale, these forces apply direct damage to the neurons, axons, dendrites and blood vessels in a focal, multifocal, or diffuse pattern and set off a dynamic series of complex cellular, inflammatory, neurochemical and metabolic alterations [37]. In a scenario of inertial loading, for instance, brain tissue deforms primarily in shear, and such shear deformation is associated with the stretching of neural axons. It is hypothesised that if the resultant axonal stretching exceeds a critical threshold, normal biochemical functions at cellular level will be disrupted, causing functional impairment of the neurons or, in severe cases, cell death [38]. Figure 11 shows the schematics of axonal damage due to shearing effects.

Experimental studies were conducted on single axons, nerve fibres, neural cell cultures and organotypic brain slice cultures to explore the cellular mechanism of neural injury [40]. These studies provide substantial evidence to support the statement that the degree of electrophysiological impairment and morphological damage of neural cells is directly related to the magnitude and rate of axonal stretch [40]. Intense research efforts have been focused on the injury tolerance criterion for brain tissues. The pilot study by Jean

Lemaitre *et al.* [41] suggests that nervous tissue damage is a gradual process that is driven, at least in part, by the applied strain. To date, various measures of injury threshold have been proposed, from pure stress and strain thresholds to combined metrics such as the cumulative strain damage measure [42]. Due to ethical reasons, most of the research was conducted in animal brain tissues or *in vitro* human brain tissues. It remains in doubt whether these injury thresholds are viable for human axonal injury, though evidence [43] implies no significant difference between the brain tissues of different species.

Computational models offer invaluable insights into the mechanics of brain deformations. The dynamic simulation encompasses multi-scale descriptions of relevant mechanical variables, from relevant deformation of brain tissues to the resultant stress and strain field. So far, the strength of computational modelling has been highlighted for accident reconstruction, as surrogates for experiments that either cannot be performed on human subjects due to ethical reasons or that are extremely difficult or expensive [44].

Provided with proper biomechanical properties of human head and specific input loading conditions, a computer simulation should be able to predict detailed local deformation levels of brain. These simulation results, when coupled with appropriate stress or strain based tissue injury thresholds, may help identify the regions at risk of injury in the brain [44]. At present, there exists no unifying damage thresholds for axonal injury. As suggested by Goriely *et al.* [45], the injury criterion varies across the scales, from single neuron via neuronal tissues (grey and white matters) to the whole brain across different cell types and is highly sensitive to the applied strain rates [45]. Nevertheless, computational models are considered as a potentially valuable tool that translates the mechanical strain and stress on a micro-scale to the herniation and damage of brain tissues on a macro-scale.

1.3.2 Material models of brain tissue

The role of mechanical modelling has gained increasing popularity as a promising tool to help understand and predict the behaviour of brain, not only in accident reconstruction but also in neurosurgery and brain development. The complexity of mathematical modelling of brain arises from two main aspects: accurate identification of biomechanical material properties, as well as the interpretation of appropriate constitutive laws [46]. In this subsection, the material testing protocols and the subsequent material models are reviewed.

Unlike traditional engineering materials, brain tissue is ultra-soft and complex in nature,

making it particularly challenging to determine its biomechanical properties. In the most recent systematic review by Goriely *et al.* [45], the neuro-mechanics of brain are classified into three mechanically regulated phenomena: "neuroelasticity, the extremely soft behaviour of the brain independent of time; neurodevelopment, the evolution of the brain at extremely long time scales; and neurodamage, the degradation of the brain at extremely short time scales".

The terms and definitions of relevant material models are summarised in table 2.

To capture the three phenomena, there exists a wide variety of testing protocols, among which *in vitro* uniaxial testing is most widely used. During a uniaxial test, the soft tissue specimen is loaded with tension [47], compression [47, 48] or cyclic tension-compression [49] under confined or unconfined conditions to explore the viscoelastic behaviour through the creep or relaxation responses. For the determination of the viscous, time-dependent component related to much shorter times (typically within 1 second), the dynamic testing methods [50] of free vibration and forced oscillation could be performed. Meanwhile, enhanced sensitivity indentation tests [51, 52] present a closer image of the characterisation of brain tissue *in vivo* or *in vitro*, though the indentation results could be difficult to interpret. Besides, the dynamic shear experiments are also performed [53] with respect to different loading time histories to interpret the complex dynamic shear. And more recently, magnetic resonance elastography [54, 55] emerges as a promising novel technique to help characterise the brain properties *in vivo*.

Material model	**Definition**
Linear elasticity	Stress and strain in a material are linearly correlated
Hyperelasticity (HE)	An ideally elastic material model for which the stress-strain relationship derives from a strain energy density function
Viscoelasticity (VE)	The property of materials that exhibit both viscous and elastic characteristics when undergoing deformation
Poroelasticity (PE)	Describe the interaction between fluid flow and solids deformation within a porous medium
Poroviscoelasticity	Combination of PE and VE to describe both the fluid-based time-dependence and solid-based time-dependence during deformation

Table 2: Definition of material models

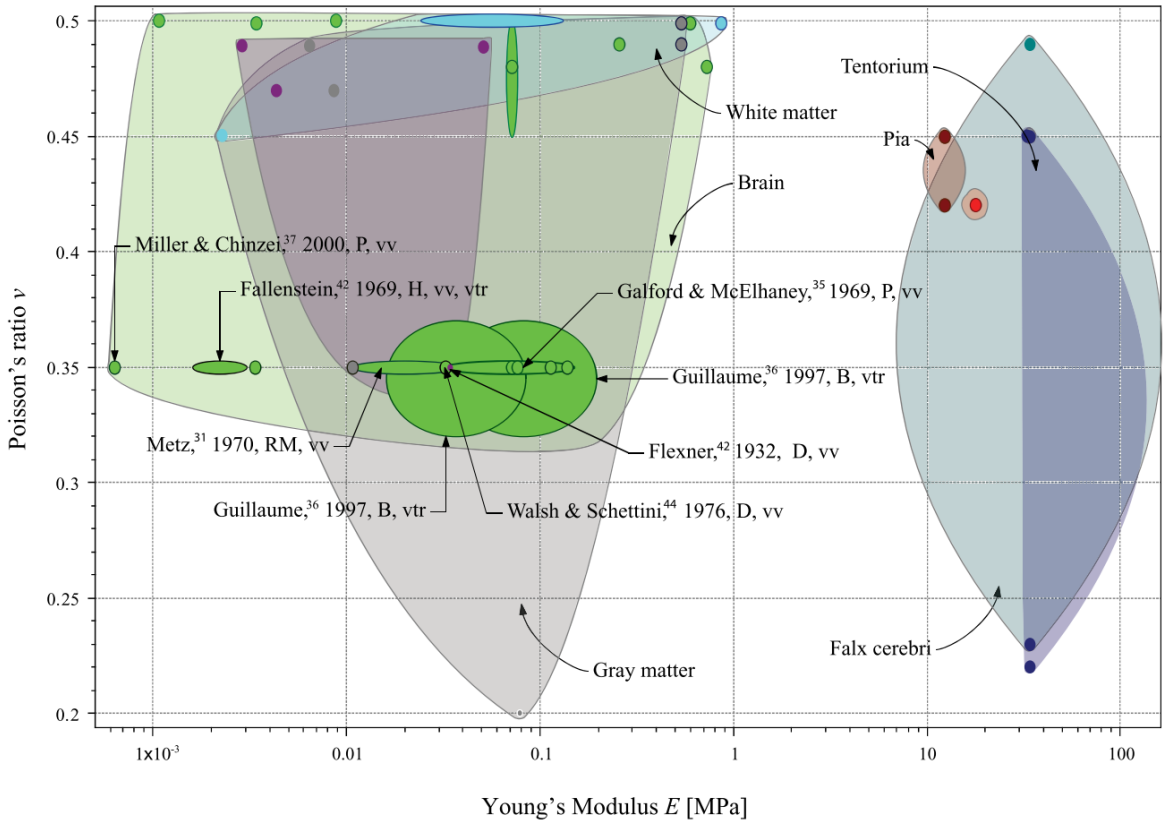

Figure 12: Plots of Young's modulus vs Poisson's ratio for various brain tissues [56]. Note, the reference numbers in the figure refer to the reference list of [56].

In 2010, Kim [56] summarised the Young's modulus vs Poisson's ratio of various brain tissues and plotted the data in a graph, as shown in Figure 12. It is seen that despite the considerable amount of data available, the reported properties of brain tissue by different research groups demonstrate significant differences between various species and the influence of post-mortem time [57], for directional, regional and age dependent properties [58], for various testing protocols and loading conditions and for *in vivo* and *in vitro* test conditions [59].

To date, the majority of experiments on biomechanical properties of brain tissues have been performed under a specific loading condition. Although such experiments provide a preliminary understanding of the brain material properties, they are insufficient to characterise brain tissue behaviours under arbitrary loading modes, as is required in computational modelling. The currently available studies rarely focus on multiple loading modes, despite the urgent need to develop a material model that fits most, if not all, experimental results. In 2013, X. Jin *et al.* [47] carried out a comprehensive investigation on biomechanical response of white and grey matter under tension, compression and shear

and concluded that strain rate dependency is significant in all loading modes. Their study also observed that white matter is stiffer than grey matter in compression and shear, and that directional dependency is significant in white matter under shear loading. However, a more recent study [46] on human brain tissue reveal contrary results: white matter is not significantly anisotropic from a mechanical point of view; human brain tissue are nearly isotropic but regional specific, with cortex being the stiffest and corpus collosum the softest; directional variation in grey matter is detected higher than white matter, though neither of them appear to be significant.

So far, there exists no universally accepted multi-scale material model that links information from the molecular, cellular, tissue and organ levels. Goriely suggests in his book [45] that machine learning could be a plausible path towards integrating diverse data, creating testable hypotheses and uncovering biological mechanisms towards a multi-scale neuro-mechanics model.

1.3.3 Recent computational models

Although a universally applicable material model is not readily available, there exists reasonable material models that best fits a particular prescribed condition. Depending on the deformation regime, Franceschini *et al.* [49] states that hyperelastic material should be used when deviatoric deformation dominates, whereas poroelastic material should be adopted when volumetric deformation dominates. On time scales from milliseconds to seconds for traumatic brain injury (corresponding to the neurodamage phenomena in section 1.3.2), the brain behaves in a poro-visco-elastic manner and is highly sensitive to loading rate [61]. While on time scales on the order of minutes or hours, characteristic for surgical procedures, a purely hyperelastic model should fit [61]. With the advances in neuroimaging techniques and computational capability, brain finite element models of high fidelity have been reconstructed to simulate brain mechanics under different scenarios. In this section, three

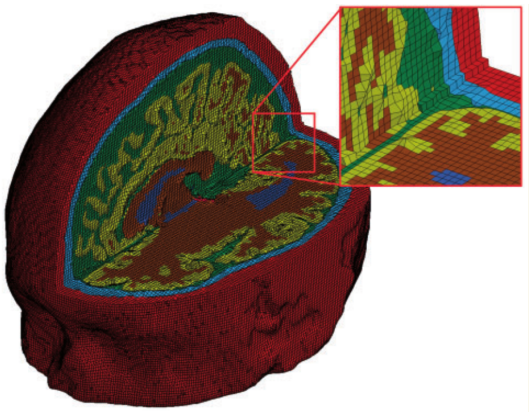

Figure 13: The finite element mesh of the high fidelity 3D model of traumatic brain injury, adopted from [60]. The colours indicate skin (red), skull (light blue), CSF (green), grey matter (yellow), white matter (brown) and ventricles (dark blue).

advanced computational models of brain are reviewed.

Over the years, computational simulation for accident reconstruction has drawn tremendous research effort. Applying high impact loading on virtual human head models helps enhance the understanding of brain deformation dynamics leading to TBI. In 2017, probably the most advanced computational model was developed by [60] to investigate the relationship between initial head impact and the pattern of progressive brain pathology. As shown in Figure 13, the computational model is constructed with high fidelity and encompasses great anatomical details. In their study, three different types of injury were simulated, all belonged to the high impact loading condition. Hyper-visco-elastic material model was adopted for such a short time scale under the neurodamage regime. The study concluded that the mechanical strain and strain rate are greatest in sulcal locations, which agrees well with clinical observations of chronic traumatic encephalopathy: neuropathology is prominently seen in deep sulci as well. Although has some limitations (*e.g.* it fails to incorporate the falx cerebri), this 3D head model still provides evidence to support the role of computer simulated mechanical strains as a predictor in traumatic brain injury.

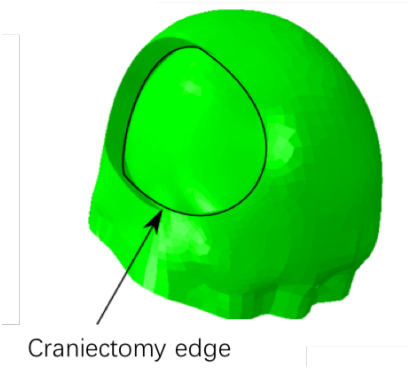

Figure 14: Finite element model with unilateral craniectomy, adopted from [62]. Only skull and brain is included in the model.

Despite the continuing efforts on simulating impact induced brain deformation, recently, there is increasing interest in computational models that best describe the behaviour of brain under surgical loadings. In particular, the resurgence in decompressive craniectomy calls for more accurate computational models to aid surgical planning and help minimise the possibility of secondary axonal damage post operation. In the DECRA trial [34], it is hypothesised that the major cause of brain damage due to herniation post DC is axonal stretching, which is basically an applied strain on the axons in the brain. Thus, computational modelling is likely to be equally promising for surgical simulations.

Early DC studies [62] focused on the effect of craniectomy edge, size and location on possible damage to the brain, but the models were over-simplified, as shown in Figure 14, and failed to take into account the anatomic details of the brain. More recently, two advanced DC models were published. The study by Weickenmeier *et al.* [61] created a

personalised craniectomy model from magnetic resonance imaging. As shown in Figure 15, the model encompasses great anatomic details including the skull, the skin, the cortical grey matter, the inner white matter, the cerebellum, and the cerebrospinal fluid. To simulate the brain behaviour during DC procedure, prescribed expansion is applied to the white matter tissue in the left, right and both hemispheres to simulate different scenarios of brain swelling. The result suggested that a collateral craniectomy with the skull opening at the side of swelling is less invasive than a contralateral craniectomy with the skull opening at the opposite side [61]. Interestingly, the other DC study by von Holst *et al.* [63] suggested diverging conclusions that opening the contralateral non-injured hemisphere could potentially improve patients' outcome. The FE mesh in the latter study was reconstructed from a CT image. As shown in Figure 16, though the model did not distinguish between grey and white matter tissues, it included the cranial,

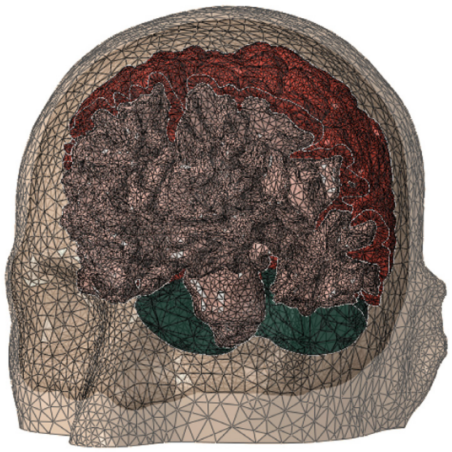

Figure 15: Personalised finite element model of the head including the skull (grey), the skin (brown), the cortical grey matter (red), the inner white matter (pink), the cerebellum (green), and the cerebrospinal fluid (beige), adopted from [61]. Note the model does not include the falx.

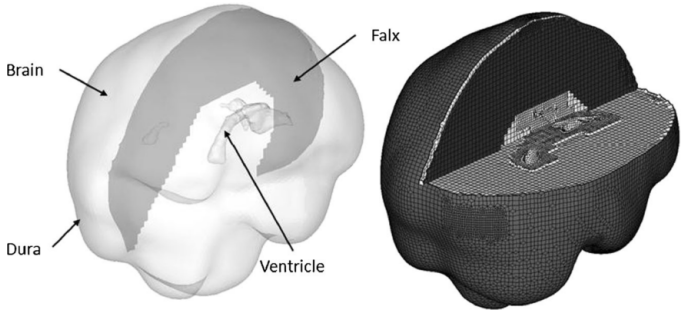

Figure 16: General FE mesh from one patient, adopted from [63]. Note, the falx is included in the model, but there is no reconstruction of grey and white matter regions.

lateral ventricles, dura mater and the falx. One possible explanation for the conflicting conclusions of the two DC studies is that the falx, being distinctly more stiff than other brain compartments (see Figure 12), possesses substantial influence on regulation of brain deformation and hence the axonal strain damage level.

So far, the majority of the TBI computational models have been focusing on topics of accident reconstruction and nerosurgical interventions, as reviewed previously in this section. The in-depth analysis of brain deformation, specifically brain herniation, caused during the evolution of primary and secondary injury following TBI has long been neglected. To the best of our knowledge, the first time that a biomechanical model has been dedicated to simulate brain herniation is in 2018 [64], when Huang *et al.* simulated the brain herniation caused by the subdural haematoma using the finite-element method. However, they only presented the simplest model which assumes the shape of the upper half of a sphere with a diameter of 160 mm for the supratentorial brain [64], as shown in Figure 17. To simulate the increased ICP caused by subdural haematoma (SDH), they applied uniform compressive pressure loads on the convexity surfaces of the cerebral hemisphere and concluded that there was a simple linear relationship between the maximum deformation of the brain and the pressure load. However, the model has some major limitations: it not only simplified the complex geometry of the head as a half sphere, but also omitted all the internal structures of the brain. Therefore, more advanced models of higher fidelity are expected to address the problems of brain herniation during lesion evolution.

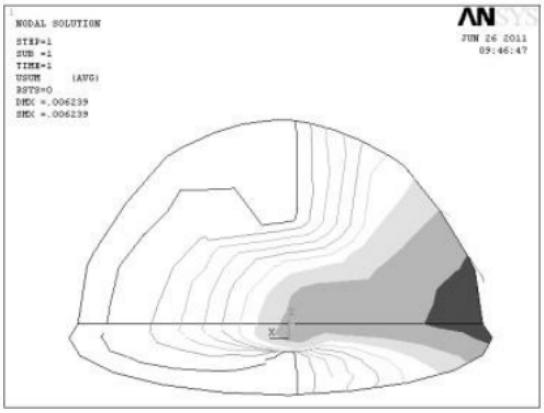

Figure 17: Contour plots showing deformation of the brain model under chronic subdural haematoma [64]. Note, cutaway views through the centre of the subfalcine space are used to display the most deformed regions (shaded).

As a result, there is clear scope for furthering the understanding of TBI related brain damage mechanism, its evolution process and optimising the surgical parameters to improve patients' outcome. Specifically, more accurate computational models should be developed, addressing the unique mechanical properties of the falx and possibly the anisotropy of white matter. Besides, rarely will two individuals experience the same

pathologies due to TBI. Primary injury can occur in various forms, shapes and locations inside the cranium, and so does the following secondary injury. It is important to study the brain behaviour in response to the diverging neuropathologies to further understand the brain deformation mechanism in TBI. Besides, patient-specific FE model reconstruction from neuroimaging will be particularly useful, as it accommodates the different skull geometry across patients and provides valuable insights on the pre-operational injury patterns. Simulation on a patient-specific basis will enable a deeper understanding of where axonal stretching may be at its worse due to herniation and provide unique information on the optimal surgical parameters for a particular patient.

1.3.4 Validation of computer models

With computational modelling, a variety of scenarios can be studied virtually to investigate the brain behaviour. However, these computational models, together with their simulation results, should be well validated before they are accepted as injury predictors and incorporated in safety regulations and clinical guidelines.

Intuitively, neuroimaging is considered as the key validation tool to support the computational simulations with potential clinical grounding. For instance, neuroimaging can be used to validate brain deformation induced during impact loadings, lesion evolution and surgical interventions. Since deformation is a macroscopic mechanical variable, validation can be achieved by finding appropriate deformation indicators in the brain tissue and comparing their degrees of deformation in the CT scans with the simulation findings from the computer models. MLS is one of such well-known deformation indicators in this case.

Validation of the strain levels, however, requires more effort. Non-rigid image registration, in particular, the Diffemorphic Demons (DD) algorithm sheds light on deriving strain information from neuroimage. The DD algorithm is a special registration technique that allows for smooth local variation and large deformation between different subjects. Such a non-rigid transformation matrix provides insight on the specific displacements and rotations for each voxel in the volume. And through Lagrangian finite strain calculations [65], the strain field could be determined at each voxel. These strain levels can be rigorously compared with the strain field generated by computational modelling to validate the simulation results.

So far, the DD algorithm has found its wide application to quantify the strain levels in different organs such as the lung and heart [66, 67]. In 2012, Li *et al.* [65] first

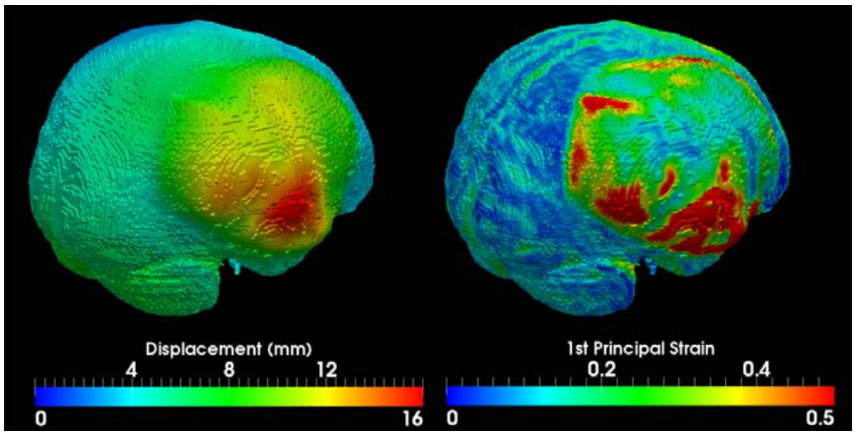

Figure 18: Displacement and strain level of the brain tissue after DC, retrospectively calculated from clinical neuroimage using the DD algorithm [65].

used this technique to quantify the stretching of brain tissue retrospectively based on the CT images of patients before and after craniectomy, as shown in Figure 18. Yet, the strain levels inferred from neuroimages were not compared with computer simulation results, due to the poor correlation between the real patient condition and FE model. In 2014, Fletcher [68] tried to used the DD algorithm to analyse strain levels of patients undergoing DC, however, the attempt failed due to poor resolution and large CT cut thickness. Besides, since there exists no ground truth for the validation of the non-rigid registration result, using DD algorithm to validate the computer simulation result may be problematic.

As a result, there is scope to develop an applicable validation algorithm from neuroimaging to validate the simulated deformation field. Such a validation algorithm should accurately quantify the brain tissue mechanical behaviours in an objective and reliable way. So that when the computer models and the validation algorithm are applied on an individual basis using the same set of CT scans, the performance of computer model could be rigorously validated. This validation should be able to provide the research with a clinical grounding and the simulation results should be readily related to realistic situation where possible.

1.4 Scope of the project

Brain shift and herniation after TBI can cause severe disability or death. Clinically, subtle changes in patients with subfalcine herniation must be taken seriously, as it will have a bearing on the morbidity and mortality of the injury. It is hypothesised that the strain and deformation of brain tissue is induced by the evolution of various traumatic intra-axial and extra-axial lesions occupying the intracranial space, while triggering secondary swelling or

oedema of the brain. Patient-specific finite element computer models have the potential to help reveal the brain deformation patterns associated with the heterogeneous TBI related pathologies. Thus, the overall aim of the thesis is to develop biomechanical models to quantitatively simulate brain deformation, specifically brain herniation, caused by an intracranial mass with increased ICP and strengthen the understanding across the full spectrum of TBI.

To conduct the research drawing on clinical evidence, computational models are to be reconstructed from neuroimaging such as CT scans, and where possible, the simulation results will be validated with clinical findings from patients' medical images and clinical outcomes. The detailed project aims are outlined as follows:

1. Develop computational tools to identify indicators of brain deformation from medical imaging. This encompasses automatic segmentation of the brain tissues and intracranial lesions, as well as automatic detection of mid-sagittal plane.
2. Develop a reliable retrospective method of quantifying brain deformation associated with various traumatic lesions and surgical operations, from medical imaging techniques.
3. Establish patient-specific biomechanical models with high fidelity to simulate and predict the brain behaviour under various kinds of traumatic injuries. Validate the simulation results with the clinical observations using the method developed in 2.
4. Based on 1, 2 and 3, investigate the mechanisms of brain herniation during TBI, by constructing patient subsets based on their brain deformation patterns and lesional characteristics.

Overall, the thesis is composed of three main parts:

- A literature review that covers both clinical and bioengineering backgrounds (chapter 1)
- A medical image computing part that derives useful information from medical image (chapter 2 and 3)
- A biomechanical modelling part that establishes patient-specific TBI models and performs head injury simulations (chapter 4, 5 and 6)
- A conclusion that summarised the research (chapter 7)

Specifically, the background of the research has been introduced in the literature review in chapter 1. Chapter 2 and 3 focused on medical image computing: chapter 2 developed the key computational tools and chapter 3 made proper use of the developed tools to interpret the brain herniation condition in CT scans. Chapter 4, 5 and 6 were about biomechanical

modelling of TBI: the patient-specific head model was introduced in chapter 4 and further assessed and fine tuned in chapter 5; in chapter 6, the established model was applied to simulate various TBI scenarios to study the brain deformation during head trauma. Finally a conclusion chapter was presented to summarise the research.

Collaboration partners

This project is co-supervised by Prof. Michael Sutcliffe, Professor of Biomechanical Engineering at University of Cambridge and Mr. Angelos Kolias, a Clinical Lecturer in Cambridge Neurosurgery. The scope and objectives were strongly influenced by Mr. Kolias to promote a solid clinical grounding for the project. Dr. Virginia Newcombe, a Clinical Scientific Fellow at Cambridge Neuroscience, has kindly provided her clinical expertise on the entire spectrum of TBI with me throughout my research. Prof. David Menon, Professor and Head of the Division of Anaesthesia at University of Cambridge, has kindly shared his clinical expertise on brain imaging analysis when I was developing the imaging tools. At the beginning of the project, Miss. Sinead Cook, an MEng student supervised by Prof. Sutcliffe, assisted in this project. The computational tools developed by Miss Sinead are highly intuitive, especially her data organisation methods. However, her code was not used in this thesis, all the algorithms and scripts were my original work. Mr. Hadie Adams, a Research Fellow in Cambridge Neurosurgery, also helped with my understanding for medical images. Dr. Eric Thelin, a post doc at Cambridge Neuroscience, and Miss. Selma Tulu, a visiting doctoral student at Cambridge Neuroscience, have helped with the imaging data annotations and segmentations.

Dr. Ben Glocker, a Senior Lecturer in Medical Image Computing at Imperial College London, has provided expertise in the imaging analysis towards the realisation of project aim 1 and 2. Prof. Alain Goriely, Director of the Oxford Centre for Collaborative Applied Mathematics, has provided suggestion for brain material properties towards the achievement of project aim 3.

The dataset used in the research has the following ethical approvals:

1. FAVO: ethical approval was obtained from the Cambridgeshire 2 Research Ethics Committee, and written informed consent, or written assent from next-of-kin where appropriate, were obtained in all cases in accordance with the Declaration of Helsinki.
2. Samcook: ethical approval for CENTER-TBI was obtained in accordance with all

relevant laws and regulations for each recruiting site. For the Cambridge University Hospital NHS Foundation Trust this was obtained via the NHS HRA (14/SC/1370) and the Research and Development Department - Cambridge University Hospital NHS Foundation Trust (AO93184).

3. RESCUEicp: Ethical approval for the RESCUEicp study has been obtained from the UK Multi Centre Research Ethics Committee (Eastern Region) and the clinical audit has been registered and approved by the Clinical Audit Department, Addenbrooke's Hospital.

All records/information were anonymised and de-identified prior to analysis.

2 Computational tools for image analysis

2.1 Introduction

In the modern era of TBI management, neuroimaging is playing an increasingly important role, as it offers evidence-based guidance on the assessment and monitoring of head injuries. Among the wide range of imaging techniques, CT has been officially recognised as the primary imaging modality for head injury assessments in NICE clinical guidelines [4]. A CT scan is a volume of voxels, which can be presented either in 2D as slices (as illustrated in Figure 6), or in 3D as volume rendering. According to the different radiodensities in the CT voxels, different bodily structures from the CT scan can be distinguished and reconstructed. In the scenario of TBI, the millions of CT voxels per scan embodies an abundance of anatomic/pathoanatomic and physiologic/pathophysiologic characteristics of the brain. The objective of this chapter is to develop useful computational tools that can be used to properly extract the clinical information from TBI related CT scans.

Recent years have witnessed a rise in medical image computing, an interdisciplinary field that couples computer science, data science, mathematics and medicine to extract clinically relevant information from medical images. In an emergency unit, a provisional radiologist's report for a given CT head scan should be prepared within 1 hour of the scan being performed, as suggested by NICE guidelines [4]. However, due to the large amount of daily TBI visits in the hospital and the dramatically increasing usage of CT, there may be a shortage in expert radiologist's analysis. Meanwhile, a tremendous amount of information is captured in the millions of greyscale voxels in a CT scan and so it is possible for the human expert to miss some less obvious life-threatening signs of injuries during assessment of CT. Advanced computational techniques from computer vision to machine learning could potentially facilitate the automation of the image manipulation and analysis procession. Overall, computer-assisted medical image analysis possesses the following superiorities:

- Powerful computational ability of modern computers enables short turnaround time for CT analysis, which could be of critical importance in the acute phase.
- Computational manipulation is free from human bias and fatigue, with higher accuracy and repeatability than visual inspection by human expert.
- Computational methods may be used to identify the heterogeneity of TBI and group the patients with similar pathologies to different sub-groups. Doctors will benefit

from such classification and prepare target-specific therapy in the shortest possible time.

- Computational methods offer the benefits of low cost, consistency and wide availability, suitable to be used in hospitals in rural areas and military hospitals.
- Image data is processed, labeled and stored in specific clinical terms or numeric figures, facilitating easy and quick comparison between different patients.

However, the automatic processing of the medical images is usually not straightforward. One of the essential prerequests for automated medical image computing and diagnosing is a standardised image format and structure. Currently, the two most popular CT image formats are DICOM and NIfTI. The DICOM standard, developed by the National Electrical Manufacturers Association (NEMA), is the default storage format for the majority of the modern neuroimage scanners. It defines the most specific dictionary of variables and objects related to the produced medical image, which is referred to as tags. Typically, there are over a hundred of tags stored in a DICOM file, ranging from radiological modalities such as pixel spacing, slice thickness, image orientation, and series number to associated audio files, patient notes and any other modalities. In contrast to the complex, verbose and comprehensive nature of the DICOM format, NIfTI is famed for its simplicity: only the most relevant metadata is retained.

By converting DICOM to NIfTI, the medical images of various modalities could be adapted to similar formats, such that multi-source neuroimage could be cross-compared and batch processing and analysis between different developer teams becomes possible. The conversion from DICOM to NIfTI has been complicated by the heterogeneous implementations from various manufacturers. In the study by [69], a variety of conversion tools developed to address different manufacturer modalities has been systematically reviewed. After conversion to the easy-to-support NIfTI file format, the CT scans are ready to be read and processed by the majority of the softwares and programming languages, where other CT parameters could be adjusted and unified prior to any further advanced batch image analysis.

This chapter first presents a CT preprocessing pipeline in chapter 2.2.1 that standardises the raw CT images for the subsequent algorithms. Then in chapter 2.2.2, the first computational tool, the automatic mid-sagittal plane detector is developed to find the mid-sagittal plane that separates the right and the left brain hemispheres with maximum symmetry. The second medical image computing tool is designed in chapter 2.2.3. It is a customised skull stripping tool for TBI related brain analysis. Lastly, in chapter 2.2.4, a novel concept called the midplane shift (MPS) has been presented. The MPS tool has

stretched the concept of midline shift from two dimensions to three dimensions.

2.2 Methods

2.2.1 CT preprocessing pipeline

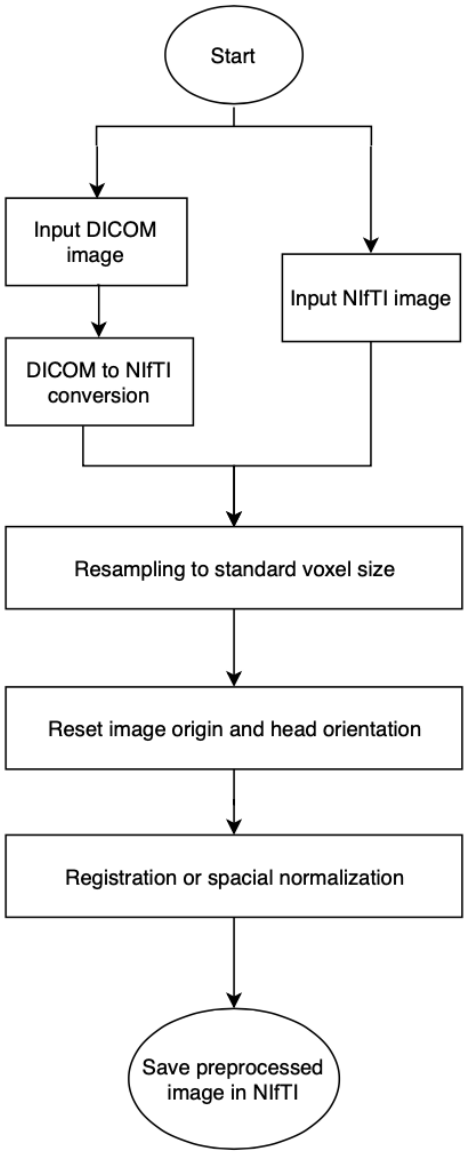

Figure 19: Flowchart outlining essential steps in CT preprocessing pipeline

Image preprocessing is often considered as a critical step after data acquisition. In general, preprocessing standardises the input medical images and checks the quality of the data before they are fed into the subsequent computational tools to avoid any potential tool breakdown and improve tool performance. In reality, there are a large number of CT parameters that can be potentially tuned to meet the specific prerequisites of various computational tools and a better preprocessing program that maximises utilisation of raw data is always needed. The raw CT image is usually in DICOM format, though in some scenarios, the raw image has already been processed into NIfTI format before data handover.

In the current section, the most commonly encountered issues during CT preprocessing will be addressed. The flowchart in Figure 19 shows the contents of the present CT preprocessing pipeline. Starting from raw DICOM images, the following steps will be carried out in the preprocessor:

1. Adjust gantry tilt to correct any distortion in volume image
2. Adapt pixel values to appropriate range in Hounsfield Unit (HU)

3. Resample to match certain resolution
4. Reset image origin and image direction
5. Registration or spacial normalisation

The first two steps normally applies to raw CT images in DICOM format. NIfTI is a simpler CT format and majority of the DICOM to NIfTI conversion software does a good job in the first two steps for gantry tilt correction and pixel value to HU adaptions. At the end of the second step, the CT image is converted and saved in NIfTI format. If the source image is already in NIfTI format, it is assumed that the conversion has been properly applied before the data handover and the pipeline starts with the third step.

The dataset used in the current research are from three major sources: the RESCUEicp trial, the FAVO dataset and the Samcook dataset from Centre TBI. The ethical approvals for each of the dataset were listed in chapter 1.4. CT scans from the RESCUEicp trial are in the original DICOM format, while the CT images from FAVO and Samcook are all preprocessed and delivered in NIfTI format.

Step 1: the gantry tilt correction

As explained in section 2.1, CT scans in DICOM format will need to be converted to NIfTI format for fast and robust processing. Here, the first enumerated step emphasises one of the critical CT parameters to be adjusted during the format conversion: the gantry tilt correction.

In a CT scanner, gantry is a ring or a cylinder that holds the source of radiation for patient diagnosis. Gantry angle is the orientation angle between the scanner gantry and the long transverse axis of the couch and the patient. As shown in Figure 5, the angle of cuts in a CT scan is in effect equal to the gantry angle. When the gantry angle is zero, the axial slices of the head CT scans represents the true axial orientation and when stacked along the sagittal direction, a standard three dimensional reconstruction of the head can be reproduced. However, in the most common scenario, gantry is purposely tilted to get around the vulnerable tissues and organs such as the eyeball and thus reduce redundant radiation exposure to such regions. Under other circumstances, tilted-gantry is also introduced to avoid tooth fillings and the resultant metal artefacts, or to take images in planes other than the traditional transverse plane. Non-zero gantry tilt angle will shear the slices of the CT scan and lead to distortion of volume geometry when reconstructed in three dimensions.

Moreover, the compatibility with gantry-tilted images in traditional image tools is usually poor, so tilted-gantry images may result in potential degradation in CT scan quality.

In fact, the main limitation in the performance of a gantry-tilted image is its geometric defect: there exists a misalignment between the mechanical and radiation isocentres, resulting in a sheared volume imaging system. To compensate for such a deviation, gantry tilt correction is proposed as an essential first step for CT image preprocessing. The data correction can be achieved by the application of an affine transformation matrix T to each of the axial slice during DICOM to NIfTI conversion. Similar gantry correction methods have been adopted by [70, 71]. The transformation matrix T takes the following form:

$$T = \begin{bmatrix} 1 & 0 & 0 \\ 0 & 1 & 0 \\ 0 & s\tan\alpha & 1 \end{bmatrix} \tag{1}$$

where s is the slice thickness and α is the gantry angle in Figure 5. The x-, y-, z- axis are defined as sagittal, coronal and transverse axes respectively. After successful gantry correction, the axial slices originally stacked along the tilted plane are sheared back to the true axial orientation and a correct data set is generated for accurate local reconstruction.

Step 2: conversion to Hounsfield units

Apart from gantry correction, the other critical step in DICOM to NIfTI conversion checks if the pixel values in the output raw image are accurately calibrated to Hounsfield units. If not, the CT numbers (pixel values) should be translated into the correct HU, where -1000 HU refers to air and 0 HU represents water. Although CT scanners are generally well-calibrated to measure radiodensity in HU, the default output values from some of the scanners are often not in this unit and will need to be adjusted before any further analysis. The conversion to HU utilises the two important tags stored in the DICOM metadata: the rescale intercept and rescale slope. These two tags specifies the linear transformation parameters required to translate the stored pixel values in the output raw image to the desired standard HU representation. Conversion is realised by the following equation:

$$HU = S \times pv + I \tag{2}$$

where HU stands for the Hounsfield Units, S is the rescale slope, pv is the pixel value in the raw image and I represents the rescale intercept.

In practice, the gantry tilt and intensity range correction are often included in DICOM to NIfTI converter tools. A variety of image conversion tools have been developed: dcm2nii [72], dicm2nii [73], dcm2niix [74] and SPM [75] are all popular open-source tools. Given the exceptional capacity of DICOM tags, different scanner manufacturers often extend the DICOM standard in every possible way to address their in-house demands. However, one consequence is that it posts numerous challenges during format conversion: tools that work for one subset of DICOM images might fail catastrophically on the others. Hence understanding of the conversion algorithm is extremely helpful in error identification.

Step 3: image resampling

After conversion to NIfTI format, the third step in the preprocessing pipeline is image resampling. In 3D images, a voxel is a volume element that represents a data point in the three dimensional space. Voxel size refers to the width, length and thickness of a regular grid in the volume image, hence it also describes the resolution of the CT scan. Namely, the smaller the voxel size, the finer the resolution and the richer the information comprised in the image. For automatic image analysis, input images of contrasting voxel size may be problematic.

Image resampling refers to the process of resetting the resolution and resizing a digital image. The resampling step in the preprocessing pipeline is capable of rescaling the input image to any desired resolution, including both downsampling higher resolution images to smaller ones and upsampling coarse images to a bigger images of smaller voxel size. Apparently, the latter approach will create a number of artificial voxels that does not exist in the raw image, thus special care is required when upscaling to finer voxel size. There are several ways to interpolate pixel contents during a resampling process. Common interpolators includes nearest-neighbour, linear, BSpline and Gaussian. It is worth noting that during resampling, in particular resampling to finer resolutions, interpolation should be restrained to ensure no artificial pixel values are invented. The current preprocessing pipeline addresses this problem by adopting the intensity from the nearest-neighbour of the original image. As a result, when upscaling, multiple voxels may be assigned with similar intensity value, which brings in jaggedness to the resampled image. SimpleITK (the simplified interface to the Insight Segmentation and Registration Toolkit) [76] offers

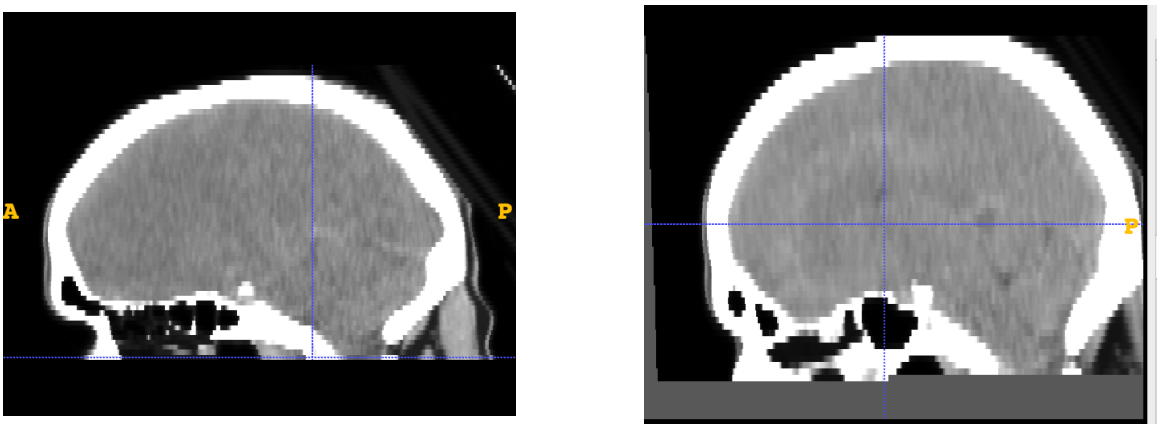

(a) Brain image before resampling

(b) Brain image after resampling

Figure 20: Illustration of image resampling for CT scans. Note, this CT scan has been upscaled to finer resolutions in the sagittal axis, so that in the post-resampling image, the CT scan becomes homogeneous in all three axis.

advanced and robust resampling features that can be applied for both downsampling and upsampling to specific resolution. The resampling step in the preprocessing pipeline was achieved with the SimpleITK tool. Moreover, in the proposed pipeline, the artefacts in the upscaled image can be smoothed out with a Gaussian filter, which is also available in SimpleITK library.

As illustrated in Figure 20, resampling provides a way to alter the image voxel size and save the treated dataset to new images of isotropic resolution. Most commonly, images are resampled to isotropic spacing so that the full dataset become homogeneous. By now, the CT images should be free from gantry tilt, in standard HU intensity range, of desired voxel size and in simplistic NIfTI format. Normally such a preprocessed CT scan should be compatible with most of the imaging tools for automatic neurological examinations.

Step 4: resetting image origin and direction

The fourth and the fifth steps in the preprocessing pipeline are actually supplementary steps designed for special purpose cross-individual data mining where there is a highly demanding requirement on the spatial alignment of input scans. In three dimensional medical images, the physical space that the image occupies is defined by arrays of voxels and its metadata including the origin, the voxel spacing and a direction cosine matrix specifying axes direction [76]. For most of the head imaging tools, a common assumption made is that the origin stored in the image header offers a reasonable estimate of the location of the anterior commissure (as illustrated in Figure **??**), which is valid for MRI.

Nevertheless, the default origin for CT often refers to the table centre, which is usually a metre away from the anterior commissure [69]. Gross deviation between the image origin and the location of anterior commissure can be problematic, because it increases the possibility of any subsequent analysing algorithm being trapped in local minimum [77]. Under such scenarios, the origin of the image will need to be modified and reset to the correct location of the anterior commissure.

This fourth step provides a translation of the image physical region by adjusting the image origin and orientation matrix stored in the image header. In SimpleITK, the origin of the image can be modified by resetting the image origin in the image header to any desired value. After warping to the standard space and resetting the origin, it is also necessary to unify the patient orientation by resetting the images to an identical direction cosine matrix. By the end of step four, the images are preprocessed to similar physical space for further registration or spacial normalisation practice. It is noted that both the image origin and direction are saved in the image header and called when they are required to define the spacial coordinates of the image for display purpose. Therefore, they cannot be illustrated but to be revealed in the image header.

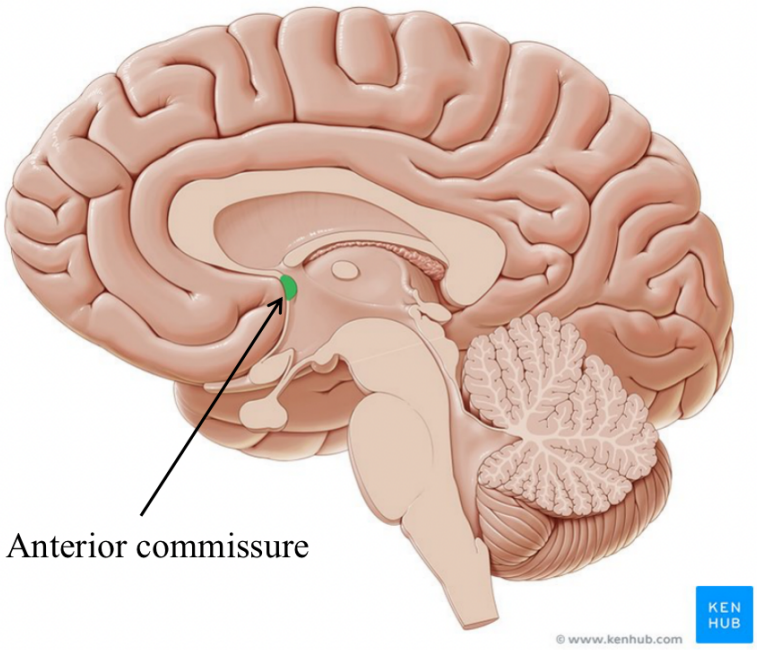

Figure 21: Illustration of anterior commissure on a sagittal CT slice. [78]

Step 5: spatial normalisation

The last component of the preprocessing pipeline offers an image registration method. Registration algorithms can be broadly categorised by their transformation characteristics into rigid registration and deformable (non-rigid) registration. On the one hand, rigid registration applies uniform transformation to the full dataset and resolves the problems of rotation, scaling, translation and other affine transforms [79]. On the other hand, the deformable registration has virtually infinite degrees of freedom to allow for non-uniform mapping between images. Due to the nature of the transformation, non-rigid registration incorporates nonlinear local warp on voxel level to minimise the differences between image pairs. Contrastingly, only global transformation is permitted during rigid registration. The choice of rigid or non-linear registration is often made upon the specific objective of research. In traumatic brain imaging analysis, it is the heterogeneity of lesion typology, morphology and possible sites of attack that makes the TBI library rich and diverse. Therefore it is worth retaining the patient-specific characteristics of lesions where possible throughout image processing steps. As a result, only rigid registration is adopted in this preprocessing pipeline to avoid excessive alterations to local abnormalities present in pathological images.

In the proposed pipeline, the "General Registration (BRAINS)" module in 3D Slicer [80] is used for its robustness and flexibility in transformation initialisation. Alternative open source brain registration tools includes MIRTK (the Medical Image Registration ToolKit) [81] and the coregistration tool in SPM8 (the Welcome Trust Centre for

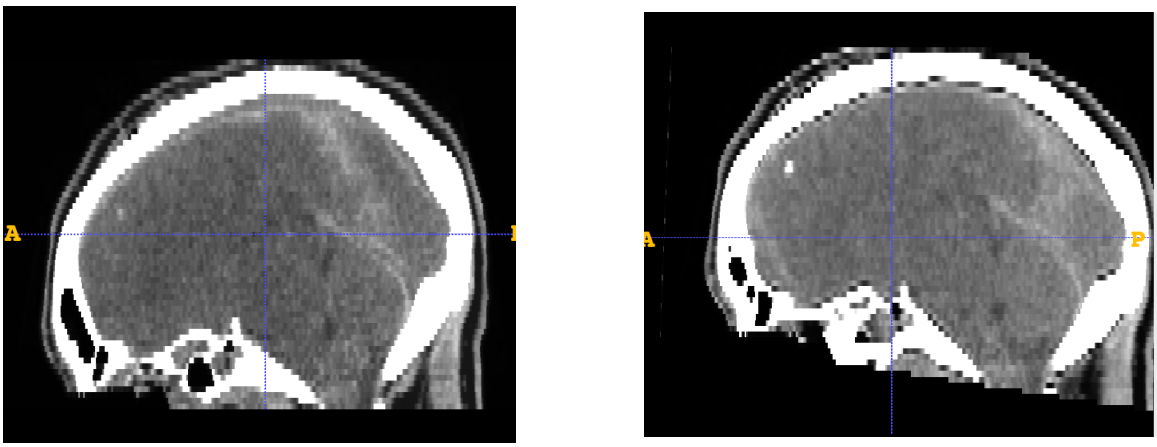

(a) Brain image before registration

(b) Brain image after registration

Figure 22: Illustration of image registration for CT scans. Note, registration to a template CT scan adjusts the diverging skew and orientation angles as a result of different patient positions during CT acquisition and map them to the same physical space.

Neuroimaging, London, UK). In fact, SPM8 is capable of spatial normalisation to map input image to standard Montreal Neurological Institute (MNI) space [82], so that point-by-point comparison could be performed between different images for further data mining tasks. However, there exists certain limitation in the latter two registration methods, which will be explained in detail in the results section.

Registration overcomes the challenges raised by image rotation, translation and skew and aligns multiple images into a common target template, as illustrated in Figure 22. Through registration, the multi-modality information enclosed in two different 3D images are fused, such that the regions of abnormality can be easily distinguished.

To sum up, a systematic preprocessing pipeline is proposed to deal with the inconsistent and non-standardised pieces of medical images for the purpose of fast and reliable batch image processing.

2.2.2 Automatic mid-sagittal plane detector

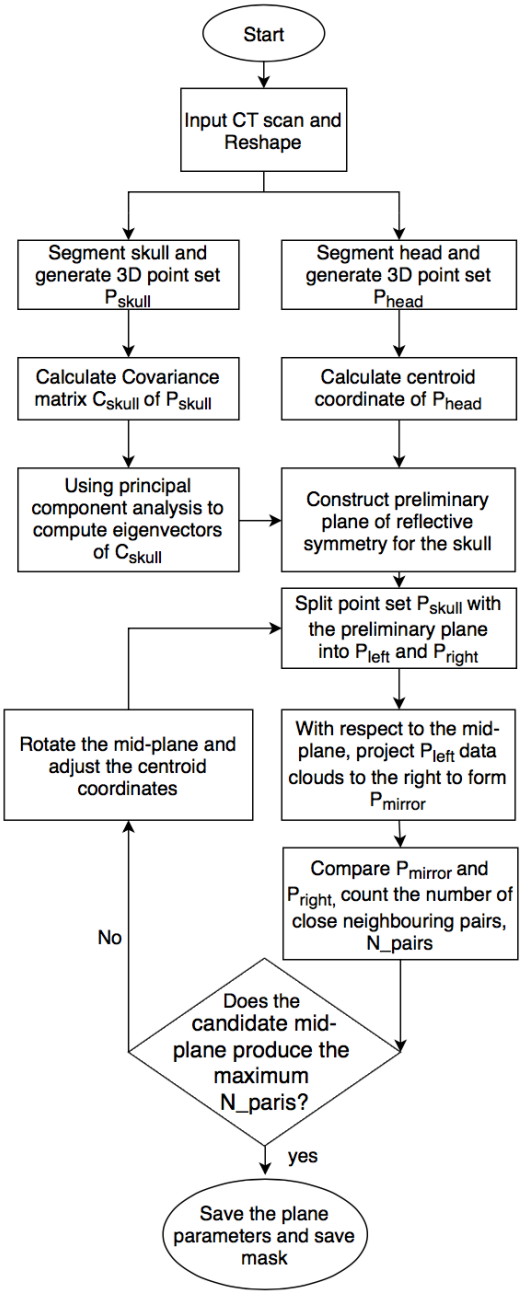

Figure 23: Flowchart denoting the algorithm for automatic midplane detector

The clinical importance of midline shift has been repetitively proved, but its estimation process is still ambiguous. The current gold standard is for clinicians to manually select a slice and take the measurement by hand. However, shifts of the brain vary between slices and different clinicians are likely to pick different slices to perform the calculation, leading to potential inconsistency. Apart from subjectivity, the manual estimation of MLS is also time consuming and prone to human bias. As a result, it is advantageous to develop an automatic tool that resolves midline shift in a fast, reliable and highly consistent way.

As an attempt to automate the entire MLS measurement process, it is imperative to first develop an algorithm to detect the ideal midline for each slice, which should serve as the reference line to draw the MLS from. In fact, these ideal midlines should all lie in the midplane, which is the inter-hemispheric sagittal plane that separates the right and left hemispheres of the brain. This section intends to develop an automatic tool to detect the mid-sagittal plane based on skull symmetry.

Previously, Miss. Sinead, an MEng student of Prof. Sutcliffe, has developed an automatic MPS detection tool by determining the relative locations of the eyes. However, in the current research, it is observed that her algorithm failed with anonymised and defaced scans, nor can it work with post-craniectomy scans with partial skull missing and thick-cut

CT scans. Therefore, a new MPS detecting tool has been developed in this section to solve the observed deficiencies.

To avoid limitations introduced by eye sockets, the current MPS detector calculates the midplane based skull symmetry. The skull for healthy adults is considered quasi-symmetric about a plane drawn between the anterior and posterior insertion of the falx cerebri to the inner table of the skull. Therefore it provides a way to detect the skull midplane by evaluating hypothetical planes of reflective symmetry. Based on this, the objectives of this midplane finder algorithm can be defined: to find a plane that maximises the reflective symmetry of skull. Provided that the developed algorithm is purely geometry-based, it is expected to output reliable midplane results for both thin cut and thick cut CT scans and for objects both before and after craniectomy (with a large portion of skull missing). The flow chart in Figure 23 gives the calculation algorithm for the developed automatic mid-sagittal plane detector.

Overall, the developed algorithm is comprised of two parts: the computation of preliminary plane of symmetry by principal component analysis (PCA) and symmetry fine tuning by an optimisation loop. The calculation starts by reading the scan into an array of CT numbers. Then through the preprocessing pipeline, each voxel is converted to a unit cuboid, erasing any bias introduced by image pixel spacings. Reshaping in the preprocessing pipeline also downsized the array, hence the total computation time is reduced.

Finding the preliminary plane of symmetry

To construct the preliminary plane of symmetry, a normal vector perpendicular to the plane and a specific point in the plane is needed. This has been achieved through two branches, as demonstrated in Figure 23. In the first branch, the entire head including the skull and the intracranial brain structures is thresholded from its background, constructing a 3D point set P_{head}. Thresholding eliminates any voxels with intensities outside the specified range of interest. By computing the centroid coordinates of P_{head}, we found a specific point in the midplane. In the second branch, a 3D point cloud P_{skull} is generated in a similar way, but includes pixels of the skull only, excluding any brain structures. Figure 25a displays the data points in P_{skull} in a cartesian coordinate. Then PCA is applied to find the normal vector.

Principal component analysis is a statistical procedure that uses orthogonal

transformations to explore the covariance-variance structure of a set of variables. Variance and covariance are measures of the "spread" of a set of points around their centre of mass. This technique highlights variation and points out strong patterns in a dataset, thus it is frequently used in dimensionality reduction in higher dimension datasets. With three dimensions, PCA generates a new coordinate system for a given dataset such that the greatest variance by any projection of the data clouds comes to lie on the first principal axis, the second greatest variance on the second principal axis and so on. The transformation works in a way similar to fitting an ellipsoid that has three principal axis (three eigenvectors), as illustrated in Figure 24. By coupling the eigenvectors with the data centroid, three potential planes of reflective symmetry are constructed for the fitted ellipsoid. When applied to this particular case, the calculation includes the following steps:

1. Calculate the covariance matrix C_{skull} using $C_{skull} = \frac{1}{m} P_{skull}^T P_{skull}$, m is the number of data points
2. Calculate the eigenvectors $PC1, PC2$ and $PC3$ from the covariance matrix
3. Evaluate the three principal axis and find the candidate normal vector for the midplane

Figure 25 is an example of candidate planes of symmetry generated by the PCA methods. It is obvious that the third candidate plane in Figure 25d is closest to the target ideal mid-sagittal plane, and hence it is selected as the preliminary midplane and forwarded as an input to the next stage of calculation. In practice, the developed algorithm selects

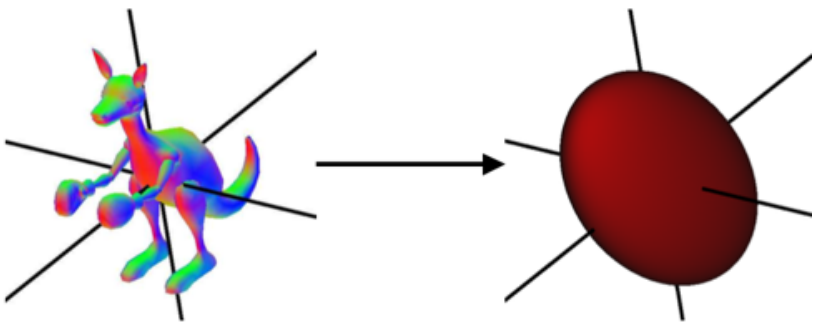

Figure 24: Illustration of using PCA to find the principal plane for a 3D object. Note the PCA works by fitting an ellipsoid and finding the three principal axis to a given 3D object. Three principal planes can then be constructed using the computed principal axis information.[83]

the normal vector by searching through the eigenvectors to find the one with maximum component in X direction. The preliminary midplane is saved in the form $ax+by+cz = d$.

Symmetry fine tuning

Although the principal plane generated by PCA captures the general direction of the midplane, it is usually prone to a few degrees of bias due to irregularity of skull pixels or partial skull missing (in particular on post op scans). An advanced optimisation loop has been established to fine tune the midplane parameters. The criterion for this fine tuning step is very specific: adjust the plane parameters to find a plane that maximises the skull symmetry. Assessment of symmetry is done by the following steps:

1. With respect to the preliminary midplane, split the data clouds P_{skull} into two subsets, $P_{leftskull}$ and $P_{rightskull}$.
2. Project (mirror) $P_{leftskull}$ to the right with respect to the preliminary midplane to

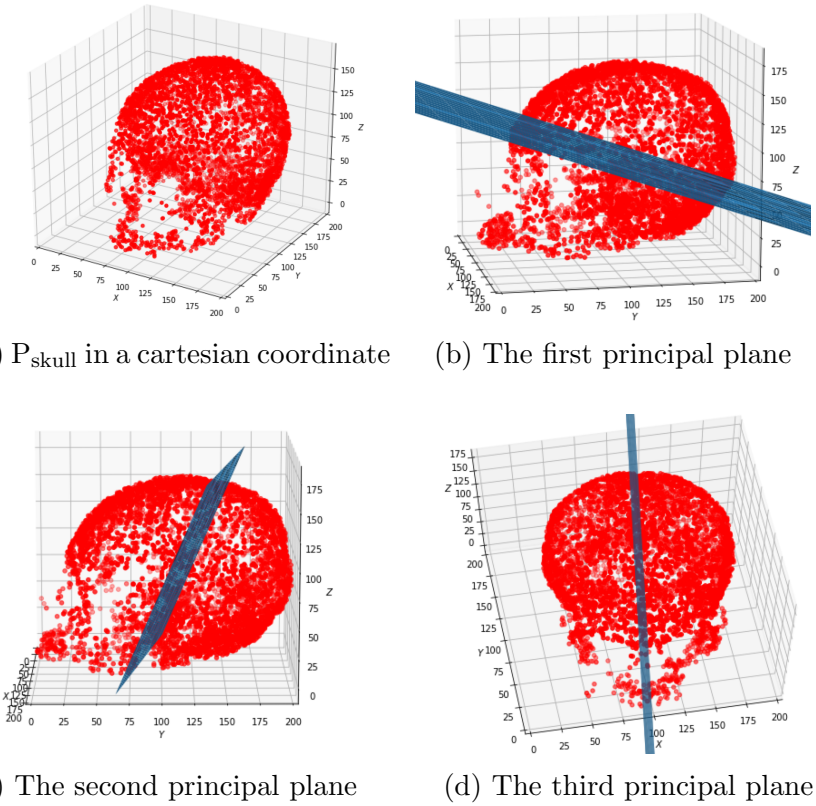

(a) P_{skull} in a cartesian coordinate (b) The first principal plane

(c) The second principal plane (d) The third principal plane

Figure 25: Data clouds for skull (P_{skull} and candidate planes of symmetry computed by the PCA method. Note the third principal plane is closest to the mid-sagittal plane and the first and second principal planes are bi-products of the PCA algorithm.

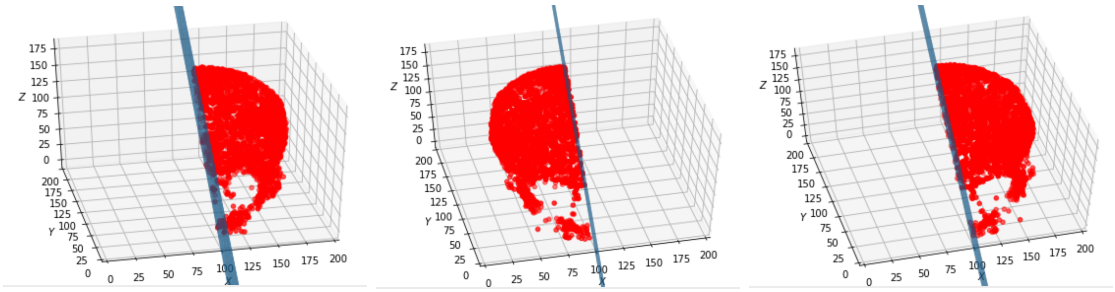

(a) $P_{\text{right skull}}$ (b) $P_{\text{left skull}}$ (c) $P_{\text{mirror skull}}$

Figure 26: Illustration of splitting and mirroring procedure for symmetry matching. Note, (b) and (c) are symmetric about the midplane; (a) and (c) are extensively compared to calculate the number of nearby pairs

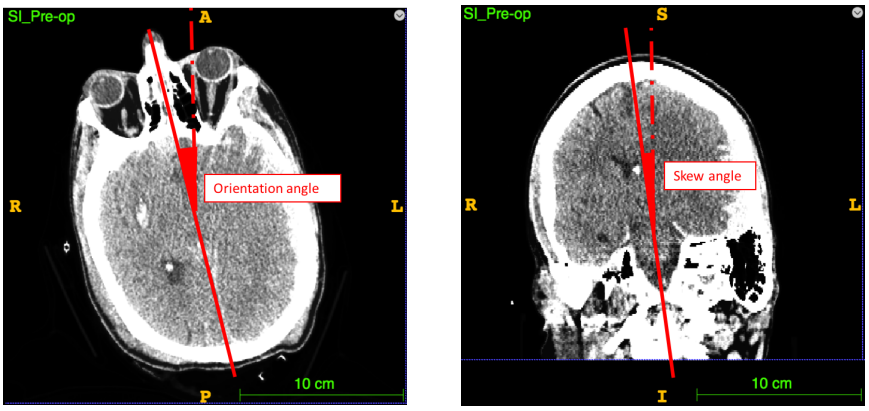

(a) Orientation angle in axial view (b) Skew angle in coronal view

Figure 27: Definition of orientation and skew angles used in midplane finder algorithm. Note, the two angles are defined in different axis to accommodate various head position. The solid red line shows the sagittal plane of the head and the dashed red line indicates the vertical plane of the image.

form $P_{mirrorskull}$

3. Count the number of close neighbouring pairs $(p1, p2)$ that can be formed. With $p1$ drawn from $P_{rightskull}$ and p2 drawn from $P_{mirrorskull}$. Note, $distance(p1, p2) <= r, r$ is the searching radius.

Figure 26 is an example of the first two procedures in the algorithm. Within the optimisation loop, three critical parameters of the preliminary midplane are passed on to the optimisation function for fine tuning. These parameters encompass the orientation angle, the skew angle and the head centroid. The orientation angle and skew angle are defined in Figures 27a and 27b respectively. During coarse calibration, the optimisation function searches for the optimal orientation angle and skew angle with a relatively large step size of 3 degrees. The midplane has been successively rotated against two distinct axis to find a better combination of these two angles that maximises the skull symmetry.

Then fine calibration is designed with a small step size of 0.5 degree, performing a refined search around the predefined angles. One additional parameter, the centroid coordinate, is also included in this fine calibration step, as an attempt to compensate any inaccuracies due to abnormalities of the head CT. This optimisation loop outputs midplane parameters that maximises the symmetry of skull. The midplane can be saved in a binary mask and superimposed on the original CT scan for direct visualisation by clinicians.

2.2.3 Automatic brain extractor

Skull stripping, also known as brain extraction, is usually the first step in many neuroimaging analysis sequences. It refers to separation of the brain from the non-brain structures, in particular the skull, scalp and muscles. In general, the majority of the brain extraction methods are developed to work on MRI, because of its better soft tissue contrast. Automatic algorithms tailored for CT skull stripping are still fairly scarce. Previous attempts [84, 85] on brain CT segmentation mainly focused on healthy objects and was not tested on severe pathological cases. Considering that in traumatic brain injury, CT scans are more frequently used due to the time urgency, low cost, as well as better discernibility of bone and blood, the development of computational tools for CT image processing calls for more research effort.

In this section, an automatic brain extractor has been developed to extract the intracranial brain from pathological CT brains. Here, we emphasise the idea of intracranial brain, as previous skull stripping tools did not specify the boundary of the brain around the

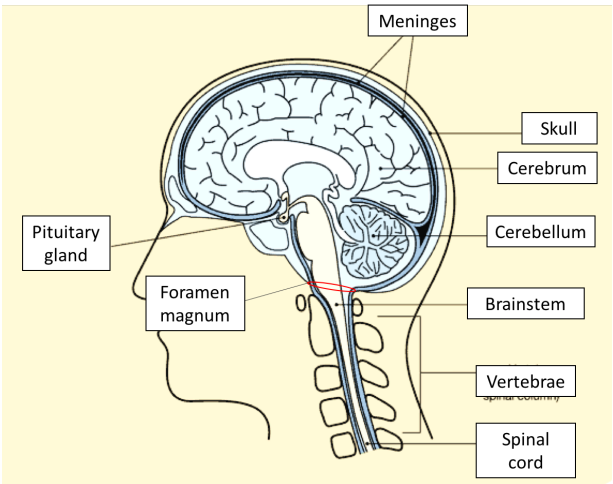

Figure 28: Simplified brain anatomy. Note, the red circle indicates the position of foramen magnum

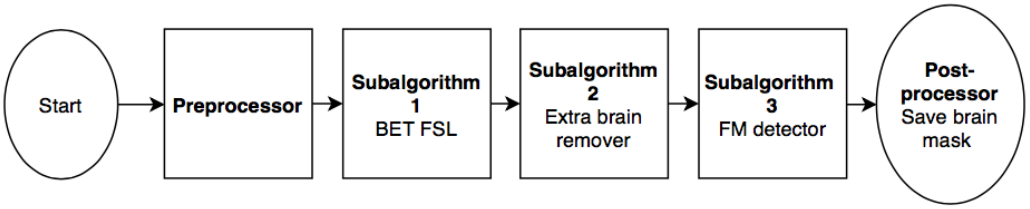

Figure 29: Flowchart denoting the steps for automatic brain extractor

brainstem. Figure 28 shows a simplified brain anatomy. The human brain consists of three main parts: the cerebrum, the cerebellum and the brainstem, among which the brainstem is structurally continuous with the spinal cord. Therefore, it is important to specify the border line between the brainstem and the spinal cord. Clinically, the large oval opening in the occipital bone of the skull base, the foramen magnum (FM), is considered as the margin for intracranial volume calculation. Based on this concept, the current brain extractor is designed to actively extract the brain beyond the FM from head CTs. Furthermore, in severe TBIs, the output brain mask should also envelop the haematoma and contusions within the cranium for further pathological analysis. The target output of this brain extractor algorithm is the result of discussion with an experienced neurosurgeon, Mr. Kolias, from Addenbrooke's Hospital.

Overall, the developed automatic brain extractor is a combined method composed of a pre-processor, three main sub-algorithms and a post-processor. A flowchart of this computational tool is shown in Figure 29.

In practice, the input CT scans to the automatic brain extractor should have been processed by the preprocessing pipeline proposed in Chapter 2.2.1. It is worth noting that the preprocessor in the automatic brain extractor is a customised procedure tailored for the skull stripping process, and it is essentially different from the previous pipeline. Specifically, the developed brain extractor is dependent on a developed tool called the Brain Extraction Tool (the first sub-algorithm), from the functional Magnetic Resonance Imaging of the Brain Software Library [86], The tool is abbreviated as BET FSL. The BET FSL tool is embedded in a Python package and can be called within Python. Though initially designed for MRI, the BET FSL has been adapted by [87] to work on CT as well. Popescu *et al.* [88] also proposed optimisation methods to improve the performance of BET FSL on CT scans. Based on the suggestion of Muschelli *et al.* and Popescu *et al.* , the preprocessor algorithm can be summarised as follows:

1. Read the CT scan into an array of pixels, save it as array 1.

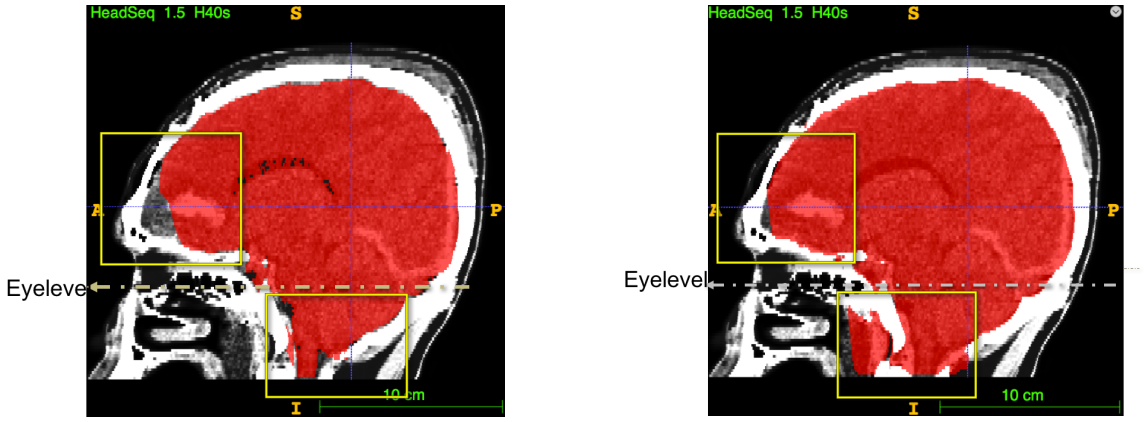

(a) Brain segmentation results on original array

(b) Brain segmentation results on smoothed array

Figure 30: Diagram showing the performance of BET FSL on original CT scan and smoothed CT scan. Note, the computed brain mask is superimposed on the CT image in red. The difference of the two brain masks are highlighted in yellow rectangular box and the eye-level line is denoted in grey.

2. Smooth a copy of the array using a Gaussian filter of size 1, and save as array 2.
3. Thresholding both array 1 and array 2 to only include voxels within intensity range between 0 HU and 85 Hounsfield units. This step erases the background and the skull, leaving the soft tissues only.
4. Dilate the arrays to fill in any "holes" or noise
5. Pass both the smoothed array and unsmoothed array to BET FSL.

After running BET FSL on both the smoothed and unsmoothed arrays, it is seen that the smoothing step tends to increase the possibility of a pixel being classified as brain. This enhancement is extremely beneficial if the extra pixels included are positive brain volumes. However, this is not always the case in pathological brains, due to the presence of contusions and bleedings in the neck and the sinus. As shown in Figure 30, smoothing enhances the performance of BET tool in the upper brain, but the extra pixels in the lower brain are more likely to be false positives. This is because there exists many foramen (structural holes in the skull) in the lower part of the skull and so intracranial bleeding, if present, may travel through these foramen and connect to the non-brain tissues outside the skull.

As a result, the developed brain extractor algorithm uses the eye-level as the dividing line, adopting the smoothed brain mask for the upper brain and the original brain mask for the lower brain. The combination mask is then passed on to the second sub-algorithm, false positive brain remover.

In the second sub-algorithm, the extra brain remover aims to eliminate any contusions or bleedings that appear as stubborn false positive brain voxels in the output of BET tool. Clinically, these contusions usually connect to the brain through tiny structural holes or fractures in the skull and spread over the sinus. As a result, in sagittal views, these contusions are not necessarily linked with the actual brain on most of the slices, as shown in Figure 31a. The extra brain remover algorithm makes use of this feature and clears the brain mask by repetitively picking out the largest connected brain mask on each of the sagittal slices. An example result of the current step is shown in Figure 31. The resultant brain mask is then passed on to the third sub-algorithm.

The foramen magnum detector

The third sub-algorithm is essentially a foramen magnum detector. Figure 32 shows the flowchart summarising the computational steps for the FM detector. Basically, the FM detector takes both the original CT array and the preliminary brain mask from subalgorithm 2 as inputs. Then the algorithm splits into two path.

In the first path, the skull mask is segmented by thresholding the original CT array using the unique intensity range of the bone. The resultant skull mask contains all bony structures in the head, including the basal bone and the teeth, as shown in the white mask in Figure 33a. Then by consecutively dilating the binary brain mask and multiplying it with the binary skull mask, a skull contour array is generated. This skull contour array

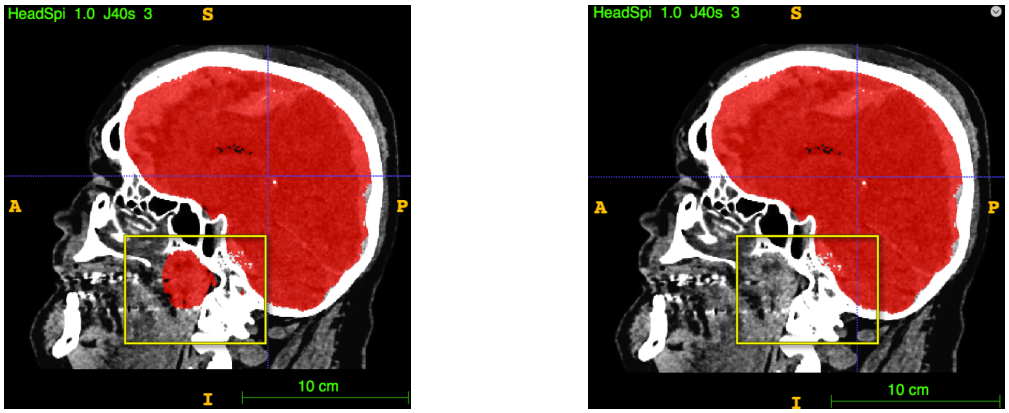

(a) Brain segmentation results before extra brain remover

(b) Brain segmentation results after extra brain remover

Figure 31: The performance of extra brain remover algorithm in subalgorithm 2. Note, the computed brain mask is superimposed on the CT image in red. The difference of the two brain masks are highlighted in the yellow rectangular box.

contains only the skull enclosing the brain, as highlighted in red in Figure 33a.

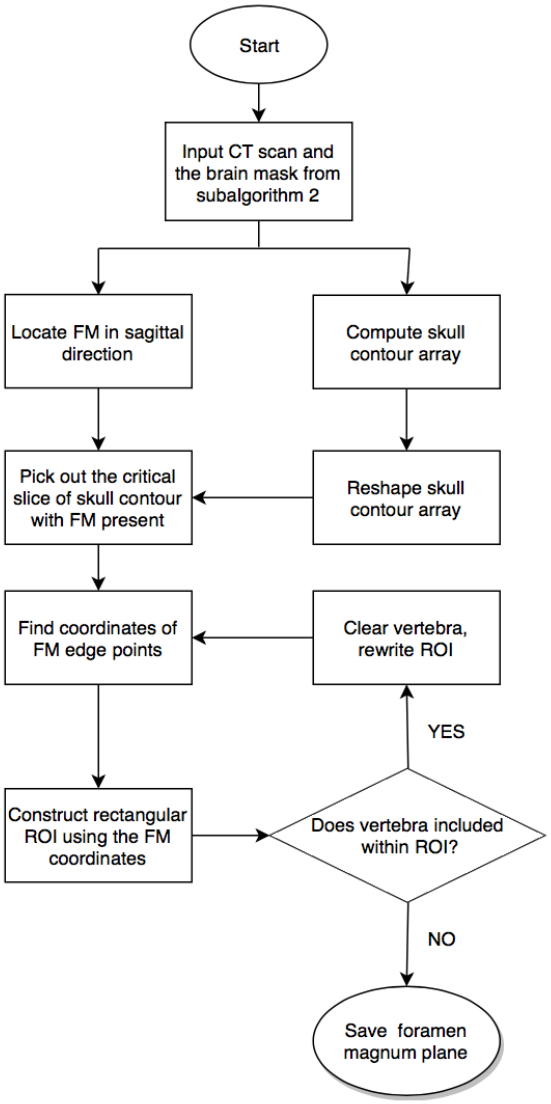

Figure 32: Flowchart denoting the algorithm for foramen magnum detector

In the second path, the algorithm scans through the brain mask to find the sequential number of the sagittal slice where the brain mask penetrates deepest into the spinal cord. Provided that the brainstem is linked with the spinal cord through FM, this slice number corresponds to the slice where FM is most likely to be present. If more than one slice is found, the algorithm takes the median of the slice number. The sagittal CT slice corresponding to this particular slice number is then extracted from the skull contour array as the critical slice. The skull contour highlighted in red in Figure 33a is an example of the critical slice. In a sagittal view, the foramen magnum comes into sight as the discontinuity of skull contour at the skull base, as demonstrated in Figure 33a.

The next step extensively processes the critical slice to find the coordinates of FM edge points. The algorithm finding the FM coordinates comprises five steps. The computational steps 1 to 5 can be summarised as follows:

1. Process the critical slice with a Sobel filter [89] to generate an edge map
2. Process the edge map with a Hough line transformer [90] to detect straight lines in the image and generate probabilistic Hough lines along the edge of the skull contour
3. Split the resultant Hough lines into the left group and the right group
4. Find the left FM edge coordinate in the left group
5. Find the right FM edge coordinate in the right group

Technically, the Sobel filter is a discrete differentiation operator that calculates an approximation of the gradient of the image intensity function [89]. The binary intensity array contained in the critical slice makes a clear distinction between edge and non-edge

pixels, which potentially guarantees the performance of the Sobel filter in step 1. Then in step 2, probabilistic Hough line transform [90] is employed to the lower half of the edge map to compute the most prominent straight lines. During Hough transform, each non-zero pixel votes for potential line candidates, and the resulting histogram indicates the parameters of the most probable lines, called probabilistic Hough lines. The output Hough lines can be seen from Figure 35. Considering that FM is located near the skull base, limiting the analysis to the lower half of the image reduces computation time. Both the Sobel filter and the Hough line transform are fundamental image processors which can be called from relevant modules within Python. By plotting the calculation results over the original critical slice, it is seen that the Hough lines essentially delineate the outlines of the skull contour, as shown in Figure 35a. These Hough lines are naturally separated by a blank space (the FM hole), therefore, step 3 divides the lines into two groups based on their relative spacial positions. The following step locates the FM by detecting the Hough lines whose right end point is closest to the FM hole and taking the coordinates of this end point as the left FM edge point, as shown in Figure 33b. Similarly, in step 5, the coordinate of the right FM edge point, as illustrated in Figure 33b, is spotted.

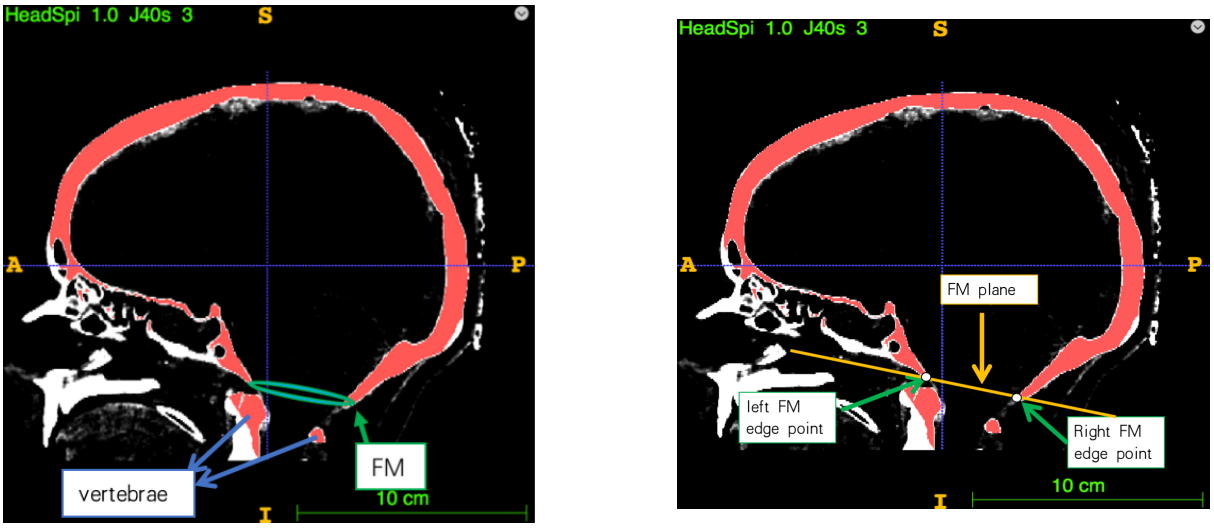

(a) (b)

Figure 33: Illustration of FM and its detection method on a sagittal skull contour. (a) Skull contour mask (in red) superimposed on original skull mask, with FM denoted as green circle. Note, the vertebrae has been highlighted with blue arrows. (b) Illustration of the left and right FM edge point, together with the FM plane defined by those two edge points.

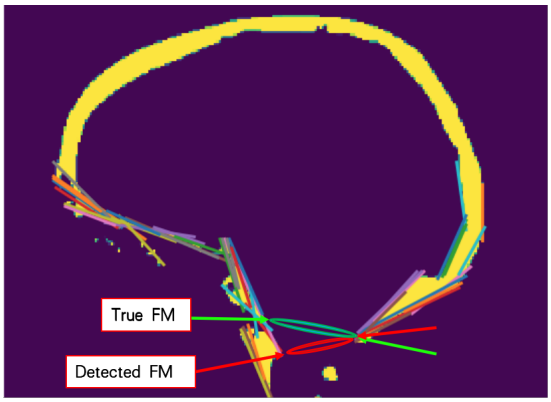

Figure 34: llustration of the detected FM and the true FM. Note, the detected FM failed to locate the left FM edge point, because of the interference of the vertebrae.

The vertebrae remover

The accuracy of the FM plane detection is strongly influenced by the accurate identification of the FM edge points. However, it is worth noting that, when applying the FM coordinates finding algorithm directly on the critical slice, the right FM edge point is usually correctly identified, but the left FM edge point is not. Figure 34 presents a typical FM detection result if only the five steps in the FM detection algorithm were executed. The inaccuracy of the detected FM was due to the error in determining the left FM edge point. Figures 35a and 35b are representatives of the inaccurate left FM edge point identification: the detected FM edge point (indicated by red arrow in Figure 35a) is lower than the true FM edge point (spotted by green arrow in Figure 35a). This is because the presence of vertebrae bones (as shown in Figure 33a) adjacent to the FM interferes with the performance of the Hough line transformer.

To address this issue, an automatic vertebrae remover algorithm is developed to erase the interfering vertebrae bones from the region of interest. The algorithm contains the following steps:

1. Construct a rectangular region of interest (ROI) near the skull base using the preliminary FM coordinates
2. Label the connected regions in the image with masks and delete any mask smaller than 10 pixels to eliminate noise in the image
3. Pick out the region mask with highest centre of mass on the left and right half of the ROI respectively. Note, the vertebrae is anatomically below the skull base.
4. Rewrite the ROI region in the critical slice with only the picked mask to get rid of the vertebrae.

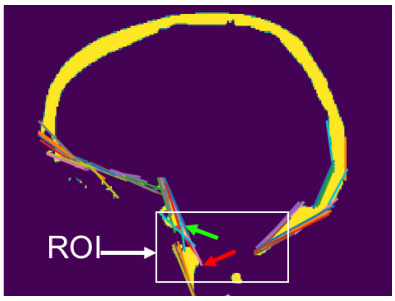

(a) Hough line transform results shown on the original critical slice

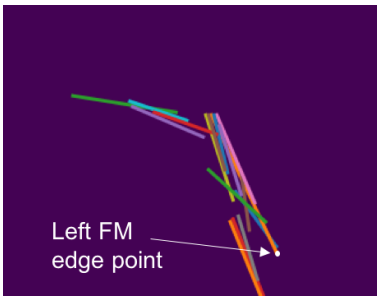

(b) The computed left FM edge point in the left Hough line group

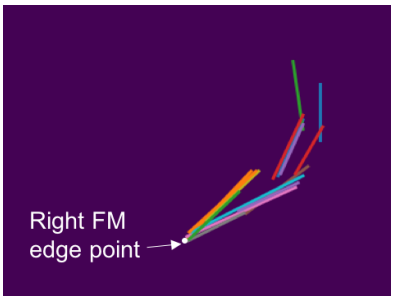

(c) The computed right FM edge point in the right Hough line group

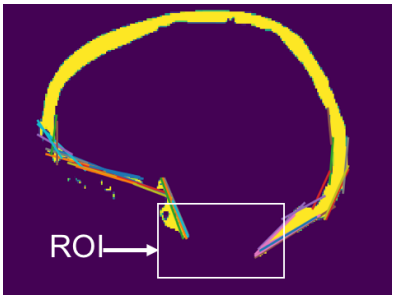

(d) Hough line transform results shown on the cleared critical slice

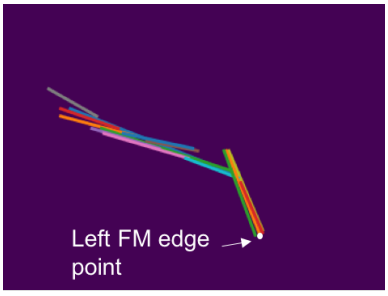

(e) The computed left FM edge point in the left Hough line group

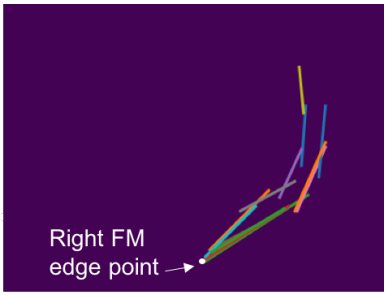

(f) The computed right FM edge point in the right Hough line group

Figure 35: Example results of the automatic FM detector. (a) (b) (c) and (d) (e) (f) correspond to the FM detection results before and after the automatic vertebrae clearance step. In (a), the green arrow points on true FM edge point and red arrow points on the detected one. The white ROI box denotes the region where vertebrae has been wiped off.

This vertebrae remover takes advantage of the preliminary FM coordinates to construct a ROI circulating the true FM area. Then the bony structures within ROI are effectively cleared by distinguishing skulls from the vertebrae and rewriting the array. After the removal of distracting vertebrae, the cleared critical slice is processed again by the FM coordinate finding algorithm. Without the interference of the vertebrae, the true FM coordinates are accurately computed, as shown in Figures 35d, 35e and 35f. The last step of the automatic FM detector constructs a FM plane using the detected FM coordinates under the assumption that the FM plane is perpendicular to the sagittal CT slice.

Lastly, the calculated FM plane from the automatic FM detector, together with the brain mask from the extra brain remover, is handed over to the post-processor to perform the final analysis. This post-processor finishes by cutting any brain volumes below the FM plane and saving the resultant intracranial brain mask as the final output of this developed automatic brain extractor.

2.2.4 3D brain shift analysis

One key complication of TBI is the development of intracranial hypertension resulting in midline shift. The clinical importance of midline shift has been continuously supported by studies suggesting that the larger the amount of the midline shift on CT scans, the poorer will be the outcome of traumatic head injury [91]. Nonetheless, as previously addressed in section 1.2.2, midline shift is a single measurement of how far the midline structure has deviated from the ideal centre line at a particular point on a single CT slice. In other words, it is a rather simplified numerical notation to represent the deformation of the brain tissue, because the degree of midline shift varies throughout the depth of the skull. Therefore, there exists scope for the brain deformation to be resolved in greater detail.

Here, we propose a novel concept, the midplane shift (MPS), to capture the full spectrum of the brain shifts across the mid-sagittal plane. The midplane shift aims to stretch the concept of midline shift from two dimensions to three dimensions.

In any pathological CT slice, for instance Figure 36a and Figure 36b, two different midlines can be drawn to calculate midline shift: the ideal midline and the actual midline. The ideal midline is essentially the centre line of the skull, while the actual midline refers to the anatomic midline represented by the brain mid-structures such as the septum pellucidum, the third ventricle, the pineal gland, the falx insertion to the skull and the longitudinal fissure, as previously introduced in section 1.2.2. These brain mid-structures normally align on the ideal midline in healthy conditions, however, in pathological cases, these anatomic structures deviate from the ideal centre line due to mass effects and increased

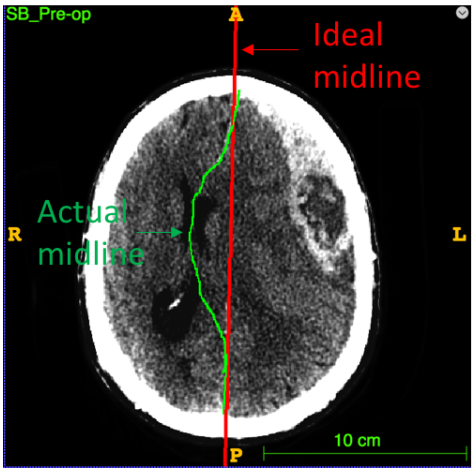

(a) Actual and ideal midlines in axial view

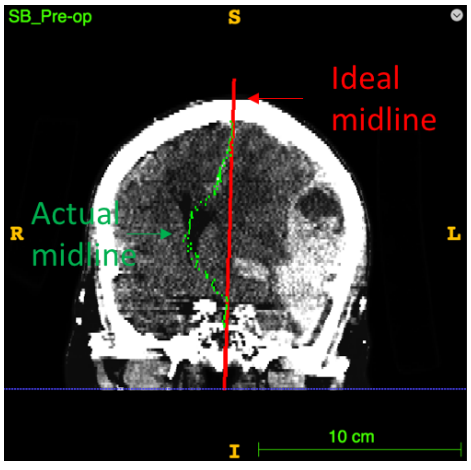

(b) Actual and ideal midlines in coronal view

Figure 36: Manually delineated actual midline and ideal midline shown in different views

ICP, forming the actual midline, in contrast to the ideal midline. Similar definition can be found in [92] and [17].

The concept can be stretched from 2D to 3D. Connecting the ideal midlines on each successive slice forms an ideal midplane, which is just the ideal mid-sagittal plane computed by the midplane detector in section 2.2.2. An example of the ideal mid-sagittal plane is shown in red in Figure 37. Similarly, connecting the actual midlines on each successive slice forms an actual midplane, as shown in green in Figure 37. In healthy subjects, the ideal and actual midplanes should overlay on one another, whereas in pathological cases, the actual midplane is deformed and thus moves away from the ideal midplane. The ideal midplane becomes an imaginary reference plane in this scenario.

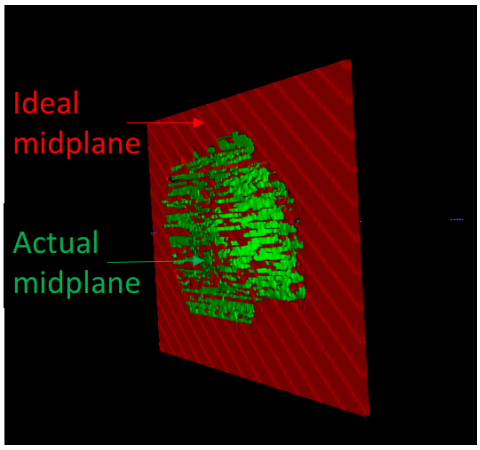

Figure 37: Illustration of the manually delineated midplane (the actual midplane) in green and the ideal midplane in red.

The idea of midplane shift is an evolution of the midline shift from 2D to 3D.

At the current stage, the MPS is calculated by firstly manually delineate the deformed midlines (the actual midlines) on each slice according to the deviated brain mid-structures, in order to generate the actual midplane. Then, each pixel on the deformed midplane is treated as an individual data point. The perpendicular distance between each data point and the ideal midplane is calculated as the midplane shift at this particular point. Each pixel on the actual midplane has its unique MPS value. These MPS values are then projected onto a heatmap plane parallel to the mid-sagittal plane, as shown in Figure 38a. By repetitively calculating the MPS for each data point in the actual midplane, a heatmap is generated. An example MPS heatmap is displayed in Figure 38b. It is noted that the dark blue region on the periphery represents the skull silhouette. In order to differentiate the skull from the actual MPS heat map, a negative value has been assigned to the skull mask as -0.2 mm. In the MPS heat map, a maximum MPS of approximately 10 mm is observed in the middle of the brain heat map.

The MPS encompasses the conventional MLS, but improves upon the original MLS because it resolves the shifts of the brain from the bottom to the top of the skull.

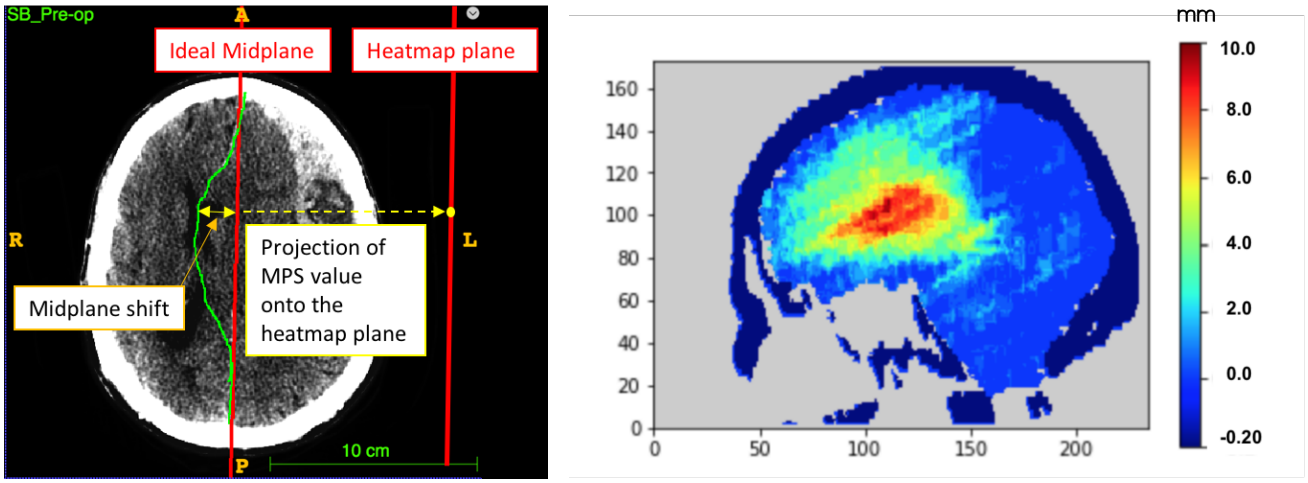

(a) MPS and formation of heatmap (b) MPS heatmap

Figure 38: Midplane shift heatmap

Standard procedures for MPS generation

Due to different orientations and modalities of the original CT scans, the resultant MPS may be essentially dissimilar in shape and thus not comparable. To accommodate this problem, the original CT scans were put through the preprocessing pipeline proposed in section 2.2.1. Basically, the current section follows the following steps for the generation of a standard MPS:

1. Preprocess the input CT scan using the preprocessing pipeline described in section 2.2.1
2. Find the ideal mid-sagittal plane for each CT scan using automatic midplane detector in section 2.2.2
3. Delineate the deformed midlines manually and calculate the MPS heat-map for each CT scan using the method described in section 2.2.4

The first preprocessing step is critical for group level analysis. It fixed the potential divergence in raw CT image modalities, resampled the image to equivalent sizes and most importantly, it transformed the input images to a common coordinate frame through registration. In this way, the patient motions and head orientations were aligned to maintain voxel-wise correspondence between a series of CT objects.

2.3 Results

2.3.1 CT preprocessing pipeline

In the modern era of scientific computing, the two important guidelines for developers are to facilitate collaboration and enable reproducibility. Preprocessing of the inconsistent and non-standardised medical images, though requires substantial efforts, is often key in relation to these guidelines. In this section, the performance for every step in the proposed preprocessing pipeline is systematically evaluated. In this research, both RESCUEicp trial data and CENTRE TBI data were used. Thus when testing the pipeline, the CT scans analysed were from various centres/scanner settings.

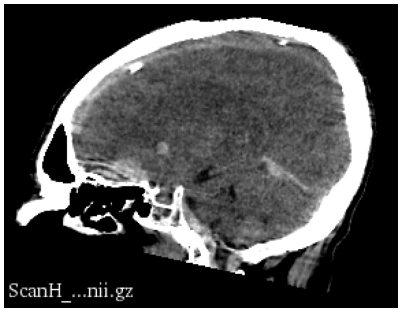

(a) A sagittal slice of Scan H with non-zero gantry tilt

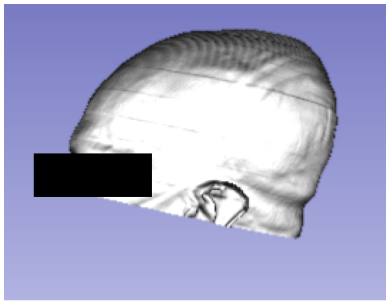

(b) 3D reconstruction of gantry tilted Scan H

(c) A sagittal slice of Scan H after gantry tilt correction

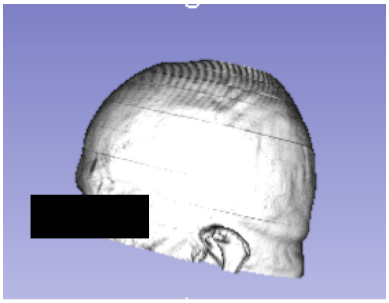

(d) 3D reconstruction of Scan H after gantry tilt correction

Figure 39: Illustration of the effect of gantry tilt correction. Note, if the gantry tilt is left uncorrected after NIfTI conversion, the resulting 3D reconstruction of the head will be distorted as shown in (b)

Step 1: the gantry tilt correction

Firstly, DICOM to NIfTI conversion has been applied to nine CT head scans in DICOM format, among which six of them are gantry-tilted. After conversion to NIfTI format, the non-zero gantry angles in all six CT scans were successfully corrected. Figure 39 illustrates the effects of gantry tilt correction using one of the test DICOM scans, Scan H, as an example. As displayed in Figure 39b, CT head scans with non-zero gantry tilt appeared to be a skewed parallelogram. Such an abnormal geometry is unrealistic and hence cannot be used for computer visualisation or simulation. Moreover, distorted head shape may not be properly processed by many image tools. While after gantry tilt correction, the misaligned axial slices were shifted back to the orthogonal axis and the resultant 3D reconstruction eventually represented a standard shape of human head. Ideally, the corresponding spatial information stored in NIfTI header should reflect this change in the spatial transformation matrix during this process. Gantry tilt correction is often considered as a fundamental preprocessing step in longitudinal studies of neurological images [93].

Step 2: conversion to Hounsfiled units

In the meantime, the pixel levels were also converted to standard HU. Figure 40 displays a typical distribution of head CT image intensities after interpretation to standard HU space, with x axis showing the HU intervals and y axis plotting the frequencies of pixel intensity values stored in the CT scan. Predominantly, there exists two main peaks in the head CT intensity histogram: the left one ranging from -1000 to -500 HU corresponds to the background of the image, including non-tissue objects or air and the right one refers to the actual region of interests. In head CT scans, the nominal radiodensity range for the brain tissue is normally between 0 and 100 HU, with bones greater than 200 HU. Since the background usually occupies a significant portion of a medical image, an additional thresholding step is usually performed in image processing tools to filter out information outside the target intensity ranges.

Among the various open source conversion tools, the one that worked best for the test dataset was dcm2niix tool. All of the nine scans were converted successfully with this conversion tool and passed the visual quality check.

Step 3: image resampling

Following the successful implementation of DICOM to NIfTI conversion, the majority of the DICOM tags are removed, only the most basic metadata remains in the NIfTI header. This simplicity is the major reason behind the popularity of NIfTI format in image processing software. However, even in the simplistic NIfTI formats, CT scans from different scanners still expose a heterogeneity in metadata. Namely, CT images could have different dimension, voxel spacing, origin and orientation, which make them less consistent and incomparable for group level analysis. Preprocessing provides a way to overcome these issues.

When testing, all the nine images were effectively resampled to the isomorphic resolution. It is worth noting that, in effect, the majority of the CT scanners take axial slices at a designated distance, thus the resolution in the axes parallel to the axial plane are finer than that in the orthogonal axis. A typical voxel size in a thick cut CT head scan is 0.5 by 0.5 by 3.0 mm. When resampling to isotropic voxels of 1 by 1 by 1 mm, the image is downsampled in the first two axes and upscaled in the longitudinal axis. So that the variation in the coarseness of the scans, in particular, the difference in slice thickness can be effectively unified. After resampling, the new voxel spacing replaced the old ones in the NIfTI header. Quite often, the new voxel spacing might not be the exact setting parameters due to rounding errors and thus the algorithm outputs the optimum spacing with rounding. Resampling prior to analysis is expected to not only increase the robustness of the subsequent algorithm, but also help reducing the real-time computing

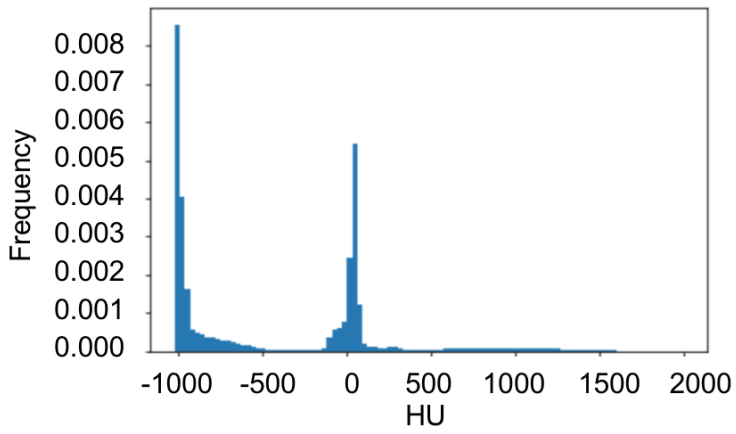

Figure 40: Distribution of intensities in HU for a typical head CT image. Note, there are two main peaks in the histogram, among which the right peak is the region of interest which corresponds to the brain tissue in the head CT scans.

workload for the designed tools.

Step 4: resetting image origin and direction

So far, many CT parameter examination and automatic diagnoses can be performed on an individual basis after the aforementioned procedures, yet when it comes to comparison or integration of multiple datasets, the current preprocessing steps are not adequate. For instance, the head orientation, in particular the skew angle and the orientation angle, as defined in Figure 27, may still vary to a great extent from scan to scan even though these scans share a unified modality. In the scenario of TBI, the head orientation in pre-operative and post-operative CT scans of the same patient may be quite different, because the patient position in the CT scanner varies during CT acquisition. This deviation in head orientation might not be a problem for radiologists' visual inspection or qualitative analysis, but it makes quantitative statistical analysis on specific structures difficult to achieve. In fact, neuropathological investigation and diagnosis often involves correlation analysis between pathological brain and healthy brain. In order to facilitate structure-wise and ultimately voxel-wise correspondence between abnormal and control dataset, the morphology of the input scans should be faithfully aligned.

The objective of step four in the preprocessing pipeline is to translate the image dataset to similar physical regions and prepare them for the subsequent registration algorithm. Image origin is a critical parameter that affects the quality of subsequent registration process, because the origin is usually a starting estimation that kicks off the formal registration algorithm. This step resets the image origin for all test CT images, while adjusting the image direct cosine matrix to the same value, to ensure that the output images from step 4 are in the same coordinate system.

Step 5: spatial normalisation

Brain image registration is a computationally consuming procedure that requires a robust algorithm to deal with all sources of image noise, ranging from different head orientation, intensity ranges, deviation of image origins, and most importantly, morphological damage in the scenario of TBI. To test the performance of the rigid registration tools, 10 CT head scans have been co-registered to a template (reference) CT image where there is no obvious gantry tilt. All the 10 test scans to be co-registered were traumatic scans with various extent of brain lesions, to assess the compatibility of the registration tool in longitudinal

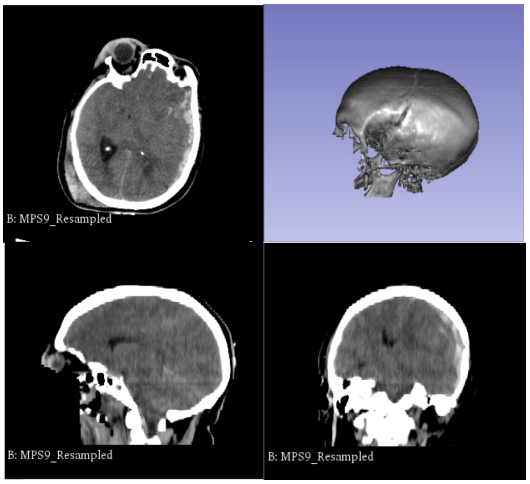

(a) Source image of an example CT scan before registration, with 3D rendering of the skull shown on the upper right corner.

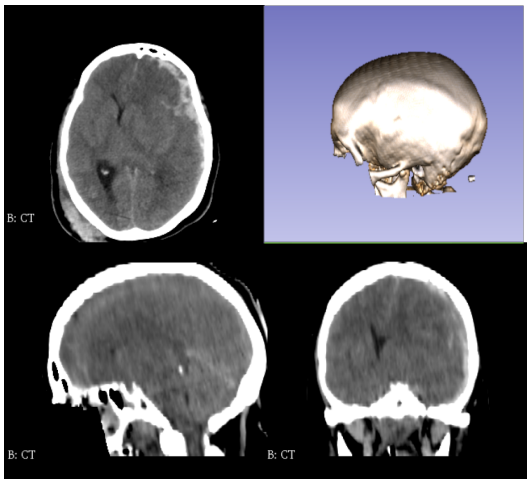

(b) Registered image of the example CT scan after registration to a template space, with 3D rendering of the skull shown on the upper right corner.

Figure 41: Example of individual CT head scan before and after registration. (a) Source image before registration, (b) registered image. Note, the orientation and distortion appeared in source image were successfully corrected after registration, with the head facing the front and the anterior-posterior axis of the head aligns well with the y-axis of the image.

TBI analysis.

When evaluating the registration results, one common problem faced by all the registration related tasks is the lack of effective universal registration quality indicator to assess the process quantitatively, especially when there is no ground truth available. As a result, visual inspection becomes the most popular quality checking method among all the possibilities. Visual inspection examines the physical plausibility of the registered image and qualitatively check if proper alignment is achieved between the source and the template images.

Among the three registration tools proposed in the preprocessing pipeline, the “General Registration (BRAINS)” module in 3D Slicer outperformed MIRTK and SPM8 in the 10 test samples. Visual examination by an experienced neurosurgeon suggests that the registration carried out by MIRTK and SPM8 constantly failed catastrophically, potentially because of the inaccurate image origin in the CT header. The importance of correct image origin in registration has been highlighted in previous preprocessing steps. Nevertheless, resetting CT image origin to the location of anterior commissure requires either manual intervention or a robust automatic anterior commissure detecter, which involves additional efforts. In actual fact, the major superiority for the ”General

Registration (BRAINS)" module is its flexibility in initialisation transform mode, which allows for various ways to initialise the registration centre, making the registration process less dependent on the image origin. Specifically, in addition to the traditional initialisation mode by image origin, the BRAINS module in 3D Slicer also offers a choice of initialising transform centre use "MomentsAlign", "GeometryAlign", "CentreOfROIAlign" and "CenterOfHeadAlign". The last option which used the top of the head together with the shape of the neck to drive the centre of mass estimation had been most helpful. All 10 head CT scan registered using this specific module settings in 3D Slicer have succeeded the visual inspection.

Figure 41 shows an example of the source and the registered CT scan. The source image as shown in Figure 41a was taken at a non-standard head position in the CT scanner, so the resultant CT scan possesses an abnormal skew angle and orientation as is shown in the axial and coronal views. The 3D reconstruction of the skull for the source image also appears to be slightly distorted. After registration, the head orientation and skew problems were resolved in the registered image as displayed in Figure 42. The distortion in 3D skull rendering was also fixed.

In addition to the visual quality check, the mean square difference (MSD) between target image and the template before and after registration is used to assess the quality of the rigid registration process. MSD is a popular quality index for registration evaluation without ground truth. MSD sums up the squared error between the source and the reference images (interpreted as N dimension voxel array), by the following equation:

$$MSD = \sum_{x} \sum_{y} \sum_{z} \big(F_1(x, y, z) - F_2(x, y, z)\big)^2 \tag{3}$$

where x, y, z corresponds to the spatial coordinates of the voxel contents, F_1 is the reference image and F_2 is the source image. Similar methods have been found in [94, 95]. Registration is best when the MSD is minimised. On average, the MSD between the 10 test images and the reference image has been reduced by 37.8% after registration, suggesting a reasonable optimisation of the mutual information.

In reality, the strength of rigid registration in aligning multi-shape geometries is demonstrated not only in lining up various head orientation, but also it corrects any remaining gantries in the source image, regardless of the image format. Thanks to the

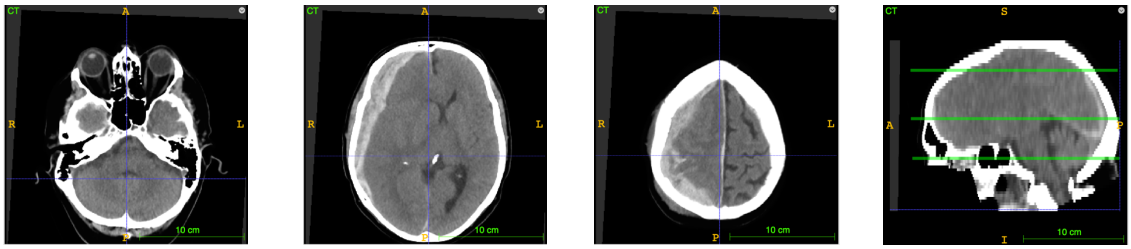

(a) Lower axial slice in Scan A

(b) Middle axial slice in Scan A

(c) Upper axial slice in Scan A

(d) Sagittal view in Scan A

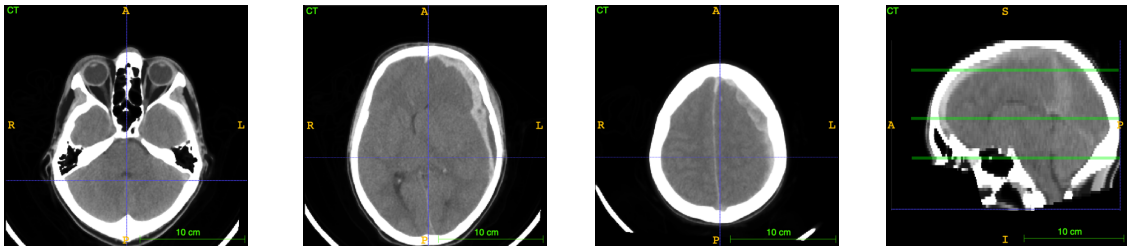

(e) Lower axial slice in Scan B

(f) Middle axial slice in Scan B

(g) Upper axial slice in Scan B

(h) Sagittal view in Scan B

Figure 42: Examples of co-registered CT head scans. Axial slices of identical depth are exhibited, with green lines in the sagittal view indicating the relative location of the slices. The top slices refer to (c) and (g), the middle slices are (b) and (f), the slices at the bottom are (a) and (e). Note, the two head CT scans are brought in to alignment after registration.

simplistic nature of NIfTI file, the majority of the medical data handover is achieved in NIfTI format, which implies the prior DICOM to NIfTI conversion has already been carried out by the raw data owner. However, the quality of the conversion remains in doubt. In fact, it is not unusual for NIfTI scans to have obvious gantry tilt angles, though these tilt angles should have been properly zeroed during format conversion. In the testing dataset, 3 out of 33 CT scans of NIfTI format were identified as non-zero gantry cases. One common concern is that many tools transform the DICOM image to correct the gantry but fail to change the acquisition tilt in the header of the resampled image. As a result, gantry tilt may be adjusted again in the subsequent tools, with the converted NIfTI image still skewed but to the opposite direction. Many gantry tilt correction tools require DICOM file as input and do not work for NIfTI image. For such cases, registration offers a way to compensate the unusual shape of image even in NIfTI format.

The source images in this research presents a diverging feature: from thin cut scans of thickness smaller than 0.5 mm to thick cut scans of thickness greater than 2 mm. By the end of the preprocessing pipeline, various CT source images were standardised in formats, sizes, resolutions, intensity ranges and various different patient head orientations are brought into alignment for longitudinal analysis. Figure 42 demonstrates two example

output images Scan A and Scan B from the proposed pipeline. In Scan A, the patient suffered from acute SDH in the right hemisphere, wheres in Scan B, left SDH is clearly visible. The two CT scans with contrasting intracranial lesions originate from different clinical centres and possess diverging image modalities in the raw images. However, after preprocessing and registration, the geometries of the head are seamlessly aligned. In the sagittal view, the images share a highly similar shape as shown in Figure 42d and 42h. Moreover, the axial slices at the same depth are associated to similar anatomic structures. The Figure presents example CT slices at the top, middle and bottom of the skull respectively. At each of the depths indicated by the green lines in Figure 42, the axial slices demonstrate highly comparable shape, size and orientation for the subject. Scan A and Scan B become ready for slice by slice comparative study after preprocessing. It is worth noting that the preprocessing pipeline standardises the scans for the purpose of slice-wise comparison, without changing the sizes of the skulls. Where necessary, the volumes of various skulls should be taken into account when performing group-level analysis.

Standardisation of image modalities prepares the healthcare data originates from various manufacturers consistent and compatible for automatic imaging tools. Algorithms of preprocessing is critical in generating high quality data and it is the quality of the provided data that determines to a large extent the strength of medical data mining models.

2.3.2 Automatic mid-sagittal plane detector

This section intends to investigate the performance of the automatic mid-sagittal plane detector described in section 2.2.2. The mid-sagittal plane is computed based on a plane that divides the skull 3D structure with maximum symmetry. It correlates to the original midlines of the brain before any traumatic injuries and pathological changes. Ideally, the calculated midplane should encompass the anatomical structures such as the falx cerebri and inter-hemispheric fissure, as they are the clinical indicator used by the radiologist when drawing the virtual midline. Here, these anatomic structures are considered as an assessment criterion to help evaluate the performance of the developed algorithm. An example of the calculated

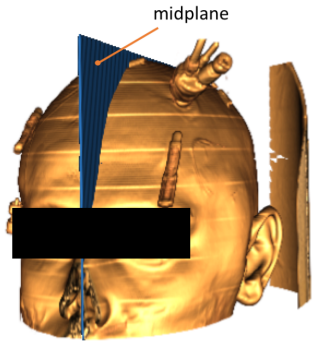

Figure 43: The calculated midplane shown on the volume rendering of a head CT scan

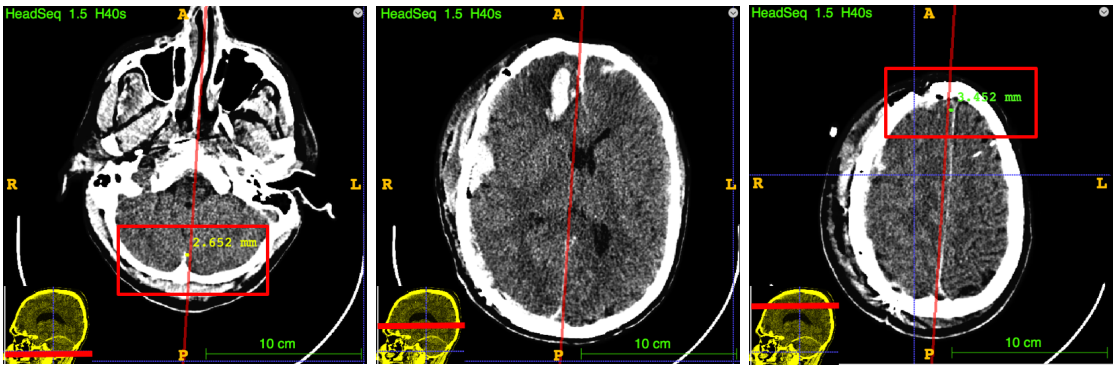

(a) A slice of ScanB around the skull base (b) A slice of ScanB in the middle of the head (c) A slice of ScanB at the top of the head

Figure 44: The performance of the computed midplane at different depth. The relative depth of each slice is denoted in a sagittal silhouette in the lower left corner. In an axial slice, the calculated midplane appears as a straight line connecting the anterior and posterior of the head. The red rectangular boxes highlight where the computed midplane deviates from the falx.

mid-sagittal plane is displayed in Figure 43.

In general, this midplane detector works well on both pre-op and post-op scans, regardless of their thickness of cuts. Of the 18 pre-op scans being analysed, a viable midplane has been successfully detected in all of the scans. For 17 out of 18 scans, the computed midplane passes precisely (misalignment angle with 1 degree) through the anterior and posterior falx insertions as is required, confirming the robustness of the detector algorithm. Figure 44 presents one of the less satisfactory midplane computed for Scan B, where the computed midplane missed the posterior falx attachment by a maximum of 2.7 mm on slices at the bottom of the skull, as shown in Figure 44a, and deviated from the anterior fissure by 3.5 mm on slices at the top of the skull, as displayed in Figure 44c. As for the post-op cases, the results were very similar: among the total number of 13 CT scans being analysed, viable midplanes were successfully generated for all of the post-op scans, though one of the calculated midplane slightly missed the attachment.

As an attempt to correct such slight misorientation of the midplane, the algorithm has been adjusted by further reducing the step size in the optimisation loop and shrinking the searching radius when counting the nearby pairs. These attempts, though helping optimise the skull symmetry, did not improve the performance of the midplane algorithm. The reason behind it is that the plane that gives maximum bone symmetry may not necessarily coincide with the anatomical features. This is also a natural issue for bone symmetry based midplane detection. It could be resolved by adding further steps to calibrate the midplane using anatomic structures such as the falx. Nevertheless, accurate detection of

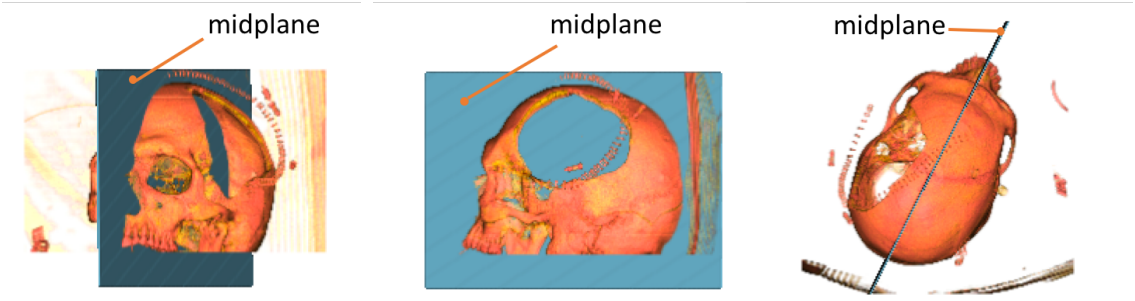

(a) Front view (b) Side view (c) Top view

Figure 45: The 3D rendering of skull and computed midplane shown in different views. Note the large portion of skull missing due to hemi-craniectomy. The midplane detector accurately calculates the midplane for the post-craniectomy patient.

the falx and the inter-hemispheric fissure can be challenging on CT scans. Considering that in this particular case, the computed midplane still passes directly through the falx on slices at the middle of skull where the midline shift is clinically measured, as shown in Figure 44b, the current midplane detector is deemed sufficiently accurate without anatomical calibration at this stage of the project. In the future, if requirements for the anatomical accuracy increases, anatomy based algorithm may be used to enhance the performance of current midplane detector.

The fact that the midplane detector performed equally well on pre-op and post-op scans reveals one of its significant advantages: this bone symmetry based method is robust to the local asymmetry due to pathological changes. In severe TBIs, intracranial hypertension may cause shift and dislocation of brain structures, breaking the natural symmetry of brain. Yet the skull, thanks to its rigid nature, is more likely to preserve its symmetry in the evolution of brain pathologies. Even if the skull is not complete in case of neurosurgery or traumatic injury, it will not be drastically out of shape. The skull may lose partial symmetry due to fracture and craniectomy, but still, there exists a mid-sagittal plane that maximises the symmetry of the fragmentary skull structure, as indicated in Figure 45.

Computation time is another important performance indicator. For the current mid-sagittal plane detector, the main time consuming factors are the process of nearby pair searching and the optimisation loop. A typical data cloud of P_{skull} contains more than 300,000 data points. Splitting by the midplane leaves over a hundred thousand data points for $P_{rightskull}$ and $P_{mirrorskull}$ respectively and searching through these data costs approximately 3 minutes per count on a 2.3 GHz Inter Core i7 processor. A typical calculation contains more than fifty counts in the optimisation loop depending on the

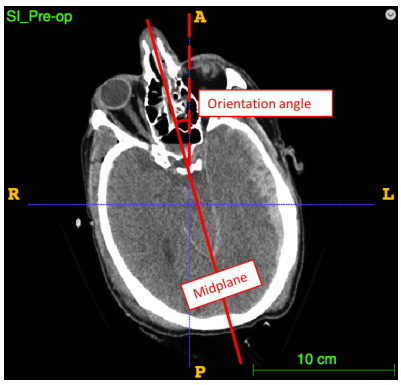

(a) Sample I before orientation correction

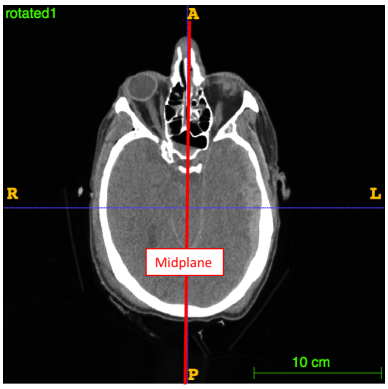

(b) Sample I after orientation correction

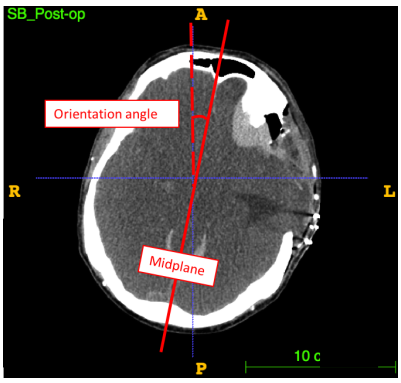

(c) Sample B before orientation correction

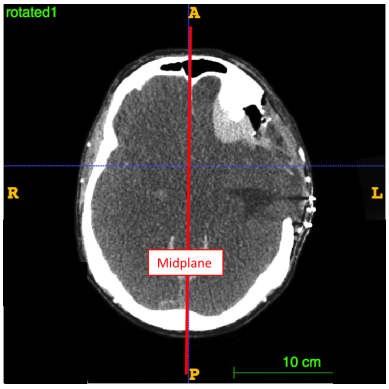

(d) Sample B after orientation correction

Figure 46: The effect of orientation correction based on the computed midplane. Note, the solid red line indicates the anterior-posterior axis of the head, and the dashed red line shows the vertical direction of the image.

step size. To mitigate the time effect, a fraction of $P_{rightskull}$ is randomly selected to form a sample array, of which the size is proportional to running time. Through continuous adjustment by trials and errors, it is seen that a sample array of five thousand data points reduces the computation time to less than 5 seconds per count, while maintaining a satisfactory symmetry assessment ability. For the optimisation loop, the step size is a critical factor, as running time is inversely proportional to the step size. Performing the whole detector algorithm with greatest sample size and minimal step size could take up to 2 hours for each scan. By regulating the step size and sample size, the current midplane detector is tuned so that the average computation time is 6 minutes. The parameters used in this current detector algorithm is considered as a reasonable compromise for achieving short CPU time and robust performance.

One potential application of the midplane detector is to use the computed midplane to

reorientate the head CT. Since the patients with severe TBI are usually unconscious and will not be able to maintain the head position when being scanned, the resulting CT scans demonstrate large variance in patient head position. Therefore it is clinically beneficial to have an automatic algorithm that corrects these head orientation angles (as defined in Figure 27a) and skew angles (as defined in Figure 27b). Figure 46 shows two examples of correcting the head position using the computed midplane. Ideally, after orientation correction, the midplane should be in the vertical line crossing through the middle of the scan. Then the head CT scan becomes more straightforward for the clinicians to interpret. Meanwhile, it is believed that the midplane based orientation-correction algorithm could be applied to enhance the performance of deformable registration on pathological CT scans, as the registration performs better when the head is well aligned.

2.3.3 Automatic brain extractor

Skull stripping on head CT, especially in pathological cases, is a challenging task, not only because of its finite resolution on soft tissues and the random noises in grey scale values, but also the boundaries between different anatomic structures are very blurry. Consequently, a long script has been produced to resolve this problem. The developed brain extractor comprises three main sub-algorithms, namely, the BET FSL tool, the extra brain remover and the FM detector. Given that the BET FSL only works on scans with intact skull, the brain extractor is tested only on the 18 pre-op CTs. In this particular scenario, the intracranial lesions including the haematoma and haemorrhages were included in the brain masks, for more complete extraction of the intracranial space.

Of the 18 pre-op scans being analysed, a reasonably practicable intracranial brain mask has been generated in 14 cases, among which 10 out of 14 cases perform satisfactorily well without any need for further manual interventions. One of these good examples is shown in Figure 47a. It is seen that the intracranial brain volumes are correctly identified, the FM plane is accurately detected and so the output brain mask fulfils the designed targets well without further processing by human. Such brain masks could be exported as 3D mesh file, as shown in Figure 47b, and reconstructed in Finite Element (FE) softwares such as ABAQUS for patient specific biomechanical simulations.

In the other 4 out of 10 cases, however, the extractor missed some false negative brain volumes while mislabeled some false positives. Figure 47c is an example. To correct the brain mask, manual interventions are conducted by myself under the supervision of a neurosurgeon, Mr. Adams. The false positives are painted in blue and the false negatives

in green. When reconstructed in 3D in Figure 47d, it becomes obvious that both the missing brain volume and the mislabeled brain volume are concentrated in the anterior region. This is potentially because the skull becomes more structurally sophisticated in the anterior part and hence it is difficult for the BET FSL to distinguish the border between brain and non-brain structures.

Meanwhile, the extractor fails catastrophically in the remaining four pre-op CT scans. When examing these failures, it is discovered that half of them are noisy with the other half being thick-cut. In scan A and C, the image appears grainy on the cross-sectional imaging, an example is shown in Figure 48a. Technically, this undesirable change in pixel values in an otherwise homogenous image is referred to as quantum mottle, possibly due to the inappropriate use of dose, hindering the contrast resolution. Such noisy CTs present no meaningful pathological or anatomical information and should be excluded

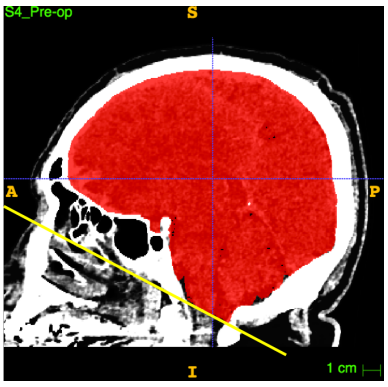

(a) Computed brain mask and FM plane, without manual intervention

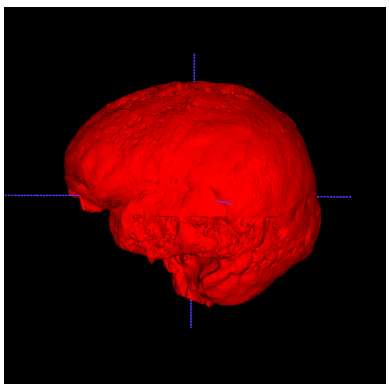

(b) Reconstructed 3D surface mesh of the brain mask

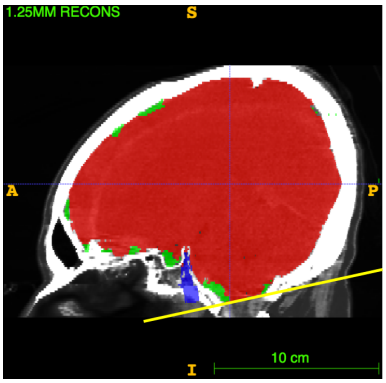

(c) Computed brain mask and FM plane, with manual correction

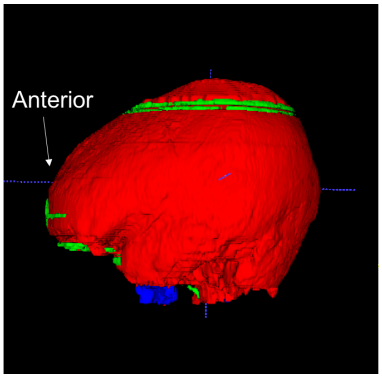

(d) Reconstructed 3D mesh of manually corrected brain mask

Figure 47: Examples of computed brain masks and their 3D mesh reconstruction. Red mask is the calculated brain mask. Green and blue masks are manual intervention labelling false negative (green) and false positive (blue) respectively. The yellow line is calculated FM plane.

when evaluating the extractor performance. As for the thick-cut CT, the increased slice thickness decreases the spatial resolution in the z-axis, as shown in Figure 48b. This limited spacial resolution causes failure of BET FSL in the first sub-algorithm, and henceforth the failure in the main extractor algorithm.

Up to now, the performance of the automatic brain extractor has been evaluated qualitatively. To obtain a better insight on its performance, the quantitative analysis is performed as well. This is achieved by manually inspecting each of the fourteen pre-op scans (excluding the thick-cut and the noisy ones) to delete the false positives and put in the false negatives. The manual inspection is done by myself and revised by a neurosurgeon (Mr. Adams), therefore these edited brain masks can be considered as the gold standard.

The automatic intracranial brain volumes are plotted against the manually delineated volumes in Figure 49. It is seen that the automatic volumes are very close to the manually delineated volume. Specifically, a linear regression of the 14 data points reveals a slope of 0.9936 and an intercept of 13.35 cm^3, indicating very little bias. Besides, the R^2 value of 0.999 also implies strong correlation between manual and automatic volumes. It is worth noting that one limitation of this performance indicator is that for one particular scan, the automatic brain mask tends to include some false positives while also miss some positive brain volumes, which might mitigate the resulting brain volume statistics. Nonetheless, it is still reasonable to conclude that the automatic brain extractor performs acceptably well on thin-cut CT scans, provided that the image is not noisy. For those less satisfactory brain masks, expert inspection and editing may be involved if accuracy is a priority. Even

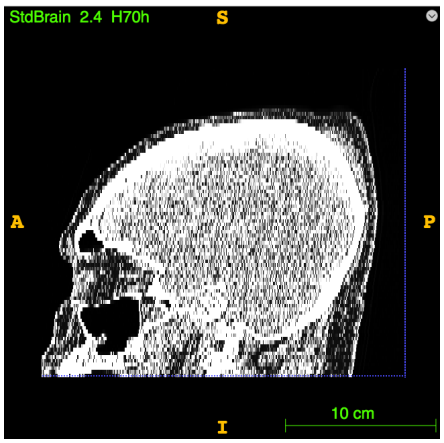

(a) A sagittal slice of noisy CT from Scan A

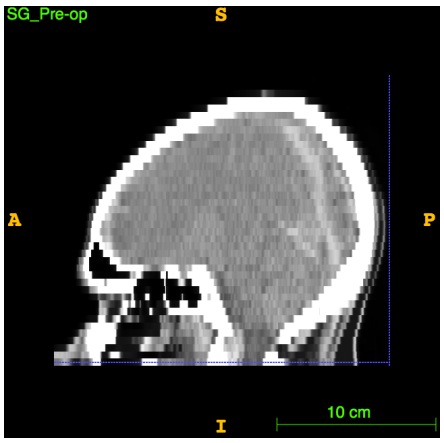

(b) A sagittal slice of thick-cut CT from Sample G

Figure 48: Examples of CTs that are incompatible with current brain extractor. Note (a) is a worst case scenario.

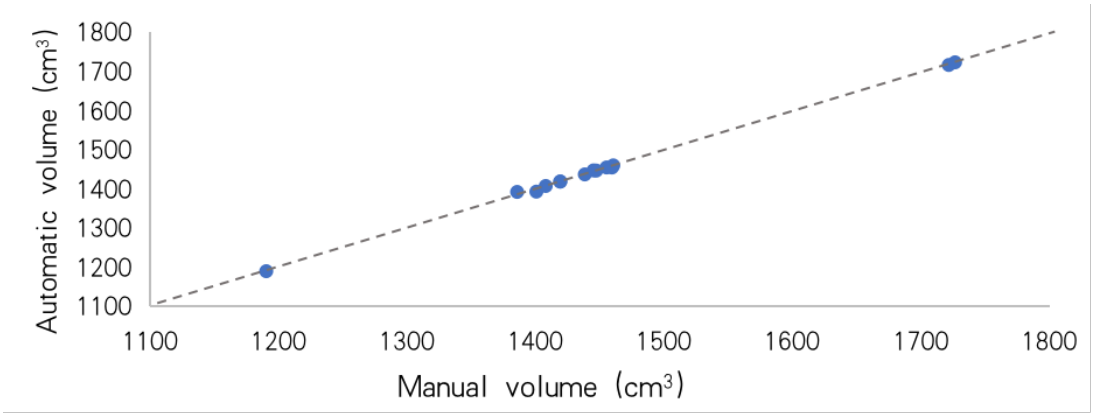

Figure 49: Automatic and manual intracranial volume analysis. Note, the dashed line indicates automatic volume equal to manual volume.

then, editing on the automatic brain mask saves a substantial amount of work for the radiologist and clinicians.

Apart from being a performance indicator for the developed brain extractor, Figure 49 also reveals the variance of total intracranial volume (TIV) between objects. TIV refers to the proxy of maximum pre-morbid brain volume and is henceforth used to account for the variation in head size. When modelling otherwise unexplained variability in brains, adjustment for TIV can be helpful if there exists imbalance in head size between groups. In future studies, the intracranial volumes calculated using the developed automatic brain extractor tool can be adopted as a normalisation measure when performing morphometric brain analysis to correct for head size.

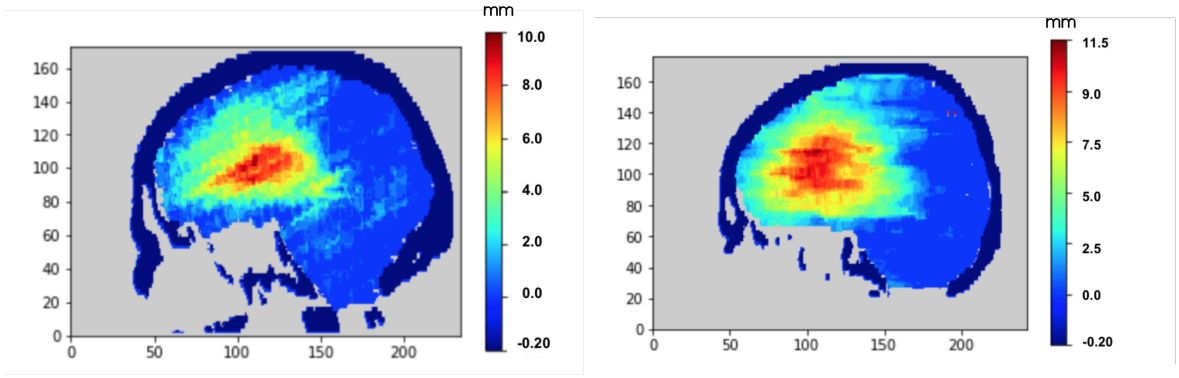

(a) MPS heatmap from sample A

(b) MPS heatmap from sample B

Figure 50: Example MPS heatmaps

2.3.4 3D brain shift analysis

MLS is considered by the clinicians as an important clinical indicator when assessing the necessity of neurosurgery. However, sometimes it could be over simplistic to make clinical decisions based on brain deformation at a single depth. In this section, we build on the concept of MLS and propose a novel way of quantifying 3D shifts of brain mid-structures using MPS. The calculated MPS is projected onto the ideal mid-sagittal plane to form a heatmap. Figure 50a and 50b are examples of such MPS heatmaps.

In both Figure 50a and 50b, the brain herniates to the left and therefore shift to the left is deemed as positive when calculating MPS. Thanks to the preprocessing pipeline, the output MPS heatmaps from Sample A and Sample B look very similar in shape, though the input original CT scans are essentially different: Sample B is a rather shallow head scan and fails to include the complete brainstem, while Sample A scans till the neck and contains the whole brain volume. The standardisation of raw CT scans plays an important role in the generation of MPS heatmaps.

Furthermore, the MPS heatmap in Sample A and Sample B share one thing in common: the shifts concentrate on the ventricular region, though the degree of shift is more severe in Sample B than that in Sample A. This is not a coincidence, but the brain anatomy dominates the shifts. The cerebral falx, as introduced previously in Figure 1, is essentially a large, crescent-shaped fold of meningeal layer of dura mater that descends vertically in the longitudinal fissure between the cerebral hemispheres of the human brain [97], as presented in 3D in Figure 51. Being a thick protective membrane attached at the midline to internal surface of the skull, the falx is rather rigid and henceforth more resistant to deformations. In contrast, the ventricles are prone to deviate from their original position, because they are filled with cerebrospinal fluid within the brain parenchyma and are susceptible to any intracranial mass lesions and high ICP.

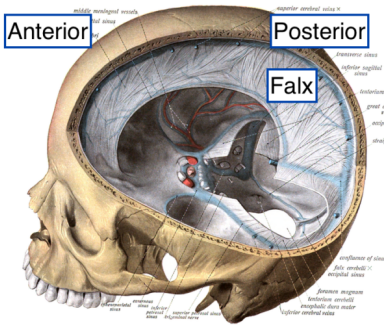

Figure 51: The falx cerebri shown in 3D [96]

The MPS resolves the cross-midplane shifts in the brain thoroughly through the full range of depths. The heatmap provides straightforward visualisation for the MPS. It encompasses the conventional MLS, but provides the whole picture instead of a single

data point. Being a more detailed and reliable substitute for MLS, the MPS is expected to support the clinicians to make more informed clinical decisions.

Although the MPS tool provides an abundance of information for the shifts of brain mid-structures, the construction process, in particular the identification of mid-structures from CT scans, is very difficult and time-consuming. The current method relies on manual delineation and it took more than half an hour to complete one set of CT scan. Since the midline structures are not visible on every slice and one has to derive the actual midline by estimating trends of deformation based on the visible signs, the process requires some expertise and judgement, and can be very time consuming. As a result, we aim to automate this process in the near future. The automation could be challenging, considering that the identification of the brain mid-structures on low-resolution CT scans is difficult. Simple thresholding may not work satisfactorily as the brain tissues have a wide range of overlap of grey scales and structures like the septum pellucidum are very thin in nature. Nevertheless, techniques such as deformable registration are hopefully feasible ways to fulfil this task.

2.4 Concluding discussion

To sum up, this chapter describes the development of a series of medical image computing tools for the analysis of head CT scans under the scenario of TBI.

Provided that the vast amount of healthcare data are often inconsistent and non-standardised, a preprocessing pipeline has been developed to prepare medical images of different modalities from different data sources to a similar format. The full processing pipeline involves gantry tilt correction, image intensity range alteration, resampling and resizing, as well as rigid registration. Depending on the status of the input CT scans, the proposed pipeline could be applied fully or partially. When source images are in NIfTI format, it is assumed that the problem of non-zero gantry has already been resolved when DICOM to NIfTI conversion is conducted, therefore there is no need to redo the gantry tilts correction. Besides, registration is not a compulsory step for many image analysis applications, particularly on the individual level. Rigid registration involves translation and rotation of image coordinate frame to maximise the mutual information between the source and the template images. This is a computationally expensive algorithm that requires substantial operations. However, excessive manipulation on the imaging data will potentially degrade the image quality and introduce artifact. As a result, it is suggested to selectively apply the preprocessing steps proposed in the pipeline under

different application scenarios for the best possible result.

Following various extent of preprocessing, three computational tools have been developed to enhance the interpretation of medical images, in particular head CT scans for traumatic head injury. The detailed methodology was presented in section 2.2. The performance of the developed tools were rigorously analysed in section 2.3 using CT scans from the RESCUE-ASDHs clinical trial.

The first script, the automatic mid-sagittal plane detector, accurately identifies the ideal midplane for both pre-DC and post-DC subjects using skull symmetry. The output ideal midplane is considered as the reference plane to help quantify any 3D brain shift and brain asymmetry due to the presence of mass lesions and abnormal intracranial hypertension. The midplane detector script also offers a reliable automatic way of correcting head orientations on CT scans. It is beneficial to conduct higher-level imaging techniques on well-aligned CT head scans for the better accuracy.

The second script, the automatic brain extractor, separates the intracranial brain volume from any non-brain structures in pathological CT scans with intact skull. Skull stripped head images are the foundations for many advanced segmentation and registration algorithms targeting in-depth analysis of various brain tissues. Segmentation of ventricular system, for example, is important for automatic identification of the brain mid-structures. Segmentation of intracranial haemorrhages and contusions is critical for the heterogeneity analysis of the brain pathologies. Segmentation of grey and white matter is crucial for the construction of anatomically comprehensive computational brain models. Basically, accurate segmentation of various brain compartments not only aids the clinicians with more information regarding the brain pathophysiology, but also it is of great significance for patient-specific FE model reconstruction. Automatic segmentation algorithm for the various brain tissues may be the next step based on the current brain extractor tool. In the meantime, an automatic skull stripping algorithm for post-DC subjects should also be worked out.

The third script, the 3D brain shift analysis, proposed an innovative way of presenting the deformation of the brain across its mid-sagittal plane. The computed MPS is a 3D evolution of the currently practiced MLS and so it expands upon the MLS with the extent of clinical information it provides. The computational process, however, is currently semi-automatic and relies on manual delineation of the actual midplane. Therefore in the near future, efforts will be made to fully automate the actual midplane detection, by then, no manual intervention will be required to calculate the MPS.

In addition, the automatic FM detector, although developed as a sub-algorithm for the brain extraction, could be an independent output itself. Clinically, it is believed that different brain compartments are responsible for diverse cognitive functions. Therefore herniation at different regions may have distinctive weightings in terms of clinical severity. Herniation of the brainstem, for instance, is potentially more deadly than that of ventricular regions. The FM detector accurately locates the foramen magnum, which is anatomically close to the brainstem. As a result, it is possible to capture any pathological changes near the brain by making proper use of the FM plane.

3 Interpretation of CT parameters related to brain deformation

3.1 Introduction

In theory, every set of CT scans contains a tremendous amount of clinical information and the findings that can be derived from each individual scan are unlimited. Over the years, there is an increasing number of CT imaging characteristics which have been proposed and studied to interpret the CT scan and better understand a patient's condition. These are called CT parameters or CT findings. The objective of this chapter is to build on the existing CT parameters and derive new ones to interpret the TBI related head CT scans, using the computational tools developed in Chapter 2.

Among the existing CT parameters describing the morphological characteristics of TBI patients, the magnitude of midline shift and the presence of mass lesions are the most frequently used indicators across all the CT scoring systems, to help recognise patients at higher risk of deterioration. Large prognostics studies have reported that the intracranial lesion types and the associated haematoma size are the most critical factors in predicting outcome [98]. Meanwhile, both of the large international trial studies in TBI, CRASH [99] and IMPACT [100] emphasise the importance of midline shift. Studies also show that the magnitude of midline shift is the most important parameter for predicting unfavourable outcome [101, 102]. Nevertheless, it is worth noting that CT findings are not always independent, in effect many of the parameters are highly correlated in a complex manner. The intracranial lesions and midline shift and for example, are believed to be strongly related. Therefore to answer the question of whether these two CT parameters should be included all together in one classification model, a detailed correlation study is carried out in this chapter.

With the recent advancement in medical image computing, more and more novel CT parameters can be developed to describe the morphologic abnormalities, in addition to the traditional MLS and intracranial mass volume. In section 2.2.2, an automatic mid-sagittal plane detector was developed to accurately identify the inter-hemispheric sagittal plane in the brain. By coupling the lesion segmentations and 3D brain shifts with this ideal midplane, the concepts of lesion heat map and MPS heat map have been established, yielding a number of novel CT characteristics that have never been investigated before. Those new emerged CT parameters should be carefully interpreted

to extract the information within the CT pixels and help clinicians to better understand a patient's condition. It is expected that, with the help of the developed computational tools, the brain deformation mechanism could be investigated with greater detail.

Overall, this chapter will first study the correlation between the volume of various intracranial mass and the degree of midline shift and also investigate the potential prognostic value of these two parameters in combination. Then the section will focus on systematic interpretation for the properties of midplane shift (MPS). The last part in this chapter will investigate the intracranial mass lesion with the various novel CT parameters computed using the developed computational tools in section 2.2.

3.2 Methods

3.2.1 Correlation analysis for intracranial mass lesion and brain midline shift

Over two hundred years ago, Alexander Monro deduced that the intracranial contents inside the cranium was of constant volume at all times [103]. This doctrine has later been validated by the experiments of Kellie [104] and known as the Monro-Kellie hypothesis. The hypothesis states that the total volume of three intracranial contents, the brain, the blood and the CSF, will remain nearly constant in the "rigid box" of the skull. Therefore an increase in one must occur at the expense of volumes to one or both of the remaining two. This doctrine has serious implication for intracranial hypertension. In accordance with the doctrine, the development of focal intracranial pathologies that occupy the volume inside the skull will reduce the perfusion by increasing the ICP level. When the compensatory mechanisms eventually exhausted, such a pathology will lead to permanent damage to the functional structures of the brain. This is called mass effect.

In pathological examinations, midline shift is often regarded as a quantitative indicator of reduced perfusion and mass effect. It develops when the pressure exerted by the build-up of haematoma and swelling around the damaged brain tissue becomes powerful enough to push the entire brain off centre. In TBI, focal hemorrhagic mass lesions are considered as the main cause of brain midline shift. Strong correlation has been repeatedly observed between the magnitude of midline shift and brain hemorrhagic lesion volume and studies have even suggested that the haematoma volumes vary nearly co-linearly with midline shift [102]. However, controversy exists on whether there exists a quantifiable causal relationship between these two parameters and more importantly, can they be substituted for each other in CT scoring systems.

In this section, we aim to investigate the correlations between intracranial mass volumes and the subsequent midline shift using a multivariate linear regression model. As compared to the traditional correlation studies, the proposed multivariate model encompasses a variety of lesions and explores whether different types of lesions play equally important roles in the formation of midline shift. The predicted midline shift from the model is then compared with the actual midline shift to further understand the prognostic value for haemorrhagic mass volume and midline shift as used in CT scoring systems and help refine the classification and prognostication for TBI patients.

Patient dataset

This study retrospectively reviewed the Samcook and FAVO dataset from the major trauma centre in Addenbrooke's Hospital in Cambridge, UK. The medical records of those TBI patients were also checked. The inclusion criteria for the present study were:

- Recent history of TBI
- Initial head CT scan available
- Major hemorrhagic lesion being unilateral
- CT scans prior to lesion evacuation

Thirty-seven patients with unilateral lesions secondary to TBI were selected. There were 85 CT scanning sessions in total including the initial and subsequent CTs prior to an operation. The interval CT scans were included when considerable change was observed in a patient's intracranial complications. Clinical information including age, gender, injury mechanism, surgical condition and Glasgow Coma Scale (GCS) score were collected for all patients. Based on GCS scores, the patients were further stratified into three subgroups: mild injury (GCS=14-15), moderate injury (GCS=9-13), severe injury (GCS=3-8).

Imaging analysis

All the non-contrast CT head scans were reviewed separately from clinical information to evaluate the two CT measures of interest in our study: the intracranial lesion volume and the midline shift. The magnitude of midline shift was measured as the perpendicular distance between the skull centreline (geometric centreline drawn between the anterior and posterior falx attachment points to the skull) and the septum pellucidum at the level of the Foraman of Monro, as shown in Figure 52a. Midline shift measurements were

made by myself and checked by a visiting neurosurgical PhD student, Miss. Selma Tulu, and compared with the midline shift recorded in the neuro-radiologist's report for each of the scans. Any disagreements were resolved by having a second radiologist check the measurement.

In addition to midline shift, any visible traumatic lesions and their volumes were analysed. The types of intracranial abnormalities under investigation includes subdural haematoma (SDH), epidural haematoma (EDH), hemorrhagic contusion (CONT), peri-contusion oedema (PCO), subarachnoid haemorrhage (SAH), intracerebral haemorrhage (ICH), pneumocephalus (PN) intraventricular haemorrhage (IVH) and petechial haemorrhage (PH). These intracranial lesions in the TBI scans have been annotated in different colors by Dr. Virginia Newcombe and her group before the data handover. In both the Samcook and

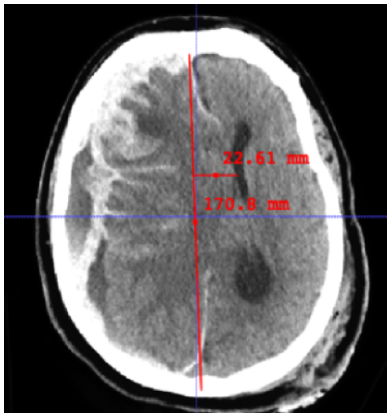

(a) original CT scan with 23 mm MLS.

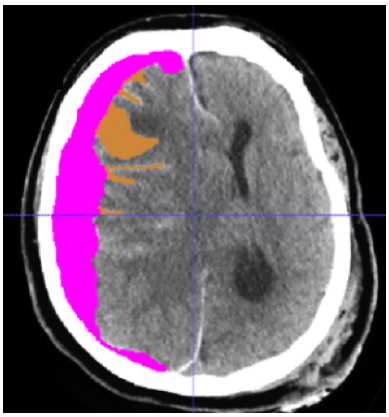

(b) expert annotation of lesions in axial view

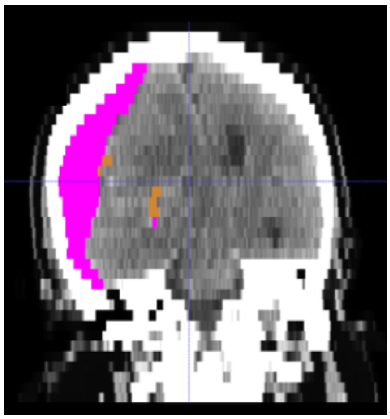

(c) expert annotation of lesions in coronal view

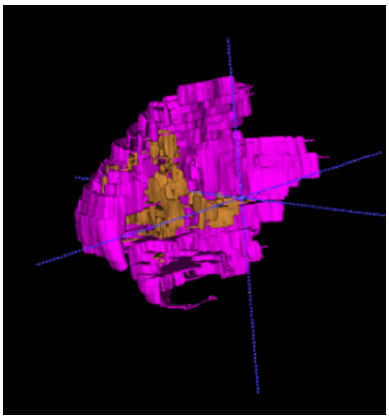

(d) 3D reconstruction of annotated lesions

Figure 52: Illustration of the lesion annotation methods. CT scan showing a patient suffered from acute SDH, labelled in pink, and SAH labelled in brown. Note, this is an example annotated CT scan from the Samcook dataset.

FAVO dataset, lesions were manually annotated by a neuro-radiologist in every axial slice of the CT scan using a "paintbrush" tool (freehand segmentation with active labelling), as shown in Figure 52 and segmentation results were checked by a second annotator for better accuracy. Figure 52 is one example showing how various types of lesions have been annotated in different colors in the Samcook and FAVO dataset.

By coupling the manually segmented lesion area with slice thickness information, three dimensional reconstruction of the lesions was obtained and the lesion volume was calculated, in similar manner to [105, 106]. An example of 3D lesion volume reconstruction is shown in Figure 52d. The current volume estimation protocol, though being labour-intensive, can provide the closest estimate for the actual lesion volume [106], as compared to other volume estimation techniques such as ellipsoid [107] and the Cavalieri [108] pragmatic methods. The method employed is considered as the current gold standard for lesion volume estimation.

Correlation analysis

Since midline shift is generally believed to be a result of mass effect, it is our hypothesis that midline shift could be reliably predicted by the intracranial lesion volumes observed in the CT scans. However, traumatic intracranial pathologies present in various different forms depending on the nature of the impact force. According to the Monro-Kellie doctrine, non-hemorrhagic injuries such as PCO and PN, must play a different role as compared to hemorrhagic injuries in mass effect. Given the heterogeneous nature of TBI, it is critical to distinguish those lesions that are more tightly correlated with midline shift.

To investigate this hypothesis, a correlation analysis was carried out to identify the independent variables associated with MLS using Pearson's correlation coefficient r, together with Welch's unequal variances t-test, in similar way to [70]. Statistical significance was reported when p is smaller than 5% level. Only lesions that were reported significantly correlated with MLS with $p < 0.05$ were selected to build the MLS prediction model. Using the identified lesion types and their corresponding lesion volumes as predictors, a multivariate linear regression model will be fitted to predict the degree of midline shift in the following form:

$$MLS = a_1 \times V_1 + a_2 \times V_2 \cdots a_n \times V_n \tag{4}$$

where MLS is midline shift, V_1, V_2 and V_n represent the volumes of corresponding lesions that are deemed significantly correlated with MLS, and a_1, a_2 and a_n are the associated

coefficient for each of the lesions. The developed lesion-MLS model actively takes the volumetric intracranial mass contents in a TBI head scan as inputs and predicts the resultant MLS in reaction to the injury.

Previous studies either consider only the one dominant type of intracranial lesion or the total volumes of a combination of haematoma lesions. To the best of our knowledge, this is the first time that intracranial mass lesions of different types have been differentiated and correlated with midline shift. A comparative analysis was also performed to evaluate whether different haemorrhagic lesions are of equal importance in the formation of midline shift. Moreover, the predicted MLS using the lesion model will be related to the actual MLS present in the CT scan to explore its prognostic values in outcome prediction.

3.2.2 Properties of midplane shift (MPS)

Despite the functional differences between the left and right hemispheres of the brain, the gross morphology of the human head is approximately symmetric about the mid-sagittal plane [109]. However, under pathological conditions, such a natural symmetry may be disrupted by a variety of abnormal pathological changes. Intracranial mass, such as hemorrhagic lesions that appears after TBI, can cause dislocations of brain anatomic structures off from its original position, known as mass effect. The shifts of brain during mass effect, if not treated properly, can cause brain herniation, brainstem compression and death. With the invention of cross-sectional imaging techniques and the improvement in its resolution, observations on the shifts of brain midline structures are playing an increasingly important role in patient diagnosis prior to further treatment.

Midline shift (MLS), which refers to the magnitude of deviation of brain midline structures from its ideal midline, is currently integrated in most mainstream CT classification systems as a routine procedure to evaluate patient's intracranial condition. However, it only reveals the brain shift condition at a specific depth. Contrastingly, midplane shift (MPS), as introduced in section 2.2.4, provide a method to resolve the cross-plane deformation of the brain through its entire range of depths and provide a comprehensive overview of the intracranial mass effect.

Direct application of the MPS tool as described in section 2.2.4 produces MPS heat-maps as shown in Figure 50. In those example MPS heat-maps, brain herniation was schematically represented for both sample A and sample B independently. In the current study, 33 initial CT scans were examined in total, all satisfying the following criterion:

1. Recent history of TBI
2. Initial head CT scan on admission
3. MLS in neuro-radiologist's report > 5 mm

Since the objective of the study is to further investigate brain shifts, any CT scans with minor MLS have been omitted from the database. The manual delineation of anatomic (deformed) midplane involved in the third step was performed by myself, together with Dr. Eric Thelin, a neurosurgeon with 5 years clinical experience. The delineation result has been checked slice by slice for each of the CT scans by a second expert, Miss Selma Tulu, to ensure the accuracy of the results.

Novel CT parameters

In addition to clinical MLS, there are a bunch of additional parameters that could be derived from the MPS heat-map. For instance, by observing the MPS cross-plane heat map, it is straightforward to find the point where maximum brain deviation happens across the midplane. Such a maximum deviation is defined as the maximum MLS. Unlike the traditional MLS, the maximum MLS may take place anywhere across the mid-sagittal plane. As a result, in a common TBI scan, the maximum MLS is usually greater in magnitude than that of the traditional MLS.

Moreover, the MPS heat-map reveals the cross-plane deviation associated with every single pixel that appears in the mid-sagittal plane and provides a better illustration of the brain movements. By integrating over the whole mid-sagittal plane, the total volume of brain shift across the midplane could be quantitatively calculated, as brain volume shift. Figure 37 shows how such a brain volume shift is achieved computed by totalling up the volume between the actual and ideal midplanes. This is the first time that the volumetric brain shifts could be estimated with reasonable accuracy.

The evolution from MLS to MPS is actually an advancement from two-dimensional to three-dimensional representation. In the 3D world, the brain shifts are also correlated with location information: whether the deformation concentrates on the anterior or posterior, upper or lower part in the midplane. To effectively estimate the brain shift locations, a parameter called MPS centroid has been defined as the centre of mass of the deviated brain volume.

To sum up, MPS offers additional information on brain deformation. In this section, 33 traumatic CT scans with various extents of brain shift were analysed to systematically

explore the properties and characteristics of MPS. It is expected that with these novel parameters, the displacement condition of brain could be evaluated with greater detail.

3.2.3 Intracranial lesion analysis

The mid-sagittal plane is an important tool for morphological brain analysis. In theory, the functional structures of the brain are roughly symmetrically situated in the left and right hemispheres. The mid-sagittal plane separates the two hemispheres with optimum symmetry, thus in healthy individuals, the different compartments of the brain should be quasi-symmetric against the midplane until the presence of intracranial mass distorts the brain compartments and introduces asymmetry. An asymmetry based mass lesion analysis is carried out through the following steps:

1. Input CT scan
2. Compute the midplane using the automatic mid-sagittal plane detector
3. Segment traumatic brain injuries and save into a lesion mask
4. Calculate volume difference of the lesion mask and generate the lesion heat map

For lesion segmentation in the second step, expert lesion segmentation was provided for the scans from the Samcook and FAVO dataset. However, for those scans from the RESCUEicp trial without professional annotations, the scans were firstly thresholded to $HU > 60$ and then manually checked slice by slice by myself, under the supervision of a neurosurgeon, Miss Selma Tulu, to fill up the false negatives and also erase the false positives. The quality of the lesion masks after manual correction is checked by another neurosurgeon, Mr Angelos Kolias, to ensure the quality of the segmented lesion masks.

The last step is the most sophisticated, but it is similar to the generation of MPS heat map. Here, the the lesion mask in the left hand side of the midplane (left hemisphere) was subtracted from the the lesion mask of the haematoma in the right hand side of the midplane (right hemisphere) and the resultant difference mask was projected onto the midplane. In this way, for every pixel in the midplane, the haematoma volume difference across the two hemispheres was calculated along its projection normal. Such a volumetric asymmetry of haematoma is then projected on to the midplane to form a lesion heat map. The volume difference across the midplane has been normalised through the following equation:

$$D(i,j) = |LH(i,j) - RH(i,j)| \tag{5}$$

where (i, j) represents the pixel location in the midsagittal plane, $D(i, j)$ is the absolute volume difference, $LH(i, j)$ is the left haematoma volume along the projection normal at (i, j) in the midplane and $RH(i, j)$ is the right haematoma volume along the projection normal at (i, j) in the midplane. Normalisation was performed to standardise the magnitude of asymmetry for different patients with respect to their own maximum.

Lesion heat maps were also created to show the intracranial mass conditions across the midplane. They were calculated in similar way as the MPS heat maps, where instead of describing the deviation of brain midline structures, the volumetric difference of lesions across two sides of the midplane has been highlighted.

Figure 53 displays an example lesion heat map generated for a patient with acute SDH. The original CT scan for this patient is shown in Figure 53a. The normalised lesion heat map offers a way to identify the intracranial mass condition by looking down the normal to the midplane. The lesion heat map is a portrayal of the asymmetry of the mass lesions about the midplane. In the axial CT scan, the SDH appears crescent-shaped in the left hemisphere, but when looking on the heat map, it is clear that the SDH is a huge sheet affecting a large proportion of the frontal and parietal lobes across a range of depths. The red area indicates a particular imbalance of the mass lesions around those locations on the midplane. In Figure 53a, the haematoma is thicker in the frontal region of the brain and this has been directly visualised in the lesion heat map with additional details. The contour on the lesion heat map is an overall representation of the injuries inside the skull.

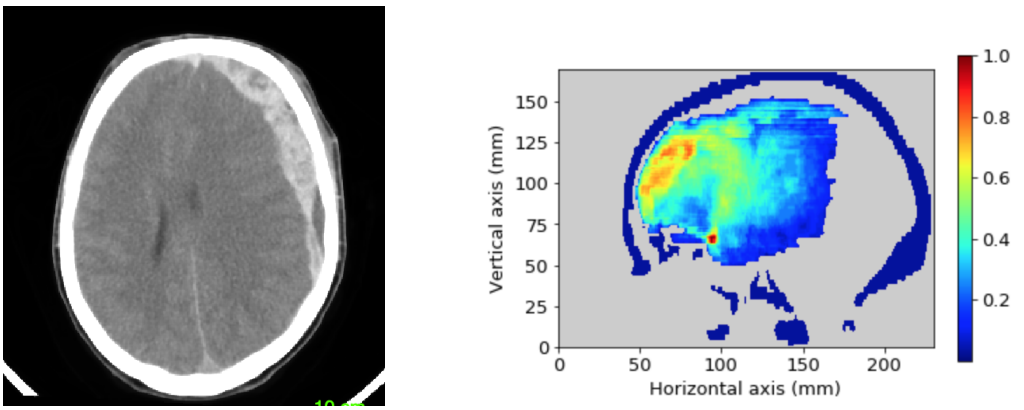

(a) Axial CT slice of patient with acute SDH

(b) Computed lesion heat map for the SDH patient

Figure 53: Illustration of the normalised lesion heat map for a SDH patient. Note the lesion heat map was plotted in a skull silhouette for ease of visualisation.

3.3 Results

3.3.1 Correlation analysis for intracranial mass lesion and brain midline shift

In total 37 TBI patients' 85 non-contrast head CT scans were reviewed. It includes 37 initial CT scans and 48 subsequent CT scans, all characterised with unilateral lateral TBI. Due to the highly labour-intensive nature of the expert manual annotation for the CT scans, it was difficult to further scale up the image database, which could be a limitation on the current study.

Patients' statistics

The mean age of the patient cohort was 46.3 ± 20.0 years (95% CI 28.3-64.5), with 78.9% of them being male. The primary cause of injury was road traffic collisions and falls accounting for over 60% of injuries, with the remainder due to alleged assault, pedestrian accidents and cycling accidents. On admission, the average GCS score of the patients was 8 ± 4 (95% CI 4-14), with a total of 13 (35.1%) patients having initial GCS scores of five or less. Eleven (29.7%) of the patients received craniotomy to evacuate the hemorrhagic lesions and 6 (16.2%) patients received craniectomy.

Glasgow outcome scale (GOS) [110] was used to evaluate the functional outcome of the

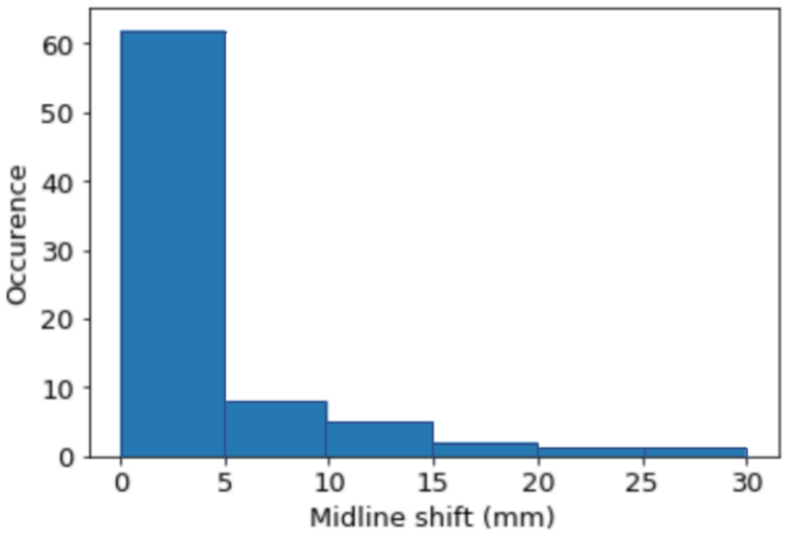

Figure 54: Distribution of midline shifts in TBI scans. Note the majority of the scans had midline shift no more than 5mm.

Lesion Type	**Occurrence** n	$\boldsymbol{V_{mean}}$ **(cc)**	$\boldsymbol{V_{std}}$ **(cc)**	**Correlation** r	**Significance** p
SDH	55	24.7	46.1	0.73	$<10^{-5}$
EDH	14	30.7	56.0	0.42	$<10^{-5}$
SAH	24	2.6	4.2	0.29	0.01
CONT	62	8.8	16.4	0.15	0.02
PCO	61	15.8	16.8	0.06	0.6
PN	17	2.9	3.4	-0.01	0.92
PH	23	0.3	0.7	-0.01	0.9
IVH	5	3.4	3.9	-0.02	0.88
Total Lesion	85	43.5	52.8	0.76	$<10^{-5}$
Total haematoma	85	31.3	47.7	0.80	$<10^{-5}$

Table 3: Descriptive statistics for the lesion annotation results and univariate correlation results between relevant lesion and MLS. Occurrence n is the number of CT scans with the particular type of lesion; V_{mean} is the mean volume of this type of lesion in cc and V_{std} is the standard deviation for the lesions in cc. The univariate correlation between the target lesion and MLS is represented by the correlation index r and significant index p. Lesions listed include subdural haematoma (SDH), epidural haematoma (EDH), haemorrhagic contusion (CONT), peri-contusion oedema (PCO), subarachnoid haemorrhage (SAH), intracerebral haemorrhage (ICH), intraventricular haemorrhage (IVH), petechial haemorrhage (PH) and pneumocephalus (PN).

TBI patients. GOS effectively stratifies the patients into five categories: dead, vegetative state, severe disability, moderate disability and good recovery, corresponding to a GOS score of 1 to 5 respectively. Follow-up data for 3 of the patients was unavailable, leaving 34 patients with available outcome records. Eleven (32.4%) patients achieved good neurological recovery, with minor physical or mental symptoms that do not affect daily life, 13 (38.2%) patients recovered with moderate disability, but were independently functioning at home, 2 (5.9%) patients recovered with severe disability and required partial or full assistance in activities of daily living, 1 (2.9%) patient survived with vegetative state and 8 (24.5%) patients died. Among the non-surviving patients, 5 (62.5%) had the worst GCS score of 3 at admission. Nevertheless, 3 (37.5%) of the non-survivors had only minor or moderate brain injuries with GCS scores between 10 and 14 at admission, but deteriorated within the next few days.

Based on neuro-radiologist's annotation, an average midline shift of 3.7 $\pm$ 5.1 mm was observed for the 85 head CT scans under investigation. The distribution of the midline shift is presented in Figure 54. The majority of the head trauma scans were characterised by a midline shift smaller than 5 mm, but 17 (20%) scans had midline shifts exceeding 5 mm. The greatest midline shift was 26 mm and it was present in a patient with the

greatest amount of hemorrhagic lesion volume (SDH 243.5 cc).

Table 3 summarises the intracranial lesion characteristics by expert segmentation from the 85 CT scans. It is noted that, unlike most CT analyses which considered only the dominant lesions, the current lesion analysis protocol takes into account all kinds of visible intracranial abnormalities such as PCO and PN that present in the CT scan. Therefore the current image analysis is expected to offer a more complete overview of the intracranial pathological conditions. Among the various lesions, CONT and its accompanying oedema (PCO) are the most common subtypes, followed by SDH. In addition, it is observed that the size of the lesion varies with types. EDH is often greatest in volume, with an average over 30 cc, followed by SDH. In contrast, the SAH, IVH, PN and PH are smaller in size, with both mean and standard deviation of volume within 5 cc. If the magnitude of MLS is proportional to the size of the injury, it is reasonable to hypothesise that lesions bigger in volume should play a more important role in mass effect. Such a hypothesis is investigated in the subsequent correlation analysis, where the univariate correlations between the particular type of intracranial lesion and the resultant MLS is examined individually.

Selecting significant lesion types

The univariate correlation results in table 3 revealed that the types of lesions which correlate with the magnitude of MLS with significance ($p < 0.05$) are SDH, EDH, CONT and SAH. One common feature shared between those significant lesion types was that they were all focal hemorrhagic injuries. Contrastingly, the lesion types which were reported not significantly correlated with MLS in the univariate correlation analysis belonged mostly to non-hemorrhagic lesions. PN, for instance, is the presence of intracranial air or gas and PCO is the extracellular accumulation of watery fluid surrounding the lesion site. Both types of injuries are less solid as compared to blood clots, and they are more likely to be absorbed during normal neuron-metabolic functions. IVH, though being a hemorrhagic lesion, is confined to the ventricular system, where CSF is circulated towards the subarachnoid space. Therefore IVH can easily expand in volume by draining the CSF and occupying the ventricular space, without much mass effect.

Furthermore, among the four types of injuries whose volumes were reported closely correlated with MLS, SDH, EDH and CONT lesions were greater in size and were usually the dominant trauma in TBI patients. SAH refers to the amount of haematoma which spreads thinly over the surface of the brain. The small size of SAH (V_{mean} = 2.6 cc,

$V_{std} = 4.2$ cc) has limited its influence on mass effect. In addition, although SAH seemed to correlate with MLS positively in univariate analysis, it was also significantly related with the presence of SDH ($r = 0.42$, $p < 10^{-5}$) when studying the interrelations between various forms of injuries. Such an interrelation revealed the underlying bonds between SDH and SAH in TBI settings. The connection between SDH and SAH could normally be visually distinguished: as shown in Figure 52a, SAH is connected to SDH in the CT scan. In fact, SAH is often more critical when the cause of the injury is by bursting of an intracerebral aneurysm rather than traumatic brain injury. As a result, in the current TBI patient database, it is reasonable to exclude SAH in the subsequent MLS prediction model, because SAH is more likely to be the incidental CT finding detected along with SDH, rather than a unique independent variable that causes MLS.

In the current analysis, a strong association has been found between the total lesion volume and the magnitude of MLS ($r = 0.76, p < 0.05$), where the total lesion volume is defined as the summed volume of all the intracranial abnormalities including those non-significant ones. Nevertheless, if only the selected significant types of lesions (SDH, EDH and CONT) are included, the Pearsons' correlation index further increases to $r = 0.80$ ($p < 0.05$). On the overall lesion level, the summed volume of haematoma and contusions were more positively related to MLS, as compared to that based on the total abnormality volumes. Such a discrepancy validated our previous conclusion that none of the four types of lesions, PCO, PN, IVH and PH, play a significantly critical role in midline shift formation, as indicated in table 3. Removing the non-significant lesions has made a better model.

The correlation analysis results suggested that only SDH, EDH and CONT were considered eligible as predictors for MLS. In fact, this was not the first time that the relationship between the haematoma volume and MLS in TBI has been examined and such a selection of CT features is in line with many previous midline shift and haematoma analysis [102, 111, 112]. In 2010, the multivariate study by Nelson et al [102] reported a near co-linearity of midline shift with the summed volume of EDH, SDH and CONT. They observed a correlation $r = 0.72$ ($p < 0.05$) using CT scans from 861 TBI patients. In the same year, Jacobs et al. [112] stated a correlation of $r = 0.73$ ($p < 0.05$) between the dominant haematoma volume and MLS in a study with 574 severe and 126 moderate TBI patients. Granting that the size of the current study is not as large as the previous one, one major superiority which potentially leads to the greater correlation index is the accurate manual estimation of lesions: all the lesion volumes were manually delineated and calculated with the best possible accuracy. Whereas in the previous study, traumatic lesion volumes were estimated roughly either

by $V_{lesion} = (length \times max - breadth \times height)/2$ [111] or ellipsoid method [107]. Such a rough estimation was due to the large size of the patient database which would not allow accurate manual delineation of lesions. This might limit the accuracy of the volume estimation and hence affect the correlation analysis.

The Lesion-MLS model

Up to now, the study treated SDH, EDH and CONT indiscriminately and the summed volume of haematoma was used as a single predictor to estimate midline shift and confirmed the close interrelations between MLS and intracranial haematoma. According to the Monro-Kellie hypothesis, the cranium is a "rigid box" that aims to keep a dynamic equilibrium among the essential incompressible compartments. Therefore, it is reasonable that the presence of substantial blood clot occupying a bigger space inside the "rigid box", will play a more important role in mass effect and push the brain further off its neutral position, leading to greater magnitude in MLS. However, it remains in doubt whether or not those three types of hemorrhagic lesions play equally important role in the formation of MLS. To better understand the nature of MLS, the haematoma volumes were further differentiated based on the types of lesions. Lesion type together with the corresponding lesion volume were considered to build a multivariate model.

In the multivariate linear regression model, only those three types of critical injuries: SDH, EDH and CONT were included to predict the magnitude of midline shift and Equation 4 becomes:

$$MLS = a_{SDH} \times V_{SDH} + a_{EDH} \times V_{EDH} + a_{CONT} \times V_{CONT} \tag{6}$$

where V_{SDH}, V_{EDH} and V_{CONT} correspond to the size of SDH, EDH and CONT respectively and a_{SDH}, a_{EDH} and a_{CONT} represent the associated coefficient for each of the volumetric lesions. In this way, the lesions of various types were further differentiated to allow for a more specific investigation on their resulting mass effects.

Table 4 lists the linear regression results for the multivariate lesion-MLS model. In table 4, it is seen that the p values for all three lesion variables have reached statistical significance, which coincided well with our previous univariate correlation results. A pearson's correlation coefficient r of 0.92 was achieved through the proposed regression model. Such a high coefficient of determination implied that the regression line approximated the real

Lesion Type	Coefficient a	std err	t	p	95% CI
SDH	0.108	0.007	16.52	$<10^{-5}$	[0.095,0.120]
EDH	0.106	0.011	9.892	$<10^{-5}$	[0.084,0.127]
CONT	0.073	0.017	4.210	$<10^{-5}$	[0.038,0.107]

Table 4: Multivariate linear regression results. Coefficient a is the estimated parameter of the fit; std err is the standard error of the estimated coefficients; t is the t-statistic value, which tells how statistically significant the coefficient is; p is the probability of the null-hypothesis that the coefficient is 0, and 95% CI are the lower and upper values of the 95% confidence interval.

data well. Figure 55 shows the predicted MLS using the multivariate model against the actual MLS measurements. A highly co-linear relationship has been observed, justifying the reliability of the multivariate model: the majority of the points fall around the line where the predicted MLS is very close to the actual MLS. In other words, MLS could be predicted by the present intracranial lesion volumes with reasonable accuracy using the developed regression model.

As compared to the previous study where various lesions were summed up indiscriminately to predict MLS, the current regression model which further differentiated between those critical types of lesions outperformed and improved the pearson's coefficient of correlation r from 0.80 to 0.92. In other words, an additional 12% of the variance in MLS can now be explained by treating the intracranial haematoma of different types as independent variables.

This is an interesting finding because it disproves the hypothesis that haematoma of various types are equally important in mass effect. In fact, in the established regression model, the coefficients of SDH and EDH in table 4 are very close, implying a similar importance in the formation of MLS. Meanwhile, the coefficient for CONT is smaller than that of SDH and EDH. Thus for identical volumes of lesion, if the lesion is consisted of pure CONT, the resultant MLS is likely to be about 30% smaller than that of SDH/EDH. In addition, it is noted that the coefficient of CONT also has a higher standard error and wider confidence interval as compared to that of SDH and EDH. This is hypothetically because of the diverse nature of CONT in the cranium. CONT often comes with more heterogeneous shapes in any random locations inside the brain. Unlike CONTs, EDHs are bleedings between the dura mater and the skull, and are often of convex and lens-shape; SDHs are bleedings between the arachnoid mater and the dura mater, and are often of

the crescent-shape.

In effect, apart from lesion types, the shapes of lesions whether they are convex or crescent-shape, the locations of the lesion whether it is next to the falx or far off from the centreline [113] and even the age of the patient might have an impact on the formation of MLS. Such factors can be included for patient-specific analysis, but they are too sophisticated for the current group-level analysis. However, based on the strong correlation and high collinearity of the current model, we believe lesion type and lesion volumes already make a powerful predictor.

So far, the high correlation between intracranial lesions and the magnitude of MLS has been addressed. The predictive value of haematoma size in MLS formation in unilateral TBI patients has implied the highly interchangeable nature of haematoma volumes and MLS as CT factors in scoring systems. The rare prevalence of Marshall Category IV, where MLS $>$ 5 mm and haematoma volume $<$ 25 cc [102], also proves the finding: according to our lesion-MLS model, it is unlikely for a patient to have MLS greater than 5 mm if the observed haematoma volume was smaller than 25 cc.

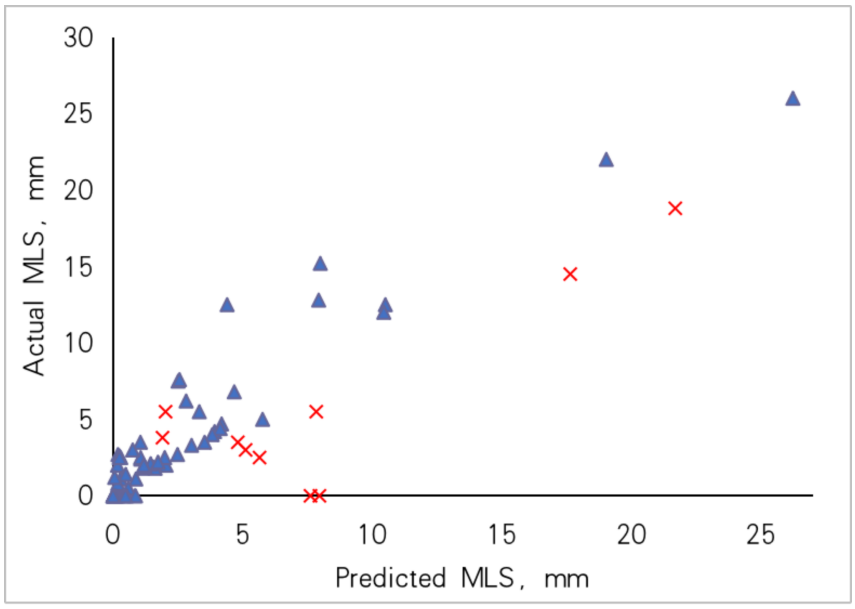

Figure 55: Multivariate linear regression between intracranial mass lesions and MLS. The predicted MLS were close to the actual value, with a minor proportion of offliers which deviated from the regression line. Note, the red crosses highlight the MLS prediction results for the scans of non-surviving patients.

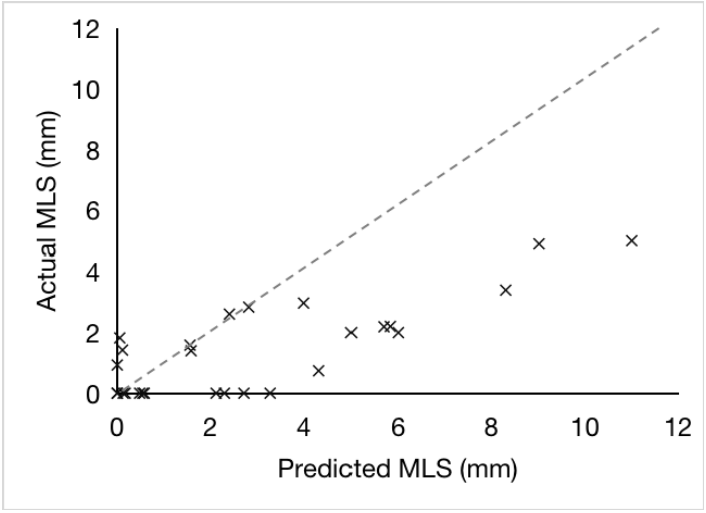

(a) Predicted MLS vs. Actual MLS in bilateral TBI patients.

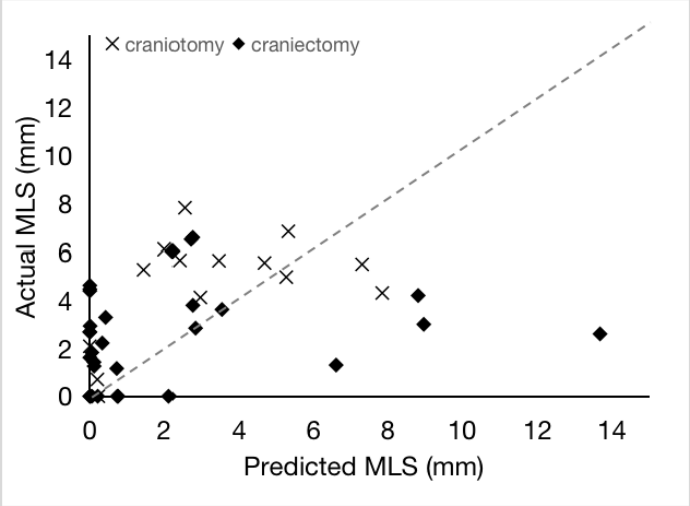

(b) Predicted MLS vs. Actual MLS in post-operative TBI patients.

Figure 56: Evaluation of the lesion-MLS model performance in patients under other clinical conditions. The dashed line shows where the prediction is equal to the actual value.

Extending the model application conditions

As stated in the inclusion criterion of this study, the aforementioned relations only hold true for unilateral TBI patients before surgery. Therefore it is of interest to see if the developed regression model also works for CT scans under other clinical conditions, especially when the lesion is bilateral and substantial abnormalities are present in both right and left hemispheres in the CT scan. Figure 56a plots the predicted MLS using the developed lesion-MLS regression model against the actual MLS, measured by the

expert, in patients with dual-sided hemorrhagic injuries. It is our finding that MLS has generally been overestimated (Predicted MLS > Actual MLS) if the unilateral regression model was applied directly to bilaterally injured patients. In other words, given the same volume of haematoma, the resultant MLS in bilateral TBI patients is generally smaller than that in unilateral TBI patients. This is reasonable because when the haematoma is present in both of the hemispheres, lesions on either side of the midplane might cancel each other. As a result, it is suggested that as outcome predictors in TBI CT scoring systems, MLS is not as ideal as haematoma volume if bilateral lesions are present and other CT findings such as basal cistern compression could be a substitute for MLS, though being less quantitative. This interesting phenomenon is also supported by [102], where they reported a 2% increase in correlation if dual-sided SDHs are pre-excluded in the correlation study between haematoma volume and MLS.

The developed lesion-MLS model was also tested in the post-operational scans, where the patients received either craniectomy or craniotomy after admission. The results are exhibited in Figure 56b. It is seen that the previous regression model failed to capture the variance of MLS by using the amount of haematoma present in the post-operative scans. One explanation for such a discrepancy is that surgical operations that removes the bone flap from the skull invalidate the Monro-Kellie doctrine by providing extra space for the brain compartments to bulge out and relax. As a result, in cases where the patients have already received operations, MLS cannot effectively reflect the intracranial lesion conditions and thus is no longer suitable for representing mass effect. In such cases, cisternal compression should be a practical substitution for evaluation of mass effect in a semi-quantitative manner [114].

Model prognostic values

The last part of this section explores the prognostic values behind those lesion based MLS predictions, especially when they are compared to the actual MLS. In 2015, Bartels et al [115] retrospectively studied the prognostic power of midline shift in relation to the thickness of acute SDH (aSDH) and observed that a difference between the midline shift and the thickness of haematoma ±3 mm at initial CT predicted mortality in all cases. To the best of our knowledge, that was the first time that a relationship between haematoma and midline shift has been studied extensively for outcome prediction in TBI analysis. Although the study concerned only a single type of traumatic mass lesion and used the thickness of haematoma on a single slice instead of lesion volume, it was a creative study that offered a simple metrics for neurosurgeons to evaluate a patient's clinical condition.

Now that in our study, lesions of various kinds were considered and their volumes were obtained to provide a more comprehensive overview of the patient's condition. The lesion-MLS model then calculates the estimated MLS from haematoma conditions. The current model, though demonstrating high co-linearity, still has some offliers. In particular, in Figure 55, the highlighted data points (red crosses) of non-surviving patients tends to concentrate on the lower part of the graph where predicted MLS is greater than the actual value. For those offliers, their intracranial conditions cannot be confidently explained by the apparent lesions under scope and additional investigation is required.

In order to carry out an outcome study, it is required that both the GCS score and GOS (Glasgow Outcome Score) of the patients are traceable. However, in the current dataset, only a very small number of patients have both of the scores in their clinical records. Though confidence in the findings may be limited due to the small sample size, it is expected that some valuable insights could still be derived from the comparison between estimated and actual MLS.

To evaluate the prediction results, we first define the discrepancy between actual and predicted MLS:

$$D = \frac{MLS_{pred} - MLS_{act}}{MLS_{act}} \tag{7}$$

where D is the relative difference between prediction and actual MLS, MLS_{pred} is the estimated midline shift according to the lesion-MLS model and MLS_{act} is the actual clinical midline shift observed in the scan. If a threshold of 20% is set to accommodate any interpersonal variations that may not be included in the MLS prediction model, the patients could be broadly categorised to underestimation ($D < -20\%$), good prediction ($|D| < 20\%$) and overestimation ($D > 20\%$) based on the divergence/similarity between the predicted MLS and the actual MLS. The mortality rates were calculated for both the severeness group (3 < GOS score < 8) patients group and all cohorts including the mild and moderate patients according to the proposed three-tier GOS score classification method. Table 5 displays the results.

It is observed that for both good prediction of MLS and underestimation of MLS conditions, the mortality rates were higher for severe TBI patients as compared to that of the total cohorts. However, what is interesting is when the multivariate MLS prediction model predicted a MLS more than 20% greater than the actual MLS (Overestimation), the mortality rate was 100% regardless of the patient's GCS scale at admission. This high

mortality rate is at least three times greater than that under normal prediction condition and ten times the mortality value of the underestimation condition.

To be more specific, among those five patients with overestimated MLS according to our lesion-MLS model, two of them had GCS score of 3 and three of them had GCS score over 10 on admission, but deteriorated afterwards and failed to survive. Our model successfully distinguished those high risk patients with moderate or mild TBI on admission. Though confidence of the finding is very limited by the small sample size, still it sheds lights on the potential new way of outcome prediction based on intracranial mass volume and observed MLS in a traumatic CT scan. Moreover, this conclusion is not in line with the previous findings by [115], who stated that MLS greater than the thickness of the haematoma is more dangerous. A possible explanation could be the age bias of our observation groups: the mean age of patients in the overestimation group is 68.2 $\pm$ 10.8 years, more than 20 years older than the average of the whole cohort.

To sum up, although the finding on the prognostic capability of the lesion-MLS prediction model still requires further investigations and validation, it suggests a new way to predict patient outcome by comparing the predicted MLS from intracranial mass condition and the real MLS. In the future, larger scale studies are encouraged, especially when automate lesion detection algorithm becomes more mature.

3.3.2 Properties of midplane shift (MPS)

Overall, 33 TBI patients with obvious brain deformation were annotated for brain shift analysis. The CT images for those patients showed an average clinical MLS of 13.4 mm, with standard deviation of 4.8 mm, according to the associated radiologist's reports.

Patient Group	**Good Prediction of MLS**	**Overestimation of MLS**	**Underestimation of MLS**
Severeness	0.25 (n=8)	1.0 (n=2)	0.1 (n=10)
All categories	0.14 (n=14)	1.0 (n=5)	0.07 (n=15)

Table 5: Mortality rate for severeness and all categories of TBIs under different MLS prediction conditions. The table shows the mortality rate with n referring to the number of patients in the associated category. Note, the mortality rates were 100% for both of the overestimation of MLS groups, regardless of the severeness of their GCS score.

Quality of preprocessing

To facilitate the extraction of statistics on a group level, it is important to obtain spacial alignments for the input CT scans. Through image preprocessing and registration, all 33 CT were co-registered to the same reference template. The registered CT scans all passed the visual quality check.

Figure 57 overlays the skull silhouettes from the 33 MPS heatmaps to evaluate the quality of registration. Specifically, for each of the MPS heat map, a skull contour map has been created with skull voxels being labelled as 1 and all other voxels in the MPS heatmap being 0. Then the skull contour maps for all 33 CT scans were overlaid on top of each other, and the regions where skull voxels typically appear add up in the overlaid skull contour map. When divided by the total number of CT scans, the overlaid skull voxel readings were normalised and presented in Figure 57. As a result, the colour bar in the figure represents the probability of relevant voxels being labeled as skull in any of the MPS heatmaps: the red region in the overlaid skull contour suggests that in almost 100% of the MPS heatmaps, the voxels in those regions have been recognised as the skull. The frequent appearance of the red skull region suggests a reasonable accuracy in the registration process.

From Figure 57, it is seen that the difference in head orientation have been effectively corrected and so the overlaid skull contours are well-aligned. Provided with such a satisfactory spacial alignment in the computed MPS heatmaps, it is possible to perform statistical analysis on a structural level and explore the overall characteristics of MPS for

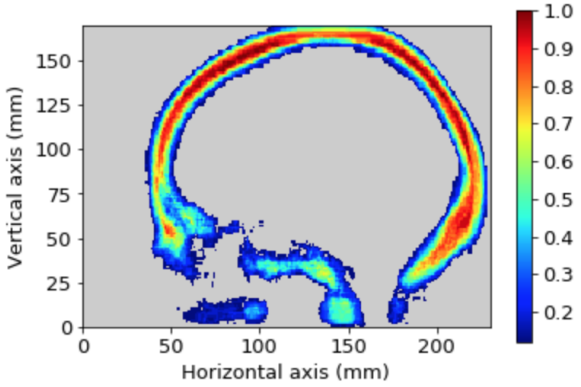

Figure 57: Overlaid skull contours from computed MPS heat-maps. Colour bar shows the probability of a skull voxel being overlapping with others in the MPS heat-maps. Note the skull contours are nicely aligned, indicating a reasonable registration for the CT scans under investigation.

TBI patients suffered from various kinds of injuries.

Findings for MPS heat maps

Previously in section 2.2.4, the value and associated colour of each pixel location in the MPS heat-maps was defined as the absolute distance from the deformed midline structures to the ideal geometric midplane. This definition, though being convenient for direct visualisation, lacked some insights on a group level analysis. In the current section, the pixel values in each of the MPS heap-maps were normalised by the heatmap maximum value. Thus all the calculated MPS heatmaps were scaled from 0.0 to 1.0, with 1.0 representing maximum deviation and 0.0 denoting no deviation. Figure 58a and 58b are two example MPS heat maps from the calculated MPS database. Figure 58a is the MPS heat map calculated for a patient suffered from acute SDH, whereas Figure 58b is

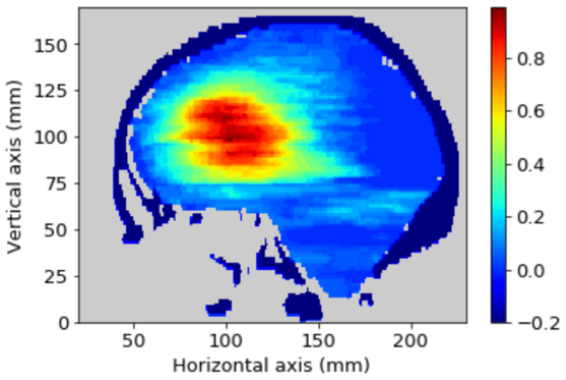

(a) MPS heat-map for a patient with SDH

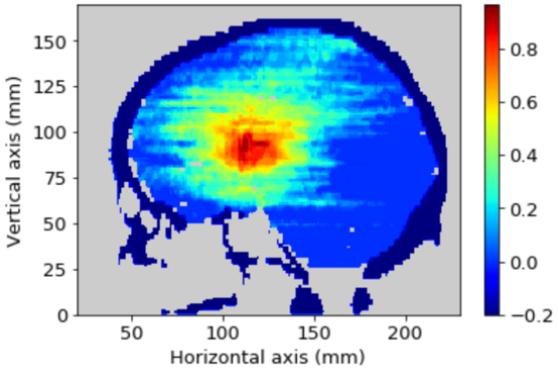

(b) MPS heat-map for a patient with intraparenchymal haematoma

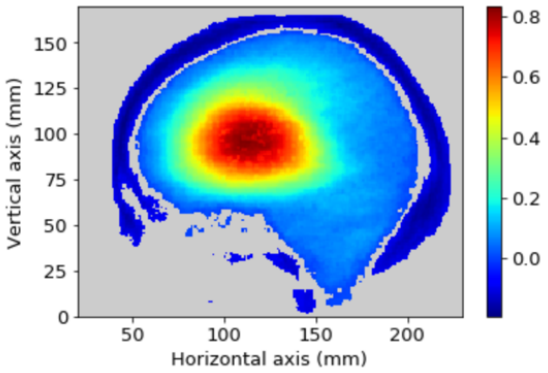

(c) Average MPS heat-map for all patients

Figure 58: Illustration of MPS heatmaps. Note, (a) and (b) are example MPS heat-maps calculated for SDH and intra-parenchymal haematoma patients respectively; (c) is the normalised MPS heat map averaged over all 33 TBI patients.

derived from a patient with intraparenchymal haematoma. Although the nature of the intracranial mass are completely different between these two patients, the resultant MPS heat-maps still look similar in pattern. In fact, the characteristics of brain midplane shifts are more obvious if a normalised MPS heat-map averaged across all 33 TBI patients was generated. The average MPS heap map was calculated using the following equation:

$$P_{ave}(i,j) = \frac{\sum_0^n P(i,j)}{n} \tag{8}$$

where $P_{ave}(i,j)$ corresponds to the pixel value in the average image at coordinate i,j; n is the total number of image to be averaged; $P(i,j)$ is the pixel value at coordinate i,j in the raw image. Since a normalised MPS heat-map is characterised with only absolute pixel values between 0 and 1, and no great variance is seen across those 33 TBI patients, an average MPS heat-map is considered reasonable as a typical heat-map for the TBI patients. Such an average MPS heat-map is displayed in Figure 58c. This average heat map is a generalised and typical representation of the constituent heat maps. It reveals that the brain cross midplane shifts for different TBI patients share a lot in common regardless of the diverging intracranial pathological conditions:

1. The red region of severe deviation (relative deviation > 0.8) intends to concentrate on a single region.
2. Brain deviation decreases radially from the peak deviation region until it reaches the periphery of the skull where it decays back to zero.
3. The peak brain deviation usually occurs at the frontal ventricular region.

Essentially, the anatomic structures of the brain play an important role in regulating the cross midplane deformation of the brain. When the relative locations on the MPS heat-map is referred to the anatomic structures of the brain, it is seen that the red region of severe brain deformation is most likely to occur at the frontal ventricular region. Due to the rather soft nature of cerebrospinal fluid, the ventricular regions are prone to deviate from their original position. By contrast the cerebral falx, as a relatively rigid protective membrane attached at the midline to internal surface of the skull, restricts movement of the brain parenchyma near it.

Novel parameter interpretations

In the developed MPS heat-map, the traditional MLS actually becomes a single datapoint. MPS, as a 3D evolution of the traditional MLS, contains greater details on the intracranial brain deformation. To better interpret the MPS, a set of novel parameters were considered including the maximum MLS, brain volume shift and the MPS centroid. Table 6 gives a summary of those deformation-related parameters for the 33 TBI patients.

From table 6, it is noted that the maximum MLS is always a few milimeters greater than the clinical MLS. In fact, the clinical MLS is considered as a critical component of modern neuroimaging diagnosis. In 2006, Brain Trauma Foundation (BTF) has proposed a standardised protocol for MLS measurements in CT procedure to reduce its inter-observer variations [109]. Based on the suggested standard protocol, clinical MLS is always measured on the axial image at the level of the Foramen of Monro (FM). In contrast to the clinical MLS, the maximum MLS could be measured wherever the off-midplane deformation is greatest.

Figure 59a and 59b plotted the relative locations of clinical and maximum MLS on a sagittal skull silhouette. As shown in Figure 59a, the points where the clinical MLS measurements were taken are highly concentrated at a certain region on the sagittal skull contour. However, the locations of the maximum MLS are more scattered across a range of depths inside the skull.

The centroid of MPS representing the centre of mass of the deviated brain volume, were plotted in Figure 59c to further illustrate the structural characteristics of MPS. It is seen that those MPS centroids tend to concentrate on the frontal ventricular region in a

Feature	$MLS_{clinical}$ (mm)	MLS_{max}(mm)	V_{shift} (cc)
mean	13.4	15.4	54.5
std	4.7	5.0	20.1
max	23.0	27.5	95.7
min	2.7	6.5	23.1

Table 6: Statistics for the derived CT parameters from MPS. The table shows the summary of the CT parameters derived from MPS and their statistics. $MPS_{clinical}$ is the clinical midline shift measured at septum pellucidum; MLS_{max} is the maximum deviation of brain midline structure that appeared on the MPS heat-map; V_{shift} is the brain volume shift by integration over the MPS heat-map.

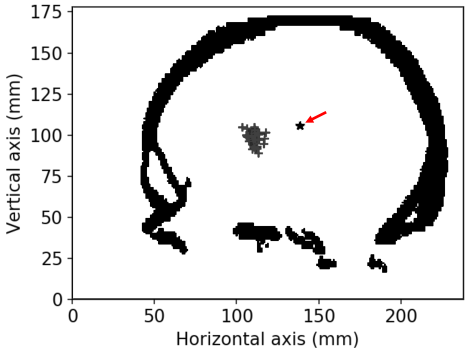

(a) Locations of the clinical MLS measurements

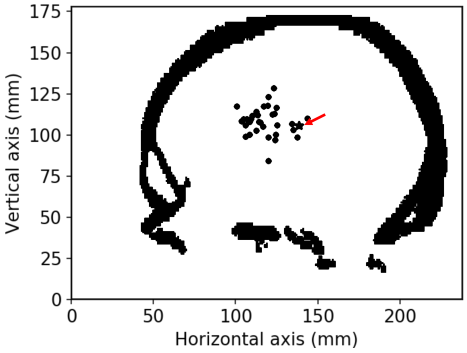

(b) Locations of the maximum MLS measurements

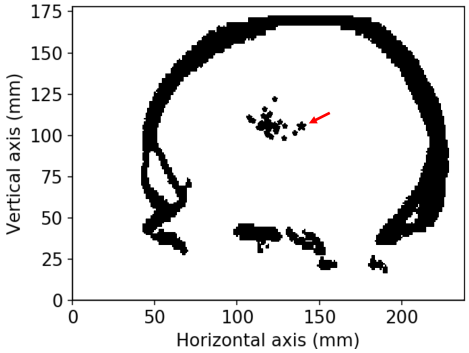

(c) Locations of the MPS centroids

Figure 59: Locations of MLS measurements plotted on sagittal skull contour, with the black star showing the centroid of skull and the red arrow pointing at the black star. (a) clinical MLS measurement points denoted in crosses. (b) maximum MLS measurement points shown in dots. (c) centroid of MPS displayed in dots.

midplane, and it is likely that those MPS centroids would set within the severe deviation region in the averaged MPS heat-map in Figure 58c. Admittedly, standardisation of MLS measurement locations in clinical settings is helpful to keep consistency between observers, but question remains on whether the clinical MLS is the best representative of brain deformation conditions.

By nature, it is more intuitive to evaluate the brain deformation and intracranial mass condition by 3D volume, rather than 1D length. Table 6 shows the statistics for the brain volume shift measured using the MPS heat-map. This is the first time that the brain volumetric deformation was quantitatively calculated to help evaluate the mass effect. As compared to MLS, the brain volume shift provides a more accurate and comprehensive overview on the overall brain deformation across the midplane. Using MLS alone, there could be cases where the measured MLS is the same, but the true brain deformation

volume is quite different. Nonetheless when using brain volume shift, it is expected that the greater the volumetric shift, the worse the intracranial mass condition. Now, it is of interest to investigate between the two types of MLS, which one is more representative of the brain volume shift.

Figures 60a and 60b show the scatter plot of the brain volume shift against clinical MLS and maximum MLS respectively. For each of the plots, a linear trend-line is fitted to describe the pattern in the data clouds. To evaluate the quality of the regression, a correlation coefficient R^2 is shown together with the linear regression equation on the lower right corner of the graph. Basically, Figures 60a and 60b show that both clinical MLS and maximum MLS are positively related to brain volume shift. However, the correlation coefficient R^2 between maximum MLS and brain volume deformation is 13% higher than that of clinical MLS. In other words, maximum MLS is actually a better representative of the brain volumetric shifts than the currently practiced clinical MLS.

The information portrayed in the MPS heat-map could itself be helpful in many clinical settings. Figure 61 illustrates a few case studies to elaborate the potential applications of MPS heat maps. Figure 61a and 61b are MPS heat maps calculated for CONT and EDH patient respectively. Both of the patients have a clinical MLS measured by the neurosurgeon as 11 mm, but their MPS patterns are completely different. The red region of severe MPS is more concentrated in the CONT patient as shown in Figure 61a and more diffuse in the EDH patient as shown in Figure 61b. So if neurosurgeons look at the

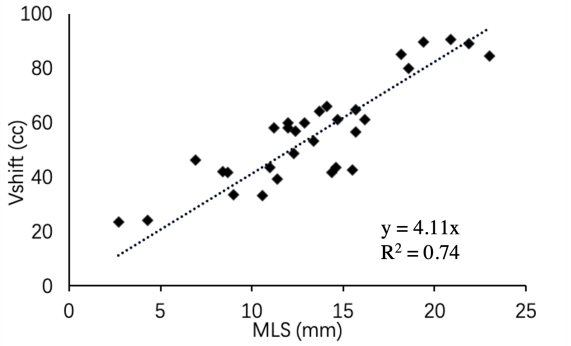

(a) Plot of clinical MLS vs. brain volume shift

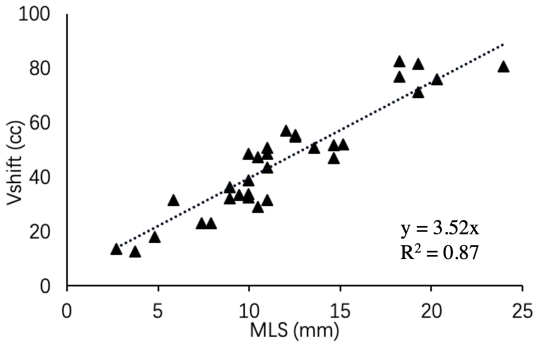

(b) Plot of maximum MLS vs. brain volume shift

Figure 60: Plots of MLS vs. brain volume shift. (a) Plot of clinical MLS vs. brain volume shift. (b) Plot of maximum MLS vs. brain volume shift. Note, a linear regression line has been fitted to the scatter plot, with the fitted equation and the correlation coefficient R^2 displayed on the lower right corner. It is observed that maximum MLS is more correlated with brain volume shift with a greater R^2.

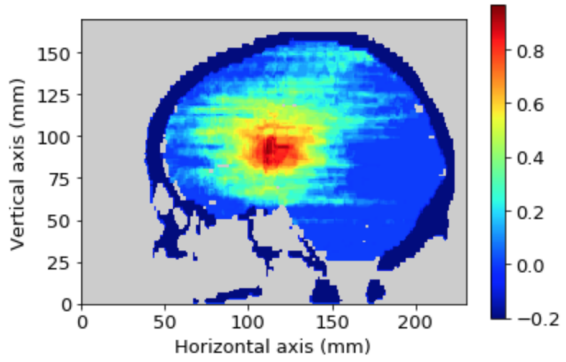

(a) MPS heat-map for a CONT patient with $MLS_{clinical} = 11$ mm, $V_{shift} = 33$ cc

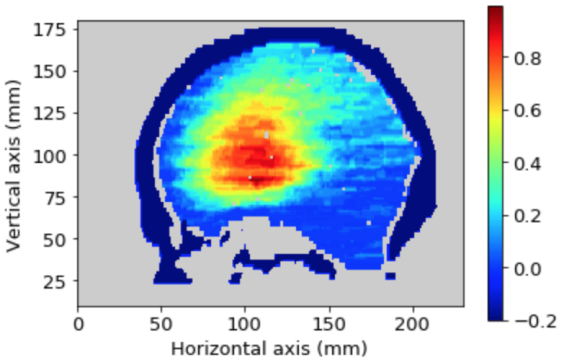

(b) MPS heat-map for a EDH patient with $MLS_{clinical} = 11$ mm, $V_{shift} = 58$ cc

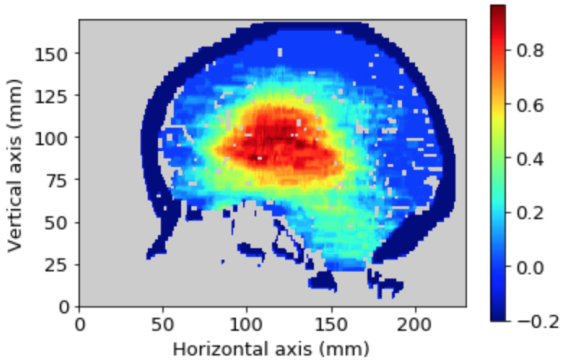

(c) Pre-operation MPS heat-map for an SDH patient with $MLS_{clinical} = 14$ mm, $V_{shift} = 66$ cc.

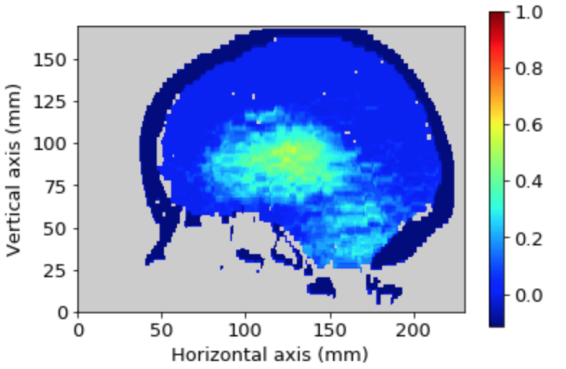

(d) Post-operation MPS heat-map for an SDH patient with $MLS_{clinical} = 5$ mm, $V_{shift} = 28$ cc

Figure 61: Example MPS heat-maps. (a) MPS heat-map for a CONT patient. (b) MPS heat-map for a EDH patient. (c) Pre-operation MPS heat-map for an SDH patient. (d) Post-operation MPS heat-map for an SDH patient. Note, heat-maps (a) and (b) have been normalised against their own maximum MPS. heat-map (c) and (d) have been normalised with the maximum MPS pre-operation for this particular SDH patient.

midline shift only, they may arrive at the conclusion that the two patients have similar level of mass effect. However, if we take a look the MPS heat-map, it is clear that the condition of the EDH patient is more severe than CONT patient: the brain volume shift in the EDH patient exceeds that of the CONT patient by 76%. Therefore, it is seen that MPS is a powerful tool to aid the evaluation of brain mass effect.

For the other case study, MPS analysis was performed for the same patient before and after surgery, as shown in Figure 61c and 61d. For the post-op scans, the MPS has been normalised to the maximum deviation value from pre-op scans. Such a comparison provides a direct visualisation and greater information on the post-operative restoration of the deformed brain structures. In this case, we can see the red regions of high deformation are gone and the brain has been restored to a large extent, but there still exists some

residual deviations in the region that had deviated most pre-operationally.

To sum up, this section has investigated the intracranial brain deformation condition of 33 TBI patients with the MPS tool. Through group analysis of patients with various extents of injuries, the basic brain deformation pattern shown in the MPS heat map has been derived. The use of MPS has yielded a number of novel parameters and those parameters have been carefully interpreted. With the help of two case studies, the potential application of MPS has also been illustrated. It is expected that MPS can help unravel more hidden information on brain intracranial mass condition and help neurosurgeons to make better clinical decisions before further treatments.

3.3.3 Intracranial lesion analysis

To keep the intracranial lesion analysis consistent with the brain deformation analysis in the previous section, the same patient database was used. The patient cohort consisted of 33 TBI cases with midline shift greater than 5 mm. All initial CT scans were co-registered to the same coordinate to obtain spacial alignments, as practiced in section 3.3.2.

Only hemorrhagic lesions including SDH, EDH and CONT were annotated during lesion segmentation, because these types of lesions were shown in section 3.3.1 to be most significantly related to brain deformation. The average size of the haematoma is 96.6 cc, with a standard deviation of 52.6 cc. Given the heterogenous nature of TBI, the resultant lesion heat maps appeared very different in pattern. While Figure 53 provides an example for the lesion heat map of a classic acute SDH extending from the frontal lobe to the parietal lobe, Figure 62a and 62b offer another example of lesion heat map for EDH concentrating on the posterior brain.

Unlike the MPS heat maps which look similar in pattern for various different injuries, the lesion heat maps can differ significantly from one patient to another. Depending on the nature of the impact force, traumatic brain injury could be differentiated by their location of attack, as well as distribution of lesion. Figure 2 in the clinical literature review illustrates some of the most typical haemorrhages inside the skull and their relative locations of attack. For the current data set, 33 TBI patients provided 33 different kinds of intracranial lesions and an average lesion heat map has been created. The calculated lesion heat maps were averaged in the same way as described in section 3.3.2 and shown in Figure 62. Since the lesion heat-map consists of only absolute normalised lesion values between 0 and 1, the resultant average lesion heat-map across the 33 TBI patients should give a reasonable representation for the spread of lesions in the midplane. This average

(a) Axial CT slice of a patient with EDH

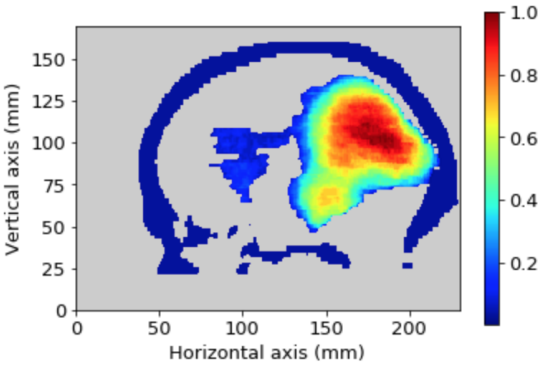

(b) Computed lesion heat map for the EDH patient on a skull silhouette.

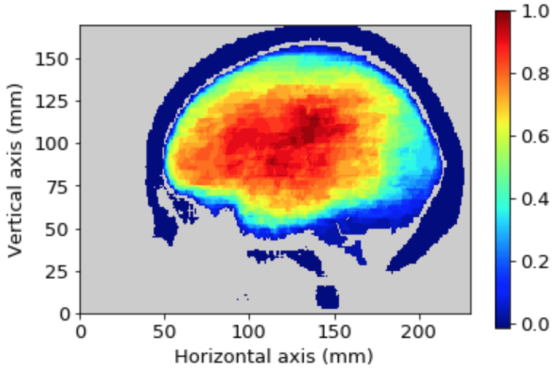

(c) Average lesion heat map for all patients.

Figure 62: Example lesion heat-maps. (a) and (b) are the example of a patient with EDH. (c) is the averaged lesion heat map for all the patients.

lesion heat map demonstrates that among those 33 TBI patients, the probability of lesion happening at the frontal, temporal and parietal lobes is quite similar. In other words, haematoma could develop anywhere inside the cranium if viewed from normal to the midplane.

Inter-relations between MPS and lesion heat-map

The lesion heat map provides a comprehensive overview of the injury conditions inside the skull. It is a direct visualisation of the relative location, distribution and severity of the intracranial lesions. Moreover, a lot of other parameters could be derived from the lesion heat map to help describe the lesion quantitatively. Example parameters include the maximum thickness of the lesion, shape of the lesion on the heat map, centroid of the lesion and so on. In this section, the centroid of the lesion, which is defined as the centre of mass of the haematoma, is analysed together with the centroid of MPS to study the

inter-relations between lesion and brain deformation.

Figure 63a plots the MPS centroids in blue and lesion centroids in red for all the 33 TBI patients under investigation. It is seen that the lesion centroids are more scattered along the horizontal axis, while the MPS centroids are more concentrated in the frontal ventricular region, as observed in section 3.3.2. However, since the intracranial mass lesion has long been considered as the inherent cause of brain deformation, it is worth investigating if the relative locations of the injuries will affect the brain deformation

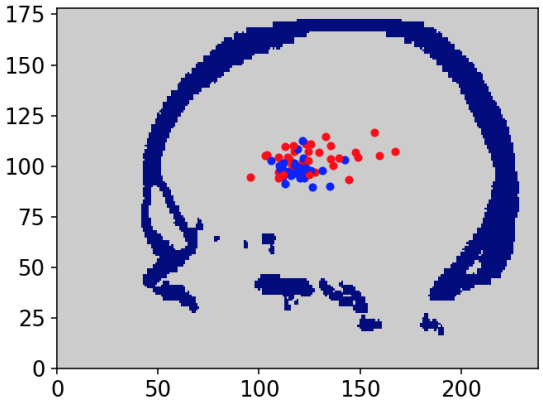

(a) Plot of MPS centroids (in blue) and lesion centroid (in red) on a skull contour.

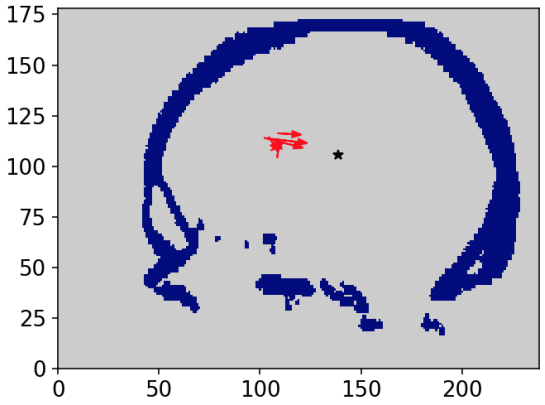

(b) Arrow plot from lesion centroids to MPS centroids for the cluster of patients with frontal injuries.

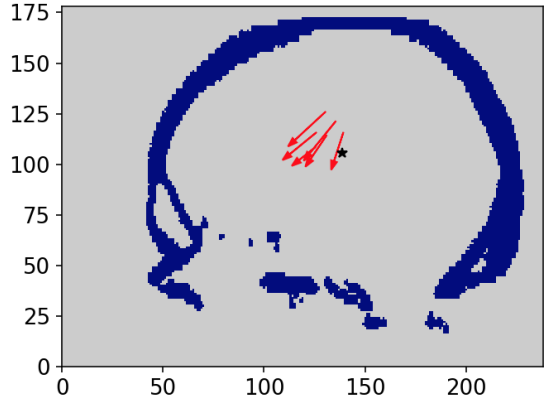

(c) Arrow plot from lesion centroids to MPS centroids for the cluster of patients with parietal injuries.

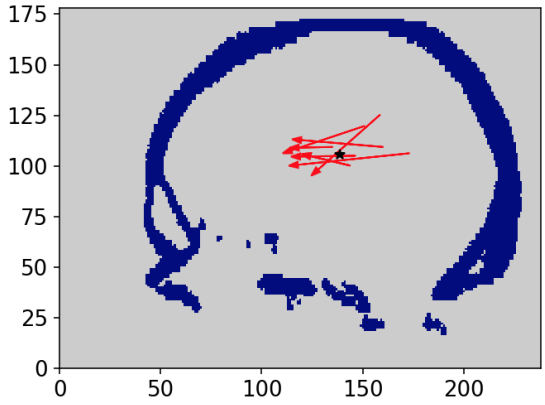

(d) Arrow plot from lesion centroids to MPS centroids for the cluster of patients with occipital injuries.

Figure 63: Graphic representation of the relative locations for lesion centroid and MPS centroid on skull contour. The black star in (a), (b) and (c) represent the skull centroid. (a) Relative location of MPS centroid and lesion centroids. (b), (c) and (d) arrow plots showing the relations between lesion centroid and MPS centroid by clustering the lesion centroids based on their coordinates.

mechanism. Such an investigation was achieved by stratifying the patients into three clusters based on their lesion centroid coordinates and their locations relative to the skull centroid.

The first patient subset is characterised with mass lesions in the frontal lobes (lesion centroids more to the anterior region of the skull, as shown in Figure 63b). For this type of TBI patients, the distance between MPS centroids and lesion centroids is short and there exists a high overlap on the region of brain deformation and the region where lesion onsets in the corresponding heat maps.

The second patient subset comprises patients with parietal lobe injuries (lesion centroid higher than the skull centroid, as shown in Figure 63c). The arrow plot demonstrates that, for those patients, the MPS centroids deviate from the lesion centroids and deformation takes place in lower levels in the skull than where the lesion lies, with the arrows pointing downwards.

The third patient subset includes patients with lesions in the occipital lobes (lesion centroids concentrating on the posterior part of the skull, as shown in Figure 63d). The distance between the MPS centroids and lesion centroids is longest in this case, implying that the brain deformation takes place in the other regions of the brain than where the lesion is. The arrows in the arrow plots in Figure 63d reveal that the cross-plane deformation of the brain still focus on the frontal ventricular region even if the lesion occurs at the occipital region.

In fact, considering these three three clusters of patients, it is concluded that brain shifts always concentrate in the frontal ventricular region regardless of the relative locations of the trauma. This conclusion is in line with our previous findings in section 3.3.2. It further proves that the brain deforms in a regulated mechanism when subjects to trauma, so that the deformation is directed and restricted to the soft ventricular region, thanks to the anatomic structures of the head such as the falx.

3.4 Concluding discussion

In neuroimaging diagnosis, the large amount of clinical information contained in a CT scan is interpreted using a variety of CT parameters to aid clinical decision making. In this section, a series of novel CT parameters derived from the tools developed in section 2 are introduced and discussed to study brain deformation in the scenario of TBI.

In the first section, the correlation between intracranial mass lesion and brain midline shift has been explored by retrospectively reviewing 85 TBI patients with unilateral haemorrhagic trauma. The study first concluded that, among all the visible lesions in a CT scan, only the haematoma type injuries including SDH, EDH and CONT are significantly associated with brain deformation. Then a multivariate lesion-MLS model has been established to predict the MLS using various intracranial lesion volumes. A high correlation coefficient of $R = 0.92$ has been revealed in the model. This is the first time that the various types of haematoma have been differentiated and explicitly correlated to MLS. As compared to the traditional correlation study that uses total haematoma volume as a predictor for MLS, the proposed multi-variate model offers an additional 12% accuracy through differentiating between specific types of haematoma. The model also shows that different types of lesions are playing different roles during brain deformation. SDH and EDH, for example, are more likely to lead to greater MLS than CONT if they are similar in size. In addition, an extremely high mortality rate has been observed in patients whose predicted MLS value from the lesion-MLS model is more than 20% greater than the actual MLS measurement. Larger scale studies are needed to support this tentative finding.

The second section investigated the properties of MPS. MPS heat maps, which quantitatively describe the cross-plane deformation of the brain, were created for 33 TBI patients with various extents of brain deformation. It has been observed that the region of severe brain cross-plane deviation tends to concentrate on the frontal ventricular region and decreases radially until when it reaches the periphery of the brain contour, where the cross-plane deformation decay back to zero. Apart from the deformation characteristics, the characterisation using MPS also facilitates a series of new CT parameters. Brain volume shift, for example, was used to quantify the volumetric deformation of brain across the ideal midplane. In addition to the traditional clinical MLS, a maximum MLS was also introduced to measure the maximum deviation of the brain midline structure from the ideal midplane. It is seen that the maximum MLS is a better representative of the volumetric brain deformation inside the skull, as compared to the clinical MLS. MPS heat map is a powerful tool that provides a more comprehensive overview of the intracranial mass effect for TBI patients.

The last section of this chapter studied the intracranial lesion condition with the help of lesion heat maps. The lesion heat map offers a direct visualisation for the relative location, distribution and severity of the intracranial injuries. Traumatic injury may occur anywhere inside the skull, therefore the resultant lesion heat maps are characterised by diverging shapes and patterns. Use of the derived parameters from the lesion heat map

could potentially help stratify patients with different injuries to form different patient subsets. By clustering TBI patients according to the location of their lesion centroids and comparing the lesion centroids with the corresponding brain MPS centroids, a better understanding of what controls brain deformation has been derived: constrained by the anatomic structures such as the falx, brain deformations concentrate on the the soft ventricular region, regardless of where exactly the mass lesion is.

4 Biomechanical model development

4.1 Introduction

While advanced neuroimaging techniques provide a powerful tool to help track the trajectory of brain damage progression, computational modelling has the potential to shed light on predicting the brain behaviour under arbitrary scenarios. Such an advanced predictor, once well-validated, may help resolve the damage mechanisms associated with various brain pathologies and ultimately aid clinicians to make more informed medical decisions.

Biomechanical modelling is capable of revealing the detailed strain and deformation patterns not only on the surface but also deep inside the brain. Over the years, 3D medical imaging techniques such as CT and MRI have been developed to uncover the intracranial conditions within the skull. Clinicians benefit from such images to examine abnormalities such as the potential fractures of the bones and pathologies of the brain. In the scenario of biomechanical analysis in TBI, CT scans could also assist in defining the relative deformation of the brain. However, such a CT based deformation exploration is only viable on the landmarks in the image where the relevant brain substructures are clearly visible. The popular application of MLS is one example use of the deformation measure from medical images. In section 3.3.2, such a CT-based brain deformation measurement has been improved from 2D to 3D by the proposed MPS tool. MPS relies on the manual examination of the brain mid-structures to elaborate the brain shifts across the mid-sagittal plane. MPS offers a way to extract brain deformation directly from medical images, but still, it only uncovers the brain shifts across the natural symmetric plane of the skull, the deformation condition in the rest of the brain remains unquantified. The key challenge of finding the complete deformation field within the brain is the lack of landmarks in the majority of the brain tissue. Unlike the bones, the falx and the ventricles, the grey and white matter of the brain tissue possess similar intensities in a CT scan. Although there exists some studies [66, 67] that applies non-rigid registration to quantify the strain levels of human organs under pathological or surgical scenarios, there is no reliable way to validate the deformable registration results, especially for the brain tissues where the landmarks are poor. Therefore pixel-wise deformation quantification is still not achievable from CT scans. Computer based simulation, on the other hand, has the known strength of providing detailed strain and deformation patterns throughout the model.

Defining an appropriate geometric model is a key step in FE analysis. A satisfactory computer model offers an appropriate level of idealisation so that the model removes the less significant complications in geometry while still maintaining the authenticity and validity of the objects. Omitting the complex geometric features in FE analysis simplifies the model and eventually saves computational time. This chapter aims to identify a suitable level of simplification for the topologies of the brain and establish a fully-functional, anatomically correct FE head model that is applicable for TBI simulations. Then the FE model built in this chapter will be further developed and assessed in chapter 5 for model optimisation.

The FE head model will be developed step by step in this chapter. Firstly, in section 4.2 an idealised finite element model is constructed from an average human brain atlas. Then following the method described in section 4.2.2, preliminary simulations are carried out on the idealised model to replicate some typical mechanical brain behaviour following TBI. By comparing the resultant preliminary results with the clinical findings from section 3, the validity of the idealised model is analysed in section 4.2.3. To resolve the deficiencies observed in the preliminary model, an advanced high-fidelity patient-specific FE brain model is constructed from the CT scan of an healthy individual in section 4.3. To address the patient-specific feature of the advanced model, section 4.3.2 also introduces a novel method of simulating real-world patient-specific brain pathology by reconstructing realistic TBI lesions from patients' CT scans. The results of this patient-specific loading condition are presented and discussed in section 4.3.3.

4.2 Preliminary model development

4.2.1 Construction of Preliminary FE model

The exploration of brain model topology starts with a preliminary head model re-created from the Visible Human Project (VHP) Female Version 2.2 [116]. The VHP model was generated using the open-source high-resolution image dataset from the US National Library of Medicine [116]. This is a highly simplified head model and only the skull, the brain parenchyma, ventricles and the cerebellum are reconstructed. The wrinkled gyri and sulci are neglected on the surface of the cerebrum, and the meningeal layers of dura mater are also omitted in the VHP model. The relevant tissue mesh from VHP is shown in Figure 64a. Independent tissue meshes were provided in the form of a triangular iso-surface. Thus the surface topology was converted into analytical models in

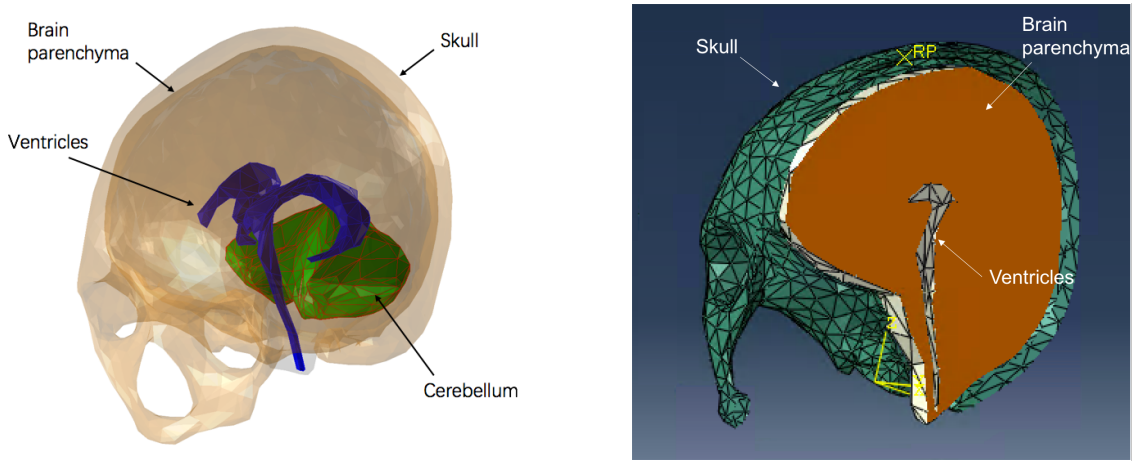

(a) Tissue mesh from VHP V2.2 [116] (b) Analytical FE model in ABAQUS

Figure 64: Reconstruction of the preliminary FE model

the following way:

1. Process the tissue mesh file in the open-source mesh editing software, MESHLAB [117]
2. Import the processed mesh file into ABAQUS as an orphan mesh
3. Create analytical volume from the orphan mesh using the "3D Mesh to Geometry" plugin offered by Dassault Systèmes [118]
4. Assemble different compartments together in ABAQUS
5. Mesh the analytical brain model

The first step smoothes the triangular iso-surface of relevant tissues as an attempt to reduce the simulation time. The brain parenchyma file, for example, has been simplified from over 40,000 elements to approximately 6,700 elements. The analytical model without such smoothing took more than 30 days to run a single simulation.

The meshed analytical components are assembled and presented in Figure 64b. The skull was imported as a discrete rigid surface and constrained from displacement by a reference point. To ensure there exists no physical contacts between the brain and the inner skull surface before loading, the skull surface was inflated by a factor of approximately 1.02 when processing the topology file. The brain was composed of 6,700 tetrahedral elements, with ventricles subtracted from the brain volume. The cerebellum was merged with the brain parenchyma when assembling the analytical model, for the purpose of simplicity. Boundary conditions were applied as follows for the whole head model: the skull was fully constrained, preventing all translational and rotational motions; the base of the brain was constrained from translational movements to simulate the connection between brain stem

and spinal cords; the remaining surfaces of the brain were added to contact pairs (surfaces that contact with each other).

It should be noted that the cerebral falx, as a strong, membraneous structure separating the two cerebellar hemispheres, was not included in the VHP head topology and hence missing in this preliminary model. The absence of the falx cerebri can be a potential deficiency of the preliminary model. As shown in the clinical review in section 1.2.2, there is no apparent brain movements along the falx attachments to the skull even if the rest of brain parenchyma is severely shifted due to the occupying brain lesions. This observation is generally evident on the axial view of CT scans for TBI patients. Moreover, in section 3.2.2, the study of midplane shifts on 33 TBI patients with severe brain deformation revealed that there exists no noticeable cross-plane shifts of brain along the periphery of brain contour where falx attaches to the inner table of the skull, which further proved the critical role of rigid falx in brain deformation. As a result, to address the nature of brain cross-plane deformations, it is necessary to take into account the effects of the falx, even if the actual compartments were missing in the preliminary model. In this study, an additional boundary condition was implemented to mimic the regulation effects of the falx. Specifically, the translational movements of the nodes along the cerebral falx connection to the skull were constrained in all directions. This falx constraint could also be deactivated in the simulation to help study the role of the falx.

To illustrate the large deformation response of the brain, a hyperelastic (HE) Neo-Hookean material model was assigned to the preliminary model. The HE model has no time-dependence and was therefore suitable for the analysis of the maximum deformation and strains induced during simulation. Quasi-static deformation was assumed.

Since there is no inherent unit set in ABAQUS, it is critical to decide on a consistent set of units before assigning material properties to the models. The set of units employed for the current simulation are displayed in table 7. Therefore,1 unit of time corresponds to 1 second in the following simulations.

4.2.2 Experimental simulation using preliminary FE model

In this section, the idealised FE model developed from VHP was used to simulate haematoma development in the brain due to TBI. In previous FE models, pressure was usually applied to certain parts of the brain to simulate ICP development. Yet intracranial hypertension characterised with high ICP is a complex clinical symptom affected by various mechanisms, from cerebral auto-regulation, through CSF absorption, to cerebral

Parameter	**Unit**
Length	mm
Force	Newtons
Time	second
Mass	tonnes
Density	tonnes/mm^3
Stress	MPa
Young's Modulus	MPa

Table 7: The set of units used in ABAQUS simulations for all chapters

infusion. Different locations in the brain would potentially have different ICP values, thus it is ambiguous to determine which value to use. Besides, the acquisition of ICP is also invasive. As a result, simply applying uniform pressure to simulate escalating ICP inside the skull may not be an ideal way for predictive computer simulations. Moreover, escalating ICP is not necessarily the key driving force for brain deformations.

Instead of pressure-driven ICP modelling, a deformation-driven loading condition has been proposed to perform the preliminary simulations. Clinically, many brain pathologies are accompanied with mechanical deformation of the ventricles. The development of haematoma, for example, is frequently associated with the translation and deformation of ventricles, as shown in Figure 6. Such a morphological change in ventricles is a distinct feature on CT scans and clinicians also take the displacement magnitude of the central membrane separating two lateral ventricles (midline shift) as a critical clinical indicator. Therefore, applying mechanical loading to the ventricles is one potential way of performing the haematoma development simulation. As compared to pressure loading, deformation loading has two main advantages: it is non-invasive to obtain from patients and it is easier to apply on FE models. To simplify the deformation-loaded boundary condition in this preliminary research, twist of the ventricles was disregarded and only the translational components were taken into account to simulate the brain behaviour during haematoma development.

Since the displacement of the ventricles is an apparent feature of brain deformation during haematoma development, it is useful to study the strain and deformation pattern across the brain due to ventricle translation. Specifically, a rigid surface copying the geometry

of ventricles was created and placed inside the real ventricular cavities in the preliminary model in this study. Such a rigid surface was scaled down so that the surface of the real ventricle was not in contact with the rigid surface before loading. Then, displacement loading was applied directly on the rigid surface, which interacted with the inner surface of the real ventricles of the analytical model to deform the brain through frictionless contact. For the present simulations, ventricle translation was applied in the direction vector (-1,0,0), with a standard cartesian coordinate system defined as (x,y,z). This direction vector is also illustrated in Figure 65(a) in the results section 4.2.3.

In this preliminary study a fixed ventricle translation is imposed, with a magnitude chosen based on clinical observations. As introduced in section 1.2.1, midline shift has been recognised as a serious indicator for the severity of the TBI. According to the Marshall scale for head trauma [119], TBI patients with MLS greater than 5 mm belong to Marshall category IV. Here, we adopted the magnitude of translation to be 6 mm, inspired by the minimum standard of clinical MLS within Marshall category IV. The application of a relatively small deformation loading could avoid potential convergence problem for such a coarse preliminary model. Ultimately, the research question here is: given that the ventricle surface has deviated 6 mm from its original position in a patient's brain after TBI, how close is the simulated overall brain deformation as compared to the reality? If the preliminary simulation is within acceptable accuracy, what are the detailed strain and deformation patterns in other brain compartments?

ABAQUS/Explicit solver was applied to solve this preliminary simulation. As suggested by ABAQUS User Notes [120], the application of dynamic explicit solver on quasi-static problems needs special attention. Specifically, the kinetic energy of the deforming material should not exceed a small fraction (usually 5 to 10 percent) of its internal energy through the majority of the step, otherwise the solution in Explicit solver is not stable and hence unrealistic. As a result, examination of the energy contents was crucial for the validity assessments of quasi-static problems simulated by ABAQUS/Explicit solver. In this study, various measures have been taken to reduce the dynamic effect of the deforming model and ensure that all the simulation results passed the energy balance check for the Explicit solver. The preliminary simulation results will be discussed in section 4.2.3.

4.2.3 Preliminary FE model simulation results

This section aimed to evaluate the performance of the developed preliminary FE model. By investigating the simulation results, it firstly confirmed the functionality of the

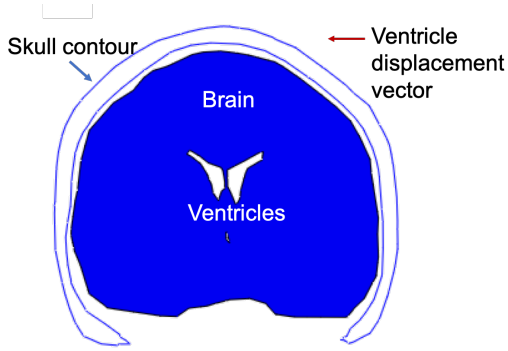

(a) Cross section of FE model before loading

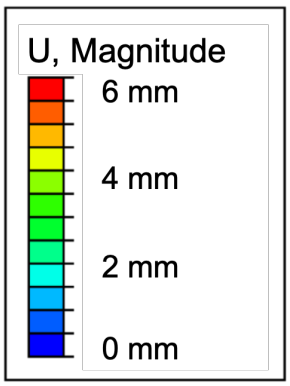

(b) The deformation magnitude of (c)

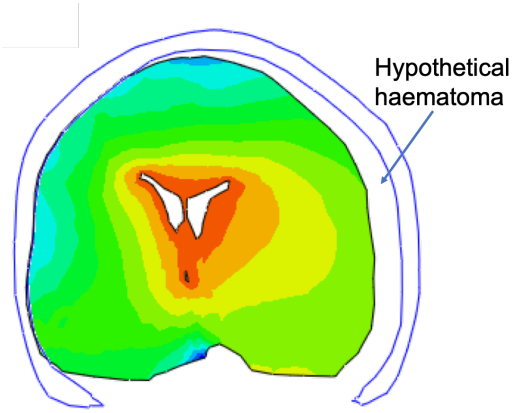

(c) Brain deformation contour for ventricle translation of 6 mm. Note, the growing gap between the skull inner surface and the brain surface is hypothesised as the developing haematoma.

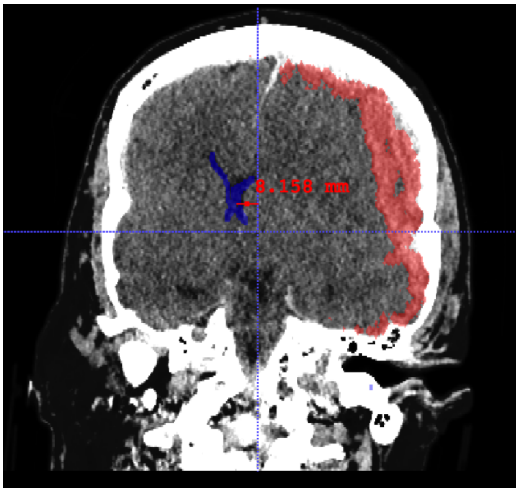

(d) A CT slice for a patient with subdural haematoma. Note, the red mask highlights haematoma and the blue mask denotes the translated ventricles. A midline shift of 8 mm is also present

Figure 65: Simulation results for haematoma development using ventricle translation. Displacement loading is applied following the ventricle displacement vector shown in figure (a).

proposed preliminary model together with its loading method. Then in the next stage, the haematoma development model is compared with a real-world clinical case to evaluate the fidelity of this preliminary model. The lack of cerebral falx in the preliminary model is pointed out here as a major deficiency of the current atlas-based FE model.

Simulating haematoma development by ventricle translation

Figure 65 presents the quasi-static solution of haematoma development simulated by ventricle translation. In Figure 65a, a coronal slice of the FE model is presented, illustrating the silhouette of the skull contour, the ventricles and the brain before loading. The red arrow also indicates the direction of the ventricle displacement vector applied in the simulation. Figure 65c plots the translational displacements of the brain tissues in the direction of the ventricle displacement vector on a coronal brain slice. The scale bar of the deformation contour is displayed in Figure 65b. When a 6-mm ventricle translation was applied in the direction of the target displacement vector, the brain near the ventricles deformed most and the deformation magnitude gradually decayed away from the ventricular space.

In the lefthand side of the Figure, the cavity between the brain and the skull reduced in size as the brain deformed and the surface of the left brain hemisphere came into contact with the skull inner table. On the other side, there is a growing cavity between the skull and the brain surface as compared to that of the unloaded case in Figure 65a. To provide the simulation with some clinical grounding, the computer simulation result was compared to a CT slice of a patient with subdural haematoma, as shown in Figure 65d. This is a coronal CT slice with a 8 mm midline shift due to the onset of SDH. In the pathological CT scan, the denoted ventricles (with the blue mask) shift to the lefthand side of the brain as the haematoma (denoted with the red mask) develops. It is seen that the interstitial space is squeezed in the contralateral side of the brain lesion, which coincides well with our observations in the simulation results. Moreover, by comparing the clinical CT scan with the laboratory simulation, it is seen that the developing cavity in the right hemisphere actually resembles the space where haematoma appears. Thus this cavity is hypothesised as the developing haematoma. As a result, it is demonstrated with this idealised ventricle translation method that this preliminary model is able to capture the pathological progression of subdural haematoma.

Evaluating the fidelity of the idealised FE model

So far, the initial attempts of the lesion simulations confirmed the basic functionality of the idealised model, but extra investigations are required to check the fidelity of such an idealised FE model. As discussed in the model development section, this preliminary FE model comes with an inherent structural deficiency that it does not include the cerebral

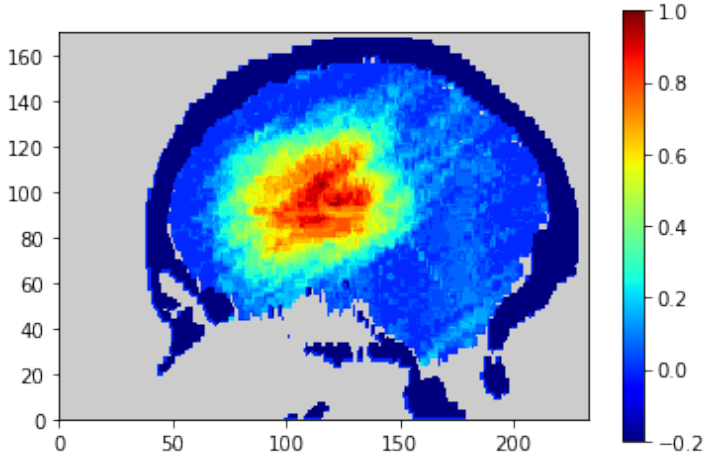

(a) MPS heatmap for the SDH patient with 8 mm midline shift

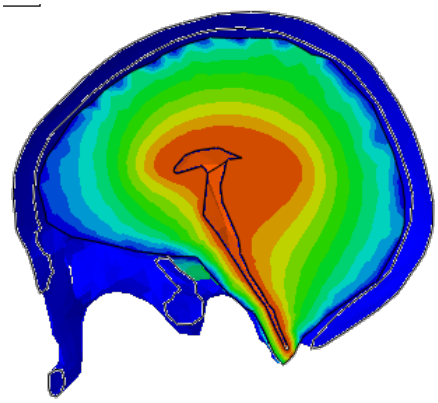

(b) MPS contour derived from the simulation with the falx constraint

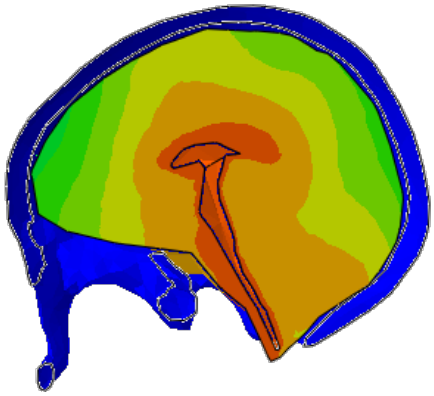

(c) MPS contour derived from the simulation with no falx constraint

Figure 66: Comparison of MPS analysis for experimental simulations and clinical observations. Note, the scale bar in (a) shows the normalised MLS between 0 and 1. The scale bar in (a) also applies to (b) and (c).

falx. Therefore it is essential to perform specific assessments to study the role of the falx and hence to evaluate the fidelity of idealised model.

To further understand the role of the falx in the scenario of brain deformations, an additional boundary condition which mimics the regulation effects of the falx has been proposed in section 4.2.2. Such a boundary condition was set to constrain the translations in all directions for the nodes on the centre line of the brain surface where the membraneous falx attaches to the skull. This falx constraint was set to simulate the falx insertion to the skull, which helped to prevent the movement of brain. In the coronal brain slice in Figure 65c, the blue region on the top of the brain indicates no deformation observed during the simulation, as a result of this falx constraint. To be able

to assess whether the falx constraint correctly regulates the cross-plane shifts of the brain, a real-world clinical reference is required.

Recall that in chapter 3.2.2, a novel computational tool has been developed to aid in the 3D brain shift analysis from CT scans. The proposed MPS tool captures the cross-plane shifts of the brain in the mid-sagittal plane and thus should be an ideal tool to help evaluate the simulation results in the current study. By investigating the brain shifts across the mid-sagittal plane, the simulated brain deformation results were explicitly compared with that derived from clinical CT scans under similar pathological conditions. On the one hand, the MPS heatmap shown in Figure 66a was derived from an SDH patient with 8 mm MLS using the developed image analysis tool. Like all other MPS heatmaps produced in section 3.3.2, this MPS heatmap has been normalised with respect to its own maximum, which is 8 mm in this case. It also follows the general properties of MPS summarised in section 3.3.2. In particular, the peak cross-plane deformation occurs at the ventricular region and gradually falls to zero around the periphery of the brain contour. On the other hand, Figure 66b and 66c present the cross-midplane deformation condition from the computer simulations. To make the experimental deformation contours closer to the definition of the MPS heatmap, only the deformations perpendicular to the mid-sagittal plane of the FE models were plotted. The view cut was also set to be at the symmetric plane (midplane) of the model in ABAQUS. In this way, the clinical MPS heatmap and the experimental MPS contour became comparable. Although the experimental MPS magnitude was not normalised, useful information can still be extracted by comparing the trend of relative MPS deformation between the simulated and clinical cases.

From the two experimental MPS contour maps, it is clear that Figure 66b was more similar to the clinical MPS heatmap, and hence closer to reality. The only difference between the two experimental simulations was the falx constraint: the boundary condition on the falx was deactivated while performing the second simulation in Figure 66c. Therefore, the brain on the periphery of the contour was free to deviate from the centre line, leading to a completely different MPS pattern as compared to the clinical observation. Unlike the second simulation, the first simulation in Figure 66b activated the falx constriant and yielded a much more realistic MPS contour. It is apparent that the deformation concentrates around the ventricles and decreases radially, similar to the trend observed in clinical MPS. To conclude, the experimental simulation with falx constraint gives more realistic results than the one without such a constraint.

4.2.4 Concluding discussion

The significant difference of the deformation contour in Figure 66b and 66c highlights the importance of the falx cerebri. Other conditions being equal, it was the inclusion of the additional falx constraint that changed the behaviour of the brain radically. This observation possibly proved our previous hypothesis in the bioengineering review section 1.3.3, that it could be the reconstruction of the falx that leads to the contradictory conclusions regarding the optimum location to perform DC in study [63] and [61]. However, although Figure 66b was a better simulation than the one shown in Figure 66c, this preliminary model still has some noticeable limitations when the solutions were compared with the real clinical MPS heatmap.

Firstly, the absence of the actual falx cerebri has degraded the effectiveness of the model. Some isolated blue dots were presented along the periphery of the brain contour in Figure 66b. This was because, without a real falx, the displacement constraint was applied directly to the nodes of the brain where the falx insertion to the skull should be theoretically. The translation regulation effect disappeared very fast away from the constrained nodes. In fact, apparent brain shifts were observed even in between the pinned nodes. Whereas in the real MPS heatmap in Figure 66a, the blue ring of no visible displacements is much thicker and smoother. The reason behind it is that the falx, as a rigid sickle-shaped membrane separating the two brain hemispheres, is a lot stiffer than the brain tissue. When the root of the falx is inserted to the skull, the extending meningeal layer would still play an important role in preventing potential brain deformations. Therefore the inclusion of falx as a separate compartment in the model is key to simulate deformation related brain pathologies.

Secondly, the current simulation was mechanically loaded with the simplistic translation of the ventricles. In Figure 66b, deformation was equally spread in the lateral, third and fourth ventricles. However, in reality, brain shifts are more likely to occur on the lateral and third ventricles but not in the fourth ventricle (the long tube that extends to the brainstem). In fact, even in the lateral ventricular region, the deformation is not uniform: there exists darker red dots within the red ventricular region in the clinical MPS heatmap, because apart from translations, the ventricles also distort in shape as a result of lesion development. Thus, applying a uniform mechanical loading to the ventricles was over simplistic and more advanced loading techniques needs to be discovered.

Last but not least, simulating TBI with a deformation loading on the surface of the ventricles failed to address the heterogeneous characteristics of the lesions. Clinically,

the development of intracranial lesion may take place in different locations across the brain, causing various degrees of deformation on the surface of the brain where the lesion attacks. When the deformation transmits to the inner brain region, they might lead to similar inner brain response. For instance, patients could develop similar magnitudes of midline shift, even if the characteristics of the TBI lesion differ a lot. The onset of brain lesions is the cause of brain deformation. As a result, using the lesion growth as the driving force for haematoma development simulation should be a better way of loading the FE model.

Moreover, apart from the disadvantages identified above, the preliminary model reconstructed from VHP also has some inherent shortcomings in its topology. The VHP offers STL files for the relevant compartments of the head. The STL file format defines a three-dimensional geometry with unstructured triangulated iso-surface formed by vertices and unit normal of the triangles. As a result, the converted brain model in ABAQUS also possessed the same triangulated surface and sharp corners that cannot be resolved by conventional mesh refinement techniques. Sharp edges in FE modelling could lead to stress concentrations and singularities, thus are generally ill-advised, according to the study by Marks *et al.* [121]. Thus the development of a smooth analytical model is highly recommended.

To sum up, although the current preliminary FE model has some obvious disadvantages, it has proved valuable in providing insights into the requirements needed for the high-fidelity model.

4.3 Patient-specific model development

This section describes the development of a more advanced high-fidelity analytical head geometry that is suitable for both surgical and non-surgical analysis of TBI related computer simulations. The aim is that the created patient-specific head geometry will offer an appropriate level of idealisation, but the critical features of the intracranial compartments should not be omitted. Such a high-fidelity FE model includes the cerebral falx and tentorium as key brain features in biomechanical brain simulations. As compared to the preliminary model, this FE model aims to resolve the problems identified in the previous simulations in all aspects and to give a reliable and realistic computational geometry.

In addition to the patient-specific FE head model, this section also presents a

patient-specific lesion simulation method. The aim of this chapter is to identify the required geometric and anatomic features for a good deformation model. Proper idealisation of model geometry and a promising preliminary result is a good starting point for more advanced computer modelling techniques. The next chapter (chapter 5) will focus on the specific model parameters needed to fine tune the model towards more realistic simulations. .

4.3.1 Construction of patient-specific FE model

Currently, there exists two ways to create the desired head model: to recreate patient-specific models from high-resolution medical images such as CT and MRI, or to utilise the averaged brain atlas from existing literature. The former method was applied in the current research. In general, re-creation of patient-specific head geometry has the following advantages:

- The majority of the open-source brain atlas did not include the falx cerebri, which is an important feature seen in medical images.
- Patient-specific models reconstructed from individualised patient-specific data capture the realistic brain anatomy of the underlying patients, whereas the brain atlas built the topology on averaged patient datasets. Normalising a large number of datasets might lead to loss of specificity in real patients.
- When CT scans are available both pre and post trauma, patient-specific head lesion can also be reproduced for a particular patient, whereas this is not possible for atlas based model.
- Patient-specific models have a stronger clinical grounding and are usually easier to be validated.
- Patient-specific models have the potential to aid in the customised diagnosis and therapeutic intervention for individual patients.

Although re-creation of a patient-specific model for every patient is ideal for personalised simulations of disease evolution and surgical interventions, it is not very practical due to the time consuming nature of the process. As an alternative, an economical solution is to develop one model from an exemplary CT scan and co-register all other CT scans to the chosen modality. In this way, the intracranial complications of all different patients can be performed on the same patient-specific model effectively.

The reconstruction of the patient-specific model has the following steps:

1. Find an appropriate set of exemplary CT scans from a healthy individual.
2. Reconstruct the brain compartments of interest in Autodesk Inventor Professional 2018 (Autodesk, San Rafael, CA).
3. Import the developed CAD model to ABAQUS, mesh the model and assign suitable material properties
4. Apply loading to the model and start simulation.

The selection of a template CT scan is crucial for a patient-specific model re-created from medical images. For the first step, a set of high resolution CT scan from a healthy individual was provided by Department of Anaesthesia, Addenbrooke's Hospital (Cambridge University Hospitals, England). In order to make this CT data a template, the spatial normalisation techniques introduced in the preprocessing pipeline in section 3.2 has been applied. After standardisation, this CT dataset is considered as a template so that any other CT scans can be processed through the proposed preprocessing pipeline and registered to this target CT scan. After preprocessing, the resultant CT scans from various patients will be spatially aligned with the target CT scan for group-level analysis.

The re-creation of the analytical CAD model from CT scans in the second step was the most challenging. Commercial package providers such as Simpleware (Simpleware Ltd, Exeter, UK) and Materialise (Materialise NV, Leuven, Belgium) have offered some automation for the conversion from medical images to analytical model. However, these

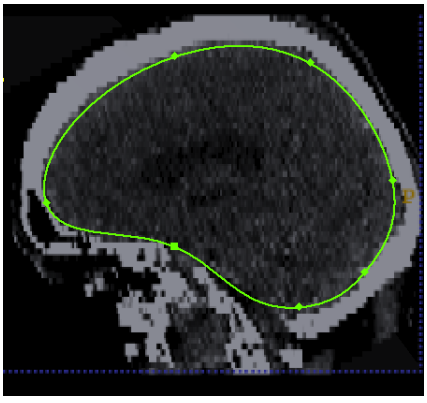

(a) Spline (in green) drawn in Autodesk Inventor for a cross section of brain in a sagittal CT slice

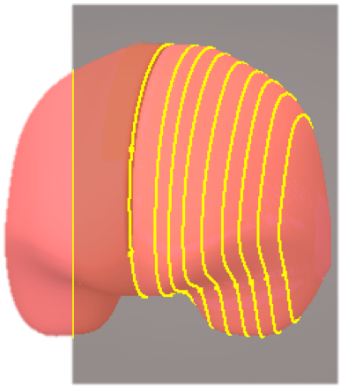

(b) Creation of analytical brain model through cross-sections (in yellow). Note the right brain hemisphere is mirrored to the left by the plane of symmetry (in grey).

Figure 67: Illustration of analytical brain construction using splines and cross-sections in Autodesk Inventor.

off-the-shelf softwares were not available. In this study, geometry production was achieved only using open-source softwares.

Creation of a satisfactory patient-specific topology requires substantial efforts. In Autodesk Inventor, the cross sections of any target compartment of the brain can be reproduced from corresponding CT slices. In Figure 67a, a spline is drawn in Inventor to delineate the cross-section of the brain on a sagittal CT slice. The flexibility of shapes constructed from splines allows for accurate reproduction for the shape of the brain. By repeating this procedure at uniformly spaced sagittal CT slices, a series of splines were generated as shown in yellow in Figure 67b. Those splines were then connected using the loft tool in Inventor to yield an analytical surface. The loft tool is capable of creating a transitional shape from a series of profiles. Since the human brain is anatomically symmetric against the mid-sagittal plane, the created left hemisphere was mirrored to the right as shown in Figure 67b. At the each end of the loft geometry, there is usually a flat surface with an edge characterised by the last profile in loft command. To smooth the edge of the end surface, the boundary patch tool was used in Inventor to create a smooth 3D surface within the boundary of the specified cross-section profile. The boundary patch tool is able to generate tangent or smooth boundary conditions for each edge of the surface, so that the resultant 3D geometry becomes edge-free. At this stage, an analytical model has been reconstructed.

For such a complex geometry as the brain, it is difficult to arrive at satisfactory results by lofting through randomly selected cross-section splines: additional efforts are needed to optimise the surface smoothness of the model. In particular, the lofted surface might not be smooth enough due to abrupt changes between connecting splines. To optimise the brain model, the splines on each of the cross-section were idealised and simplified as an attempt to capture the geometry with a minimum number of control points. The optimum spacing between splines was found experimentally, so that a geometrically accurate brain model with satisfactory surface smoothness was reproduced, as shown in pink in Figure 67b.

Apart from the brain, the same method was applied to generate the ventricles, the cerebrum, the falx and the tentorium from the chosen template CT scan. The skull, however, due to its complexity in geometry, cannot be reproduced in the same manner. Thanks to the distinct intensities of the skull in CT scans, it can be easily segmented by the basic thresholding method as discussed in section 2.2.2. The segmented skull file was then manually smoothed in ITK-SNAP and imported into Inventor to create an analytical model.

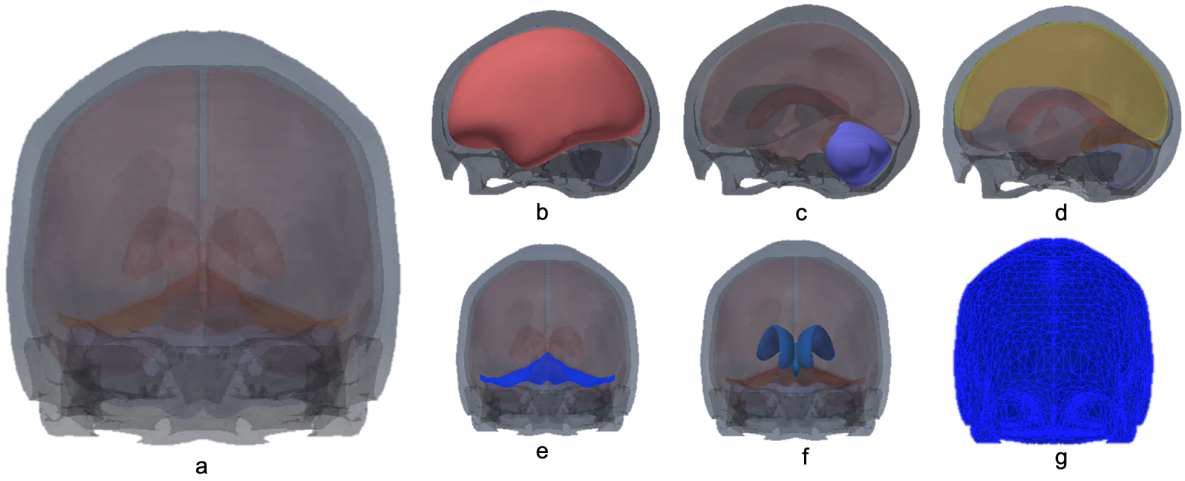

Figure 68: Patient-specific analytical head model including (a) the assembled head, (b) the brain, (c) the cerebellum, (d) the cerebral falx, (e) the tentorium, (f) the ventricles and (g) the skull.

For each of the brain compartments, the same set of cartesian coordinates was used for ease of assembling. The analytical ventricle model was subtracted from the whole brain model to create the ventricular space. The cerebral falx was also subtracted from the brain. The fillet tool was applied on the resulting edges produced by falx subtraction to avoid step-wise changes in the model geometry. In addition, considering the inner skull surface might be exposed to potential contacts with the brain surface during simulation, the skull inner surface must be smoothed. This was achieved by inflating the whole brain surface by a small factor and then subtracting the inflated brain from the skull geometry. A gap of approximately 1 mm was left between the skull inner surface the brain surface.

In the third step, the assembled head model was imported into Abaqus as a STEP file for mesh generation. Exporting the head model as a whole avoided further assembling processes in Abaqus. Boundary conditions were applied on relevant brain compartments: the entire skull was constrained from movements; the falx was rigidly inserted to the skull; the tentorium attachment to the skull was also constrained from movements. Since all substructures were analytical CAD model, mesh refinements can be easily performed for each of the substructures.

Figure 68 illustrates the assembled head geometry and the relative locations of all those individual substructures including the cerebrum, the cerebellum, the falx cerebri, the tentorium, the ventricles and the skull. It is seen that the created analytical brain compartments all demonstrate satisfactory levels of surface smoothness. Moreover, unlike the preliminary model, the patient-specific model obtained a satisfactory level

of idealisation while keeping the key stiff meningeal layers of the brain. This high-fidelity head model derived from the geometry of the selected template CT scan also demonstrated better anatomic accuracy as compared to that of the preliminary head model.

The newly created head model requires some preliminary testings for qualitative evaluation of its performance. For this purpose, a set of preliminary material properties was utilised in the preparatory simulation, though detailed material model tuning will be performed in the next chapter. In the final step, appropriate loadings can be applied on this high-fidelity FE model.

4.3.2 Patient specific simulation with realistic model

The developed patient-specific head model has a number of advantages over any idealised models or models rebuilt from an averaged brain atlas. Above all, there exists a stronger clinical grounding behind it, because the model was reconstructed from a real patient's CT scans. Real-world references can be found for every cross section of the computer model. In fact, for any random CT slice, whether it is in the sagittal, coronal or axial direction, a corresponding cross-section replicating the head geometry on this particular CT slice can be accessed in the computer model by calculating the CT slice thickness and converting it to the coordinates in the computational space.

Such a slice to cross-section correspondence not only allows the reconstruction of the head model, but also it could be utilised to replicate a realistic brain pathology. In this section, a method of regenerating a real-world pathology was developed to simulate brain lesion evolution on the realistic FE model.

The mechanics of indentation-based loading

In TBI settings, the brain deforms as a result of the growing blood clot (SDH, EDH or contusion) inside the skull. When looking at this pathological process from a biomechanical point of view, the lesion evolution process can be considered as the driving force behind any shifts of brain parenchyma. Therefore, by capturing the unique contact surface between the brain and the lesion, it is possible to imitate the lesion evolution process by "indenting" the lesion surface to the FE brain model.

Traditionally, the word "indentation" refers to a hardness test where a stiff indenter is pressed against a softer test material until an impression is formed. Inspired by the

traditional indentation test, in this circumstances, a rigid lesion surface simulating the shape of the haematoma acts as the stiff indenter and the brain tissue can be considered as the soft tested material. As illustrated in Figure 69, through indentation, the rigid lesion surface gradually indents deeper into the brain, leading to potential brain substructures deviating from their original location. Ultimately, the lesion-brain interaction surface replicates the exact patient-specific lesion geometry extracted from the pathological CT scans. In this way, the interaction between the brain tissue and the growing lesion can be closely monitored. This indentation-based mechanical loading method has a major advantage that it facilitates full control over the customised lesion geometry. However, it applies only to the lesions developed between the inner surface of the skull and the brain surface. For any intracerebral lesions, the proposed indentation-based method is not applicable.

Creation of lesion indentation surface

The re-creation of the unique brain lesion surface follows a similar manner as introduced in section 4.3.1. Specifically, the procedure involves a 2D delineation of the lesion profile in the corresponding CT slices and a 2D to 3D evolution to form the actual lesion indentation surface. Thanks to the nature of indentation, only the geometry of the lesion-brain contact surface interacts with the brain so as to deform it. Thus it was not necessary to reproduce the complete geometry of the lesion: the surface of the lesion facing the skull was not of interest. Therefore the lesion-skull dividing line was ignored in Figure 70a.

In Figure 70a, the lesion segmentation (in red) was done by an experienced neurosurgeon

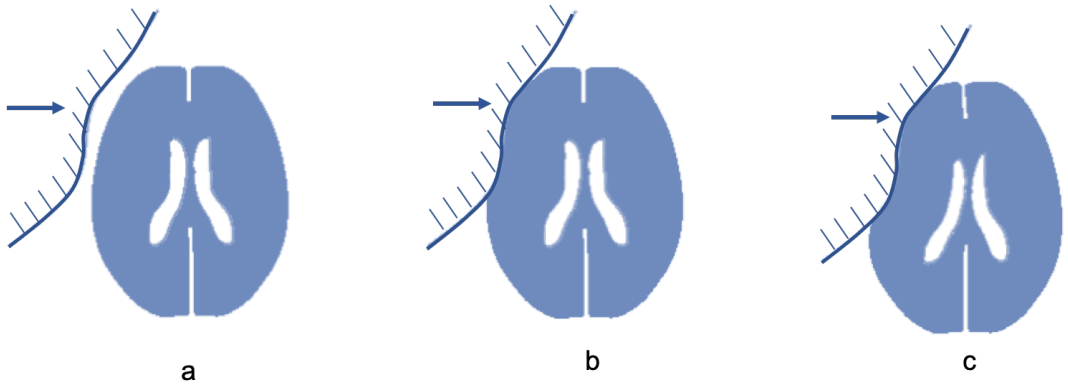

Figure 69: Illustration of the indentation process (a), (b) and (c) as the rigid lesion surface indents deeper into the brain parenchyma.

and a spline was generated following the shape of the lesion. It is worth noting that the proposed lesion characterisation method has a strong clinical grounding that for every slice in the pathological CT scan, it is possible to find a corresponding cross-section in the reconstructed computer model for a slice-wise comparison. In Figure 70b, the lesion spline extracted from the patient's CT scan was shown on the corresponding cross-section of the patient-specific head model. It is seen that the CT view in Figure 70a and the model view in Figure 70b are highly similar, except that in the model view, the ventricles and the skull contours are undeformed. Presumably, the FE model was under pre-trauma (pre-loading) condition, as compared to what is shown in Figure 70a. Hypothetically, after indentation loading, the brain substructures in the developed FE model would deform towards the pattern in the pathological CT scan.

So far, the creation of the lesion profile is constrained to be in 2D CT slices. Those lesion profiles from the successive CT slices need to be organised to form the actual 3D lesion surface. In Figure 71a, the customised lesion splines created from corresponding CT slices were connected using the loft tool and a characteristic 3D lesion surface was regenerated. Figure 71b demonstrates the lesion surface intersecting with the original brain model. Theoretically, the part of the brain tissue split by the lesion geometric surface represents the hypothetical volume of the SDH in the TBI patient.

Following the completion of the lesion geometry, the developed lesion surface was then

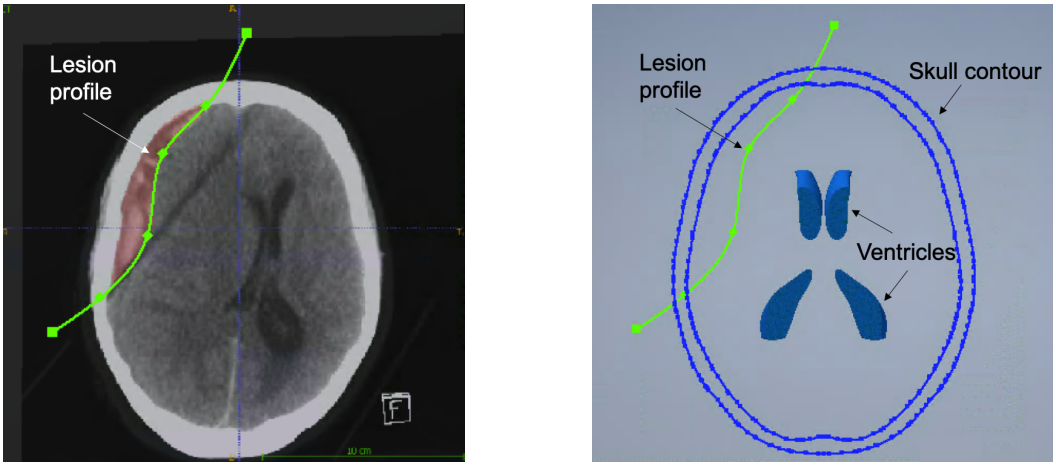

(a) (b)

Figure 70: (a) Spline (in green) drawn in Autodesk Inventor on a sagittal CT slice to delineate the SDH profile; (b) Lesion profile drawn on the corresponding cross-section of the developed head model. Note, (b) is the cross-section in the patient-specific model which corresponds to the CT slice in (a). The relative locations of ventricles and the skull contour in (b) denote the intracranial situations pre-loading (under healthy conditions).

imported into Abaqus as a 3D discrete rigid element. In Abaqus, the indentation surface must be translated for a specific distance, L, away from the brain surface until there is no substantial contact detected between the lesion surface (indenter) and the brain. Prior to the actual simulation, the lesion surface should not be in contact with the brain surface, thus the brain was considered in a relaxed situation and free from lesions. During simulation, indentation was gradually applied by translating the rigid lesion surface towards the brain for the same distance L until the indentation surface was back to the position where the original lesion sits. Throughout the indentation process, it is essential that the interaction between the skull and the rigid lesion surface was set to be ignored, so that the skull does not interfere with the indenter. Frictionless contact condition was assigned between the lesion indentation surface and the brain tissue, so the brain surface was free to deform during simulation. In this way, the indentation technique is able to simulate the brain deformation following a change in the shape of the external boundary of the parenchyma associated with a specified unique lesion.

Moreover, the pathological CT scans of various injuries were standardised and brought into alignment in the same physical space after preprocessing. Such a spatial normalisation of medical images offers a solid foundation for the reconstruction of realistic lesions of various kinds in the developed high-fidelity head model. As explained in section 4.3.1, this patient-specific FE model was re-created from a spatially normalised CT scan from a healthy patient. In order to perform TBI related simulations on the developed realistic model, any pathological CT scan from a random patient can be registered to the template CT dataset. Such a registration is achieved by firstly treating the pathological CT scan with the preprocessing pipeline in section 3.2, then applying image registration using the

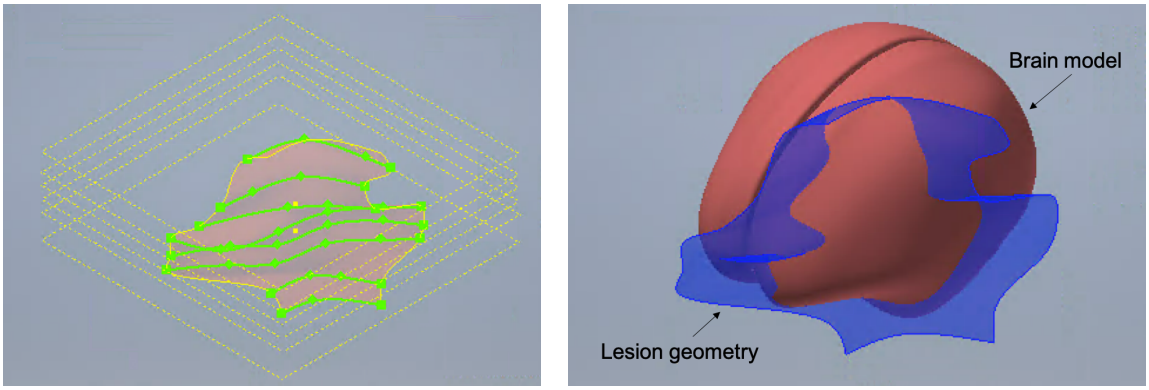

(a) (b)

Figure 71: (a) Formation of lesion-brain interaction surface by lofting through characteristic splines (in green). (b) Lesion characteristic surface (in purple) intersecting in the FE brain model (in pink). Note, patient-specific lesion-brain interaction surface is reproduced.

target CT scan as a template in 3D Slicer. After registration, the CT scans of various sources are mapped to the same physical space, with the same head orientation and intensity ranges. Figure 42 in section 2.3 shows an example registration results for two CT scans with SDH. It is seen that the two pathological CT scans are brought into alignment with the template CT scan, facilitating slice-wise comparison.

This section aimed to investigate the effectiveness of the proposed patient-specific lesion simulation method. For a better comparison with the preliminary model, the same material properties of the skull and the brain were adopted. As for the newly created compartments, the cerebellum used the same material property as the brain. The falx and tentorium shared the same set of linear elastic material properties ($E = 31.5$ MPa, $v = 0.45$). The current set of material parameters was preliminary and more advanced model parameter tuning is performed in the next chapter.

4.3.3 Patient-specific model simulation results

This section presents the experimental simulation results from the advanced high-fidelity FE model. It is seen that the model is patient-specific not only in terms of the realistic head topology, but also it encompasses a set of patient-specific lesion simulation method. The objective of this section is to perform some initial simulations and test the functionality of the model, and where possible, the preliminary simulation results will be evaluated qualitatively. More quantitative assessments will follow in the model assessment section in chapter 5.1.

For the current model, the lesion evolution process is made patient-specific by the indentation-based deformation technique. Specifically, the characteristic lesion surface recreated from a real SDH patient was indented into the high-fidelity FE head model. The unique indentation-based loading conditions allow for close monitoring over the pathology evolution process. At the end of the simulation, the surface of the brain deforms to the exact geometry as reconstructed from the lesion-brain interface of the patients' CT scan. The high-fidelity model, together with customised loading conditions, has the potential to resemble the post-traumatic brain deformation satisfactorily.

The quasi-static explicit solver was used in Abaqus, considering the complicated contacts between the brain substructures. Furthermore, as a feasibility study for the advanced patient-specific lesion simulation model, the current head model adopted the same grade of mesh as the idealised model, though mesh refinements can be easily adapted in the current analytical model. This preparatory realistic lesion simulation took 7 hours to run

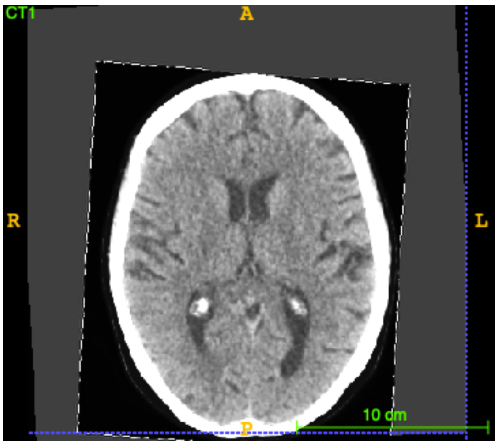

(a) An axial CT slice from the template CT scan.

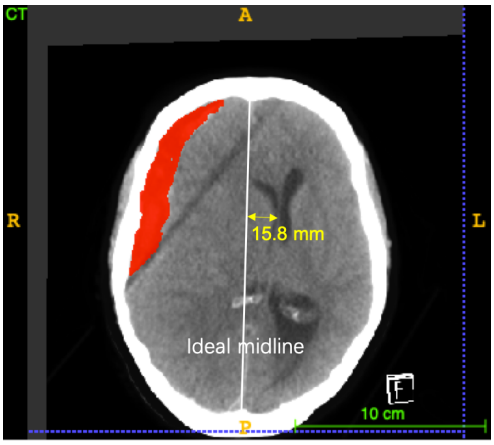

(b) A axial CT slice from the SDH patient.

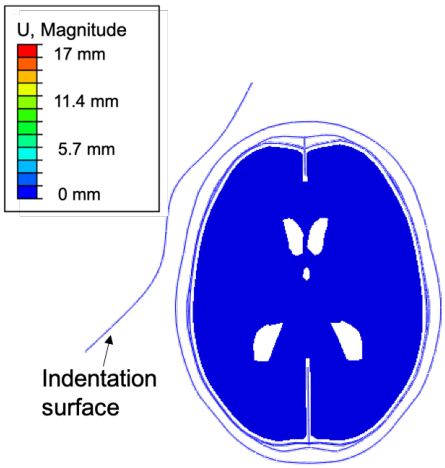

(c) Cross-section of the head model before loading.

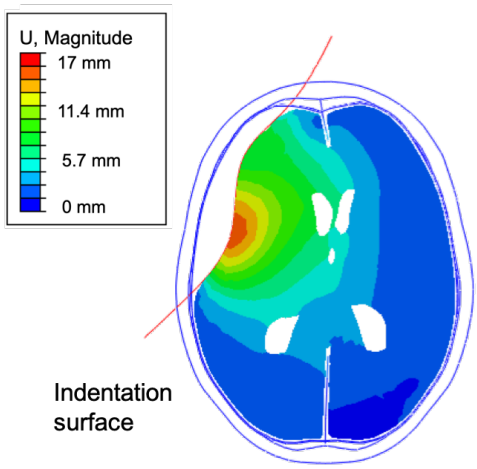

(d) Cross-section of the head model after loading

Figure 72: Illustration of the patient's intracranial condition change before and after the onset of SDH. Note, the first row imitates the brain intracranial complications pre and post lesion from medical images. And the second row shows the corresponding deformations during simulation in the corresponding cross-sections from the FE model.

in a double threads simulation system without any mass scaling. The longer simulation time was caused by the introduction of additional contacts between the falx, tentorium and the brain.

One strength of this high-fidelity FE model is that both the lesion surface model and the head model were patient-specific, with real patient's medical images as clinical references. In other words, for any CT slice, it was possible to find a corresponding cross-section in the computer model. Hence slice-wise comparison between the post-injury CT scan and the simulation results was available. Figure 72 demonstrates the simulation results at an

example cross-section before and after simulation. Clinically, the pre and post trauma CT scans are usually not available at the same time for a patient, because medical images are normally taken for TBI patients following the trauma in the emergency department at the hospital. The lack of healthy CT scans is considered as the main obstacle for real patient-specific head injury simulations. In the current research, the CT scans from an SDH patient were brought into alignment with the CT template of a healthy patient with the help of image registration. In this way, the registered pathological CT scans can be regarded as the post-injury scans for the same patient as the template healthy CT scan. Thus Figure 72a and 72b can be regarded as the CT slices of the same patients before and after TBI.

What's more, such a preliminary simulation also demonstrates satisfactory level of applicability of the developed high-fidelity FE model. In Figure 72b, a thick slice of SDH is segmented in red. As compared to the pre-injury image in Figure 72a, the ventricles deviate from their original position with the maximum shifts of 15.8 mm from the ideal midline. This pathological process has been replicated in the developed patient-specific FE model using the proposed indentation method. The second row in Figure 72 illustrates what happened during the specified SDH evolution in the corresponding cross-section in the FE model. In Figure 72c, the indentation surface was away from the head model and the whole brain was healthy and free from trauma. As the simulation advanced, the indentation surface penetrated deeper into the brain, pushing on the brain surface until the designed SDH pattern was achieved. Figure 72d shows the deformation contour in the selected cross-section of the head model at the end of simulation. The growing cavity formed by the indentation surface and the inner skull surface was the hypothetical volume of brain haematoma. As compared to the SDH segmentation (in red) in Figure 72b, the hypothetical haematoma slice in the FE model agreed with the exact geometry delineated from the real TBI patient. As opposed to the previous hypothetical haematoma in the idealised model in section 4.2.2, the current more sophisticated simulation methodology described in this section gives more control over the detailed loading condition and gives a more effective patient-specific lesion simulation.

So far in this section, the brain surface deformation of a particular TBI patient has been successfully resembled with high accuracy, thanks to the patient-specific lesion indentation technique. Nevertheless, shifts of the brain tissue occurs not only at the surface, but also deeper inside the brain. An accurate simulation on the surface of the model does not necessarily guarantee high quality of inner brain behaviour. In the simulation results in Figure 72d, the maximum deformation occurred at the interface of the brain-lesion contact surface.Specifically, a peak deviation of 7 mm was observed at the point where

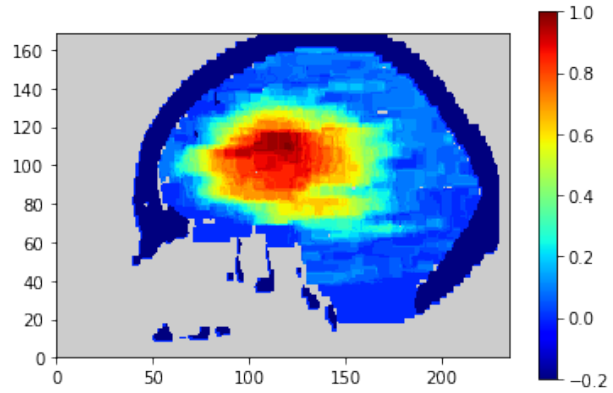

(a) MPS heatmap from clinical CT scan.

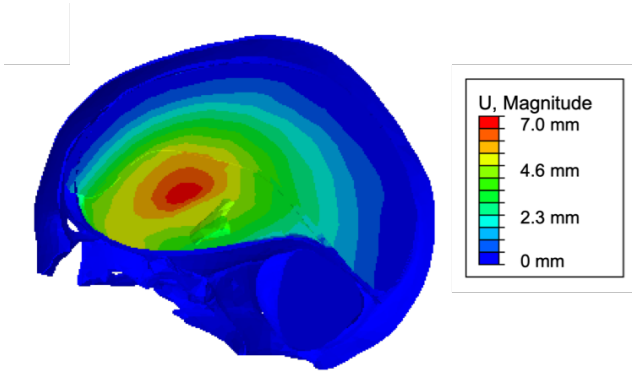

(b) MPS contour derived from simulation results

Figure 73: Comparison of clinically and experimentally derived MPS for the SDH patient. Note, in (a) the MPS heatmap has been normalised between 0 - 1, while in (b) the MPS contour retains its natural scale.

the thickness of the haematoma was the greatest. Next to the maximum deviation region, the brain deformation gradually decayed while transmitting to the deeper brain tissues away from the indentation surface. In general, the brain herniation was worse on the collateral half of the brain where haematoma was developed. There existed no visible brain shifts at the falx insertion to the skull, while the tip of the falx deviated slightly from the symmetric centreline (the ideal midline). In the ventricular region where there is no falx protection, brain deformation was more concentrated than that of the tissue near the falx, even if the absolute distance from the indentation surface was similar. In the contralateral hemisphere, the deformation effects of the indented lesion was limited. In particular, the dark blue region next to the posterior falx in Figure 72d suggests that no deformation was present and thus this part of the brain tissue remained undeformed throughout lesion evolution.

To perform a qualitative validation of the simulation results, the clinically derived MPS heatmap for this particular SDH patient was compared with the MPS contour derived from the FE model in a similar manner with the preliminary study for the idealised model in section 4.2.3. Results are shown in Figure 73. It is seen that the derived MPS contour was similar to the clinically developed MPS heatmap: the trend of shifts being most severe in the central ventricular region and decaying radially was clearly observed. As compared to the MPS contour from the preliminary model, the current one resembled the realistic MPS with much better accuracy, especially around the skull periphery. The reason behind this improvement is that in the idealised model, the falx constraint was applied directly to brain surface, which resulted in distortion of brain when the model

was loaded. Whereas in the current high-fidelity FE model, with the inclusion of falx as an independent brain compartment, boundary conditions were exerted directly on to the falx-skull attachment and the brain displacements were regulated through the interaction with the rigid falx membrane, which better replicated what was happening clinically. The high resemblance of MPS contour between the clinical finding and the simulation results give more confidence in the validity of the developed FE model. It confirmed that the developed high-fidelity head model is structurally correct with key intracranial features.

As well as showing good agreement qualitatively with deformation results, it is also possible to use clinical data to derive a quantitative validation. An advantage of the current patient-specific model over an idealised model is that it facilitates not only qualitative, but quantitative comparison between the simulation results and clinical ground truth. It is possible to find a landmark in the CT scan, locate the selected landmark in the FE model and compare the detailed deformation magnitude. At the septum pellucidum between the two lateral ventricles, for instance, the deformation was found to be around 7 mm, which was significantly smaller than the 15.8 mm MLS shown in the clinical ground truth in Figure 72b. In fact, similar findings were seen when looking closer into the MPS contour in Figure 73b: the red region of intense deformation was greater in both size and magnitude in the clinical MPS heatmap. This interesting finding reveals that, even if surface of the brain is regulated well enough to replicate the pathological development of lesion, the subsequent inner brain tissue deformation might still differ from the clinical reality. The significantly smaller midline shifts in the simulated FE model could be a result of a series of factors. The material properties and the mesh size of substructures, the applied boundary conditions and even the loading rate might affect the inner brain herniation in simulation. It does not challenge the validity of the model, but the precision of the model needs to be improved. These detailed model parameters are to be tuned and assessed towards more realistic simulations in the next chapter.

4.3.4 Concluding discussion

Under pathological conditions, the brain parenchyma deforms as a result of the evolving lesion. Such a brain deformation occurs not only at the surface, but also in deeper brain structures. The FE based simulation method is capable of investigating the brain deformation contour throughout the brain under any prescribed loading condition. Thus FE based computer modelling is a powerful tool for both retrospective and predictive study in TBI analysis. The objective of this chapter was to develop an analytical head model with relevant anatomical features and appropriate deformation behaviour.

The process of developing an FE head model started with a highly idealised geometry comprising the basic brain anatomy from the VHP. A simple deformation loading was applied to the ventricle surface to simulate the development of subdural haematoma. The simulated brain deformation as a result of ventricle translation was compared with the clinical brain deformation ground truth and three main limitations were revealed: the lack of falx cerebri as an important brain substruture; the limited accuracy in the model topology; the loading conditions of ventricle translation that did not accurately represent the real driving force of lesion evolution. As a result, a more realistic head topology is needed.

To address the identified defects in the preliminary head model, a high-fidelity patient-specific model was developed from a template CT scan of a healthy individual. The patient-specific model includes the falx cerebri and tentorium, because such rigid membranes play a critical role in regulating brain deformation. With the help of open-source softwares, smooth analytical models have been developed to capture the detailed anatomy of the underlying healthy individual and slice-wise comparison between FE model and CT scan was undertaken. As well as upgrading the model topology, a set of patient-specific loading conditions were designed to obtain the most realistic and clinically relevant simulation results. The similarity of the simulated brain deformation results and the clinical observations of MPS confirmed the computer model as being qualitatively correct. However, quantitatively the model was not found to predict the deformation response accurately with the chosen material properties. In the next chapter an in-depth study of this aspect of the modelling procedure is explored to derive a model able to simulate clinical situations realistically.

5 Biomechanical model assessment

5.1 Introduction

An accurate FE analysis comprises a series of steps including geometry creation, discretisation of elements, material assignments, definition of boundary conditions and loading conditions, before it can be sent to the solver. The successful identification of an appropriate geometry in chapter 4 was the first step towards a suitable computer model. In this chapter, the overall aim is to assess the potential developments and alterations to the patient-specific head model to identify an optimised model which can capture realistic brain deformations observed clinically. Explicit assessments will be made on one particular patient case in this chapter. Then in the next chapter, the assessed computer model will be adjusted by changing its loading conditions to simulate the heterogeneous traumatic brain behaviour under various other scenarios.

A key issue in developing the model is determining how to assess the model effectiveness. This will be done using both qualitative and quantitative components in this chapter. Thanks to the patient-specific nature of the head geometry which has been developed in chapter 4, it is possible to extensively compare the simulated brain behaviour with the brain deformations extracted from medical images. In the qualitative assessment, the cross-plane brain deformation pattern from computer simulation will be compared with the MPS heat maps derived from the post-trauma CT scans of the same patient. As for the quantitative assessment, the magnitude of deformation in the deeper brain tissues such as the septum pellucidum will be examined. In the model simulation in chapter 4, the indentation based loading condition was shown to be able to deform the surface of the brain to a target shape. However, in the deeper brain tissues away from the lesion-brain interaction surface, the simulated brain deformation pattern was found to be only qualitatively correct in the mid-sagittal plane. In particular, the model failed the quantitative assessment because the magnitude of MLS was found to be a lot smaller than the clinical observations. So while Chapter 4 has demonstrated a promising approach towards patient-specific modelling, the model has to be developed to give a desirable level of accuracy for the modelling approach.

With explicit assessment criterion identified, it is now possible to thoroughly explore the various potential developments to the model. The exploration starts with an assessment of whether the numerical implementation is of an appropriate accuracy. Having assessed the relevant numerical methods, it is important to then evaluate the loading conditions

to simulate target brain pathology. Specifically, a thermal expansion based boundary condition will be investigated to simulate the secondary swelling in TBI patients, in addition to the primary damage introduced in chapter 4.3.2. Besides, a range of material models for the brain and its substructures will be assessed to find the appropriate set of material parameters to describe the brain behaviour. Furthermore, to capture the unique deformation behaviour of the ventricles, a fluid filled cavity method will be applied to facilitate adjustable levels of deformable behaviour for the ventricles during TBI. At the end of this chapter, a fully developed FE head model will have been assessed and optimised for the applications of more sophisticated TBI scenarios in chapter 6.1.

5.2 Numerical parameter tuning

This section aims to explicitly tune the numerical parameters of the patient-specific head model developed in chapter 4, assess its numerical sensitivity and find the optimum set of numerical methods when using the model.

5.2.1 Methods

In FE analysis, it is critical to find the optimum set of numerical methods that yield an appropriate level of accuracy in the simulation results before the implementation of any other model alterations. With other model specifications and loading conditions being identical, orders of magnitude discrepancies were found in the simulation results through simple alterations of the numerical methods, according to the parametric study by [122]. Specifically, such numerical parameters include the choice of FE solver, the mesh element type, the mesh size, as well as some formulation options such as hourglass control. Considering the complex contact problems in the indentation-based lesion simulation model, quasi-static analysis was used with the Abaqus/Explicit solver given its known efficiency in modelling highly-nonlinear problems with large deformation. With the chosen FE solver, the types of mesh and element size were found to have the biggest impacts on simulation results [122]. Thus in the current section, the effect of these two parameters on the numerical evaluations will be evaluated.

Choice of element types

Tetrahedral and hexahedra solids are the two most popular three-dimensional elements in bioengineering simulations. It is essential to choose the right element type which is more suitable for the current analysis. Despite the greater stability of hexahedral elements in highly nonlinear simulations, their generation process is usually demanding and involves substantial human intervention, especially for such a complex geometry as the brain. In fact, attempts to generate hexahedral meshes for the patient-specific geometry all failed in Abaqus. The tetrahedral elements, on the other hand, adapted well to the fine anatomic details of the complex geometry developed in section 4 with great ease of automation in Abaqus. In addition to the better geometric representations, the application of tetrahedral based mesh also facilitates convenient mesh regeneration of different mesh densities for a convergence study.

Conventional tetrahedral elements may possess some limitations due to their reduced degrees-of-freedom, but it is possible to take actions to alleviate it. The main concern of using tetrahedral elements is that they may be overly-stiff under large deformation and prone to volumetric locking when simulating incompressible materials like the brain [123]. However, such deficiencies can be alleviated via using higher-order elements and finer meshes. In Abaqus/Explicit element library, C3D10M, the 10-node modified quadratic tetrahedron is the only available high-order tetrahedron element. Hence C3D10M was applied in the discretisation of the brain and cerebellum model for all subsequent studies. According to the parametric study by Giudice *et al.* [122], their simulation results become comparable for 10^6 tetrahedral elements model and 10^5 hexahedral elements model. Consequently, mesh refinements are crucial in the current study.

In addition to the definition of the cerebrum model, it is equally important to find appropriate element types for other brain substructures in the patient-specific FE model. For the falx and tentorium, a general-purpose three-dimensional quadrilateral shell element, S4R, was utilised to account for finite membrane strains. The skull surface, being relatively rigid as compared to the brain tissue, has been simulated using conventional shell elements, S3. As for the characteristic lesion indentation surface, R3D4, a four-node, bilinear quadrilateral 3D rigid element was adopted to achieve smooth contacts between the interacting surfaces.

Mass scaling

FE computations for such a complex geometry as the head model can be very time-consuming, thus it is important to find a numerical method that accelerates the target computations while maintaining appropriate accuracy. In quasi-static studies, the required computational time can be infeasibly long in the natural timescale, especially with added refinements of meshes. According to the Abaqus User manual [120], there are two ways to reduce the simulation time for quasi-static simulations incorporating rate-independent material behaviour. On the one hand, the designed time period of analysis can be reduced. On the other hand, mass scaling can be used to increase the mass of the model artificially. While both of the methods can be helpful towards an economical solution, the latter one was preferred because it preserved the natural time scale. Although accelerating the analysis helps reduce the computation time significantly, it might also lead to unrealistic simulation results if the consequent increases in the inertial forces dominated the simulation process. Therefore, an appropriate amount of mass scaling must be found to improve the computational efficiency while maintaining acceptable accuracy.

As an attempt to find the appropriate level of mass scaling, a series of mass scaling factors are tested on a moderately-refined mesh. Mass scaling increases the stability limit of the time increment by artificially increasing the material density. In Abaqus/Explicit, semi-automatic mass scaling was applied to the whole model throughout the step, so that when the stable increment time was below a designated value, element mass would be scaled. By assessing the simulation results, the optimum mass scaling factor that accelerates the computation without significant outcome degradation can be found and applied to later simulations.

Mesh convergence study

A mesh convergence study is essential to all kinds of FE modelling problems, as it tests the appropriateness of the FE model and finds the optimum mesh size that yields sensible simulation results with the minimum computational costs. Since the deformation and strains of the cerebrum are of our greatest interest during simulation, the convergence study firstly investigated the cerebrum model and then the concluding mesh size was directly applied on other brain compartments to make the model consistent in mesh density. To study model sensitivity to mesh density, the simulation was primarily carried

out on a model with the finest mesh. In this case, the finest mesh comprises approximately 500,000 elements in the cerebrum and more than 800,000 elements overall. This is of the same order-of-magnitude as the finest mesh adopted by [68]. The solutions from the finest mesh was then adopted as the reference simulation results to evaluate the simulation quality for other mesh densities. By gradually decreasing the mesh grade and reducing the number of elements, the total simulation time dropped drastically and eventually a tradeoff between computation time and simulation quality was found.

Assessments of the sensitivity of the model mesh size are primarily quantitative. Since the model was loaded by indentation, the maximum deformation was likely to occur at the deepest indentation point on the surface of the brain regardless of mesh size. Therefore comparison of the maximum displacement for the whole brain compartment was not appropriate. Instead, the analysis of the deformation in the inner brain tissue is more representative of the mesh quality. Here, the maximum displacement magnitude on the surface of the third ventricle was taken as the numerical assessment criterion. For models of various mesh densities, their maximum deformation in the third ventricle surface was compared with that of the finest mesh to evaluate the quality of that mesh.

5.2.2 Results

Mass scaling

Accelerating the simulation by mass scaling requires repetitive test runs. On a moderately-refined mesh with approximately 25,000 tetrahedral elements in the cerebrum model, the Explicit solver advanced the solution with a maximum time increment at the order of 10^{-6} s, which resulted in a total computational time of approximately 2 weeks without mass scaling. In the meantime, if the target time increment was set greater than 1×10^{-4} s using mass scaling, the simulation aborted halfway because the deformation speed exceeded the wave speed in some elements. Hence a reasonable range for the target time increments was between 1×10^{-6} s and 1×10^{-4} s. After a series of experiments on the mass scaling factor, it was noted that setting the target time increment as 1×10^{-5} s has effectively reduced the computation time from weeks to within 1 hour, without substantial degradation in outcome accuracy. Such a mass-scaled model also passed the energy balance check to ensure that the kinetic energy of the deforming material should not exceed a small fraction (usually 5 to 10 percent) of its internal energy through the majority of the step, otherwise the solution in Explicit solver is not stable and hence unrealistic. As a result, a mass scaling factor that increased the stable time increment to

1×10^{-5} s was deemed optimum and applied in the mesh convergence study and later simulations for the purpose of time efficiency.

Mesh convergence study

With suitable levels of mass scaling, it is now possible to obtain more economical solutions for the simulations of each individual mesh grade in the convergence study. A range of meshes from coarse to fine has been generated, yielding total elements of approximately 3,000, 7,000, 10,000, 25,000, 40,000 and 75,000 elements in the brain model respectively. Quantitative assessments of the mesh sensitivity calculated the percentage error for the maximum displacement U_{max} on the surface of the third ventricle as compared to the finest mesh which comprises of 500,000 elements. The results were plotted in Figure 74. It is noted that the percentage error dropped sharply as the number of elements was increased from the smallest value, and levelled off when the number of total elements

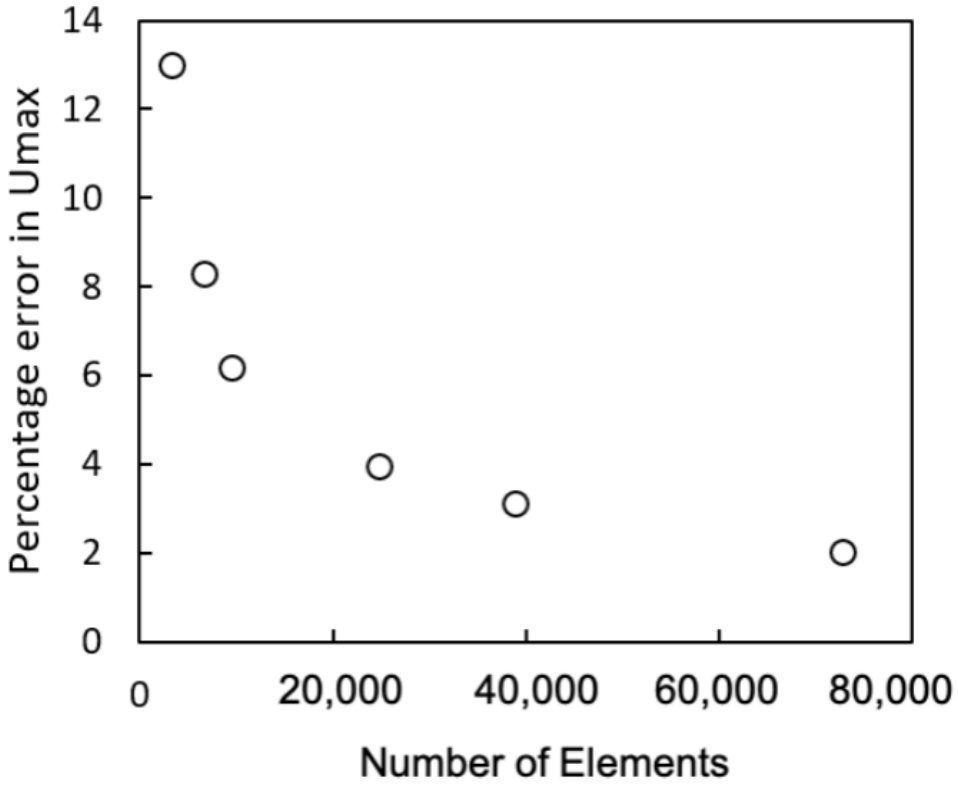

Figure 74: Percent error in maximum displacement U_{max} on the surface of third ventricle compared to the finest mesh, plotted against the total number of elements in the brain model

exceeded 25,000.

In FE analysis, convergence is observed when the outputs from simulation become stable and less sensitive to the changing mesh. For our FE head geometry, a global mesh of around 25,000 elements showed a percentage error under 5% as compared to the finest mesh. In the meantime, further mesh refinements with total elements greater than 20,000 did not indicate significant improvements in percentage error, but extended the total simulation time from several hours to 3 days. Thus a fine mesh composing of approximately 25,000 tetrahedral elements was chosen as the optimum size for the current FE model.

In addition to the numerical evaluation of simulation outcomes, it is also helpful to analyse the deformation pattern as the mesh density is refined. Figure 75 shows the results with an increasingly fine mesh density on a selected slice of the brain. In the first mesh slice, it is observed that the deformed shape of the ventricles differed significantly from the other two, with the lower left lateral ventricles being effaced under indentation. The lesion-brain interaction surface was also visibly fragmented due to the poor quality of coarse mesh. The second and third mesh slice are from analyses with fine and ultra-fine mesh quality. Both of them were featured with a smooth lesion-brain interaction surface and the ventricle shapes were also similar. In fact, the second mesh comprising 25,000 brain elements exhibited similar deformation contours as the finest mesh, which again supports our previous conclusion, that a mesh with over 25,000 elements is able to give satisfactory simulation results.

To sum up, for the optimum numerical performance of the current FE model, the core brain model will be meshed with approximately 25,000 tetrahedral elements in Abaqus/Explicit solver, and a mass scaling that facilitates a target time increment of

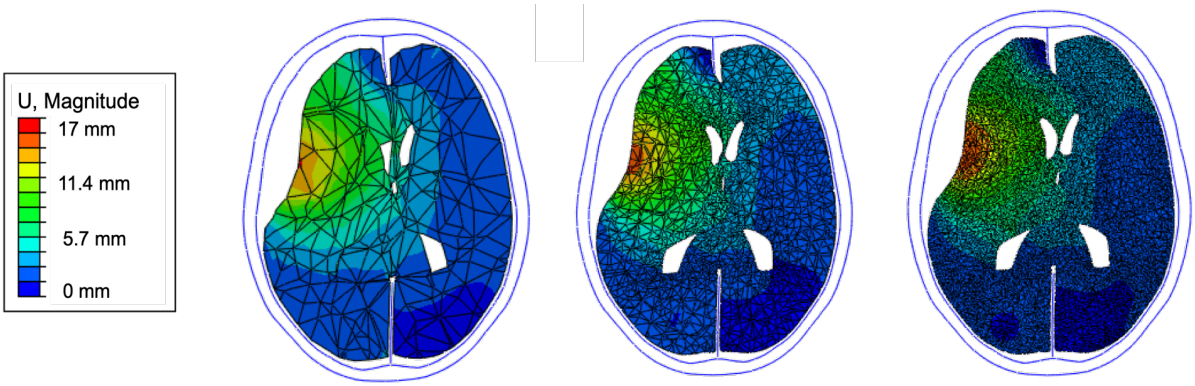

Figure 75: Brain deformation results from meshes of approximately 3,000 (left), 25,000 (middle) and 500,000 (right) elements respectively.

1×10^{-5} s will be added to accelerate the simulation time.

5.3 Simulating traumatic brain injury

At the end of chapter 4, the assessments of the preliminary patient-specific simulation results revealed an over 55% discrepancy between the experimentally derived MLS and the value observed clinically. Specifically, the 7 mm simulated MLS was found to be significantly smaller than the 15.8 mm MLS observed clinically, suggesting a significant underestimate of the deformation inside the brain tissue. Such a serious underestimate was not unreasonable, because the proposed indentation-based lesion simulation only captured the apparent primary injury, which was SDH in this case, but it ignored any secondary pathologies activated by the primary one. In the pure indentation test, the maximum deformation normally occurs on the surface of the material where the indenter is compressing. If the development of the lesion is a simple indentation process, the induced deeper brain deformation will never exceed the maximum depth of indentation. Nevertheless, in the current model setting, the MLS observed clinically was 17.7 % greater than the maximum thickness of the characteristic lesion, which implies a potentially more complex injury mechanism for the evolved lesion. In fact, MLS is in effect a common clinical indicator for the severity of intracranial swelling under various pathological scenarios including stroke, cancer and trauma. Its formation process is not only associated with the growing volume of haematoma alone, but secondary injuries including the swelling that takes place in the axons inside the brain also play a critical role. Clinically, it is not uncommon in the CT scans of TBI patients that clinical MLS is greater than the maximum thickness of the haematoma. The study by Bartels *et al.* [115] even proposed a way to predict mortality by comparing thickness of acute SDH with MLS. This section of the thesis intends to use thermal expansion to simulate brain swelling, so as to explicitly study brain deformation as a result of secondary swelling.

5.3.1 Methods

Following the assessment of the model numerical accuracy, this section considers appropriate loading conditions for simulating the target traumatic brain pathology. Fundamentally, traumatic brain damage is classified into primary and secondary injury, as introduced in the clinical review in section 1.2.1. Primary injury refers to the immediate brain damage at the initial trauma, while the secondary injury introduces a series of pathophysiological cascades that leads to disordered brain functions and further damage.

Among various secondary complications, the ischemic damage is found the most common and important, because the swelling brain raises intracranial pressure and triggers the hypoxic-ischemia vicious cycle that further deteriorates brain oedema. In section 4.3.2, the indentation-based boundary condition replicated the observed primary injury pattern, but failed to address the essential secondary injuries in a TBI patient. This section considers the simulation of the frequently occurring swelling in secondary injury using a thermal expansion-based method.

Feasibility of simulating swelling using thermal expansion

Given the popular occurrence of brain swelling in TBI settings, it is important to find a viable way to simulate the secondary swelling process in our computer models in addition to the primary injury loadings. In this section, a thermal expansion based method has been proposed. Essentially, brain swelling is characterised with bulging brains due to the accumulation of fluid inside the brain tissue. Hence a natural way to model this process is to apply a boundary condition such as thermal expansion that effectively inflates the brain. In the past, brain swelling has been modelled with thermal expansion in the simulations of decompressive craniectomy [61, 62]. Their neurosurgical model used thermal expansion as the driving force to bulge the brain and create intracranial hypertension to study the mechanical response of the brain during the invasive surgical process. Similarly in the current study, it is proposed that thermal expansion can be applied to simulate the process of brain swelling and intracranial hypertension that happens in the development of secondary TBI injuries. This section intends to explore the feasibility of the proposed method.

To be more specific, a prescribed amount of thermal expansion was applied to certain parts of the patient-specific brain model under healthy conditions. As the selected brain tissue grows in volume, the resultant deformation field including the MLS can be analysed to test the feasibility of using thermal expansion to create increasing intracranial pressure and simulate brain swelling. To further understand how different types of brain swelling affect the brain deformation, thermal expansion is applied either universally across the whole brain or unilaterally in a single hemisphere. Hypothetically, unilateral thermal expansion in a single hemisphere creates pressure difference and hence MLS across the two hemispheres, while the uniform swelling across the whole brain, though raising the overall intracranial pressure, may not lead to any pressure difference. The detailed simulation results are discussed in section 5.3.2.

Simulating the complete TBI process

By superimposing the proposed thermal expansion-based swelling method with the indentation-based lesion evolution method, it is now possible to simulate the complete process of primary and secondary TBI injuries. As introduced in section 4.3.2, the replication of primary injury was made patient-specific. However, unlike haematoma and contusions that normally feature in hyperdensity in CT imaging, it is challenging to accurately distinguish brain oedema from healthy brain tissues. Clinically, the vasogenic oedema is relatively observable because it surrounds the underlying primary injury with hypodensity in CT imaging. However, other types of oedema including the diffuse cytotoxic oedema in subcortical regions, are more difficult to determine from CT images. As a result, the lack of accurate segmentation methods for detailed swelling patterns makes it not possible to replicate the exact geometry to simulate swelling on a patient-specific basis. Instead, thermal expansion was applied to the ipsilateral hemisphere, counter lateral hemisphere and whole brain to explore the brain response under unilateral swelling and universal swelling scenarios in the current study. In this way, the proposed TBI simulation method not only replicates the primary injury on an individual basis, but also it provides a way to address the underlying secondary swelling process that happens after TBI.

5.3.2 Results

Feasibility of simulating swelling using thermal expansion

There existed two ways that thermal expansion can be exerted on the developed brain model: unilaterally or universally. For unilateral swelling, a prescribed amount of 20% volume expansion will be applied to a single brain hemisphere. As for universal swelling, a 10% volume expansion will be employed across both hemispheres. This corresponds to approximately 114 ml volume increase when the brain is allowed to expand freely. Figure 76 presents the transverse brain deformation perpendicular to the sagittal plane on an axial cross-section of the swelled brain model. In unilateral swelling, it is seen that when swelling occurred only in the left brain hemisphere, as shown in Figure 76a, intracranial pressure in the ipsilateral hemisphere become higher than that of the right hemisphere and severe transverse shifts have been developed. The falx and ventricles deviated from their neutral position and significant MLS was observed. The bulging left hemisphere pushed the brain tissue across the mid-sagittal plane and the right hemisphere

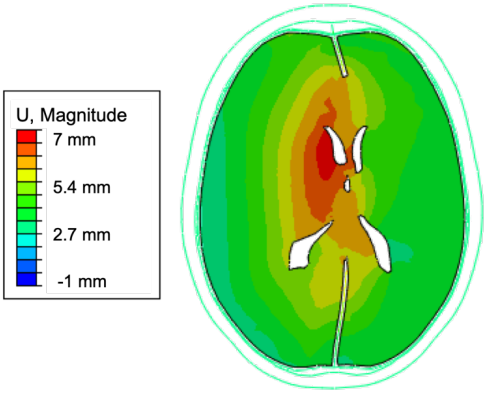

(a) Transverse deformation contour of brain under unilateral swelling.

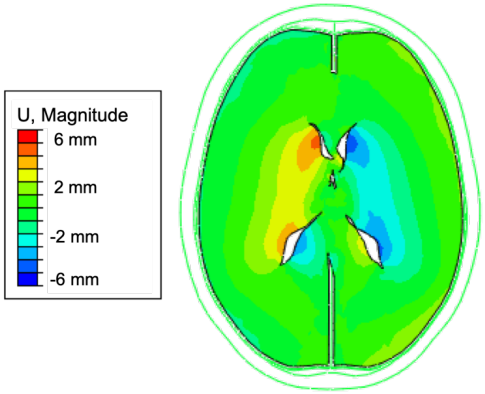

(b) Transverse deformation contour of brain under universal swelling.

Figure 76: Illustration of brain transverse deformation contour under unilateral and universal swelling.

was compressed. The magnitude of deformation was greatest in the left lateral ventricular region. Essentially, this single hemisphere swelling model provided an explanation and modelling approach for some clinical cases where MLS was observed without any sign of haematoma, but pure pressure difference was present across the two hemispheres. The results suggest that it is feasible to simulate brain swelling and MLS development with thermal expansion method.

On the other hand, when the same amount of thermal expansion was applied to both hemispheres, compression in the ventricles was noted but there was no visible MLS. As shown in Figure 76b, the falx stayed at its neutral position while both lateral ventricles were severely squeezed. The resultant transverse shifts were nearly symmetric across the central line: brain tissue surrounding the left lateral ventricle shifts to the right and vice versa. Such a symmetric motion cancelled out any effect at the symmetry line, therefore the septum pellucidum and the falx remained undeformed. As a result, it is concluded that universal swelling, though raised intracranial pressure, will not lead to development of significant MLS. The compression of cisterns and effacement of ventricles become key indicators of intracranial hypertension in this case.

To conclude, thermal expansion is an effective way to simulate brain swelling, but MLS only develops when there is a pressure difference between the two brain hemispheres.

Simulating the complete TBI process

After validating thermal expansion as a viable way to simulate brain swelling, this technique was utilised in our patient-specific lesion evolution model to complete the simulation of traumatic brain pathology. An additional thermal expansion step was defined following the first lesion indentation step to the ipsilateral, contralateral and both brain hemispheres. Figure 77 demonstrates the simulation results for all three types of swelling, with the deformation profile shown on the first row and the relevant deformed and undeformed geometry displayed on the second row. Looking from the left to the right, the three columns correspond to simulated swelling in the ipsilateral, contralateral and both hemispheres respectively. While all six deformed brain contour were characterised with an identical amount of indented (primary) lesion on the surface of the left brain hemisphere, thermal expansion was superimposed to the indented model in different locations.

In the first column in Figure 77a, the brain shifted most towards the right hemisphere, with the shifts concentrated in the brain tissue between the lesion surface and the frontal region of the left lateral ventricle. In the meantime, the corresponding deformed brain

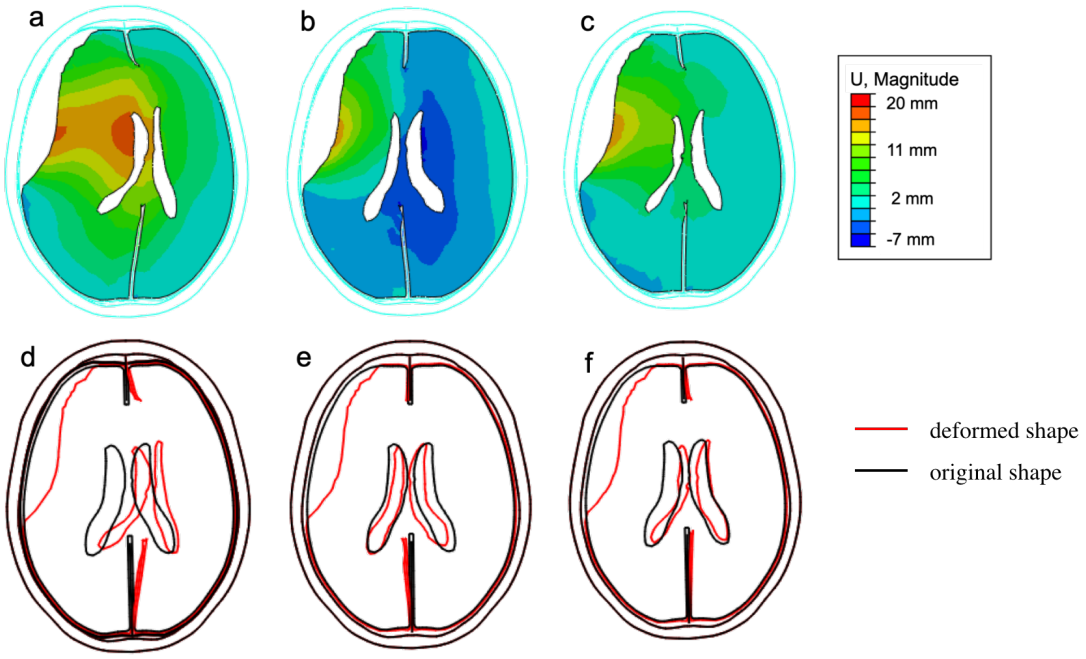

Figure 77: Illustration of simulation results when swelling effect is superimposed on a lesion effect in three different swelling sites. The first row presents the induced transverse brain shifts in an axial slice and the second row plots the deformed geometry (in red) superimposed on the undeformed one (in black). Note the left, middle and right columns correspond to ipsilateral, contralateral and uniform universal swelling respectively.

silhouette plotted in Figure 77d highlights the deviation of the falx and the ventricles from their original positions. An MLS of 18 mm was observed when 30% thermal expansion was applied to the ipsilateral hemisphere. In the second column when the same amount of thermal expansion was applied to the brain hemisphere contralateral to the lesion site, Figure 77b reveals an abnormal deviation towards the lesion. The blue contour surrounding the right lateral ventricular region denotes a negative deformation towards the injured brain hemisphere, which is against the clinical intuition of mass effect. Figure 77e further confirms this finding: the red silhouette of both of the deformed lateral ventricles were compressed, with the falx and the septum pellucidum even shifted slightly towards the lesion site. It was noted that when swelling gradually developed in the contralateral side to the lesion, the growing pressure first pushed the deviated midline structures back to restoration, then as the pressure further escalated, those midline structures even started to swing reversely towards the lesion. Clinically, the observation of MLS towards the lesion site is not common. However, a strength of computer modelling is to provide insights not only on the common clinical cases, but also on those rare cases which might seem unusual and strange to clinicians. Computer simulations from common to rare cases could provide a more complete picture to help the clinicians better understand the underlying mechanism behind first and secondary injuries. In the last column, swelling was exerted uniformly across both hemispheres. In Figure 77c, it was clear that the magnitude of deformation in the contralateral hemisphere was compensated to a greater extent as compared to that of Figure 77b. Meanwhile, there is a noticeable reduction in brain shifts in the severely displaced region in between the indentation surface and the left lateral ventricle. Figure 77f also confirmed this finding: the resultant MLS and falx deviation from universal swelling were a lot smaller than that found in the ipsilateral swelling model.

Furthermore, Figure 78 illustrates the temporal change of experimental MLS for all three complete TBI simulation scenarios. The total simulation time of 2 seconds can be further divided into two stages: pre and post swelling. The first 1 s was pre-swelling stage, where characteristic lesion surface was indented into the left brain hemisphere. And during this indentation period, the three MLS trend line overlapped with each other. It was noted that in the first 0.5 s, no essential experimental MLS was observed in the brain model. There were two reasons behind it: firstly, an initial gap was left between the indentation surface and the brain surface, to make sure that there existed no contacts before the actual indentation; secondly, when the indenter started to press the ipsilateral brain, the brain tissue and the ventricles attempted to change in shape in order to accommodate the incoming lesion volume, this was considered as the compensation functions of the brain. MLS only developed when the compensation effects exhausted, as illustrated in

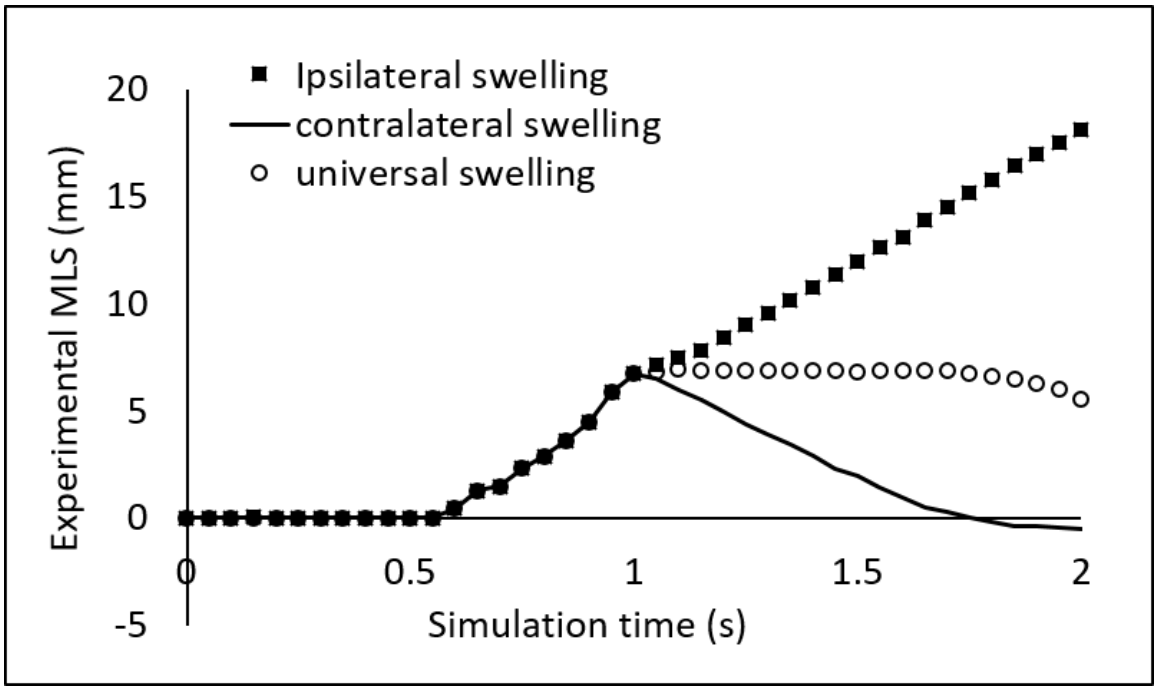

Figure 78: Illustration of the observed MLS throughout computer simulation. Note, the temporal change of experimental MLS was presented for ipsilateral, contralateral and universal swelling conditions. Swelling was applied after 1 s and later, the amount of applied swelling is proportional to the step time.

simulation time between 0.5 and 1 s.

After 1 s, thermal expansion was exerted to different brain compartments to simulate swelling under various conditions. It is shown that if ipsilateral swelling was developed, the experimental MLS grew quickly after 1 s. By contrast, when swelling was exerted in the contralateral hemisphere, the experimental MLS gradually decayed and even approached a negative value at the end of swelling process. In universal swelling, however, the observed MLS remained relatively constant despite the slight decrease at the end of the simulation. In this side-by-side comparison, it was clear that transverse brain shifts were most severe when secondary injuries evolved in the ipsilateral side to the lesion, which coincided well with the common clinical findings. Nevertheless, the latter two swelling scenarios, though being less frequent clinically, were considered as valuable reminders: MLS might not be a universal indicator for intracranial pressure, especially when swelling occurs in the contralateral side of the lesion. To sum up, when approximately equal amounts of swelling were applied to various brain regions post primary trauma, the resultant MLS differs significantly. Therefore, MLS should be jointly considered with other clinical findings such as the compression of ventricles and cisterns, to evaluate the severity of intracranial hypertension.

In conclusion, mass effect is observed to be the most severe when the secondary swelling is applied to the ipsilateral side of the primary lesion, which is intuitive for majority of the TBI cases. Whereas when swelling takes place at the contralateral hemisphere to the primary lesion, brain deformation markers like the MLS become less significant.

Temporal change of MLS during simulation

In the current loading condition, it was worth noting that indentation and thermal expansion were performed separately during computer modelling, though it was possible to trigger the two process simultaneously. There were two reasons behind this modelling approach. On the one hand, swelling usually took place after the attack of lesion. It was the natural sequence that the secondary injuries gradually developed following the primary trauma. On the other hand, by gradually inflating the brain hemispheres at the end of lesion indentation, it was possible to control the expansion volume and analyse the brain response at different levels of swelling amount. This section aims to analyse the temporal change of simulated MLS in order to find the optimum combination of primary and secondary injury that best describes the TBI case.

Recall from chapter 4 that by simulating primary lesion evolution alone, the induced simulated MLS was 55% smaller than the actual clinical value. Such significant discrepancy can be resolved by incorporating the secondary injury in addition to the primary one. Theoretically, the developed FE head model was capable of acquiring any given value of MLS by adjusting the amount of thermal expansion (representing the secondary injury). For the current model, a simulated MLS equal to the clinical finding (15.8 mm) is achieved at 1.83 s in the ipsilateral swelling scenario in Figure 78. Since the

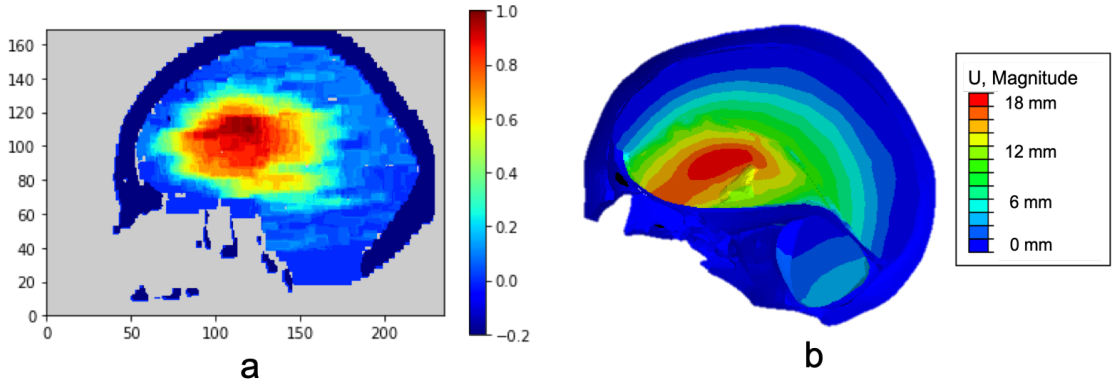

Figure 79: Comparison of clinical MPS (a) and experimental MPS (b). Note, scale bar in (a) is normalised according to the definition of clinical MPS.

assigned brain material is time-independent, the unit of time is in fact not important by itself. Given that swelling is applied uniformly, a swelling time of 0.83 s corresponds to approximately 24.9% volumetric expansion (141 ml) in the ipsilateral hemisphere. In other words, the complete TBI process can be described as the combination of its customised primary injury together with a 141 ml swelling in the ipsilateral brain hemisphere.

Ultimately, by adding further swelling to the injured brain, a realistic magnitude of MLS was successfully replicated in the FE model developed in chapter 4.3.2. Now that the simulation model passed the quantitative assessment of deformation magnitude, to further assess the computer model qualitatively, the experimental MPS contour was compared with the clinical MPS heat map as shown in Figure 79. It is seen that the simulated and clinical MPS appeared very similar in pattern. Up to now, it is proved that the proposed thermal expansion method, together with the indentation based method, is capable of replicating any SDH and EDH types of brain trauma observed clinically in CT scans to an appropriate level of accuracy in the developed computer model.

Importance of primary injury

Having found that swelling was potentially a powerful way to shift brain tissues, with or without the primary lesion pushing the brain, it remains to be considered how the primary lesion pattern affects the resultant brain motion. To answer this question, Figure 80 presents the transverse deformation contour for the same axial slice from the model with pure swelling on the right and the one with swelling and haematoma on the left, using

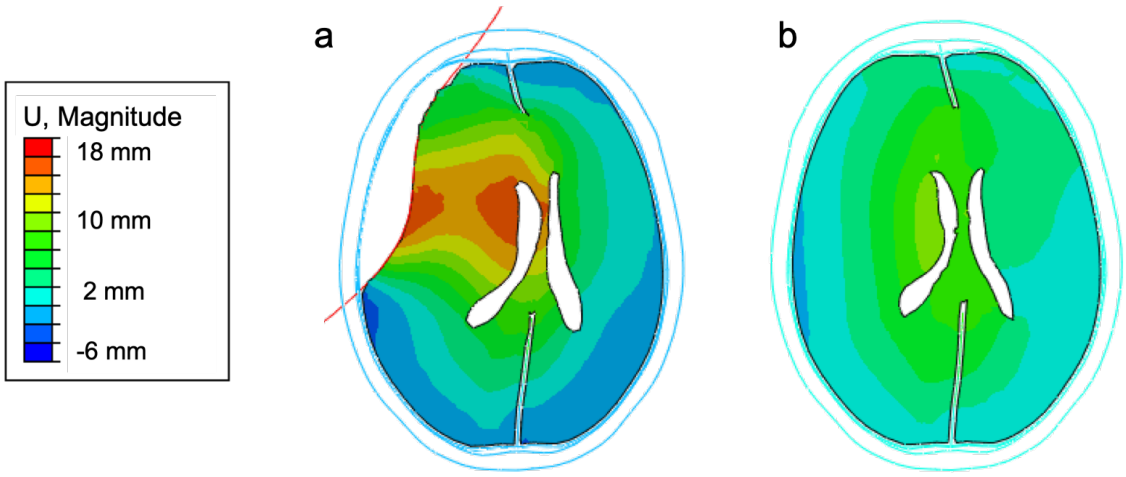

Figure 80: Comparison of brain deformation contour under indentation plus thermal expansion (a) and pure thermal expansion (b)

the same scale bar. The figure shows that the existence of primary injury (SDH in this case) not only increased the magnitude of induced brain motion, but more importantly, the resultant brain deformation pattern also changed drastically. Instead of affecting the whole ipsilateral hemisphere almost uniformly when pure swelling was developed in the left hemisphere, the deformation tended to concentrate on the frontal region between the lesion site and the ipsilateral lateral ventricle as a result of the developed primary injury. Therefore, although swelling was applied uniformly across the selected hemisphere, the accurate description of the patient-specific primary injury geometry also played an important role in shaping the brain deformation pattern towards a more realistic representation.

To conclude, the proposed combination of mechanical loading and thermal expansion effectively simulated the primary and secondary injury that attacks after TBI. The indentation based method in section 4.3.2 replicates well the patient-specific feature of the primary injury and the adjustable levels of thermal expansion based swelling in section 5.3.2 helps shape the final deformation magnitude of the brain. This proposed method forms the basis of our patient-specific TBI loading condition in the computer model. In the next chapter, patient-specific primary injury will be created for various TBI cases, and the corresponding swelling factor will also be applied to shape the final brain deformation contour to the most realistic level.

5.4 Brain material property

5.4.1 Methods

The inclusion of the secondary swelling in the model loading conditions has resolved the discrepancy in deformation between the experimental model and the clinical observations. Nevertheless, it is important to consider other relevant model parameters affecting the deformation behaviour. Material property is one of the most fundamental features of a computer model of deformation. With other conditions being equal, the experimental simulation only gives reasonable outcomes when a correct set of materials are assigned. The current section considers the model performance with various material models, in the absence of the thermal expansion step.

Brain tissue compressibility

The brain, being the centre of the human nervous system, is the most complex organ in the body. In section 1.3.2, a variety of material models ranging from linear elasticity to poroviscoelasticity has been reviewed, but so far, a one-size-fits-all constitutive law that describes the ultra-soft nature of the brain tissue is still lacking. Considering that the patient-specific primary injury simulation is a deformation-controlled indentation process, the maximum brain deformation on the surface of the brain will be the maximum depth of indentation, regardless of the brain stiffness. However, even if the ultimate surface deformation is identical at the end of indentation, the choice of different material properties will define how the applied indentation penetrates into the middle of the brain and hence affect the detailed displacement pattern in the deeper brain tissue. Compressibility is the material property that describes the material behaviour under compression. Therefore it is important to assess the model sensitivity to the brain tissue compressibility.

In order to study the effect of material compressibility on simulation outcome, linear elastic material with a range of Poisson's ratio was utilised. Poisson's ratio, v, is a parameter that describes the strain in a material in the direction perpendicular to the loading condition. Figure 12 in section 1.3.2 shows a wide range of Poisson's ratios and Young's modulus for brain tissue reported by various researchers. Since the deformation-activated indentation model deforms a material to the designated shape regardless of its stiffness, such models are relatively insensitive to model stiffness due to the nature of the deformation method. As a result, a reasonable Young's modulus of $E = 10{,}000$ Pa was used in the current study. Using this value of modulus, values of Poisson's ratios in the range of 0.45 to 0.49 were used. To allow for realistic comparison with the CT findings, the experimental MLS is considered as the assessment criterion to aid the evaluation of model outcomes.

Advanced brain material models

A proper mathematical material model comprises two main aspects: an accurate set of material properties, as well as an appropriate constitutive law. This section aims to assess more advanced material models for the brain. In the review section 1.3.2, table 2 summarises the definition of five most commonly used material models. The range of material properties, together with the variety of material models, makes the available property combination excessive. Fortunately, the systematic review by Goriely

et al. [45] summarised the biomechanics of brain into three categories with respect to the underlying time scales. Although a universal material model is lacking, it is often possible to find a set of material parameters that best describes the brain tissue behaviour under a specific loading condition. In the current study, the developed patient-specific FE model is designed to investigate the brain behaviour under the gradual development of lesion post TBI, the process of which occurs on the order of minutes or hours. Thus a pure hyperelastic model is suggested by [45]. A pure hyperelastic model ignores the time-dependent components such as relaxation that could occur during deformation and concentrates only on the maximum deformation and strain pattern as a result of any applied loading.

Table 8 lists the range of hyperelastic models considered, with appropriate values taken from the literature for neo-Hookean, Mooney-Rivlin and Ogden models. The sensitivity of results to the choice of these more advanced material models will be investigated in this chapter.

Stiffness of the Falx

Apart from brain tissue elasticity, the material models for other brain features are also critical in simulating brain biomechanical behaviour. The falx, being the extended layer from the dura mater, plays an important role in regulating shifts of the brain across the mid-sagittal plane under deformation, as observed in section 3.3.2. The cerebral falx is known to be much stiffer than the grey and white matter, which are generally reported to have a stiffness in the order of 0.1 MPa. However, the specific properties of the falx

Hyperelastic model	Material properties	Reference
Neo-Hookean	$C_{10} = 333.28$ Pa	[124]
Mooney-Rivlin	$C_{10} = 0.28$ Pa, $C_{20} = 333$ Pa	[124]
Ogden ($1^{st} order$)	$\mu_1 = 121$ Pa, $\alpha_1 = -18.7$	[125]
Ogden ($2^{nd} order$)	$\mu_1 = 71.33$ Pa,$\alpha_1 = 11.61, \mu_2 = 826.35$ Pa, $\alpha_2 = -6.07$	[126]

Table 8: Table of hyperelastic models

that best describes its behaviour in pathological brain deformation are not known. In this chapter, a series of simulations with varying falx stiffness ranging from 0.1 MPa to 100 MPa were performed to find the falx stiffness that led to the optimum MPS contour as compared to clinical observations.

5.4.2 Results

In this section, various material models were applied to the developed high-fidelity FE model under the same loading condition and numerical methods. The ultimate goal of this section was firstly to test the model sensitivity to different material properties, and more importantly, to find a proper set of material parameter that yielded the most realistic experimental results as compared to the clinical reference.

Brain tissue compressibility

The first material parameter being investigated was the solid compressibility of the brain tissue. By adjusting the values of Poisson's ratio, the resultant experimental MLS changed as a result of varying compressibility, as shown in Figure 81. It was observed that the magnitude of simulated MLS increased from 6.2 to 7.0 mm as the Poisson's ratio changed from 0.45 to 0.49. Such a 13% increase in the simulated MLS with growing Poisson's ratio implied a greater deformation in the inner brain tissue when the assigned material becomes more incompressible. If greater inner brain motion is considered closer to reality, a material model with higher incompressibility should be applied. Nevertheless, as compared to the clinical MLS of 15.8 mm, the increase caused by changing compressibility was clearly insufficient. Therefore it is concluded that reasonable changes of Poisson's ratio, though affecting the resultant deformation somewhat, do not make a significant change on the model behaviour during the displacement-based simulation.

If greater inner brain motion is considered closer to reality, a higher incompressibility should be applied to describe brain tissue. This finding was also in line with the general consensus that brain material was almost incompressible. However, it was worth noting that although some recent brain material models suggested incompressible behaviour for brain tissues ($v = 0.5$), a completely incompressible model was not viable in Abaqus/Explicit analysis. The reason behind it is the lack of mechanisms to impose such a constraint at each material calculation point in the program, according to the Abaqus User Notes [120]. Consequently, at least some level of compressibility was required for

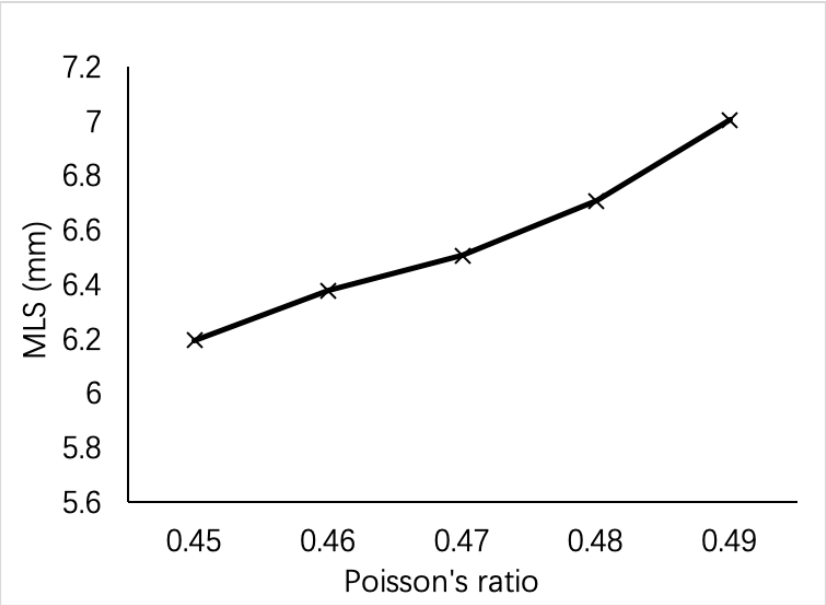

Figure 81: Plots of simulated MLS at different compressibility.

the code to work properly. A quasi-incompressible compressibility at the equivalent level of $v = 0.495$ was applied instead.

Advanced brain material models

To investigate the model response to different hyperelastic materials, an additional series of simulations were performed. The tested material properties, together with the obtained experimental MLS results, were presented in table 9. When comparing the cross-sectional

Hyperelastic model	Simulated MLS (mm)
Neo-Hookean	7.0
Mooney-Rivlin	6.94
Ogden ($1^{st} order$)	7.03
Ogden ($2^{nd} order$)	6.79

Table 9: Table of hyperelastic models and the corresponding simulation results. Note, the table compares derived experimental MLS results against the corresponding hyperelastic material properties.

deformation contour for those models, no noticeable difference in deformation pattern was found. And even when comparing the specific experimental MLS derived from those simulations, no more than 5% difference was found between those hyperelastic models. One reason behind this finding is unique loading conditions of the model: the material is loaded with a deformation-controlled approach. Consequently, though the simulated stress contour differs as a result of the changing material model, the induced deformation remains relatively consistent.

Thus it is concluded that for the current displacement-loaded indentation process, the choice of hyperelastic materials does not make a significant impact in model outputs. Furthermore, no obvious advantages are observed for hyperelastic materials as compared to linear elastic models, at least for the indentation-based loading condition like the current one. Therefore for future simulations, a linear elastic model with $E = 10{,}000$ Pa and $v = 0.495$ will be used for its satisfactory performance and simplicity in material model.

Stiffness of the Falx

As well as finding the proper material property for the brain tissue, it is equally important to look for the appropriate stiffness for the cerebral falx. From the literature, a Young's

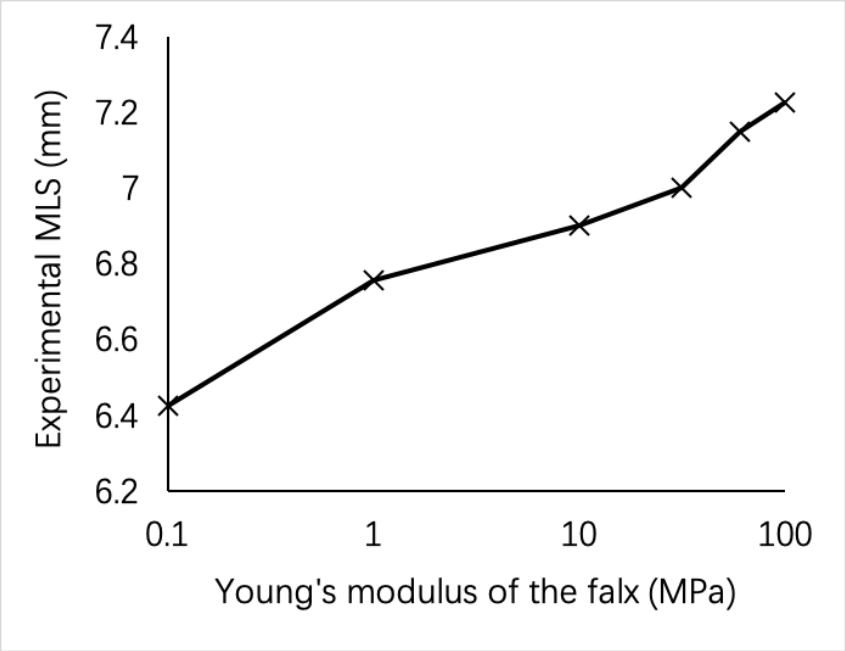

Figure 82: Simulated MLS plotted against falx stiffness in logarithmic scale.

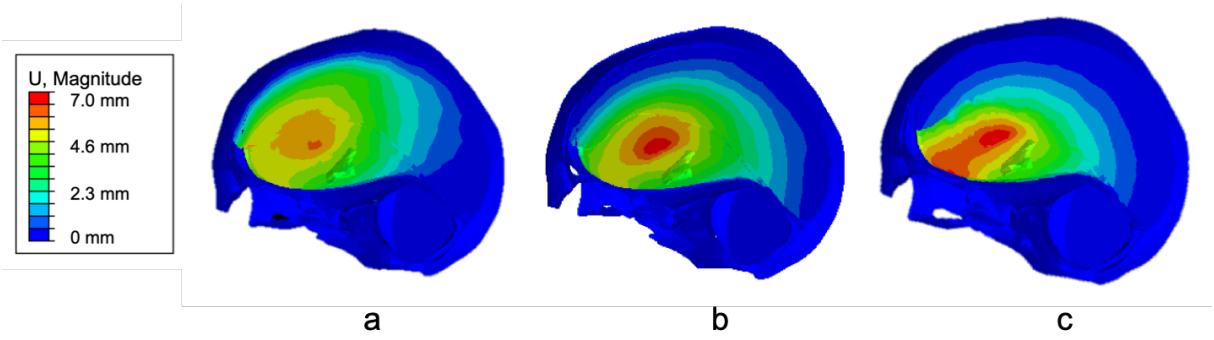

Figure 83: Computational MPS results from models with falx stiffness of (a) 0.1 MPa, (b) 31.5 MPa and (c) 100 MPa respectively.

modulus of 31.5 MPa has been reported to describe the falx mechanical behaviour in previous FE models [127]. The current analysis calculated the brain deformation condition when falx stiffness ranged from 0.1 MPa to 100 MPa to test the appropriateness of such a falx stiffness. In this series of simulation, the brain has been assigned with linear elastic material properties while the falx stiffness changed from very soft to strong. As shown in Figure 82, it is observed that the stiffer the falx, the greater the observed experimental MLS in the simulation outcome. One potential explanation behind this phenomenon is that the deformation of the brain tissue is forced to the regions away from the falx as a result of increasing falx stiffness. The brain deformation profiles in Figure 83 confirm this hypothesis. In the first MPS profile in Figure 83, the falx was assigned with the softest material. It is seen that while the maximum shift was smaller in the MPS contour, the area of deformed region was more widely spread over the entire brain silhouette. As the falx stiffness increased in the second and third MPS profile in Figure 83, the maximum deformation region became more concentrated in the ventricular region. The model with 100 MPa falx stiffness yielded the greater experimental MLS, but the one with 31.5 MPa stiffness generated the MPS contour most similar to the clinically derived one shown in Figure 73a. As a result,it is concluded that Young's modulus of 31.5 MPa is an appropriate stiffness to describe the behaviour of the falx in the subsequent TBI related simulations.

5.5 Simulating behaviour of ventricles

5.5.1 Methods

The ventricles are unique compartments of the brain that are prone to change in shape in pathological settings. As introduced in the clinical review in section 1.2.1, the ventricles of

the brain are cavities within the brain parenchyma, filled with cerebral spinal fluid (CSF). The CSF, as a clear body fluid, is effectively incompressible in nature. Nevertheless, the constant production and reabsorption of CSF means that the amount of fluid within the ventricles is at dynamic equilibrium in healthy individuals. Therefore when the auto-regulation of the brain is disturbed pathologically, the ventricles can move from their original position while changing shape via the circulation of CSF. Clinically, ventricle effacement and MLS are both important indicators of intracranial hypertension followed by TBI.

It is believed that the compression and deformation of ventricles play a critical role during lesion evolution and it is important to simulate them correctly. Historically, the intraventricular CSF in FE head models has been modelled with soft elastic solids [128–130]. In these models, the simulated ventricle response was significantly affected by both the mesh density and the constitutive laws, similar to other solid brain compartments. However, the discretisation of CSF inside the ventricles required high mesh resolution because of the complex ventricle geometries. The contacts between the ventricle surface and the nearby brain parenchyma also imposed convergence problems during simulation. Moreover, one of the main limitation of modelling fluid structure as finite solids is that there exists shear stresses in the elements that are not realistic in actual fluids. To resolve this problem, researchers attempted to use Smoothed Particle Hydrodynamics (SPH) technique to simulate the fluid-like behaviour of CSF layer in interstitial space between skull and the brain [131], but these early attempts failed because of interaction problems between the finite solids of the brain and the smoothed particles of CSF. It remains an open question how to accurately simulate the behaviour CSF.

It is worth noting that in 2014, Baillargeon *et al.* [132] employed the surface-based fluid cavity in Abaqus to simulate the blood flow model for the heart ventricles in their living heart project. The definition of fluid cavity in Abaqus requires only a surface enclosing the cavity and a corresponding reference node, therefore no specific mesh elements are needed for the liquid or gas encapsulated within the cavity. In addition, the fluid cavity function allows for convenient evaluation of cavity volume and pressure. Although this method was applied for heart ventricles, it is considered that a similar approach is viable and intuitive for brain ventricles.

Effective ventricle compressibility

Inspired by the heart project, the brain ventricles in the current FE model were also simulated with surface-based fluid cavities. With the capability of the fluid cavity, the challenge in discretising fluids with realistic finite elements is avoided. Mesh elements were only present in the surface of the cavity, while inside the cavity fluid is present with uniform properties and states as assigned. In this way, the behaviour of the ventricles can be actively adjusted by changing the fluid properties within the cavity and the deformable feature of the ventricles can be addressed by adding a compressibility parameter to the ventricles. Specifically, it is known that ventricles can change in volume during brain lesion evolution, and it is proposed that such a volumetric change could be modelled by adjusting the compressibility of the ventricles. The compressible feature of the cavity can be addressed by the bulk modulus B of the fluids. Bulk modulus is defined in the following equation:

$$B = -\frac{\triangle P}{\triangle V} \times V \tag{9}$$

where B is bulk modulus, $\triangle P$ is the change in pressure, $\triangle V$ is the change in volume and V is the original volume. Thus the higher the bulk modulus, the more difficult for the material to deform. By changing the bulk modulus of the fluid filling the ventricles, various levels of the ventricular volume reduction during TBI lesion development can be simulated experimentally.

Relative volume change of brain and ventricles

Adjusting the volume change of the ventricles has the potential to further our understanding on the interplay between the lesion, the brain and the ventricles. In this chapter, the assessment of the model not only aims to validate the model, but also, it is intended to find out about how those model parameters affects the deformation behaviour of the brain. In this case, as the ventricles reduce in volume, it is likely to affect the brain deformation pattern as well. To help investigate how the deformable ventricles impact the brain deformation behaviour, ventricle models with a range of bulk modulus are considered in this chapter.

5.5.2 Results

In this section, a surface-based fluid cavity was used to simulate the behaviour of intraventricular CSF within the brain parenchyma. Since ventricles are unique compartments of the brain which are prone to change in shape, it is important to model the ventricle behaviour appropriately to better describe the brain behaviour. To address the deformable feature of the ventricles, the fluid within the cavity was assigned with properties that represented the compressibility of the encapsulated cavity space. It is noted that so far, one significant limitation of the developed head model was that the model lacked a proper description of the ventricular behaviour during simulation. Namely, although the geometries of the ventricles were subtracted from the cerebrum, the resultant ventricular spaces were not defined with any materials, leaving them as purely empty cavities. The proposed fluid cavity method allows for controls over ventricle volume reduction without raising convergence problems, hence it is an ideal tool to address the deformation of ventricles while studying the brain behaviour under lesion evolution.

Effective ventricle compressibility

The effective compressibility of the fluid cavity is dominated by the bulk modulus. Bulk modulus controls the ventricles' resistance to deformation under compression and it is essential to assign an appropriate level of bulk modulus that generates the most realistic ventricular response. The brain tissue is characterised with a bulk modulus between 1×10^2 MPa and 1×10^3 MPa, and is nearly incompressible. Therefore for a ventricular bulk modulus 1×10^3 MPa, it is assumed that the ventricle will not reduce in size. Meanwhile, when the bulk modulus becomes extremely small as 1×10^{-6} MPa, the ventricles can be considered ultra-soft and easy to deform under compression. In this section, the model response was explored for bulk modulus ranging from 2.5×10^{-6} to 2.5×10^2 MPa.

The maximum deformation magnitude on the surface of the third ventricle is used to assess the inner brain tissue deformation instead of the simulated MLS. The reason behind this was that the experimental MLS was taken at the septum pellucidum in between the two lateral ventricles; and so there was a concern that the compressible effects on the two lateral ventricles might lead to a compensated magnitude of deformation there. The third ventricle, being an isolated landmark located on the ideal mid-sagittal plane originally, was therefore a better landmark for overall brain deformation evaluation when studying the effective compressibility of the ventricles. Figure 84 presents the maximum third

ventricle deformation as the CSF bulk modulus increased by orders of magnitudes.

In Figure 84, convergence of brain response has been observed at the extreme values of bulk modulus on the two ends of the x-axis. In general, it is noted that the shifts of third ventricle surface U_{max} became less significant with increasing bulk modulus. In other words, the more compressible the ventricles, the greater the deviation in the deeper brain tissue, given the same loading conditions. However, when the applied ventricular bulk modulus is > 0.25 MPa, the maximum 3rd ventricle deformation levelled off towards a minimum value, implying that the ventricles were almost incompressible at such level and further increase in bulk modulus will not make any difference in the brain response. On the left end of the x-axis of Figure 84, the assigned bulk modulus is extremely small, simulating ultra soft fluid cavity for the ventricles, the measured third ventricle displacements approached a maximum value. Since the ventricle deformation converged at both end of the extremes of bulk modulus, a bulk modulus ranged from 0.0025 MPa to 0.25 MPa should be capable of describing the ventricle behaviour from ultra-soft to fully incompressible. Figure 85b presents the relative volume change of all three ventricles at different levels of ventricular bulk modulus. It is observed that there is almost no volume change in all three ventricles when ventricle bulk modulus was 0.2 MPa. As the ventricular bulk modulus becomes smaller, the ventricles reduce more in volume and the maximum volumetric reduction occurs at the bulk modulus of 0.0025 MPa.

In this section, it is confirmed that it is feasible to model the deformable ventricles with the fluid filled cavity method. Before the adoption of the proposed ventricular simulation method, the ventricle property was left undefined in the developed brain model. The proposed ventricular simulation method filled up the gap of absent ventricular properties

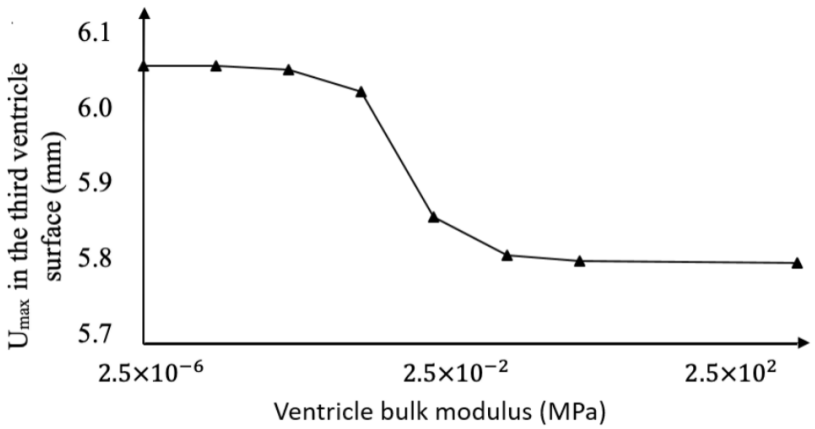

Figure 84: Maximum deformation U_{max} on the surface of the third ventricle plotted against ventricular bulk modulus.

without any convergence issues, hence completed the head model definition. In the next paragraph, the brain response to various changes of ventricle effective compressibility will be further analysed.

Relative volume change of brain and ventricles

This section aims to study the interplay between the lesion swelling, ventricle volume change and brain deformation behaviour, as an attempt to further the understanding of TBI related brain deformation mechanism.

In addition to the ventricle volume reduction, Figure 85 presents the reduction of brain volumes at various levels of effective ventricle compressibility. Combining the findings for Figure 85 a and b, it can be seen that, as the simulated ventricles become more incompressible, there is less volume reduction in ventricles but greater volume reduction in the brain. This was a reasonable observation. According to the Monro Kellie doctrine, the volume inside the cranium is constant. And when the same rigid-lesion surface was pushed mechanically into the brain, an equal amount of hypothetical lesion was developed within the skull and the brain and the ventricles reduced in volume to accommodate the growing lesion. Initially, when the ventricles were defined with small bulk modulus, they were free to deform and reduce in size to make space for the lesion. While as the ventricles became more and more incompressible, the ventricles started to resist the applied pressure and thus the volume reduction was directed to the brain tissue.

Distribution of brain deformation with different ventricular behaviour

The existence of ventricles has a critical impact on the redistribution of brain deformation in pathological cases. In 2002, the study by Ivarsson *et al.* [133] suggested that the CSF within the lateral ventricles relieves the strain in regions inferior and superior to the ventricles during sagittal plane head rotation. While in the current study, although the primary scope was to investigate brain behaviour under longer time-scales such as lesion evolution and neurosurgery, it was reasonable to assume that ventricles played an equally critical role during brain deformation. Therefore it is critical to investigate the induced brain tissue motion as a result of varying ventricle effective compressibility, in addition to the known volume reduction changes in both the ventricles and the brain. Figure 86 presents the cross-plane brain deformation contour at different levels of ventricle effective compressibility. It is seen that when the effective bulk modulus is small in

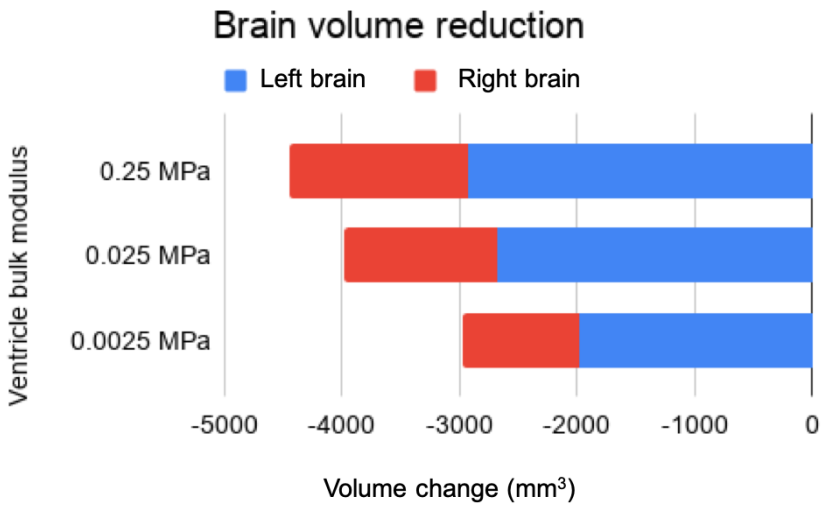

(a) Illustration of brain volume reduction at different ventricle bulk modulus.

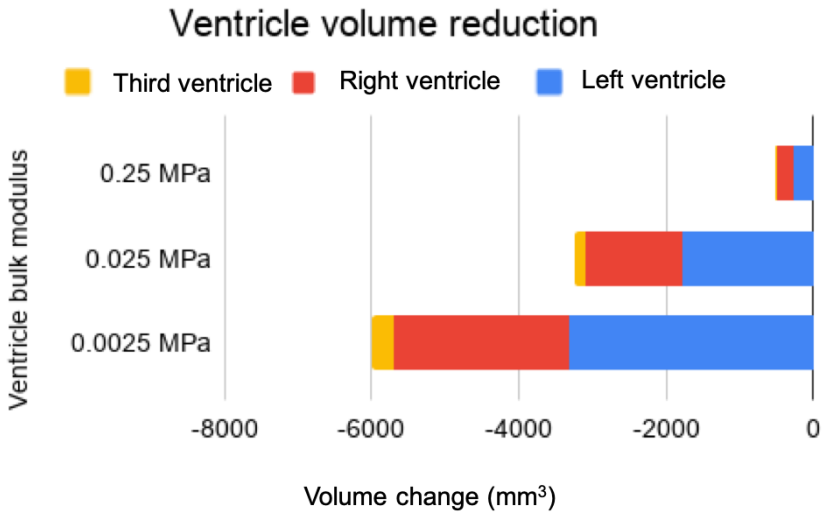

(b) Illustration of ventricle volume reduction at different ventricle bulk modulus.

Figure 85: Illustration of model volume change for different effective compressibility of the ventricles.

Figure 86a, the two lateral ventricles are effaced to a large extent and the shifts of the brain tissue surrounding the left lateral ventricle is the most severe among the three cases. In Figure 86b and c, the ventricle volume reduction is reduced as a result of the increasing effective bulk modulus. No apparent ventricle effacement is observed, however, it is still seen that the two lateral ventricles in 86b is more compressed than that in 86c, because of the relatively smaller bulk modulus.

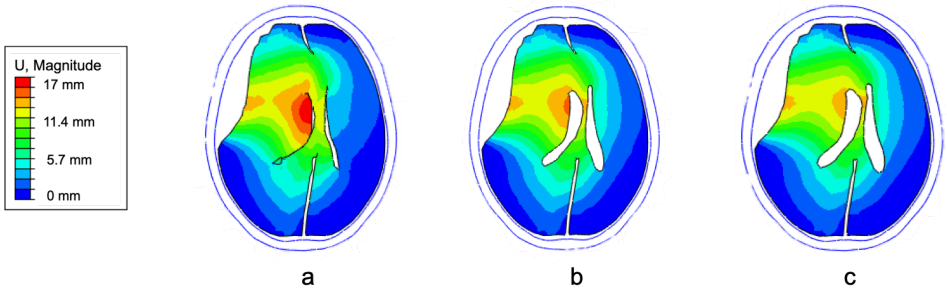

Figure 86: Illustration of brain deformation contour at different levels of ventricle bulk modulus (a) 0.0025 MPa (b) 0.025 MPa (c) 0.25 MPa.

To further evaluate brain shifts in the deeper brain tissue in a quantitative way, the two lateral ventricles and the third ventricle were considered as ideal landmarks. In the current FE model, for the ease of model discretisation, the left, right and third ventricles were modelled separately, each assigned as an independent fluid cavity. Consequently, the three ventricular surfaces could be three natural landmarks to help assessing relative brain shifts. Figure 87 presents the maximum transverse displacement in the direction perpendicular to the mid-sagittal plane that happened on the surface of each ventricle, with respect to different ventricle bulk modulus. Firstly, it was clear that the maximum displacements on the surface of left ventricle was always the greatest, followed by the right ventricle, and lastly the third one. This was because the simulated lesion was applied to the left side, thus the left ventricle and the left brain hemisphere were co-lateral to the lesion and were compressed more in volume as compared to that of the counter-lateral side, as illustrated in Figure 85 and Figure 86. More volume reduction usually implied greater surface distortions and shifts, therefore max U1 on the left ventricle surface was always greater than that on the right ventricle surface.

Interestingly, the maximum displacements measured in the three ventricles demonstrated different trends with increasing ventricular bulk modulus. Looking from right to left in Figure 87, it is shown that the maximum shift on the surface of the left and third ventricle increased as the CSF filling the cavities became more compressible. In the meantime, the maximum shift on the right ventricle surface decreased. As a result, we can conclude that the induced deeper brain tissue shifts are not simply proportional to the increasing ventricle compressibility, at least not for some region inside the brain. In the inner brain tissue, it is likely that the complex geometry and unique compressibility of ventricles interferes with the universal brain deformations and leads to variance in shifts for brain

tissue nearby those ventricular cavities. In fact, when the ventricles become more resistant to reductions in volume (with increasing bulk modulus), the indented surface deformation penetrates deeper to the contralateral hemisphere of the brain.

To conclude, this section not only proved the feasibility of using a surface-based fluid cavity to simulate the ventricles in the brain model, but also it helped us understand the interaction between the ventricular space, the haematoma development, the secondary swelling and the brain deformation behaviour. Although at the current stage, it is difficult to precisely customise the deformable behaviour of the ventricles on an individual basis, due to the lack of quantitative estimation techniques available, the attempted investigations are considered worthwhile. In the next chapters, to keep the computer head model consistent and functional, a moderately compressible ventricle with bulk modulus of 0.025 MPa was used throughout the study.

5.6 Concluding discussion

This chapter provided an all-round assessment of the developed patient-specific FE model. The aim of the current chapter was to explore the series of parameters that could potentially optimise the simulation results.

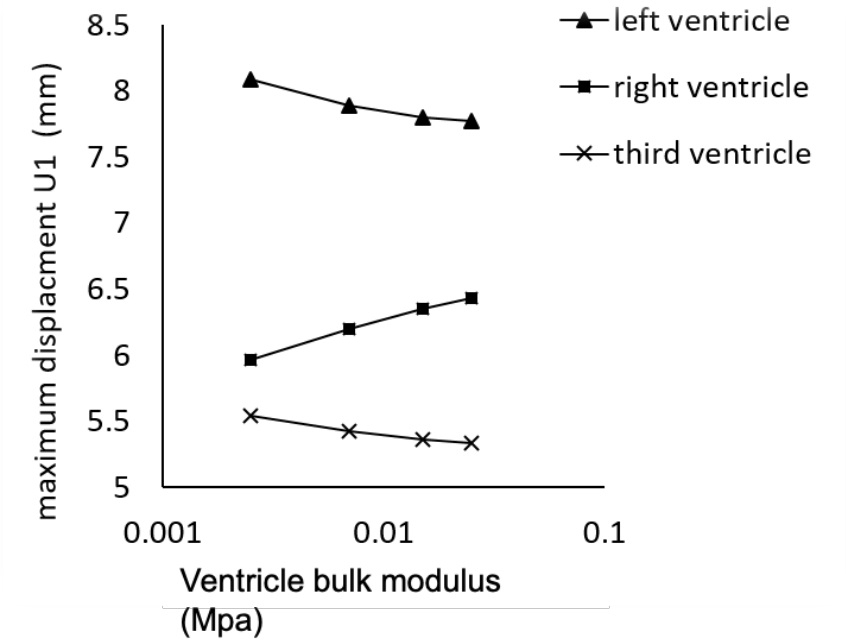

Figure 87: Illustration of maximum displacement U1 on the surface of the three ventricles plotted against ventricle bulk modulus.

The first aspect of the assessment was evaluating the numerical accuracy of the FE model. Among the range of numerical parameters, the mesh size was explicitly studied in a refinement test, due to its significance in finite element computation algorithms. The mesh refinement study suggested a total number of elements of around 25,000 in the cerebrum model.

To address the secondary swelling associated with TBI, thermal expansion was applied to different compartments of the brain to explore the feasibility of simulating the secondary swelling in TBI. Then by superimposing thermal expansion to the indented model, a complete TBI simulation method which comprises both primary and secondary injury has been created. In this way, a lesion simulation method was successfully established to reproduce the observed TBI pattern from CT scans. The resultant brain simulation outcomes are proved to be both qualitatively and quantitatively correct with the clinical reference.

In addition, the model sensitivity to material properties has been assessed. By exploring the brain motion under various levels of brain tissue compressibility, a linear elastic model was first applied. The result suggested that the brain deformation behaviour is not very sensitive to the changing brain tissue compressibility. In addition to a linear elastic model, a range of different hyperelastic models were also explored. However, no significant improvement was observed with the hyperelastic models as compared with the linear elastic model in terms of the overall brain deformation pattern. It is noted that such an insensitivity to material properties is potentially a result of the displacement-based loading condition. Therefore the linear elastic model with limited compressibility has been adopted for future simulations. In the meantime, a stiffness of Young's modulus $E = 31.5$ MPa for the falx cerebri was also found to be most appropriate in the current FE head model.

Ventricles play a critical role in the brain. Therefore it was important to properly describe the behaviour of ventricles under TBI scenarios. Inspired by the heart project [132], the surface-based fluid cavity model was applied to simulate the intraventricular CSF within the brain parenchyma. By altering the bulk modulus of the fluid inside the cavity, we adjusted the amount of ventricle volume reduction during the evolution of a lesion. It was observed that the effective compressibility of ventricles not only affects the magnitude of brain motion during lesion evolution, but also it plays a critical role in the distribution of deformations of brain tissues surrounding it.

6 Biomechanical model simulation

6.1 Introduction

A high-fidelity patient-specific TBI head model has been developed in chapter 4 and further validated both qualitatively and quantitatively in chapter 5. Having established validated bio-fidelity and model stability, this chapter aims to exploit the model to the brain deformation behaviour with various kinds of TBI lesions by altering its loading conditions using the patient-specific TBI model. One of the overall aim of the thesis is to study the interplay between the haematoma development, the secondary swelling, the ventricle behaviour and the brain response for TBI related pathologies. In particular, the onset of the primary injury is considered as the starting point of the pathological cascades, thus it is critical to analyse the variety of haematoma observed clinically. In this chapter, the lesion simulations performed address two main scenarios: one for the realistic lesion case studies, and the other for idealised traumatic lesion simulations.

Firstly, the realistic lesion case studies replicate real-world lesions from patients' CT scans. While the indentation-based lesion simulation method described in section 4.3.2 provides a way to re-create the primary mass lesion in a patient-specific way, the thermal expansion method described in section 5.3.1 offers a way to simulate the secondary swelling which frequently occurs in the development of TBI. By coupling both primary and secondary injury in a particular TBI patient, the computer simulation is able to generate results of appropriate accuracy. In the current chapter, the brain herniation results from the realistic lesion simulation will also be extensively validated with the CT findings. Moreover, these realistic case studies will be further analysed to help explain the brain behaviour under trauma.

Additionally, idealised lesions will be created and considered to the same head model. It is noted that, depending on the nature of the impact force, the pathoanatomy of TBI patients varies with the anatomic characteristics of intracranial abnormality as well as their locations of injury onset. It is of interest to study how the brain reacts to mass lesions of various sizes, shapes and at different locations. Nevertheless, the TBI cases that can be found in reality are limited and it is almost impossible to perform any parametric study using the real-world data. The usefulness of computer modelling is highlighted under such a scenario. By creating synthetic lesions of various kinds and incorporating them into the high-fidelity head model, it is possible to perform a parametric study where we control the location, size and shape of the lesion, in order to evaluate how brain reacts

mechanically to lesions occurring at various sites inside the skull.

Over the years, TBI related experiments have been performed on cadavers, animals, physical human simulacra, and under some special circumstances *in vivo* in healthy volunteers [134]. The *in vivo* experiments are usually associated with high cost. In particular, cadavers and animals experiments have a limited usage count, while damaged dummy parts require replacements after each round. Moreover, despite the technical difficulty in measuring internal brain response during physical experiments, there exists serious ethical issues regarding the experimental procedure. The *in vivo* experiments use tagged magnetic resonance imaging to track brain motion in life human subjects, but only the mildest acceleration far below the damage threshold could be applied for the safety of the volunteers. In this study, the developed high-fidelity head model offers a cost-efficient and potentially more accurate alternative to those experimental laboratory tests.

6.2 Realistic lesion simulation case studies

6.2.1 Methods

Depending on the initial impact force, TBI could theoretically develop in any head compartments, appearing in the form of scalp laceration, skull fracture, epidural and subdural haemorrhages, subarachnoid haemorrhage, brain contusion and intraparenchymal and intraventricular haemorrhages. In addition, each type of the injury could be further distinguished by its location, distribution and complexity inside the skull. To investigate the brain response to the heterogeneous intracranial complications, the proposed indentation-based lesion evolution method in section 4.3.2 offers a potential solution. The developed lesion simulation method is capable of replicating the customised geometry of a specific lesion, as long as the lesion is between the brain and the skull. As a result, the proposed lesion loading can be applied to simulate the subdural and epidural haematoma development effectively, but not for other types of TBI. For intracerebral or intraventricular haemorrhages, the indentation-based method is not applicable and alternative ways must be explored. For the current study, the research scope focuses only on SDH and EDH related TBI cases.

To further understand the brain herniation followed by TBI, the combined indentation and thermal expansion methods described in section 5.3.2 has been applied to six TBI patients as a set of case studies. The post TBI CT scans from all six patients were provided by Department of Clinical Neurosciences, Addenbrooke's Hospital (Cambridge

University Hospitals, England). Each of the pathological CT scans has been treated using the developed preprocessing pipeline in chapter 2.2.1 and registered to the template CT scan, hence the subjects are aligned in the same physical space. In particular, the haematoma in the CT scan has been manually delineated by an experienced anesthetist and reviewed by another neurosurgeon from the Hospital, to ensure the accuracy of the segmentation results.

Figure 88 presents the axial CT slices for the six different TBI patients. It is apparent from the figure that the intracranial mass lesion appears in various geometric characteristics at different locations inside the skull. The first row in the figure are EDH lesions, while the second row corresponds to SDH lesions. Table 10 summarises the basic information for each of the TBI patients. The six patients have an average lesion size of 71.4 ml (std = 27.6 ml). The average maximum lesion thickness is 16.0 mm (std = 8.62 mm). The observed average clinical MLS is 11.4 mm (std = 3.76 mm). By comparing the maximum lesion thickness with MLS findings, it is noted that for all three EDH cases, the clinical MLS is smaller than the maximum lesion thickness, while the opposite is observed for the SDH cases.

The assessments of the realistic case study models follows a similar approach as described in chapter 5. Specifically, the simulation result for each of the six TBI cases is firstly

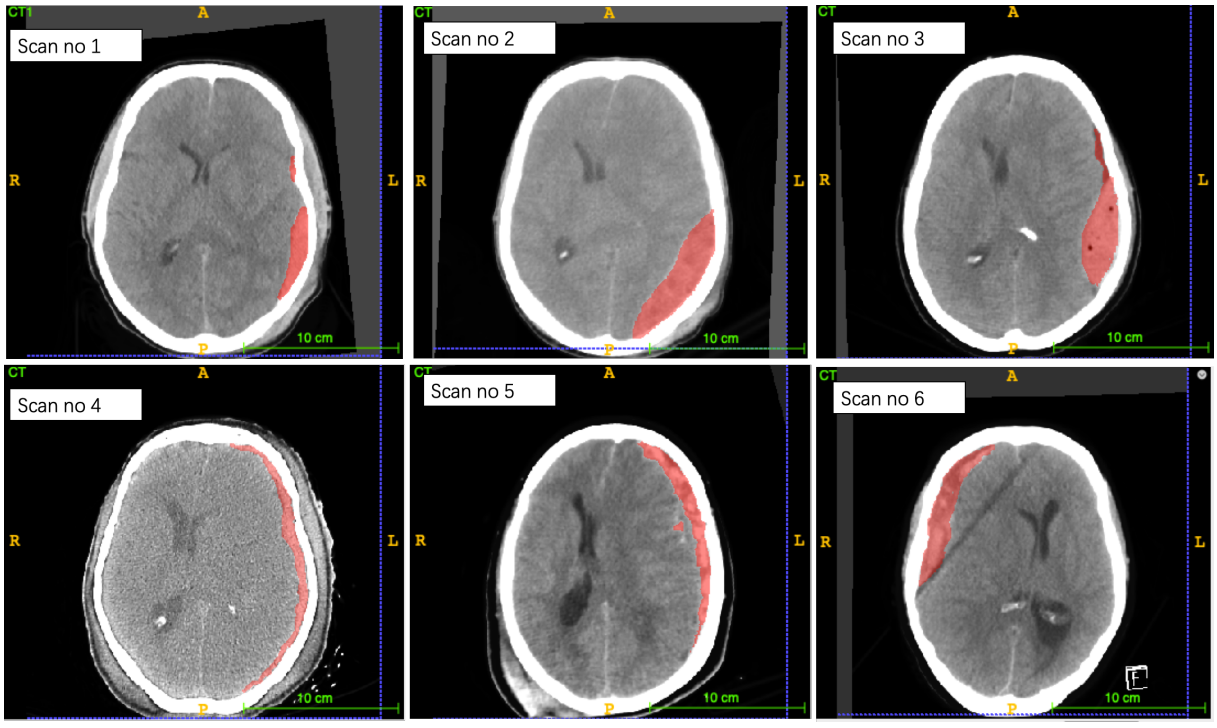

Figure 88: Illustration of pathological CT scans of six different TBI patients after preprocessing. Note, haematoma has been highlighted with the red mask in each CT slice.

ID	Type	location	Volume of lesion (ml)	MLS (mm)	Max lesion thickness (mm)
Scan no 1	EDH	right temporal parietal	34 .0	4.80	14.3
Scan no 2	EDH	right temporal occipital	94.1	11.2	20.0
Scan no 3	EDH	right temporal parietal	111	11.4	31.1
Scan no 4	SDH	right frontal occipital	61.6	11.0	6.50
Scan no 5	SDH	right frontal parietal	69.3	14.3	11
Scan no 6	SDH	left frontal	57.8	15.7	13

Table 10: Table of basic lesion information for six TBI patients. Note, the table shows the summary of the lesion characteristics for the six TBI patients. Only SDH and EDH types of lesion are of interest.

evaluated qualitatively by comparing the simulated brain deformation contour from the bioengineering model with the MPS heatmap generated from the CT scans. Then the quantitative assessment ensures that the simulated MLS from the computer model is equal to the clinical MLS observed. After the qualitative and quantitative assessments, the detailed brain herniation under lesion evolution can be further investigated from the six case studies.

6.2.2 Results

Following the method described in section 4.3.2, the customised haematoma geometry has been reconstructed and shown in Figure 89. Those delineated rigid lesion surfaces are reconstructed uniquely from the patient-specific lesion-brain interaction surface shown in Figure 88. Through the proposed indentation method, the customised lesion surface pushes on the brain surface and a hypothetical lesion gradually develops between the inner skull surface and the brain. At the end of the indentation, the resultant hypothetical lesion copies the exact shape of the SDH/EDH observed in the pathological CT scans in Figure 88.

Resemblance of the computer lesion model to reality

As a case study for the real-world TBI patients, it is critical to ensure that the lesions are re-created correctly from the underlying pathological CT scans. Thus evaluating the

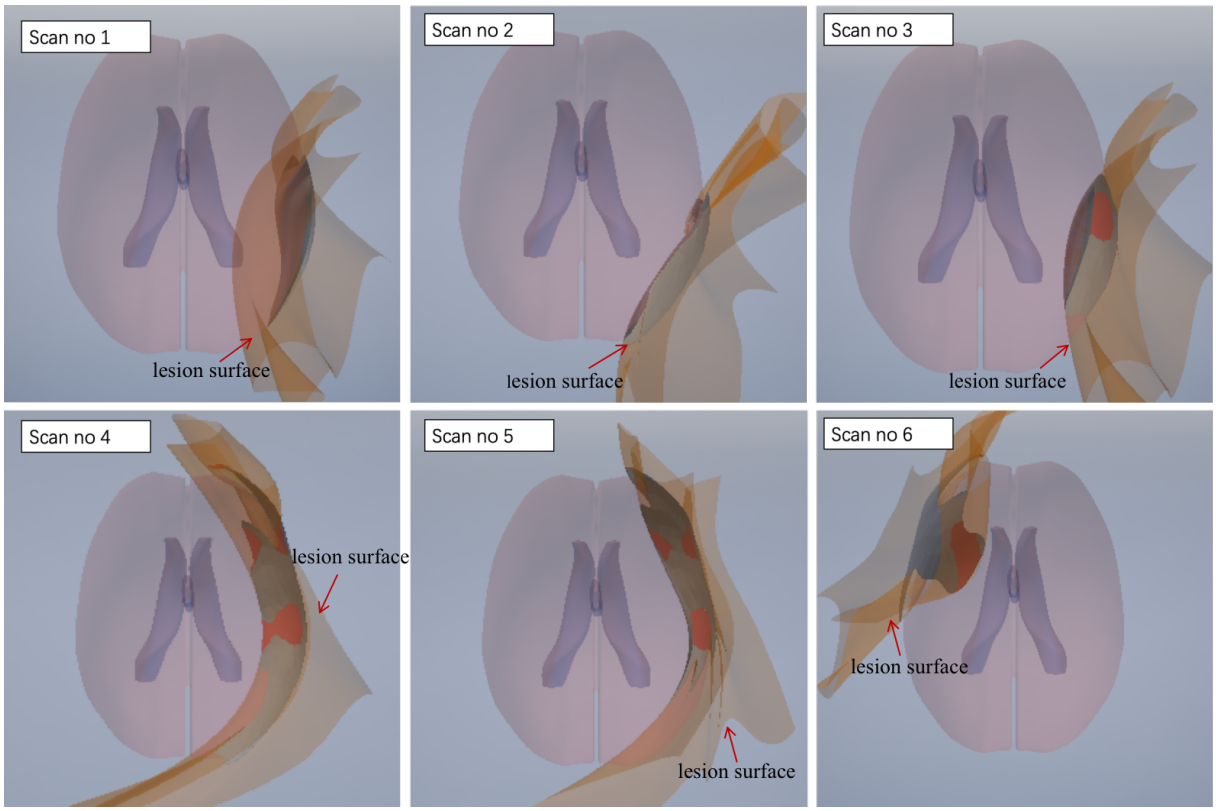

Figure 89: Illustration of reconstructed lesion geometry for six different TBI patients plotted on brain silhouette in Autodesk Inventor. Note, the simulated haematoma is the encapsulated volume between the skull inner table and the delineated lesion surface.

resemblance of the computer lesion model to the realistic lesions is necessary. For a qualitative assessment, the shapes of the previewed computer lesions shown in Figure 89 are compared with the appearance of the haematoma in Figure 88. Such a morphological similarity between the corresponding TBI cases confirms that the computer lesion model is a qualitative reconstruction of the real lesion.

In addition to qualitative assessment, a more explicit evaluation is also performed. Since the lesion model is a re-creation of the geometry of the actual haematoma, it is important to check if the reconstructed lesions possess the same numerical features as the clinical ones. Table 11 displays some basic statistics about the reconstructed lesion in the developed computer model. By comparing the contents in table 11 and table 10, the statistical difference between the developed computer lesions and the actual lesions observed in CT scans can be revealed. The mean absolute percentage error (MAPE) has been utilised to measure the numerical deviation of the computer models from the actual ones. MAPE is defined as:

$$MAPE = \frac{1}{n}\sum_{t=1}^{n}\left|\frac{A_t - S_t}{A_t}\right| \tag{10}$$

where A_t is the actual geometric feature from the realistic lesion, S_t is the simulated geometric feature of the computer lesion model. Such a geometric feature can be either the lesion volume or the maximum lesion thickness. The MAPE in this calculation is summed over each case t and divided by the total number of cases n. The MAPE is a popular loss function used in the model evaluation of regression problems. This concept has been adopted here because of its known intuition in the interpretation of relative errors.

The calculated MAPE for the lesion volume and the lesion maximum thickness between the actual haematoma and simulated lesion is 4.73% and 1.1% respectively. For both of the numerical lesion parameters, the percentage deviations are below 5%, which indicates a satisfactory replication of the actual lesion in the computer model. As compared to volumetric MAPE, the relative error in maximum lesion thickness is a lot smaller. This is because although the detailed haematoma characteristics has been retained with great accuracy on each selected slice, the minor deviation in geometric lesion contours accumulates via the operation of loft and eventually results in the observed MAPE of 4.73% in lesion volume.

To sum up, although there exists slight deviation between the reconstructed and actual lesion, such a small relative error is considered acceptable and the developed lesion model

ID	Type	Volume (ml)	Max thickness (mm)	MLS (mm)
Scan no 1	EDH	32.4	14.5	3.22
Scan no 2	EDH	94.8	20.2	5.34
Scan no 3	EDH	114	31.2	8.38
Scan no 4	SDH	65.3	6.43	5.71
Scan no 5	SDH	75.2	11.2	7.47
Scan no 6	SDH	61.2	13.1	6.76

Table 11: Table of basic information for the reconstructed lesion model for six TBI patients. The table shows the summary of the lesion characteristics for the reconstructed computer lesion model for the six TBI patients. Note, the MLS here is a result of pure primary injury.

is deemed as being a qualitatively and quantitatively accurate representation for the reality.

Inclusion of swelling effects

So far, the comments on the simulated haematoma volume and thickness ensures that the model is set up correctly, the next step is to evaluate the output and result of the simulation, such as the MLS. Unlike the parameters considering lesion characteristics, the relative difference (MAPE) between the actual and simulated MLS is as high as 44.1%. However, it is worth noting that the value of MLS shown in table 11 is the results of pure indentation. In other words, the current MLS magnitude only takes into account the direct consequence of brain herniation following pure primary injury: any swelling effects initiated by primary trauma has been ignored. As emphasised in chapter 5.3.2, TBI is a complex pathology that comprises not only primary but also secondary injuries. The elevation of ICP is considered as an important manifestation of secondary injury. After trauma, the edematous cerebral hemisphere may herniate through the subfalcine space to compress the other half of the cerebrum, which appears as MLS on brain images.

As a result, following the indentation of primary damage, thermal expansion has been applied to the injured cerebrum hemisphere to simulate swelling in secondary injury, as described in section 5.3.2. With the prescribed thermal expansion, the resultant MLS starts to grow until it reaches the exact value of corresponding clinical MLS. Figure 90 compares the simulated MPS contour with the clinically derived MPS heatmap. It is noted that despite the minor difference on detailed concentration of brain shifts, the simulated MPS contour is highly representative of the clinical MPS derived from patients' CT scans: the cross midplane shifts of brain tissue intend to concentrate on the frontal ventricular region and gradually decays until it reaches the periphery of the skull, where the rigid falx prevents the brain tissue around it from moving. Moveover, the relative sizes of the red region of severe brain shifts are comparable in the clinical MPS and the simulated MPS across all six different TBI cases. This observation again confirmed the feasibility of the proposed lesion simulation method.

Differentiating primary and secondary related deformations

Historically, researchers have been tried to describe the brain swelling condition in some simplistic ways. In fact, in 1996, Zumkelly *et al.* [135] first introduced the concept of

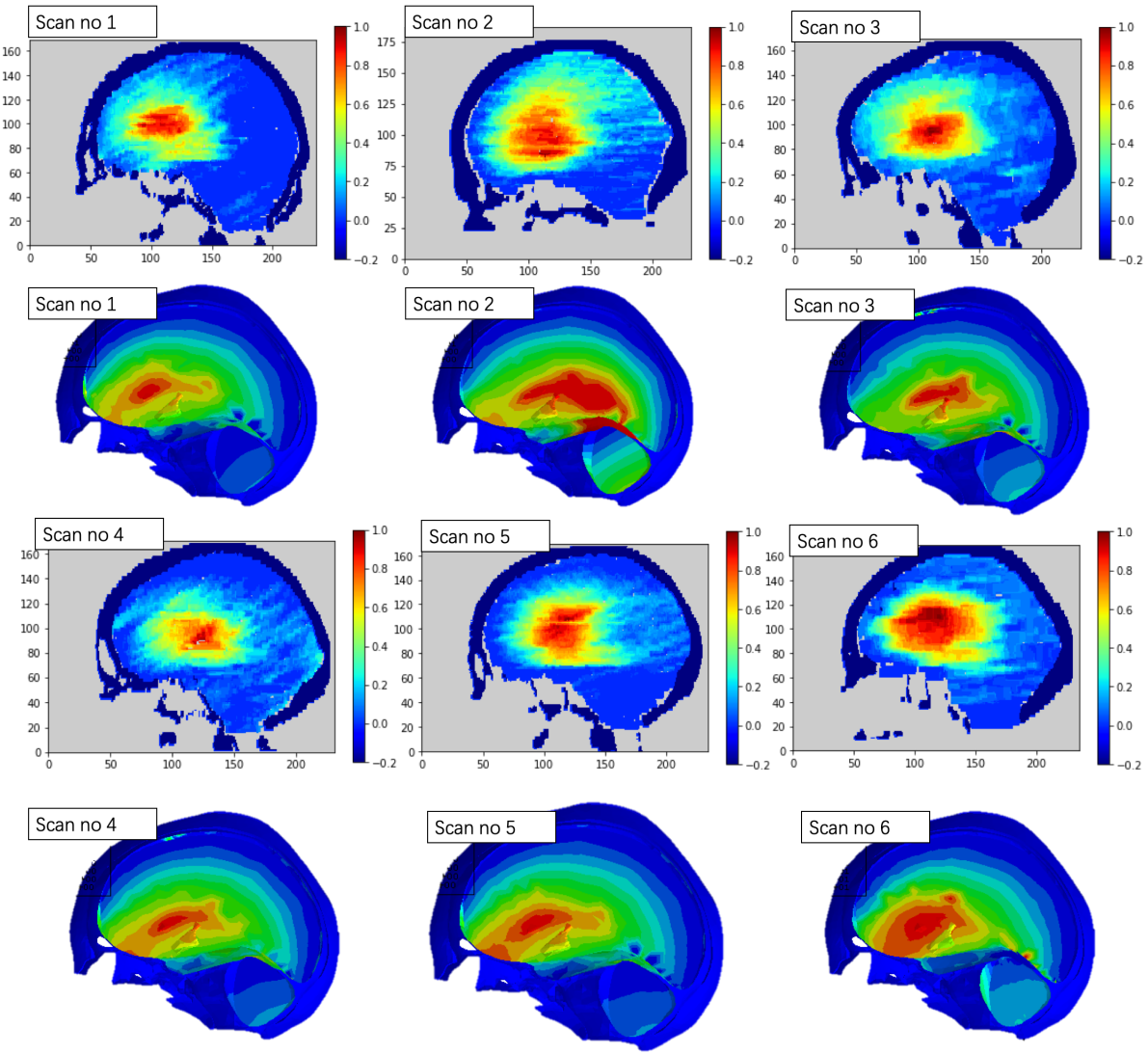

Figure 90: Illustration of simulated MPS contour and clinical MPS heatmap for six different TBI patients. Note, the scale bar represents the normalised MPS values between 0 and 1. The first and the third row show the clinical MPS heat map and the other two rows displace the simulated MPS contour. For each scan, the clinical MPS is placed on top of the simulated MPS contour.

brain swelling factor to describe the difference between the MLS and the thickness of the haematoma. They reported that a negative differences ($MLS < haematomathickness$) of up to -5 mm were associated with a high survival rate [135]. Later in 2015, Bartels *et al.* [115] published similar results, stating that a MLS more than 3 mm greater than haematoma thickness predicts mortality in all cases. Since then, the difference between MLS and haematoma has become a potential outcome predictor. Nevertheless, it is over simplistic to assume that haematoma thickness is directly related to the clinical MLS, so

that their difference can represent the level of swelling. As compared to these studies, our developed computer lesion model provides a more realistic and effective way to quantify swelling brain damage.

Overall, the lesion evolution process for a given TBI patient is simulated in two steps: firstly the indentation of lesion surface replicates the development of primary injury and then the subsequent thermal expansion in the injured hemisphere mimics the swelling process for the secondary injury. By coupling the primary and secondary damage, the developed traumatic lesion model is able to replicate any EDH/SDH dominated TBI in a patient specific way. One great advantage of the developed computational lesion evolution model is that it is able to tell to what extent is the brain herniation a result of primary injury alone and therefore distinguish the amount of brain deformation resulted from the primary injury compared with that caused by secondary injury.

Namely, the apparent MLS can be decomposed into two portions: one portion is attributed to the brain herniation as a result of haematoma itself, the other portion is associated with the underlying swelling during secondary injury. Figure 91 illustrates the relative compositions of simulated MLS for all six different cases. It is seen that the primary and secondary injuries carry different weights from case to case in TBI patients. There exists a wide range of factors that could potentially affect such a composition: the lesion type, the lesion size, the intracranial lesion location, the geometric characteristics of the lesion, the age of the patients, the nature of the impact and so on. According to the author's knowledge, it is the first attempt that the brain deformation following secondary injury has been differentiated from the total deformation with the help of computer modelling explicitly. It is expected that, this will help the clinicians to better understand the spectrum of TBI related brain response.

In Figure 91, it is observed that the brain damage associated with secondary injury ($MLS_{secondary}$) for SDH patients is generally greater than that of the EDH patients. This coincides well with the clinical findings that SDH triggers more severe secondary swelling than EDH.

To sum up, six realistic TBI patients have been reconstructed and simulated in the developed patient-specific head model. It is found that the reconstructed computer lesion represents the realistic CT findings with good fidelity. By imposing the primary injury and secondary injury to the healthy computer head model step by step, the brain deformation associated with swelling effects were effectively differentiated. It is observed from the case study that while EDH patients are normally present with greater haematoma thickness than that of the SDH patients, their accompanying secondary swelling effect is generally

less significant, which agrees well with the historical clinical observations.

6.3 Idealised traumatic lesion simulations

6.3.1 Methods

Historically, research has considered not only the assessments, treatments and clinical guidelines, but also the outcome predictors for TBI. It is expected that improved predictors can further advance our understanding of TBI related mechanisms and therefore enhance the medical decision-making ability and ultimately improve patients' outcomes. In the previous realistic case studies in chapter 6.2.1, the simulation of TBI is predominately retrospective. However, in the current section, synthetic TBI lesions are created and applied to the validated high-fidelity FE model. The simulation of arbitrary synthetic TBI lesions sheds light on more predictive modelling techniques.

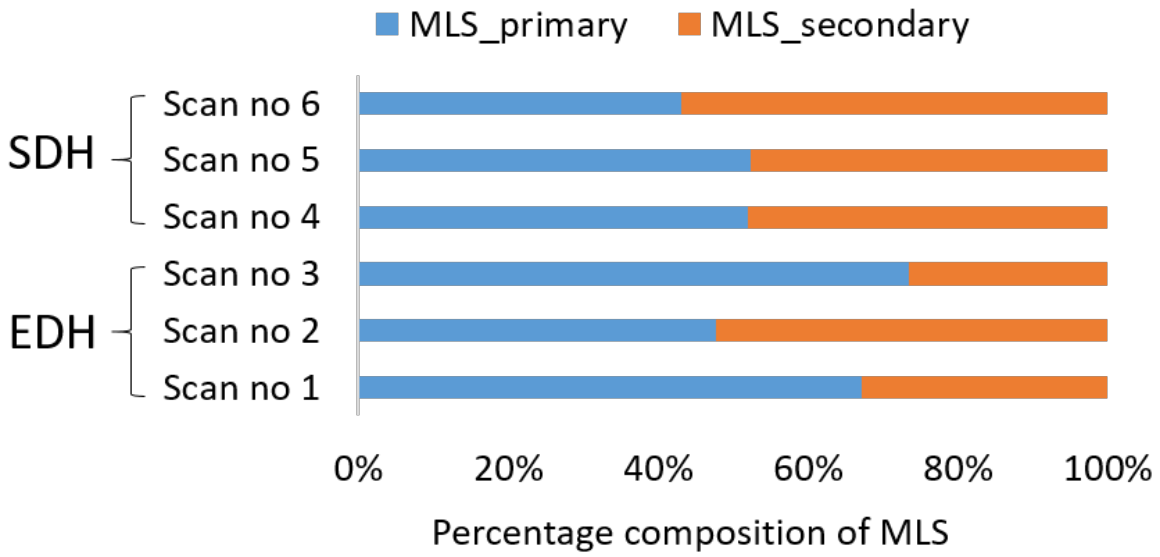

Figure 91: Illustration of the relative contributions to MLS for six different cases. Note, it is assumed that the final MLS is composed of a $MLS_{primary}$ portion attributed to primary injury and a $MLS_{secondary}$ portion attributed to secondary injury.

Identification of TBI heterogeneity

Primarily, the heterogeneity of TBI arises in three main aspects: the nature of the impact, the brain region affected and the individual variance between patients. For computer modelling, the heterogeneity associated with individual variance is no longer a problem: once a patient-specific FE head model is reconstructed and validated, a series of injury experiments could be performed repetitively on the same model without additional costs. Having eliminated the heterogeneity caused by individual patient's characteristics, the domain of complication factors narrow down to the damage nature and affected brain region. Essentially, these are the two test parameters to be further analysed in the idealised simulation study described in this section.

Firstly, among the various types of TBI, the prevalence of SDH and EDH remain relatively high in the range of focal injuries. Also, the developed patient-specific lesion simulation method offers an approach to study these two types of head injuries. Thus SDH and EDH will be the two main types of impacts to be investigated in this chapter. SDH and EDH are inherently different TBI lesions and it is important to effectively differentiate them in a mechanical way. In clinical settings, though EDH and SDH both happen between the skull and the brain, they are further differentiated by their relative locations of onsets between the meningeal layers of the brain. However, since those meningeal layers are not included in the developed computer head model, it is not possible to distinguish EDH and SDH by their anatomic locations of onsets. Fortunately, the apparent geometric characteristics of SDH and EDH in CT scans also differ and so it has provided some intuitions on their mechanical simulations. Typically, SDH appears as a cresent-shaped hyperdense collection of blood, as shown in Scans 4 to 6 in Figure 88. Whereas, the classic appearance of EDH is bi-convex or lentiform in shape and sharply demarcated by the cranial sutures, as shown in Scans 1 to 3 in Figure 88. When comparing the morphology of EDH and SDH in a pure geometric view, it is seen that EDH is normally more concentrated spatially, with SDH being more spread over the brain surface. Thus it is hypothesed that the morphologies of the haematoma may represent a typical type of lesion and play a critical role in TBI settings.

In addition to lesion morphology, the injury onset locations is also an important source of TBI related heterogeneity. Studies of whether the relative locations where the trauma attacks affects the extent of brain damage can be crucial in early diagnosis of TBI patients. For the current idealised lesion simulation, both the lesion morphological characteristics and their relative onset locations are investigated in a parametric simulation study.

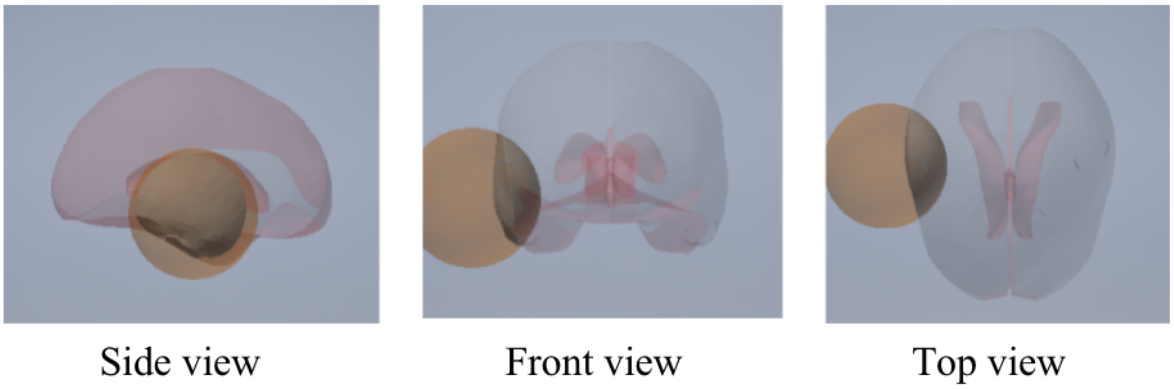

Figure 92: Modelling view of the synthetic lesions in Autodesk Inventor. Note, the volume of haematoma is defined by the intersecting solid region between the brain surface and the lesion indentation surface.

Evaluation of lesion morphology

In the idealised lesion simulations, the morphological characteristics of the synthetic lesions are defined first. As shown in Figure 92, a synthetic lesion described with a spherical indentation surface has been created. Like all other parametric studies, it is of great importance to specify the design constraints, and constrain the parameters other than the designed primary variable strictly. For the proposed indentation-based lesion simulation method, it is the geometric characteristics of the indentation surface that plays a critical role in the formation of hypothetical brain lesions. Defining the indentation surface as spheres has one major advantage: a sphere has a uniform curvature everywhere on its surface, therefore it is guaranteed that when the spherical lesion surface starts to interact with the brain, the resultant brain-lesion interface is of uniform curvature regardless of the angle of attack.

By adjusting the indentation depth of the spherical indentation surface, the volume of the synthetic lesions can be defined. Quantification of the synthetic lesion volume is done with the help of Autodesk Inventor. Specifically, the hypothetical lesion is wrapped by the lesion indentation surface and the skull inner surface, as shown in Figure 92. The solid grey volume in Figure 92 shows the intersection between the indentation sphere and the brain parenchyma, and this is the synthetic lesion previewed in CAD modelling. In this study, the synthetic lesion volume is fixed as 50 ml across all the simulations. It is noted that the average haematoma volume of the six realistic TBI patients is 71.25 ml, but they are selected patients with severe brain shifts. Thus a 50 ml lesion volume should be a reasonable and adequate estimate for the current analysis.

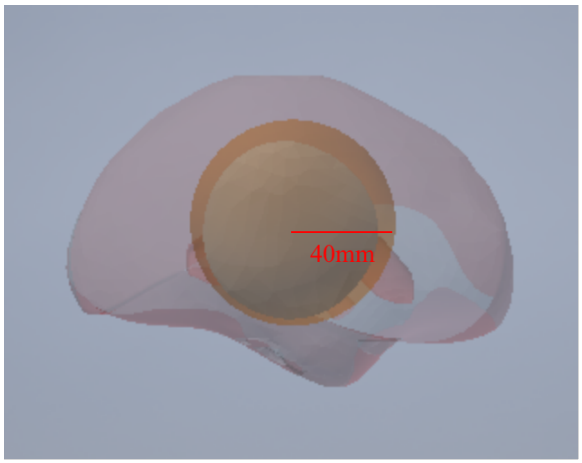

(a) Idealised indentation sphere with 40 mm radius

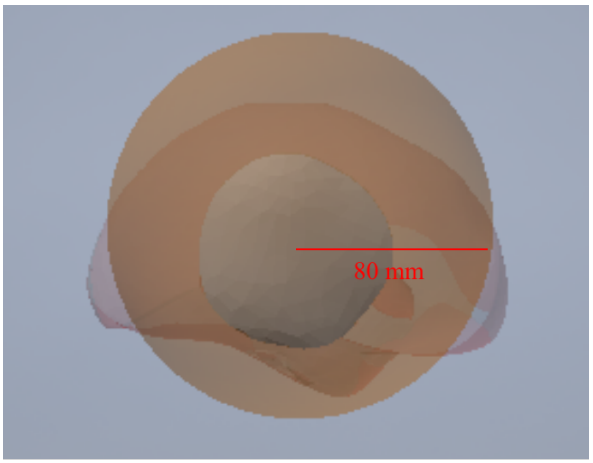

(b) Idealised indentation sphere with 80 mm radius

Figure 93: Synthetic spherical lesion indentation surfaces with 40 and 80 mm radius. Note the figure is showing the intersection between the indentation sphere and the brain parenchyma as the synthetic lesion.

By restricting the lesion volume and surface geometry, it is now possible to parametrically study the role of lesion spatial concentration level, as hypothesised previously, in TBI related brain damage. An effective way to evaluate the spacial concentration level of the mass lesion (lesion spread) is to calculate their surface area per unit volume. Normally, the greater the surface area-volume ratio, the more diffuse the lesion is. In the developed computer model, it is possible to construct synthetic lesions of different levels of area-volume ratio and investigate the role of mass lesion spread in TBI related brain deformations. In particular, two synthetic lesions, one with 40 mm radius (S40) and the other with 80 mm radius (S80) have been created and shown in Figure 93.

With the specified synthetic lesion volume and surface geometry, we could now vary the surface area of the lesions to perform the first parametric study on the area-volume ratio. This is achieved by indenting the two spheres of different radius (S40 and S80) into the brain. The resultant brain-lesion interface from the one with smaller radius (S40) will be featured with a curvature that is 4 times bigger than that of the S80 indentation surface. It is hypothesised that given a specified volume, the geometry associated with greater surface curvature is associated with smaller area-volume ratio and hence more concentrated spatially. Geometric parameters such as the surface area and the volume of the created synthetic lesions will be discussed together with the simulated brain response in chapter 6.3.2.

Relative locations of lesion

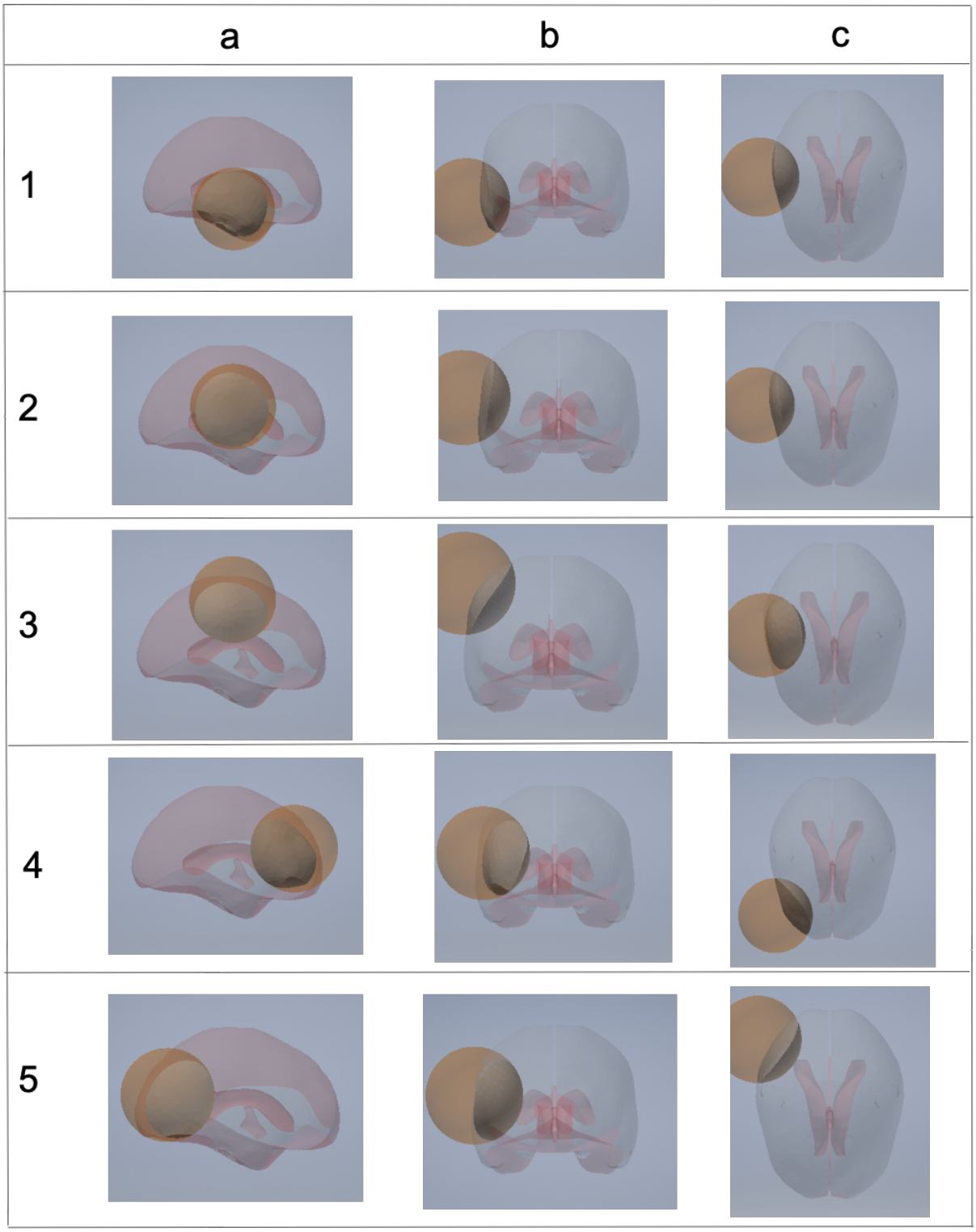

Figure 94: Illustration on the synthetic lesions at different locations. Row 1, 2, 3, 4 and 5 denote different lesion locations and column a, b and c show the side, front and top view of the synthetic lesions respectively.

In addition to the lesion concentration levels, their relative locations of onsets is the other

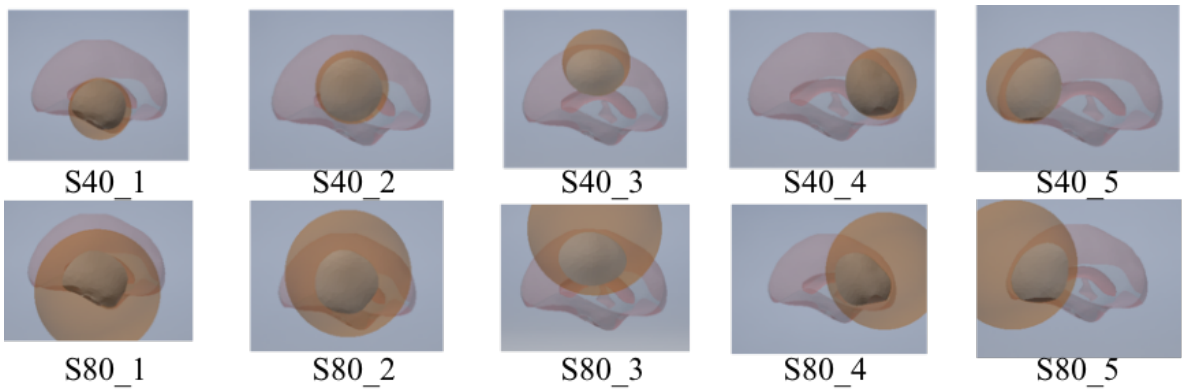

Figure 95: Illustration on the synthetic lesions created by S40 and S80 spherical surfaces respectively. Note, the first shows the lesions related to S40 indentation surface, while the second row demonstrates the lesions from the S80 indentation surface. Columns are associated with lesion location 1, 2, 3, 4 and 5 respectively.

key parameter to investigate in the current idealised TBI model. The lesion location is described by the coordinates of the centre of mass, which can be directly derived from the CAD model of the synthetic lesion assuming that the lesion is homogeneous. Synthetic lesions can be applied anywhere inside the skull by adjusting the centre of mass of the artificial haematoma in the developed patient-specific model.

By manipulating the centre of mass of the synthetic lesions, it is possible to apply artificial head trauma to specified locations inside the brain. Figure 94 demonstrates the series of synthetic lesions created using the S40 indentation sphere. In total, 50 ml of haematoma are applied to five different locations in the right hemisphere. Since the anatomic structures of human head are nearly symmetric across the mid-sagittal plane, evaluation of lesion evolution in one hemisphere is considered sufficient. The first row in Figure 94 described a synthetic lesion that affects in the temporal lobe. While in the second row in Figure 94, a synthetic lesion is applied more to the fronto-temporo-parietal region as compared to that of location 1. In the third row in Figure 94, the synthetic lesion is moved higher and to the parietal lobe. For location 1, 2 and 3, their lesion centre of mass share the same sagittal (anterior-posterior) axis, only the longitudinal coordinates vary so that it simulates haematoma which develops from temporal to parietal regions.

Moreover, in Figure 94, an artificial lesion is developed in the frontal lobe in the fourth row and in the temporo parietal junction and the occipital lobe in the fifth row. As a result, the lesion location 5, 2, 4 imitate head trauma that strikes from the posterior to the anterior region of the brain, but they all share the same height in the vertical direction. Furthermore, the a, b and c columns in Figure 94 corresponds to the sagittal, coronal and axial views of the synthetic lesions in the translucent brain silhouette.

In addition, Figure 95 illustrates the creation of the synthetic lesions for S40 and S80 respectively. It is apparent that the S80 indentation spheres are bigger in size as compared to that of the S40 indentation surfaces. Moreover, it is visible that the relative lesion onset locations are consistent across the two groups of lesions, due to the strict control over the coordinates for the lesion centre of mass at a specified target lesion location. Meanwhile, it is noted that the apparent shape of synthetic lesions looks similar from the sagittal view for S40 and S80 lesions when they share the same location information, though the specific area-volume ratio of the synthetic lesions will be different across the two groups. The detailed lesion morphologies resultant from S40 and S80 will be discussed in section 6.3.2.

Last but not least, the proposed lesion simulation method is capable of separating the primary injury and the secondary swelling, as discussed in section 4.3.3. In the idealised lesion simulation analysis, we first evaluate the brain deformation due to pure indentation, which models only the haematoma but not any associated swelling. Then by applying gradual thermal expansions to the ipsilateral brain hemisphere, synthetical swelling effects are applied on top of the idealised lesions to help investigate the brain shifts associated with secondary injuries.

6.3.2 Results

Biomechanical computer modelling facilitates a strict parametric study for the exploration of brain response to a variety of TBI related lesions. In this idealised lesion simulation study, the lesion concentration level evaluated by area-volume ratio, together with the location of attack described by the centre of mass of the synthetic lesion are the two primary variables to investigate.

Synthetic lesion morphologies

Table 12 displays the morphological characteristics including the lesion volume, the surface area of the lesion, the area volume ratio, as well as the maximum lesion thickness of the developed synthetic lesions. In total, there exists two groups of artificial lesions, the S40 group is created from a sphere of 40 mm radius, whereas the S80 group originates from the indentation sphere of 80 mm radius. Table 13 presents an overview for the lesion characteristics of the two synthetic lesion groups. As shown in the table, the mean lesion volume for S40 group is 50.77 ml, with a standard deviation of 0.12 ml; While for the S80

	lesion volume (ml)	**lesion surface area (mm^2)**	**Area volume ratio (1/mm)**	**Max lesion thickness (mm)**
S40_1	50.66	8335	0.1645	23.24
S40_2	50.84	8745	0.1720	21.66
S40_3	50.95	8335	0.1636	20.52
S40_4	50.73	8393	0.1654	19.12
S40_5	50.67	8259	0.1629	18.54
S80_1	50.37	9902	0.1960	18.22
S80_2	50.95	10793	0.2118	15.60
S80_3	50.6	10090	0.1994	15.60
S80_4	50.07	10457	0.2088	15.25
S80_5	50.35	10443	0.2074	14.55

Table 12: Table of idealised lesion characteristics. This table shows the summary of the synthetic lesion characteristics for the reconstructed idealised computer lesion model. Note, S40_1 to S40_5 correspond to the five different locations of lesion attack created from S40 indentation surface. S80_1 to S80_5 correspond to comparable simulated lesion locations as compared to S40_1 to S40_5 respectively, only the indentation surface changed from S40 to S80.

group, the mean lesion volume is 50.47 ml, with a standard deviation of 0.33 ml. The highly comparable simulated lesion volumes across the two groups demonstrate the great potential of the proposed idealised lesion creation method in controlling test parameters. Similar levels of control has been exhibited in regulating the lesion centre of mass when alternating the location of lesion onsets, such that simulated lesion S40_1 and S80_1 were applied at similar locations relative to the skull.

Despite that the two groups of synthetic lesions were of the same volume, their featured brain-lesion interface were inherently different due to the curvatures of the leading

	lesion volume (ml)	**lesion surface area (mm^2)**	**Area/Volume (1/mm)**	**Max lesion depth (mm)**
S40 group	50.77 ± 0.12	8413 ± 191	0.17 ± 0.0036	20.62 ± 1.91
S80 group	50.47 ± 0.33	10337 ± 348	0.20 ± 0.0065	15.84 ± 1.4

Table 13: Table of comparison for the morphological characteristics of S40 and S80 lesion groups. This table presents the mean and standard deviation of the lesion characteristics for each of the synthetic lesion groups.

indentation spheres. The lesion surface characteristics was evaluated by the lesion surface area, where the S80 group is featured with a greater lesion surface area than the S40 group. As a result, the subsequent area-volume ratio is also greater in S80 group. For synthetic lesions of similar shapes, a greater area-volume ratio usually implies a more spread and less concentrated haematoma in skull. This is further confirmed by the deviation of the maximum lesion thickness in the two lesion groups: the S40 group is shown to possess a larger maximum lesion thickness (20.62 ± 1.91 mm) as compared to that of the S80 group (15.84 ± 1.40 mm). To sum up, it is reasonable to evaluate the spatial concentration level of synthetic brain lesions with the proposed area-volume ratio, and in our developed models, the S40 group is demonstrated to be more concentrated than that of the S80 group.

Brain herniation and lesion spatial concentration levels

Given that the S40 synthetic lesion group has a greater lesion thickness as compared to that of the S80 lesion group, it is possible to evaluate the brain herniation as a result of lesion concentration levels. Figure 96 presents an overview of the brain shift conditions at the five different lesion locations for both S40 and S80 synthetic lesion groups. There are two main findings from this figure.

Firstly, it is observed that the brain models imposed with the S80 lesion group are shown to have less significant clinical MLS across all five different lesion locations as compared to that of the brain models from the S40 lesion group. In other words, with the lesion volumes being equal and the lesion onset location being comparable, the more concentrated the striking lesions, the greater the brain deforms due to mass effects of the lesion. A greater concentration of haematoma is not only characterised with a smaller area-volume ratio, but also, it is accompanied with a greater maximum lesion thickness, as shown in table 12 and 13. It is reasonable to conclude that when brain trauma is a pure result of primary injury, the shift of brain is proportional to the characteristic lesion thickness. If not, one should consider other intracranial complications such as the brain oedema. In 2015, Bartels el. al [115] also relates the midline shift to the thickness of the traumatic acute subdural haematoma to predict mortality in TBI patients. Their observations also emphasised the apparent concentration of the SDH using maximum haematoma thickness and further relates it back to the midline shift.

Secondly, it is apparent that the applications of exactly the same volume of lesions to the brain have resulted in different levels of brain deformations, because of the varying

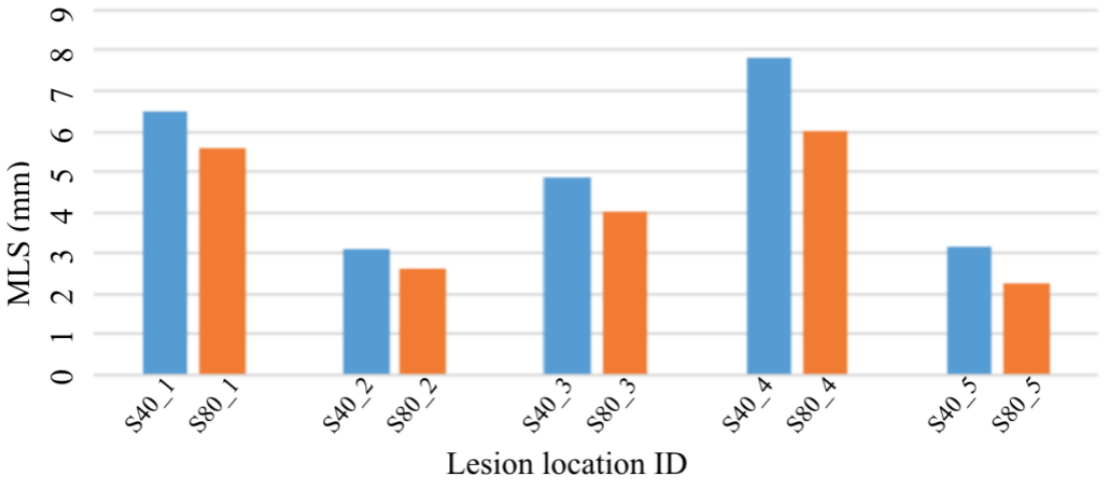

Figure 96: Illustration of the resultant MLS when synthetic lesions were applied at the five different lesion locations. Note, S40_1 to S40_5 and S80_1 to S80_5 correspond to the five different locations illustrated in Figure 95 and it revealed that across all five different locations, the S40 group is more likely to lead to greater MLS as compared to that of the S80 group.

locations of lesions inside the skull. Moreover, the variance in the simulated MLS as a result of changing lesion locations remain consistent between the S40 and S80 lesion groups. The brain response on account of lesion locations are further illustrated in Figure 97 and 98.

Brain herniation and lesion locations

One of the strengths of computer modelling is that synthetical lesions of equal volume and morphology can be applied to different sites across the brain to study the sensitivity of brain response to lesion onset locations. To better describe the lesion locations, the sagittal axis is defined as y axis, while the vertical axis of the brain is labeled as z axis, as shown in Figure 97a. x axis refers to the transverse axis of the brain, which is not of interest here. The origin of the coordinates is set at the centre of mass of the brain parenchyma. Therefore, the lesion location 1 at the temporal lobe has a negative z coordinate, whereas the lesion location 3 in the parietal lobe has a positive z coordinate. At all three lesion locations, their lesion centre of mass share the same y coordinates, the only changing parameter is the lesion's relative locations in the vertical axis. The simulated brain response is shown in Figure 97b. It is observed that with other conditions being equally controlled, the lower the lesion in the vertical axis, the greater the resultant

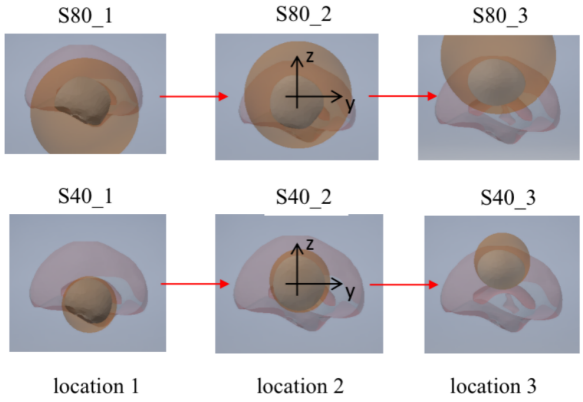

(a) Illustration on lesion location 1, 2 and 3

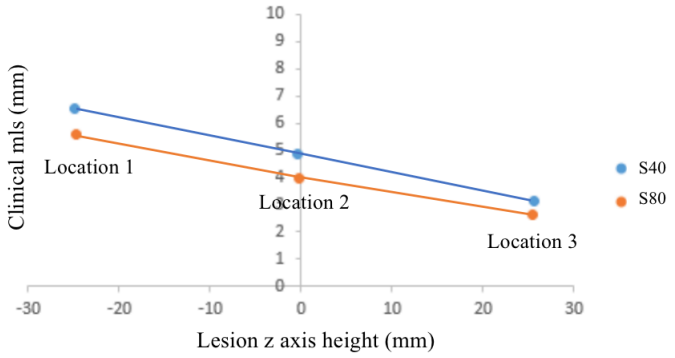

(b) Brain response to lesions at location 1, 2 and 3 respectively.

Figure 97: Brain response to lesions at different heights in the z axis. Note, the y and z axes are illustrated in the figure.

midline shift. The brain is more sensitive to haematoma that strikes on the temporal lobe, rather than the parietal lobe, when the amount of lesions occupying the intracranial space are at a similar level.

Similarly, Figure 98 simulates the brain response to the applied lesions at different locations on the sagittal axis. As shown in Figure 98a, the sagittal axis of the skull is labelled as the y axis. The centre of mass of the lesion at location 5, 2 and 4 all share the same z coordinates, only their y coordinates change from negative value to positive value as the synthetic lesions are applied from the posterior to the anterior regions of the brain. The resultant brain deformation due to the varying lesion locations has been

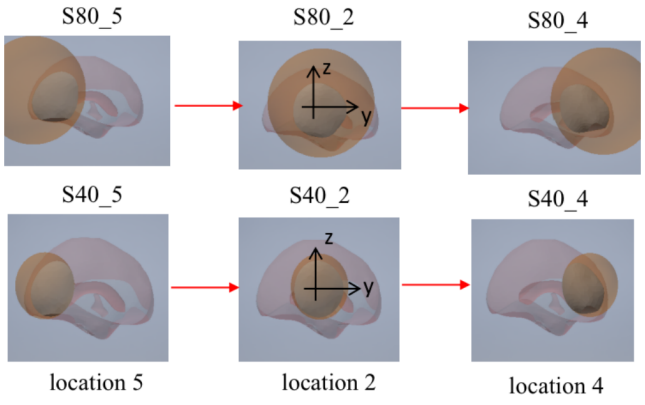

(a) Illustration on lesion location 5, 2 and 4

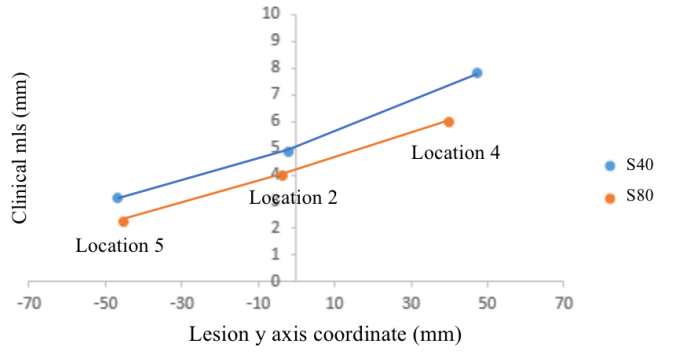

(b) Brain response to lesions at location 5, 2 and 4 respectively.

Figure 98: Brain response to lesions from anterior to posterior locations in the y axis. Note, the y and z axes are illustrated in the figure.

illustrated in Figure 98b. It is revealed that with other conditions being equal, the brain is more sensitive to lesions in the frontal lobe, as compared to that in the occipital lobe.

To sum up, the developed biomechanical model suggests that TBI that strikes on the temporal lobe and frontal lobe are more likely to lead to greater MLS, even if the applied lesion volumes are the same.

From MLS to MPS

So far, the way the brain deformation condition has been evaluated using the clinical MLS as an indicator. Nevertheless, it remains in doubt whether the clinical MLS is a satisfactory representation for the overall intracranial shifts condition. The clinical MLS is measured at the level of foramen of Monro, which corresponds to the axial slice 34 in the developed head model. The first row in Figure 99 presents the axial view of brain deformation contours at slice 34 for all the lesion locations concerned. About 10 mm higher in the vertical axis, the axial slice 38 in the patient-specific head model relates to the level where the two lateral ventricles are both present but the third ventricle is invisible. The brain deformation contour at slice 38 is illustrated in the second row of Figure 99. It is observed that the brain deformation contour varies a lot by just changing the depth of the axial slice by 10 mm.

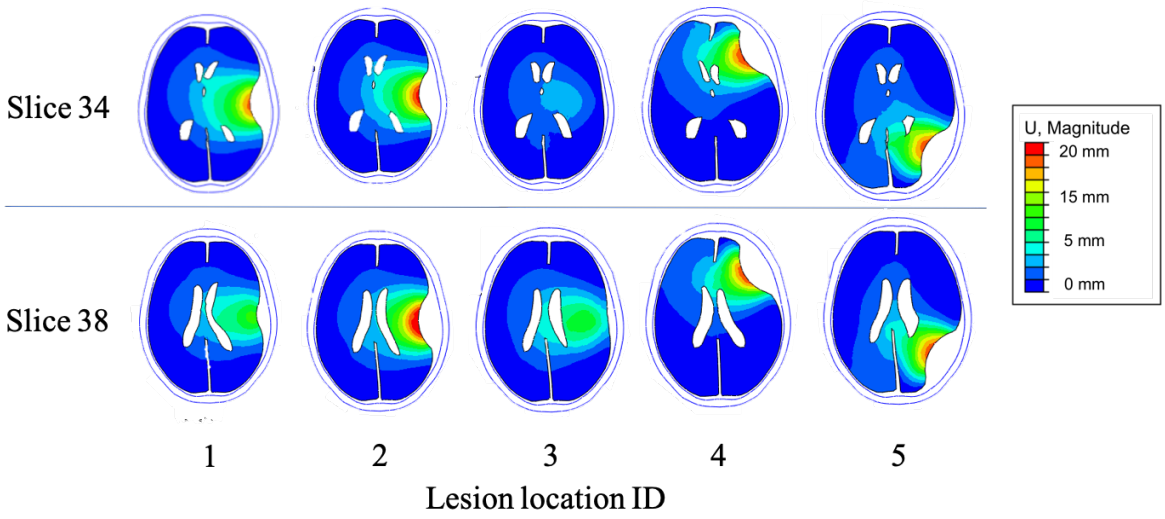

Figure 99: Illustration of the brain deformation condition at axial slice 34 and 38 for lesion locations 1, 2, 3, 4 and 5 respectively. Note, the lesion locations 1 to 5 correspond to the illustration in Figure 95

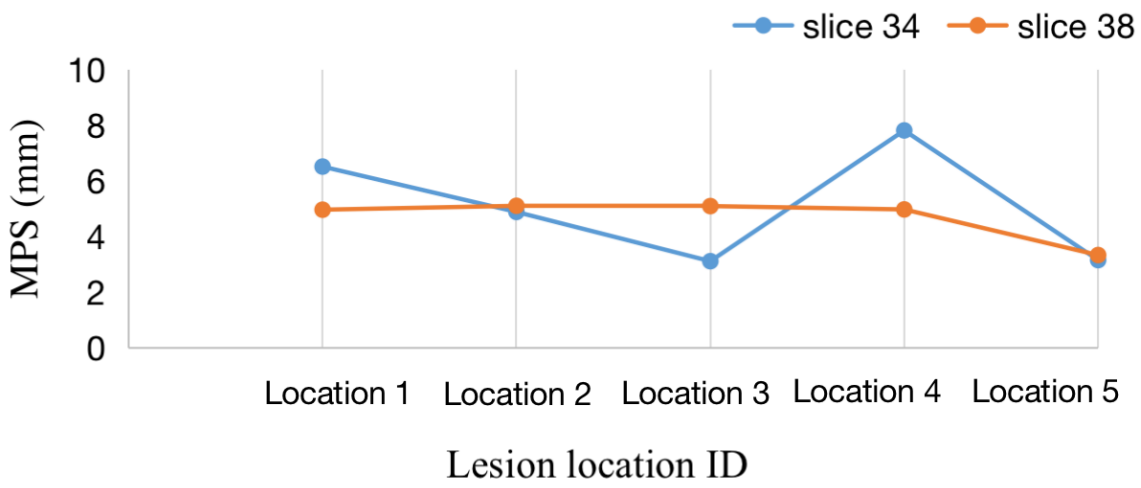

Figure 100: Comparison of brain MPS at different axial slices for all five lesion locations.

When the synthetic lesions were applied at the prescribed locations, the hypothetical haematoma grow in the interstitial space between the skull and the brain parenchyma, yielding various degrees of brain surface deformations. As the lesion attack location changes from the posterior to the anterior region of the brain, following the illustration in Figure 98a, the region of the most deformed brain surface (the hypothetical haematoma) also changes from the occipital to the frontal lobe, as depicted in turn at lesion location 5, 2 and 4. For those three lesion locations, the brain deformation contours remains similar between slice 34 and slice 38. However, as the lesion centre of mass evolves in the longitudinal axis, following the illustration in Figure 97a, the apparent brain surface deformation starts to diverge between slice 34 and slice 38, as shown in lesion location 1, 2 and 3 respectively in Figure 99. At the lesion location 1, the brain surface in slice 34 suffers from more severe deformation than that at slice 38. Moreover, at lesion location 3, the brain surface deformation is almost invisible at both slices. If only those two slices were under investigation for patients' severity assessment, it is easy to mistake the patient characterised with lesion location 3 as less severe than the other patients, though their lesion volumes are known to be all the same. This is because at the lesion location 2, 4 and 5, the centre of mass of the applied synthetic lesion is at approximately the same level as those axial slices, whereas at the lesion location 1 and 3, the lesion is exerted at a different height to where the axial slice 34 and 38 are. The brain surface deforamtion is sensitive to the location where the lesion takes place.

It has been shown that the brain surface deformation is sensitive to the location where the lesion attacks, but what is of equal interest is whether the deeper brain response follow

the same pattern or not. In fact, shifts at the surface of the brain penetrates to the deeper brain tissue and pushes them from their original position. The brain mid-structures which lie on the mid-sagittal plane of the head are natural indicators for the extent of deep brain tissue deformation. The magnitude of deformation of brain mid-structures is defined in section 3.2.2 as midplane shift (MPS). Figure 100 displays the simulated maximum MPS measured at slice 34 and slice 38 at all five different lesion locations. On the one hand, it is noted that given identical amount of synthetic lesions to the same computer head model, various extents of clinical MLS (MPS at slice 34) have been observed due to the variation in the lesion attack locations. As a result of 50 ml artificial haematoma, the case with lesion location 4 demonstrates the maximum clinical MLS of 7.81 mm, while the minimum clinical MLS is observed as 3.11 mm in the subject with lesion location 3. The lesion location of attack plays an important role in the formation of clinical MLS.

On the other hand, the degree of brain deformation at different axial slices, as depicted by the magnitude of maximum MPS in Figure 100, can be quite different, except for the scenarios when lesions are applied to the occipital lobe (lesion location 5) and fronto-temporo-parietal region (lesion location 2), where the observed maximum MPS at slice 34 and 38 are similar. At other scenarios, depending on the specific locations of attack, sometimes the shifts at slice 34 is greater than that at slice 38, sometimes the opposite becomes true. The maximum difference of MPS between slice 34 and slice 38 is as large as 3 mm when the lesion strikes at the frontal lobe at lesion location 4.

To conclude, the observed variance in brain MPS across different brain slices supports our previous conclusion in section 3.3.2: MLS is very sensitive to the slice chosen, because the degree of brain shift varies across the depth of the brain. Moreover, it remains in doubt whether the measurement of midline structure deviation at a single position can be representative of the whole brain behaviour across the entire mid-sagittal plane. The MPS heat map, as introduced in section 3.2.2, should be a better visualisation tool for the assessment of intracranial complications.

Simulating swelling

Recall from section 5.3.2 that one of the strength of proposed computer modelling method is that it separates the complete TBI process into two sub-processes: the first one due to pure haematoma volume increase and the second one as a result of pure swelling. In this section, the MPS heatmap of the idealised lesion models will be analysed following these two sub-processes.

In the first part of the analysis, the brain response to the heterogeneous lesion attack locations has been simulated using a pure indentation-based idealised lesion model and the resultant MPS heat maps are shown in the second column in Figure 101. It is seen that in the MPS heat maps due to pure indentation process (simulating primary injury only), the regions of severe brain shifts in the mid-plane demonstrate a strong correlation with the lesion onset locations: at lesion location 4, when synthetic lesion is applied to the frontal lobe of the visual patient, the resultant brain cross-midplane shift (MPS) heat map demonstrates severe shift in the frontal lobe; while when the lesion attack location changes to the occipital lobe, the region of severe brain shifts in the MPS heat map changes to the occipital lobe as well. As a result, it is concluded that if the traumatic brain response is merely a consequence of the growing haematoma volume, then the inner brain deformation is a direct projection of the exerted lesion in the mid sagittal plane.

In the second part of the analysis, a secondary swelling effect has been superimposed in addition to the primary injury model. For the current idealised lesion study, a total of 50 ml thermal expansion has been applied to the ipsilateral hemisphere of the brain at the end of the indentation process for each of the lesion location models and the resulting MPS heat maps are displayed in Figure 101. It is noted that the MPS heat maps for the models including swelling effects demonstrate greater magnitude of deviations. Moreover, the brain deformation contour on those MPS heat maps also look more similar and closer to the ones observed from real patient's CT scans in section 3.3.2. As compared to the MPS heat maps due to pure indentation, the swelling effects of the brain have redistributed the inner brain shifts to a distribution where the maximum region of deformation starts to concentrate on the frontal ventricular region and decays radially until it reaches the periphery of the skull silhouette. The simulated MPS heat maps demonstrate similar characteristics as is observed from real patients' CT scans, which not only proves the validity of the idealised lesion model, but also it enhances our previous conclusions that together with the secondary swelling, the brain deforms in a regulated way in response to any random traumas.

To sum up, it is shown that although the onset location of TBI lesion plays an important role in deforming the brain, the accompanying swelling effects of the injured brain tissue tends to redistribute the inner brain deformation patterns in a regulated way.

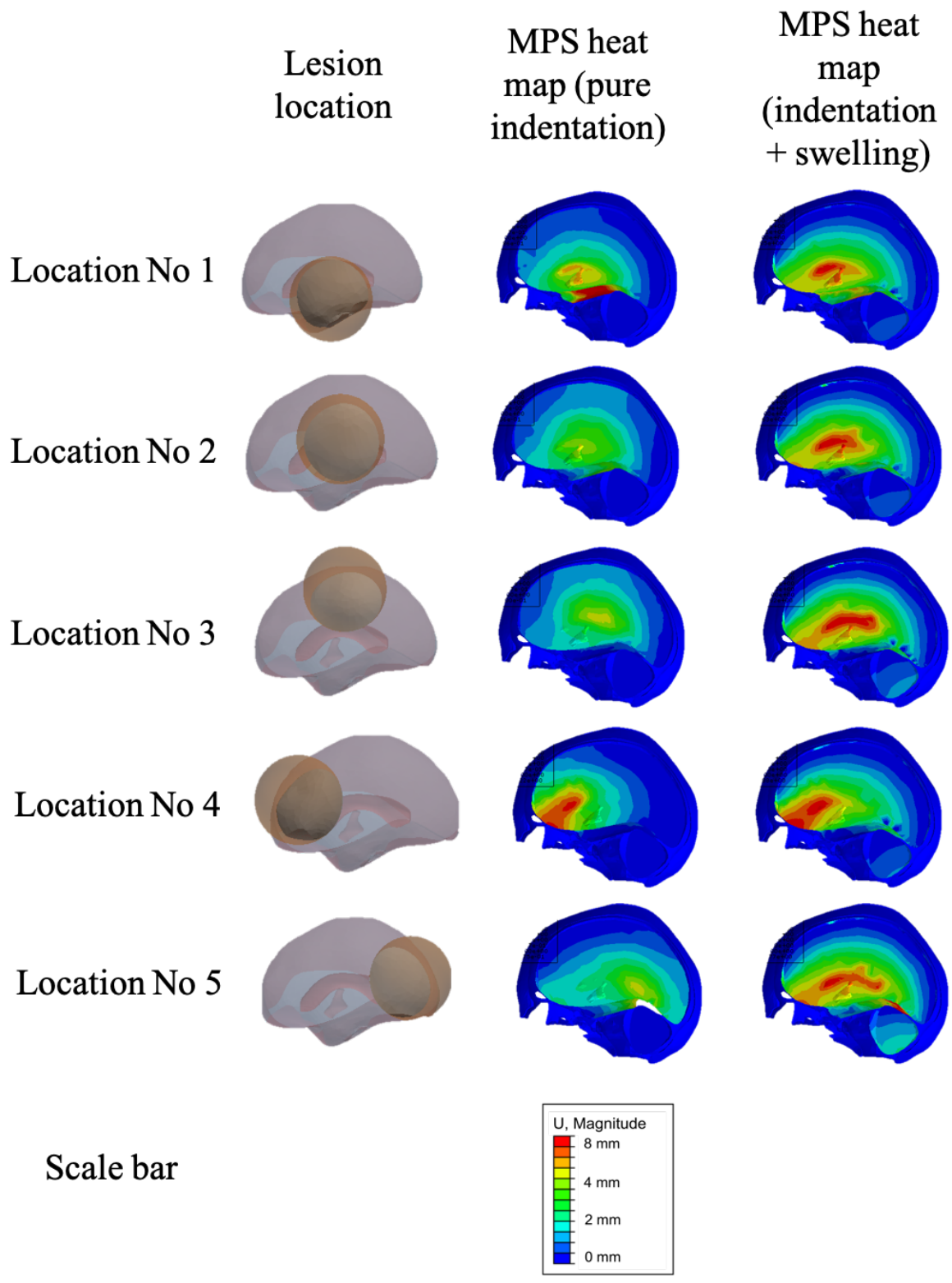

Figure 101: Overview of brain MPS heat maps

6.4 Concluding discussion

TBI is one of the most complex diseases that happens to the most complex organ, the brain. Depending on the nature of the impact, brain injury could take the form of focal

or diffuse, with acute or chronic symptoms. Moreover, the immediate neurologic damage produced by primary trauma often leads to a cascade of secondary events, which make the intracranial complication more unpredictable. The objective of this chapter is to perform a series of TBI simulations, both retrospectively and predictively, and study the traumatic brain response to the heterogeneous TBI lesions, using the validated high-fidelity FE head model developed in chapter 4 and tuned in chapter 5.

The first part of the simulation is predominately retrospective. Six TBI patients, half of whom suffered from SDH and the other half suffered from EDH, have been selected to perform the realistic TBI case study. The unique intracranial complications for all six patients have been reconstructed by imposing both indentation-based primary lesion and the thermal-expansion-based secondary injury to the high-fidelity head model. The simulated brain deformation results were assessed both qualitatively and quantitatively comparing the findings from real patient's CT scans for validity check. Furthermore, the described computer lesion simulation methodology is capable of differentiating the brain herniation as a result of secondary swelling from that due to the pure mass effect of haematoma itself. It is observed from the case study that while EDH patients are normally present with greater haematoma thickness than that of the SDH patients, their accompanying secondary swelling effect is generally less significant, which agrees well with the historical clinical observations.

The second part of this chapter considers idealised traumatic lesion simulations, where synthetic lesions are created and imposed on the developed high-fidelity FE model to study TBI related brain herniations. Computer modelling is a natural solution to solve the problems related with heterogeneity using parametric studies. The potential source of heterogeneity on the individual variance, the nature of the impacts and the affected brain regions can all be effectively controlled during simulations. Two test parameters are designed to be investigated for the idealised simulations: one on the lesion morphology, especially the spacial concentration levels of the haematoma; the other one on the lesion locations of onsets, both of which are inspired by clinical observations as the key factors impacting the way the brain deforms.

By imposing synthetic lesions of different concentration levels, it is concluded that given the same amount of haematoma at the same locations inside the skull, the brain is more sensitive to haematoma that is more concentrated spatially. In terms of lesion onset locations, it is observed that the brain is more sensitive to lesions that strike on the temporal lobe, rather than parietal lobe, in the vertical axis when other conditions are controlled equally. While as the applied lesion is moved from the posterior to the anterior

region of the brain in the sagittal axis, the observed clinical MLS also grows in magnitude. Furthermore, it is observed that swelling effects associated with secondary injury plays a critical role in redistributing the inner brain tissue deformation caused by the onset of primary injury.

7 Conclusion and future work

7.1 Conclusion

Traumatic brain injury (TBI) is a rising global health concern affecting over 1 million people in the UK annually. Stages in the evolution of TBI can be broadly classified into primary and secondary injury, with uncontrolled brain swelling and raised intracranial pressure considered most devastating. Brain herniation as a result of TBI is an important clinical indicator and is closely associated to high morbidity and mortality rates. This thesis aims to develop biomechanical models to quantitatively analyse the brain herniation condition in reaction to the heterogeneous head trauma and help further the understanding of TBI related brain deformation mechanism.

The methodology of the PhD project contains two main parts: medical image computing and biomechanical modelling. The main conclusions of the project for each chapter are as follows:

7.1.1 Computational tools for image analysis

The first part of the research has been concentrating on building computational tools for medical image analysis. It should be noted that medical images are the building blocks for patient-specific bioengineering analysis and any simulation results without the support of clinical evidence cannot be considered as guidelines in clinical practice. In total, four computational tools have been developed:

1. A CT preprocessing pipeline was developed. This pipeline is capable of standardising the raw CT images from various sources and preparing high quality images for the subsequent algorithms.
2. An automatic mid-sagittal plane detector was constructed to compute the mid-sagittal plane that separates the right and the left brain hemispheres with maximum symmetry.
3. A customised skull stripping algorithm was established to extract the intracranial brain from traumatic head CT scans with intact skulls. As compared to other skull stripping tools, the developed automatic brain extractor clearly defines the boundary of intracranial volume by automatically detecting the plane of Foramen Magnum.

4. Based on those developed tools, a novel concept called the midplane shift (MPS) has been proposed to quantitatively evaluate the brain herniation condition across the mid-sagittal plane.

7.1.2 Interpretation of CT parameters related to brain deformation

In chapter 3, the computational tools developed in chapter 2 have been applied to better interpret TBI-related head CT scans. Various novel CT parameters including the brain volume shift, the maximum midline shift, the MPS centroid and the lesion centroid have been considered to help better understand the mechanisms of TBI. The conclusions are as follows:

1. From a retrospective study of 85 TBI patients who only have symptoms in a single hemisphere (unilateral TBI), it was observed that while the clinical MLS is significantly associated with the volume size of the intracranial mass lesions, different types of haematoma play different roles in brain deformation. Among all the visible lesions in a CT scan, only subdural haematoma (SDH), epidural haematoma (EDH) and haemorrhagic contusion (CONT) are significantly associated with the development of MLS. A lesion-MLS model has been proposed to predict the clinical MLS using the various lesion volumes. This lesion-MLS model predicted the actual MLS with high correlation ($r = 0.92$). The model also suggested a new way to predict a patient's outcome by comparing the MLS predicted from the model with the actual MLS.
2. The MPS heat-maps of 33 different TBI patients indicated that, in the scenario of TBI, the brain shifts across the mid-sagittal plane demonstrate a highly similar pattern: the region of severe shifts tends to concentrate on the frontal ventricular region and decreases radially towards surface of the brain.
3. The maximum MLS is a better representation of the overall volumetric brain deformation than the traditional clinical MLS.
4. The clustering of patients based on their lesion heat-maps showed that the brain deforms in a regulated mechanism when subjects to trauma, so that the deformation is directed and restricted to the soft ventricular region, thanks to the anatomic structures of the head such as the rigid falx.

7.1.3 Biomechanical model development

In chapter 4, preliminary and patient-specific head models were developed for the simulation of TBI. The outcomes from this chapter are as follows:

1. The simulation results from the preliminary model suggest that the cerebral falx plays a critical role in TBI related brain deformation and should be included in more realistic TBI models.
2. A high-fidelity patient-specific model was successfully developed. The model provided reasonable geometry idealisation while maintaining the key brain substructures such as the falx and tentorium.
3. An indentation-based lesion simulation method was developed to customise the lesion occurring on the surface of the brain. It was shown that this patient-specific model outputs qualitatively-correct TBI simulation results as compared to the clinical observations.

7.1.4 Biomechanical model assessment

In chapter 5, an in-depth assessment of the patient-specific model was performed to further finalise the model. The conclusions are as follows:

1. For the current model, the optimum numerical performance was achieved with approximately 25,000 tetrahedral elements and a mass scaling that facilitates a target time increment of 1×10^{-5} s to accelerate the simulation.
2. The stages of TBI were successfully decomposed into the primary and secondary injuries in TBI simulations. An indentation-based mechanical loading method was applied to simulate the progress of haematoma developing and pressing on the surface of the brain, during the development of primary injury. As for the secondary swelling, a thermal-expansion-based loading method was used to simulate the bulging effects of the brain. With a combination of indentation-based mechanical loading and thermal-expansion-based loading, it is possible to retrospectively reproduce an observed head trauma with satisfactory accuracy both qualitatively and quantitatively.
3. The model sensitivity to material properties was observed to be very limited for the proposed deformation-dominated simulation scenario.
4. A surface-based fluid cavity was shown to be a viable way to simulate the ventricles inside the brain. The deformable natures of the ventricles were simulated with

the effective compressibility of the fluid cavity during lesion evolution. It was observed that the volume change of ventricles not only affects the magnitude of brain motion during lesion evolution, but also it plays a critical role in the distribution of deformations of brain tissues surrounding the ventricles.

7.1.5 Biomechanical model simulation

In chapter 6, both realistic TBI case studies and idealised TBI simulations were performed using the model developed and tuned in previous chapters. The conclusions are listed below:

1. Six TBI patients have been reconstructed successfully in the realistic case study. It was shown that the computer lesion simulation methodology is capable of differentiating the brain herniation as a result of secondary swelling from that due to the pure mass effect of the haematoma itself (primary injury). The SDH patients, as compared to the EDH patients, were exposed to more significant secondary swelling, which agrees well with the historical clinical findings.
2. A way of creating synthetic lesions was presented: by creating rigid spherical surfaces and indenting the rigid sphere into the brain. In this way, the lesion-brain interaction surface has been controlled and synthetic lesions can be applied across different locations. It was concluded from the idealised simulation that given the same volumes of mass lesions at the same locations inside the skull, the brain is more sensitive to lesion that is more concentrated spatially .
3. In terms of lesion locations, the brain is more sensitive to lesions in the temporal lobe, rather than the parietal lobe; and on the anterior region, rather than the posterior region, with other lesion morphologies being equal.
4. Swelling effects play an important role in redistributing the inner brain tissue deformation caused by the onset of primary injury.

7.1.6 Summary

The main outcome from the current study can be decomposed in to two main parts: medical image computing and biomechanical modelling.

On the one hand, several computational tools have been developed to customise the CT processing procedures for traumatic head injury patients. The application of the developed tools produced a set of novel CT parameters and enhanced the understanding

of TBI related brain deformation mechanism: the brain deforms in a regulated mechanism when subjects to trauma, so that the deformation is directed and restricted to the soft ventricular region, thanks to the anatomic structures of the head such as the rigid falx.

On the other hand, a patient-specific FE head model has been successfully developed. The decomposition of primary injury from secondary swelling during TBI simulation revealed that SDH patients are associated with more severe secondary swelling as compared to EDH patients. The idealised TBI modelling also suggested that the brain is more sensitive to lesions occurring at the temporal and anterior regions of the brain.

7.2 Limitations

The medical computing procedure was limited by the manual interventions required during the semi-automatic computations. The generation of MPS still relied on the manual expert delineation of the midline structures, which limited the efficiency of the procedure. The segmentations of the intracranial lesions also required manual inspections after crude segmentation by thresholding.

The outcome analysis of the developed multi-variant lesion-MLS model was limited by the number of TBI patients included in the study. However, despite the sample size being a potential limitation, it offered a new way to predict patients' outcome by comparing the predicted MLS with the actual MLS.

A number of simplifications were made in the patient-specific FE head model. The grey and white matter have not been differentiated in the model. The gyri, sulci and CSF in the interstitial space have been neglected on the surface of the cerebrum.

7.3 Future work

Firstly, there still exist some manual interventions in the semi-automatic computational tools in chapter 2. These tools should be fully automated in the future to increase the efficiency of the medical image computing process. In particular, the manual delineation of the brain mid-structures included in the generation of MPS still requires substantial works. Although the automatic delineation of mid-structures may be challenging, it seems possible to be solved by deep-learning-based image analysis method. Similarly, the accurate segmentation of various intracranial TBI lesions are expected to be fully

automated in the near future. With the help of the automatic MPS tools, more MPS heatmaps and lesion heatmaps should be generated. This will gain more confidence on the current hypotheses made based on the 33 TBI patients.

Secondly, more TBI patients are expected to be included to test the multi-variant lesion-MLS model in chapter 3. Factors including the patient ages and the cause of the injury can be added to further fine tune the model. The outcome analysis using the developed lesion-MLS model should also be expanded to include a larger number of patients in order to gain more insights on its prognostic values.

Thirdly, the currently developed FE head model can be further improved by differentiating the grey and white matter in the cerebrum, adding the gyri, sulci on the surface of the brain and including CSF in the interstitial space. Inclusion of more brain details will further improve the fidelity of the model towards a more realistic simulation result.

Fourthly, the way of simulating primary injury by an indentation-based mechanical loading requires further improvements. Now it only works for TBI that strikes on the surface of the brain, such as the subdural haematoma and the epidural haematoma, but not for those lesions which take place inside the brain, for example the intracerebral contusion. As a result, a more advanced primary-injury-simulation method is needed to expand the applicability of the model in TBI scenarios. Besides, the current way of simulating secondary swelling is to apply a uniform thermal-expansion to half or both of the brain hemispheres. In the future, when various swelling sites of the brain can be distinguished, it will be interesting to investigate the effect of non-uniform swelling across the brain.

Last but not least, axonal stretching of the brain tissue after a decompressive craniectomy (DC) will have a bearing on the efficacy of the surgery. So far, there exists continuing debate on the optimal timing and surgical parameters, as well as the long-term functional outcome of DC. Therefore, there is scope to use the developed patient-specific finite element computer model to simulate the brain behaviour after DC, help furthering the understanding of DC and optimising the surgical parameters, to improve patient outcome.

References

[1] M. Parsonage, "An economic analysis Traumatic brain injury and offending," Centre for Mental Health, Tech. Rep., 2016. [Online]. Available: https://www.t2a.org.uk/wp-content/uploads/2016/07/Centre-for-Mental-Health-Traumatic-brain-injury-and-offending-July-2016.pdf

[2] A. I. R. Maas, N. Stocchetti, and R. Bullock, "Moderate and severe traumatic brain injury in adults," *The Lancet Neurology*, vol. 7, no. 8, pp. 728–741, 2008.

[3] Headway, "Traumatic brain injury." [Online]. Available: https://www.headway.org.uk/about-brain-injury/individuals/types-of-brain-injury/traumatic-brain-injury/ [Accessed:2017-11-02].

[4] National Institute for Health and Care Excellence, "Head Injury - Triage, assessment, investigation and early management of head injury in children, young people and adults," no. August 2013, pp. 1–69, 2014.

[5] H. Neuroscience, B. Sharma, and D. W. Lawrence, "Top-cited articles in traumatic brain injury," *Frontiers in human neuroscience*, vol. 8, no. November, pp. 1–14, 2014.

[6] "English: Layers Covering the Brain." Mar. 2014. [Online]. Available: https://commons.wikimedia.org/wiki/File:Blausen_0110_BrainLayers.png A.

[7] C. Beynon, "A glimmer of hope for a devastating complication," *Blood*, vol. 129, no. 22, pp. 2952–2953, Jun. 2017.

[8] K. E. Saatman, A.-C. Duhaime, R. Bullock, A. I. Maas, A. Valadka, and G. T. Manley, "Classification of Traumatic Brain Injury for Targeted Therapies," *Journal of Neurotrauma*, vol. 25, no. 7, pp. 719–738, 2008.

[9] A. G. Kolias, P. J. Kirkpatrick, and P. J. Hutchinson, "Decompressive craniectomy: past, present and future," *Nat Rev Neurol*, vol. 9, no. 7, pp. 405–415, 2013.

[10] Brain herniation - wikipedia. [Online]. Available: https://en.wikipedia.org/wiki/Brain_herniation

[11] G. Teasdale and B. Jennett, "Assessment and prognosis of coma after head injury." *Acta Neurochir (Wien)*, vol. 34, no. 1-4, pp. 45–55, 1976.

[12] ——, "Assessment of coma and impaired consciousness: A practical scale," *The Lancet*, vol. 304, no. 7872, pp. 81 – 84, 1974, originally published as Volume 2, Issue 7872.

[13] "TBI: Mild Traumatic Brain Injury Symptoms | Concussions | Mild Head Injuries | Resources and Support." [Online]. Available: http://www.traumaticbraininjury.com/symptoms-of-tbi/mild-tbi-symptoms/ AA.

[14] R. K. Narayan, M. E. Michel, B. Ansell, A. Baethmann, A. Biegon, M. B. Bracken, M. R. Bullock, S. C. Choi, G. L. Clifton, C. F. Contant, W. M. Coplin, W. D. Dietrich, J. Ghajar, S. M. Grady, R. G. Grossman, E. D. Hall, W. Heetderks, D. A. Hovda, J. Jallo, R. L. Katz, N. Knoller, P. M. Kochanek, A. I. Maas, J. Majde, D. W. Marion, A. Marmarou, L. F. Marshall, T. K. McIntosh, E. Miller, N. Mohberg, J. P. Muizelaar, L. H. Pitts, P. Quinn, G. Riesenfeld, C. S. Robertson, K. I. Strauss, G. Teasdale, N. Temkin, R. Tuma, C. Wade, M. D. Walker, M. Weinrich, J. Whyte, J. Wilberger, A. B. Young, and L. Yurkewicz, "Clinical trials in head injury," *Journal of Neurotrauma*, vol. 19, no. 5, pp. 503–557, May 2002.

[15] "CT scan," Nov. 2017. [Online]. Available: https://en.wikipedia.org/w/index.php?title=CT_scan&oldid=808229121 Page Version ID: 808229121.

[16] "Magnetic resonance imaging," Nov. 2017. [Online]. Available: https://en.wikipedia.org/w/index.php?title=Magnetic_resonance_imaging&oldid=808683801 Page Version ID: 808683801.

[17] C. Wenan, "Automated Measurement of Midline Shift in Brain CT Images and its Application in Computer-Aided Medical Decision Making," 2010.

[18] "Central Nervous System (CNS) - ppt download." [Online]. Available: http://slideplayer.com/slide/10771451/ D.

[19] L. R. Gentry, J. C. Godersky, B. Thompson, and V. D. Dunn, "Prospective comparative study of intermediate-field MR and CT in the evaluation of closed head trauma," *AJR. American journal of roentgenology*, vol. 150, no. 3, pp. 673–682, Mar. 1988.

[20] P. C. Davis and Expert Panel on Neurologic Imaging, "Head trauma," *AJNR. American journal of neuroradiology*, vol. 28, no. 8, pp. 1619–1621, Sep. 2007.

[21] C. Hawthorne and I. Piper, "Monitoring of intracranial pressure in patients with traumatic brain injury," *Frontiers in Neurology*, vol. 5 JUN, no. July, pp. 1–16, 2014.

[22] M. Khan, H. Shallwani, M. Khan, and M. Shamim, "Noninvasive monitoring intracranial pressure - A review of available modalities," *Surgical Neurology International*, vol. 8, no. 1, 2017.

[23] K. L. Triebel, R. C. Martin, T. A. Novack, L. Dreer, C. Turner, P. R. Pritchard, R. Raman, and D. C. Marson, "Treatment consent capacity in patients with traumatic brain injury across a range of injury severity," *Neurology*, vol. 78, no. 19, pp. 1472–1478, May 2012.

[24] N. Carney, A. M. Totten, C. O'Reilly, J. S. Ullman, G. W. J. Hawryluk, M. J. Bell, S. L. Bratton, R. Chesnut, O. A. Harris, N. Kissoon, A. M. Rubiano, L. Shutter, R. C. Tasker, M. S. Vavilala, J. Wilberger, D. W. Wright, and J. Ghajar, "Guidelines for the Management of Severe Traumatic Brain Injury, Fourth Edition," *Neurosurgery*, vol. 80, no. 1, pp. 6–15, Jan. 2017.

[25] H. Cryer, G. Manley, D. Adelson, A. Alali, F. Calland, M. Cipolle, C. Cribari, M. Davis, O. Harris, M. Hemmila, C. Hemphill, M. Huang, R. Jawa, T. Kilbaugh, R. Kozar, A. Maas, L. Merck, A. Nathens, C. Robertson, G. Rosenthal, P. Tarapore, S. Timmons, J. Ullman, A. Valadka, and D. Wright, "ACS TQIP Best Practices in the Management of Traumatic Brain Injury," *Journal of the American College of Surgeons*, vol. 220, no. 5, pp. 981–985, 2015.

[26] H. Adams, A. G. Kolias, and P. J. Hutchinson, "The Role of Surgical Intervention in Traumatic Brain Injury," *Neurosurgery Clinics of North America*, vol. 27, no. 4, pp. 519–528, 2016.

[27] E. M. Bulger, A. B. Nathens, F. P. Rivara, M. Moore, E. J. MacKenzie, G. J. Jurkovich, and Brain Trauma Foundation, "Management of severe head injury: institutional variations in care and effect on outcome." *Critical care medicine*, vol. 30, no. 8, pp. 1870–6, aug 2002.

[28] S. Badri, J. Chen, J. Barber, N. R. Temkin, S. S. Dikmen, R. M. Chesnut, S. Deem, N. D. Yanez, and M. M. Treggiari, "Mortality and long-term functional outcome associated with intracranial pressure after traumatic brain injury," *Intensive Care Medicine*, vol. 38, no. 11, pp. 1800–1809, nov 2012.

[29] E. Bor-Seng-Shu, E. Figueiredo, R. Amorim, and E. al., "Decompressive craniectomy: A meta-analysis of influences on intracranial pressure and cerebral perfusion pressure in the treatment of traumatic brain injury," *Journal of Neurosurgery*, vol. 117, no. 3, pp. 589–596, 2012.

[30] I. Timofeev, M. Czosnyka, J. Nortje, P. Smielewski, P. Kirkpatrick, A. Gupta, and P. Hutchinson, "Effect of decompressive craniectomy on intracranial pressure and cerebrospinal compensation following traumatic brain injury." *Journal of Neurosurgery*, vol. 108, no. 1, pp. 66–73, 2008.

[31] P. J. Hutchinson, A. G. Kolias, I. S. Timofeev, E. A. Corteen, M. Czosnyka, J. Timothy, I. Anderson, D. O. Bulters, A. Belli, C. A. Eynon, J. Wadley, A. D. Mendelow, P. M. Mitchell, M. H. Wilson, G. Critchley, J. Sahuquillo, A. Unterberg, F. Servadei, G. M. Teasdale, J. D. Pickard, D. K. Menon, G. D. Murray, and P. J. Kirkpatrick, "Trial of Decompressive Craniectomy for Traumatic Intracranial Hypertension," *New England Journal of Medicine*, p. NEJMoa1605215, 2016.

[32] J. Wright, "Glasgow Outcome Scale – Extended," in *Encyclopedia of Clinical Neuropsychology*, J. S. Kreutzer, J. DeLuca, and B. Caplan, Eds. Springer New York, 2011, pp. 1152–1153, dOI: 10.1007/978-0-387-79948-3_1940. [Online]. Available: http://link.springer.com/referenceworkentry/10.1007/978-0-387-79948-3_1940

[33] A. Taylor, W. Butt, J. Rosenfeld, F. Shann, M. Ditchfield, E. Lewis, G. Klug, D. Wallace, R. Henning, and J. Tibballs, "A randomized trial of very early decompressive craniectomy in children with traumatic brain injury and sustained intracranial hypertension," *Child's Nervous System*, vol. 17, no. 3, pp. 154–162, feb 2001.

[34] P. Mitchell, M. Med, C. Wriedt, S. Graves, D. Phil, M. P. Staples, D. Ph, B. Murphy, and B. Sc, "New England Journal," *Sciences-New York*, pp. 557–568, 2009.

[35] R. Rahme, M. Zuccarello, D. Kleindorfer, O. M. Adeoye, and A. J. Ringer, "Decompressive hemicraniectomy for malignant middle cerebral artery territory infarction: is life worth living?" *Journal of Neurosurgery*, vol. 117, no. 4, pp. 749–754, Oct. 2012.

[36] R. G. Whitmore, J. P. Thawani, M. S. Grady, J. M. Levine, M. R. Sanborn, and S. C. Stein, "Is aggressive treatment of traumatic brain injury cost-effective?" *Journal of Neurosurgery*, vol. 116, no. 5, pp. 1106–1113, May 2012.

[37] D. D. H. MCKEE Ann C., *The neuropathology of Traumatic brain injury*, 2015, vol. 15.

[38] D. H. Smith, J. A. Wolf, T. A. Lusardi, V. M. Lee, and D. F. Meaney, "High tolerance and delayed elastic response of cultured axons to dynamic stretch injury,"

The Journal of Neuroscience: The Official Journal of the Society for Neuroscience, vol. 19, no. 11, pp. 4263–4269, Jun. 1999.

[39] "Illinois Diffuse Axonal Injury Recovery | Illinois Brain Lawyers | Illinois' Comprehensive Brain Injury Website." [Online]. Available: http://illinoisbrainlaw.com/illinois-diffuse-axonal-injury-recovery/ A.

[40] R. M. Wright and K. T. Ramesh, "An axonal strain injury criterion for traumatic brain injury," *Biomechanics and Modeling in Mechanobiology*, vol. 11, no. 1-2, pp. 245–260, 2012.

[41] *Mécanique des matériaux solides*, Nov. 2017. [Online]. Available: https://www.dunod.com/sciences-techniques/mecanique-materiaux-solides

[42] E. G. Takhounts, R. H. Eppinger, J. Q. Campbell, R. E. Tannous, E. D. Power, and L. S. Shook, "On the Development of the SIMon Finite Element Head Model," *Stapp Car Crash Journal*, vol. 47, pp. 107–133, Oct. 2003.

[43] A. C. Bain and D. F. Meaney, "Tissue-Level Thresholds for Axonal Damage in an Experimental Model of Central Nervous System White Matter Injury," *Journal of Biomechanical Engineering*, vol. 122, no. 6, p. 615, 2000.

[44] S. Ganpule, N. Daphalapurkar, K. T. Ramesh, A. Knutsen, D. L. Pham, P. Bayly, and J. Prince, "A 3D Computational Human Head Model that Captures Live Human Brain Dynamics," *Journal of Neurotrauma*, vol. 13, p. neu.2016.4744, 2017.

[45] A. Goriely, S. Budday, and E. Kuhl, "Chapter Two – Neuromechanics: From Neurons to Brain," in *Advances in Applied Mechanics*, 2015, vol. 48, pp. 79–139.

[46] S. Budday, G. Sommer, C. Birkl, C. Langkammer, J. Haybaeck, J. Kohnert, M. Bauer, F. Paulsen, P. Steinmann, E. Kuhl, and G. Holzapfel, "Mechanical characterization of human brain tissue," *Acta Biomaterialia*, vol. 48, pp. 23–29, 2016.

[47] X. Jin, F. Zhu, H. Mao, M. Shen, and K. H. Yang, "A comprehensive experimental study on material properties of human brain tissue," *Journal of Biomechanics*, vol. 46, no. 16, pp. 2795–2801, 2013.

[48] J. E. Galford and J. H. McElhaney, "A viscoelastic study of scalp, brain, and dura," *Journal of Biomechanics*, vol. 3, no. 2, pp. 211–221, 1970.

[49] G. Franceschini, D. Bigoni, P. Regitnig, and G. A. Holzapfel, "Brain tissue deforms similarly to filled elastomers and follows consolidation theory," *Journal of the Mechanics and Physics of Solids*, vol. 54, no. 12, pp. 2592–2620, 2006.

[50] J. F. V. Vincent, *Biomechanics–materials: A Practical Approach*, ser. Practical approach series. IRL Press at Oxford University Press, 1992. [Online]. Available: https://books.google.co.uk/books?id=AOJqAAAAMAAJ

[51] T. P. Prevost, G. Jin, M. A. De Moya, H. B. Alam, S. Suresh, and S. Socrate, "Dynamic mechanical response of brain tissue in indentation in vivo, in situ and in vitro," *Acta Biomaterialia*, vol. 7, no. 12, pp. 4090–4101, 2011.

[52] J. A. W. van Dommelen, T. P. J. van der Sande, M. Hrapko, and G. W. M. Peters, "Mechanical properties of brain tissue by indentation: Interregional variation," *Journal of the Mechanical Behavior of Biomedical Materials*, vol. 3, no. 2, pp. 158–166, 2010.

[53] G. T. Fallenstein, V. D. Hulce, and J. W. Melvin, "Dynamic Mechanical Properties Tissue "?" *J. Biomechanics*, vol. 2, pp. 217–226, 1969.

[54] J. Braun, J. Guo, R. Lützkendorf, J. Stadler, S. Papazoglou, S. Hirsch, I. Sack, and J. Bernarding, "High-resolution mechanical imaging of the human brain by three-dimensional multifrequency magnetic resonance elastography at 7T," *NeuroImage*, vol. 90, pp. 308–314, 2014.

[55] M. C. Murphy, J. Huston, C. R. Jack, K. J. Glaser, M. L. Senjem, J. Chen, A. Manduca, J. P. Felmlee, and R. L. Ehman, "Measuring the characteristic topography of brain stiffness with magnetic resonance elastography," *PLoS ONE*, vol. 8, no. 12, pp. 1–14, 2013.

[56] D. j. Kim, "Clinical and engineering models of brain compliance and deformation associated with neurological disorders by," no. March, 2010.

[57] A. Garo, M. Hrapko, J. A. W. Van Dommelen, and G. W. M. Peters, "Towards a reliable characterisation of the mechanical behaviour of brain tissue: The effects of post-mortem time and sample preparation," *Biorheology*, vol. 44, no. 1, pp. 51–58, 2007.

[58] M. T. Prange and S. S. Margulies, "Regional, Directional, and Age-Dependent Properties of the Brain Undergoing Large Deformation," *Journal of Biomechanical Engineering*, vol. 124, no. 2, pp. 244–252, mar 2002.

[59] A. Gefen and S. S. Margulies, "Are in vivo and in situ brain tissues mechanically similar?" *Journal of Biomechanics*, vol. 37, no. 9, pp. 1339–1352, 2004.

[60] M. Ghajari, P. J. Hellyer, and D. J. Sharp, "Computational modelling of traumatic brain injury predicts the location of chronic traumatic encephalopathy pathology," *Brain*, vol. 140, no. 2, 2017.

[61] J. Weickenmeier, C. A. M. Butler, P. G. Young, A. Goriely, and E. Kuhl, "The mechanics of decompressive craniectomy: Personalized simulations," *Computer Methods in Applied Mechanics and Engineering*, vol. 314, pp. 180–195, 2016.

[62] T. L. Fletcher, A. G. Kolias, P. J. A. Hutchinson, and M. P. F. Sutcliffe, "Development of a finite element model of decompressive craniectomy," *PLoS ONE*, vol. 9, no. 7, pp. 1–9, 2014.

[63] H. von Holst and X. Li, "Decompressive craniectomy (DC) at the non-injured side of the brain has the potential to improve patient outcome as measured with computational simulation," *Acta Neurochirurgica*, pp. 1961–1967, 2014.

[64] J.-M. Wong, K.-C. Huang, F. Xiao, Y.-H. Tsai, C.-C. Liao, I.-J. Chiang, and Y.-L. Chen, "Modeling and simulation of brain herniation caused by subdural hematoma using finite-element method," *MATEC Web of Conferences*, vol. 169, p. 01046, 2018.

[65] X. Li, *Finite Element and Neuroimaging Techniques to Improve Decision-Making in Clinical Neuroscience*, 2012, no. May. [Online]. Available: http://kth.diva-portal.org/smash/record.jsf?searchId=1{&}pid=diva2:487687

[66] B. T. Smith and J. M. Boyle, *Lecture notes in computer science*, 2009. [Online]. Available: http://www.ulb.tu-darmstadt.de/tocs/79304567.pdf

[67] J. Gee, T. Sundaram, I. Hasegawa, H. Uematsu, and H. Hatabu, "Characterization of regional pulmonary mechanics from serial MRI data," *Medical Image Computing and Computer-Assisted Intervention-Miccai 2002, Pt 1*, vol. 2488, no. c, pp. 762–769, 2002.

[68] T. L. Fletcher, "Brain deformation during decompressive craniectomy," *Methods*, 2011.

[69] X. Li, P. S. Morgan, J. Ashburner, J. Smith, and C. Rorden, "The first step for neuroimaging data analysis: DICOM to NIfTI conversion," *Journal of Neuroscience Methods*, vol. 264, pp. 47–56, 2016.

[70] T. L. Fletcher, A. G. Kolias, P. J. Hutchinson, and M. P. F. Sutcliffe, "A new improved method for assessing brain deformation after decompressive craniectomy," *PLoS ONE*, vol. 9, no. 10, 2014.

[71] H. Liang, C. Zhang, and M. Yan, "Data correction for gantry-tilted local CT," *Computerized Medical Imaging and Graphics*, vol. 32, no. 4, pp. 251–257, 2008.

[72] "NITRC: dcm2nii: Tool/Resource Info." [Online]. Available: https://www.nitrc.org/projects/dcm2nii/

[73] "xiangruili/dicm2nii - File Exchange - MATLAB Central." [Online]. Available: https://www.mathworks.com/matlabcentral/fileexchange/42997-xiangruili-dicm2nii

[74] "Dcm2niix :: Anaconda Cloud." [Online]. Available: https://anaconda.org/conda-forge/dcm2niix

[75] "SPM software - Statistical Parametric Mapping." [Online]. Available: https://www.fil.ion.ucl.ac.uk/spm/software/

[76] Z. Yaniv, B. C. Lowekamp, H. J. Johnson, and R. Beare, "SimpleITK Image-Analysis Notebooks: a Collaborative Environment for Education and Reproducible Research," *Journal of Digital Imaging*, vol. 31, no. 3, pp. 290–303, 2018.

[77] M. Jenkinson, P. Bannister, M. Brady, and S. Smith, "Improved optimization for the robust and accurate linear registration and motion correction of brain images," *NeuroImage*, vol. 17, no. 2, pp. 825–841, Oct. 2002.

[78] Commissural pathways: Anatomy and function | kenhub. [Online]. Available: https://www.kenhub.com/en/library/anatomy/commissural-pathways

[79] (2019, 2) Image registration - Wikipedia. [Online]. Available: https://en.wikipedia.org/wiki/Image_registration#cite_note-5

[80] "CitingSlicer - SlicerWiki." [Online]. Available: https://www.slicer.org/wiki/CitingSlicer

[81] "MIRTK – BioMedIA." [Online]. Available: https://biomedia.doc.ic.ac.uk/software/mirtk/

[82] About the MNI space(s) – lead-DBS. [Online]. Available: https://www.lead-dbs.org/about-the-mni-spaces/

[83] Principal component analysis: a review and recent developments | philosophical transactions of the royal society a: Mathematical, physical and engineering sciences. [Online]. Available: https://royalsocietypublishing.org/doi/10.1098/rsta.2015.0202

[84] A. Lauric and S. Frisken, "Soft Segmentation of CT Brain Data," p. 12, 2007.

[85] H. Li, R. Deklerck, B. D. Cuyper, A. Hermanus, E. Nyssen, and J. Cornelis, "Object recognition in brain CT-scans: knowledge-based fusion of data from multiple feature extractors," *IEEE Transactions on Medical Imaging*, vol. 14, no. 2, pp. 212–229, Jun. 1995.

[86] S. M. Smith, "Fast robust automated brain extraction," *Human Brain Mapping*, vol. 17, no. 3, pp. 143–155, Nov. 2002.

[87] J. Muschelli, N. L. Ullman, W. A. Mould, P. Vespa, D. F. Hanley, and C. M. Crainiceanu, "Validated automatic brain extraction of head CT images." *NeuroImage*, vol. 114, pp. 379–85, jul 2015.

[88] V. Popescu, M. Battaglini, W. S. Hoogstrate, S. C. J. Verfaillie, I. C. Sluimer, R. A. van Schijndel, B. W. van Dijk, K. S. Cover, D. L. Knol, M. Jenkinson, F. Barkhof, N. de Stefano, H. Vrenken, F. Barkhof, X. Montalban, F. Fazekas, M. Filippi, J. Frederiksen, L. Kappos, D. Miller, J. Palace, C. Polman, M. Rocca, A. Rovira, and T. Yousry, "Optimizing parameter choice for FSL-Brain Extraction Tool (BET) on 3D T1 images in multiple sclerosis," *NeuroImage*, vol. 61, no. 4, pp. 1484–1494, 2012.

[89] "scipy.ndimage.sobel — SciPy v0.19.1 Reference Guide." [Online]. Available: https://docs.scipy.org/doc/scipy-0.19.1/reference/generated/scipy.ndimage.sobel.html S.

[90] "Straight line Hough transform — skimage v0.14dev docs." [Online]. Available: http://scikit-image.org/docs/dev/auto_examples/edges/plot_line_hough_transform.html S.

[91] A. Ratnakar, "A study on correlation of degree of midline shift on CT scan and Glasgow coma scale in patients of acute traumatic head injury," *International Journal of Research in Medical Sciences*, vol. 2, no. 3, pp. 1063–1066, 2014.

[92] F. Xiao, I. J. Chiang, J. M. Wong, Y. H. Tsai, K. C. Huang, and C. C. Liao, "Automatic measurement of midline shift on deformed brains using multiresolution binary level set method and Hough transform," *Computers in Biology and Medicine*, vol. 41, no. 9, pp. 756–762, 2011.

[93] T. Nasada, S. Hirayama, M. Tanooka, T. Fujita, and T. Sakai, "Evaluation of gantry tilt correction in multi detector-row CT : Effect on multi-planar reconstruction images," vol. 59, pp. 136–42.

[94] S. Raghunathan, D. Stredney, P. Schmalbrock, and B. D. Clymer, "Image Registration Using Rigid Registration and Maximization of Mutual Information," *Entropy*, pp. 1999–1999, 1999.

[95] M. Jenkinson, P. Bannister, M. Brady, and S. Smith, "Improved optimization for the robust and accurate linear registration and motion correction of brain images," *NeuroImage*, vol. 17, no. 2, pp. 825–841, Oct. 2002.

[96] H. Gray. (before 1858) "drawing of a cast of the ventricular cavities, viewed from above. (retzius.)". [Online]. Available: https://commons.wikimedia.org/wiki/File:Gray735.png

[97] "Falx cerebri - Wikipedia." [Online]. Available: https://en.wikipedia.org/wiki/Falx_cerebri 1.

[98] M. C. T. MRC CRASH Trial Collaborators, P. Perel, M. Arango, T. Clayton, P. Edwards, E. Komolafe, S. Poccock, I. Roberts, H. Shakur, E. Steyerberg, and S. Yutthakasemsunt, "Predicting outcome after traumatic brain injury: practical prognostic models based on large cohort of international patients." *BMJ (Clinical research ed.)*, vol. 336, no. 7641, pp. 425–9, feb 2008.

[99] P. Edwards, M. Arango, L. Balica, R. Cottingham, H. El-Sayed, B. Farrell, J. Fernandes, T. Gogichaisvili, N. Golden, B. Hartzenberg, M. Husain, M. I. Ulloa, Z. Jerbi, H. Khamis, E. Komolafe, V. Laloë, G. Lomas, S. Ludwig, G. Mazairac, M. d. l. A. Muñoz Sanchéz, L. Nasi, F. Olldashi, P. Plunkett, I. Roberts, P. Sandercock, H. Shakur, C. Soler, R. Stocker, P. Svoboda, S. Trenkler, N. K. Venkataramana, J. Wasserberg, D. Yates, S. Yutthakasemsunt, and C. trial collaborators, "Final results of MRC CRASH, a randomised placebo-controlled trial of intravenous corticosteroid in adults with head injury-outcomes at 6 months." *Lancet (London, England)*, vol. 365, no. 9475, pp. 1957–9, jun 2005.

[100] A. I. Maas, E. W. Steyerberg, I. Butcher, R. Dammers, J. Lu, A. Marmarou, N. A. Mushkudiani, G. S. McHugh, and G. D. Murray, "Prognostic Value of Computerized Tomography Scan Characteristics in Traumatic Brain Injury: Results from The IMPACT Study," *Journal of Neurotrauma*, vol. 24, no. 2, pp. 303–314, feb 2007.

[101] P. Chiewvit, S.-O. Tritakarn, S. Nanta-Aree Md, and S. Suthipongchai, "Degree of Midline Shift from CT Scan Predicted Outcome in Patients with Head Injuries," *J Med Assoc Thai*, vol. 93, no. 1, pp. 99–107, 2010.

[102] D. W. Nelson, H. Nyströ, R. M. Maccallum, B. R. Thornquist, A. Lilja, B.-M. Bellander, A. Rudehill, M. Wanecek, and E. Weitzberg, "Extended Analysis of Early Computed Tomography Scans of Traumatic Brain Injured Patients and Relations to Outcome," *J Nerotrauma*, 2010.

[103] *Observations on the structure and functions of the nervous system : illustrated with tables. | Anatomia Collection: anatomical plates 1522-1867.* William Creech, and by T. Cadell, P. Elmsley, J. Murray, and T. Longman, London, Monro, Alexander 1783. [Online]. Available: https://anatomia.library.utoronto.ca/islandora/object/anatomia%3ARBAI051

[104] G. Kellie, "Appearances Observed in the Dissection of Two Individuals; Death from Cold and Congestion of the Brain," *Tr. Med.-Chir. Soc. Edinburgh*, vol. 1, pp. 84+, 1824.

[105] K. A. Chun, G. T. Manley, S. I. Stiver, A. H. Aiken, N. Phan, V. Wang, M. Meeker, S.-C. Cheng, A. D. Gean, and M. Wintermark, "Interobserver Variability in the Assessment of CT Imaging Features of Traumatic Brain Injury," Tech. Rep., 2009. [Online]. Available: www.liebertpub.com

[106] N. Stocchetti, M. Croci, D. Spagnoli, F. Gilardoni, F. Resta, and A. Colombo, "Mass volume measurement in severe head injury: accuracy and feasibility of two pragmatic methods." *Journal of neurology, neurosurgery, and psychiatry*, vol. 68, no. 1, pp. 14–7, jan 2000.

[107] A. Pasqualin, G. Barone, F. Cioffi, L. Rosta, R. Scienza, and R. Da Pian, "The relevance of anatomic and hemodynamic factors to a classification of cerebral arteriovenous malformations." *Neurosurgery*, vol. 28, no. 3, pp. 370–9, mar 1991.

[108] R. E. Clatterbuck and E. P. Sipos, "The efficient calculation of neurosurgically relevant volumes from computed tomographic scans using Cavalieri's Direct Estimator." *Neurosurgery*, vol. 40, no. 2, pp. 339–42; discussion 343, feb 1997.

[109] C.-C. Liao, Y.-F. Chen, and F. Xiao, "Brain Midline Shift Measurement and Its Automation: A Review of Techniques and Algorithms," 2018. [Online]. Available: https://www.hindawi.com/journals/ijbi/2018/4303161/

[110] B. Jennett and M. Bond, "ASSESSMENT OF OUTCOME AFTER SEVERE BRAIN DAMAGE: A Practical Scale," *The Lancet*, vol. 305, no. 7905, pp. 480–484, Mar. 1975.

[111] J. M. Gebel, C. A. Sila, M. A. Sloan, C. B. Granger, J. P. Weisenberger, C. L. Green, E. J. Topol, and K. W. Mahaffey, "Comparison of the ABC/2 Estimation Technique to Computer-Assisted Volumetric Analysis of Intraparenchymal and Subdural Hematomas Complicating the GUSTO-1 Trial," Tech. Rep., 1998. [Online]. Available: http://ahajournals.org

[112] B. Jacobs, T. Beems, T. M. Van Der Vliet, R. R. Diaz-Arrastia, G. F. Borm, and P. E. Vos, "Computed Tomography and Outcome in Moderate and Severe Traumatic Brain Injury: Hematoma Volume and Midline Shift Revisited."

[113] R. Liu, S. Li, and C. L. Tan, "FROM HEMORRHAGE TO MIDLINE SHIFT : A NEW METHOD OF TRACING THE DEFORMED MIDLINE IN TRAUMATIC BRAIN INJURY CT IMAGES * School of Computing , National University of Singapore ** National Neuroscience Institute *** Institute for Infocomm Research," *Work*, no. iML, pp. 2637–2640, 2009.

[114] C. C. Liao, Y. F. Chen, and F. Xiao, "Brain midline shift measurement and its automation: A review of techniques and algorithms," *International Journal of Biomedical Imaging*, vol. 2018, 2018.

[115] R. H. Bartels, F. J. Meijer, H. van der Hoeven, M. Edwards, and M. Prokop, "Midline shift in relation to thickness of traumatic acute subdural hematoma predicts mortality," *BMC Neurology*, vol. 15, no. 1, 2015.

[116] "NEVA EM | Electromagnetic Modeling and Simulation." [Online]. Available: https://www.nevaelectromagnetics.com/vhp-female-2-2 A.

[117] P. Cignoni, M. Callieri, M. Corsini, M. Dellepiane, F. Ganovelli, and G. Ranzuglia, "MeshLab: an Open-Source Mesh Processing Tool," 2008, dOI: 10.2312/LocalChapterEvents/ItalChap/ItalianChapConf2008/129-136.

[118] "Add-ons Extensions | ABAQUS - Dassault Systèmes®." [Online]. Available: https://www.3ds.com/products-services/simulia/products/abaqus/add-ons/extensions/ A.

[119] L.F. Marshall, S. Bowers Marshall, M.R. Klauber, M. van Berkum Clark, H.M. Eisenberg, J.A. Jane, T. G. Luerssen, A. Marmarou, and M.A. Foulkes, "A

new classification of head injury based on computerized tomography," *Journal of Neurosurgery*, vol. 75, no. 1s, pp. S14–S20, 1991.

[120] E. Dynamics, S. C. Problems, E. Procedure, S. T. Increment, B. V. Damping, E. Balance, and M. D. Messages, "Overview of ABAQUS / Explicit What is Explicit Dynamics ?" 2005.

[121] L. W. Marks and T. N. Gardner, "The use of strain energy as a convergence criterion in the finite element modelling of bone and the effect of model geometry on stress convergence," *Journal of Biomedical Engineering*, vol. 15, no. 6, pp. 474–476, 1993.

[122] J. S. Giudice, W. Zeng, T. Wu, A. Alshareef, D. F. Shedd, and M. B. Panzer, "An Analytical Review of the Numerical Methods used for Finite Element Modeling of Traumatic Brain Injury," *Annals of Biomedical Engineering*, 2018.

[123] S. C. Tadepalli, A. Erdemir, and P. R. Cavanagh, "Comparison of hexahedral and tetrahedral elements in finite element analysis of the foot and footwear," *Journal of Biomechanics*, 2011.

[124] L. A. Mihai, L. Chin, P. A. Janmey, and A. Goriely, "A comparison of hyperelastic constitutive models applicable to brain and fat tissues." *Journal of the Royal Society, Interface / the Royal Society*, vol. 12, no. 110, p. 0486, 2015.

[125] M. Hosseini-Farid, M. Ramzanpour, M. Ziejewski, and G. Karami, "A compressible hyper-viscoelastic material constitutive model for human brain tissue and the identification of its parameters," *International Journal of Non-Linear Mechanics*, 2019.

[126] R. Moran, J. H. Smith, and J. J. García, "Fitted hyperelastic parameters for Human brain tissue from reported tension, compression, and shear tests," *Journal of Biomechanics*, 2014.

[127] D. C. Viano, I. R. Casson, E. J. Pellman, L. Zhang, A. I. King, and K. H. Yang, "Concussion in professional football: Brain responses by finite element analysis: Part 9," *Neurosurgery*, vol. 57, no. 5, pp. 891–915, 2005.

[128] T. J. Horgan and M. D. Gilchrist, "The creation of three-dimensional finite element models for simulating head impact biomechanics," *International Journal of Crashworthiness*, vol. 8, no. 4, pp. 353–366, 2003.

[129] R. Willinger and D. Baumgartner, "Human head tolerance limits to specific injury mechanisms," *International Journal of Crashworthiness*, vol. 8, no. 6, pp. 605–617, 2003.

[130] L. Zhang, K. H. Yang, R. Dwarampudi, K. Omori, T. Li, K. Chang, W. N. Hardy, T. B. Khalil, and A. I. King, "Recent Advances in Brain Injury Research: A New Human Head Model Development and Validation," in *SAE Technical Papers*, no. November. SAE International, nov 2001.

[131] K. Baeck, J. Goffin, and J. Sloten Vander, "The use of different CSF representations in a numerical head model and their effect on the results of FE head impact analyses," *8th European LS-DYNA Users Conference*, no. May, 2011.

[132] B. Baillargeon, N. Rebelo, D. D. Fox, R. L. Taylor, and E. Kuhl, "The living heart project: A robust and integrative simulator for human heart function," *European Journal of Mechanics, A/Solids*, vol. 48, no. 1, pp. 38–47, 2014.

[133] J. Ivarsson, D. C. Viano, and P. Lövsund, "Influence of the lateral ventricles and irregular skull base on brain kinematics due to sagittal plane head rotation," *Journal of Biomechanical Engineering*, vol. 124, no. 4, pp. 422–431, aug 2002.

[134] A. K. Knutsen, E. Magrath, J. E. McEntee, F. Xing, J. L. Prince, P. V. Bayly, J. A. Butman, and D. L. Pham, "Improved measurement of brain deformation during mild head acceleration using a novel tagged MRI sequence," *Journal of Biomechanics*, vol. 47, no. 14, pp. 3475–3481, 2014.

[135] M. Zum, R. Behrmann, H. E. Heissler, and H. Dietz, "Computed Tomographic Criteria and Survival Rate for Patients with Acute Subdural Hematoma," *Neurosurgery*, vol. 39, no. 4, October 1996.